

Doctoral Dissertation
博士論文

**Search for the Slepton Cascade Decay using
Final States with Opposite or Same Sign
Three Leptons in the LHC-ATLAS experiment**

**(LHC-ATLAS 実験における逆符号または同符号の
3つのレプトンを持つ終状態を用いた
スレプトンカスケード崩壊の探索)**

A Dissertation Submitted for the Degree of Doctor of Philosophy
December 2024

令和6年12月博士(理学)申請

Department of Physics, Graduate School of Science,
The University of Tokyo

東京大学大学院理学系研究科物理学専攻

Takumi Aoki

青木 匠

**Search for the Slepton Cascade Decay using Final
States with Opposite or Same Sign Three Leptons in
the LHC-ATLAS experiment**

Doctoral dissertation

Takumi Aoki

Department of Physics,
School of Science,
The University of Tokyo

February 17, 2025

Abstract

The Standard Model of particle physics (SM) provides a remarkably successful framework for describing nearly all known phenomena in particle physics. Despite its successes, the SM leaves several fundamental issues unresolved, such as the fine-tuning problem associated with the Higgs boson mass, the nature of dark matter, and the muon $g - 2$ anomaly, among others. The Minimal Supersymmetric Standard Model (MSSM) is one of the most compelling extensions of the SM. Supersymmetry (SUSY) posits a symmetry between bosons and fermions and predicts the existence of new partner particles, referred to as “superpartners”, for every SM particle. Although no direct evidence for SUSY particles has been observed in collider experiments to date, ongoing searches at the Large Hadron Collider (LHC), which operates at high center-of-mass energies and accumulates large data sets, continue to probe the phase space for heavier and rarer SUSY particles. To account for the muon $g - 2$ anomaly within the SUSY framework, at least three SUSY particles must have sufficiently light masses, typically of the order of 100 GeV. A promising model that addresses both the muon $g - 2$ anomaly and a portion of the dark matter abundance involves a specific mass hierarchy where the light-flavored left-handed sleptons ($\tilde{\ell}_L$; \tilde{e}_L or $\tilde{\mu}_L$), along with a nearly degenerate sneutrino ($\tilde{\nu}$), are the heaviest states, while the bino-dominated neutralino ($\tilde{\chi}_3^0$) occupies an intermediate mass range, and the Higgsino consists the lightest SUSY particle ($\tilde{\chi}_1^0$). Due to the small coupling between sleptons and the Higgsino, determined basically by the Yukawa coupling, sleptons predominantly undergo cascade decays into $\tilde{\chi}_1^0$ via $\tilde{\chi}_3^0$ in collider experiments. This characteristic decay pattern plays a crucial role in experimental searches for this model.

This thesis presents a search for the cascade decay of left-handed sleptons and sneutrinos using 140 fb^{-1} of proton-proton collision data at $\sqrt{s} = 13 \text{ TeV}$, collected by the ATLAS detector. The search focuses on events characterized by a final state with exactly three leptons. Two distinct analysis strategies are employed: one requiring a same-flavor opposite-sign lepton pair with a large transverse mass and significant missing transverse energy (SR0S), and the other requiring three leptons with the same electric charge (SRSS). These strategies are optimized to enhance the sensitivity to targeted SUSY signals while suppressing the SM background contributions. The phase space probed by these strategies has not been explored in previous LHC analyses, making this search a novel contribution to SUSY studies. Strategies for estimating the dominant backgrounds have been developed and rigorously validated. In particular, a unique background estimation method is developed specifically for regions containing two or more muons in the SRSS category.

The observed event yields, after applying the optimized selection criteria, are carefully compared to the expected background and signal yields. This comparison, along with the analysis of the features of selected events, revealed no significant deviations from the predictions of the null signal hypothesis. Consequently, it is concluded that no evidence of a data excess indicative of the targeted slepton decay scenario is found within the dataset. Exclusion limits are therefore established for the targeted slepton decay scenario. Slepton masses up to 450 (420) GeV are excluded at the 95% confidence level for a lightest SUSY particle mass of 100 (150) GeV.

Contents

Abstract	2
1 Introduction	6
2 Theoretical Backgrounds	8
2.1 The Standard Model of Elementary Particles	8
2.1.1 The Gauge Principle and Interaction	9
2.1.2 Perturbation and Renormalization	9
2.1.3 QED, QCD and Electroweak Theory	10
2.1.4 Electroweak Symmetry Breaking and the Higgs boson	11
2.2 Remained Problems for the Standard Model and the Supersymmetry Solution . .	13
2.2.1 The Fine-tuning Problem in Higgs Mass	13
2.2.2 Grand Unification	14
2.2.3 Dark Matter	14
2.2.4 The Muon $g - 2$ Anomaly	15
2.3 Supersymmetry and the MSSM	20
2.3.1 Particle Contents in MSSM	20
2.3.2 The MSSM Lagrangian	21
2.3.3 Mass Spectra	23
2.3.4 Running Masses and GUT	25
2.4 MSSM and the Dark Matter Direct Detection	27
2.5 MSSM and the Muon $g - 2$ Anomaly	27
3 SUSY Mass Hierarchy Motivated by Muon $g - 2$ Anomaly and Dark Matter	30
3.1 Muon $g - 2$ Anomaly and Dark Matter Motivated SUSY scenarios	30
3.2 Identification of Viable MSSM Mass Space	33
3.2.1 W-L-H sub-scenario	35
3.2.2 L-B-H sub-scenario	38
3.3 Target SUSY Scenario	40
4 Experimental Apparatus: The ATLAS Detector at the LHC	43
4.1 The Large Hadron Collider	43
4.2 The ATLAS detector	43
4.2.1 Overview	43
4.2.2 Coordinate System	46
4.2.3 Inner Detectors	47
4.2.4 Calorimeter	48
4.2.5 Muon Spectrometer	49
4.2.6 Trigger and Data Acquisition System	51

5	Dataset and Monte Carlo Samples	53
5.1	Actual collision data used for this work	53
5.2	Monte Carlo Samples	54
5.2.1	General Description	54
5.2.2	SM Background Simulation Samples	55
5.2.3	Signal Simulation Samples	56
5.3	Trigger Selection	58
6	Object Reconstruction and Identification	60
6.1	Overview of Event Reconstruction	60
6.2	Tracks	60
6.3	Primary Vertices	63
6.4	Topo-clusters	63
6.5	Electrons	63
6.6	Muons	65
6.7	Jets	66
6.8	Overlap Removal between the Reconstructed Objects	68
6.9	Missing Transverse Energy	68
6.10	Object Definition in the Analysis	69
7	Event Selection	70
7.1	Event Cleaning	70
7.2	Preselection	71
7.3	Optimization and Definition of SRs	71
7.4	Signal composition in SRs	77
8	Background Estimation	81
8.1	Background Breakdown in the Signal Regions	81
8.2	Semi Data-driven Background Estimation for WZ	83
8.2.1	Control Regions and Validation Regions	83
8.2.2	Fit Result for WZ normalization	83
8.3	Charge-flip Background Estimation	86
8.3.1	Methodology for Charge-flip Scale Factor Estimation	87
8.3.2	Measurement of Charge-flip Scale Factor	92
8.3.3	Charge-flip Source Dependency	98
8.3.4	Validation Regions for Charge-flip Background	98
8.4	Fake/Non-prompt Lepton Background Estimation	99
8.4.1	Fake Factor Method	100
8.4.2	Measurement of Fake Factors	101
8.4.3	Systematic Uncertainties of the Fake Factor Method	102
8.4.4	Validation of Fake Factors	109
8.4.5	Fake Background Estimation for $SRSS-2\mu$	110
8.4.6	Top-like Backgrounds	113
8.5	Summary of Background Estimation	116
9	Systematics Uncertainties	119
9.1	Uncertainty for Theoretical Calculation in the Simulation	119
9.2	Experimental Uncertainty	120
9.3	Uncertainties from Data-driven Background Estimations	122
9.4	Summary of Systematic Uncertainties	122

10 Result	124
10.1 Statistical Analysis and Hypothetical Test	124
10.2 Unblinded Signal Regions with Background-only Fit Results	126
10.3 Model-dependent Interpretation – Constraints on the Benchmark Models	130
10.4 Model-independent Search – Upper Limits on BSM Events	133
11 Discussion	136
11.1 What is Unique/Important in This Study?	136
11.2 Implication to Muon $g - 2$ Anomaly	136
11.3 Limit on the Higgsino Mass	137
11.4 Future Prospect	138
12 Conclusion	142
Acknowledgement	143
Appendices	144
A End-cap Muon Trigger Upgrade for the HL-LHC	145
B Charge-flip probabilities and scale factors	151
C Comparison of the magnitude of systematic and statistical uncertainties	153
D Kinematic Distributions in Signal Regions	154
E Auxiliary Materials	163

Chapter 1

Introduction

Particle physics is the study of the elementary building blocks of matter and radiation, and their interactions. According to the today’s best knowledge, the indivisible element of the world, so called *elementary particles*, consist of quarks and leptons that form matter, gauge bosons that mediate forces, and the Higgs boson that emerges by the quantum excitation of the Higgs field. The Standard Model (SM) of particle physics is the theory describing the behavior of elementary particles and interactions between them. Despite its remarkable success, the SM suffers from some outstanding problems such as missing of the dark matter candidate, fine-tuning problem in Higgs mass, and problems to be solved towards an ultimate theory, for example the unification of the three gauge forces (grand unification) and inclusion of gravity. There are also several experimental results that showed tensions from predictions of the SM, such as B -physics anomalies or the muon $g - 2$ anomaly. Along a number of theories attempting to address these problems, supersymmetry (SUSY) is a highly attractive theoretical framework that may potentially solve multiple problems simultaneously. SUSY postulates a space-time symmetry between bosons and fermions and predicts new particles called “superpartners” that differ in spin by $1/2$ from each SM particle.

This work is done in the context of experimental searches of new particles predicted by the SUSY theory, using the proton-proton collisions in the Large Hadron Collider (LHC) at a center-of-mass energy of $\sqrt{s} = 13$ TeV. This thesis describes the search for light scalar-leptons, gauginos, and higgsinos with the mass of a few 100 GeV which is particularly motivated by the muon $g - 2$ anomaly. Search was conducted including the same sign three lepton phase space which had remained to be unexplored so far.

The dissertation is organized as follows.

In Chapter 2, we will provide the details of the theoretical aspects of the SM and SUSY. We examine the underlying principles and concepts behind both theories, including their implications for particle physics. Target SUSY scenario is defined in Chapter 3 by examining the implication of the muon $g - 2$ anomaly and constraints by the presence of dark matter and dark matter direct detections.

Chapter 4 provides an overview of the LHC accelerator and the ATLAS detector, followed by a detailed description of the data used in the study, including both actual collision data and the Monte Carlo (MC) simulations, in Chapter 5. Chapter 6 describes the algorithms for reconstructing the particles generated from the proton-proton collisions.

In Chapter 7, the analysis strategy for this search is first described. The selection applied to the reconstructed particles is then discussed, which is defined to enhance targeted signal and

suppress backgrounds in an optimal manner.

Chapter 8 provides detailed information on the primary background and the strategy used to estimate background yields. Optimal estimation methods have been used for each background process, and this chapter discusses them in detail. In addition, the methods used to validate these estimation strategies are presented, followed by the results of the validation procedure.

Systematics uncertainties for background and signal yield estimation is discussed in Chapter 9. Uncertainties associated to reconstruction algorithms, estimation strategies and theoretical modelings of MC simulations are considered.

Chapter 10 provides the results of this analysis obtained by comparing the estimated number of background events with the actual data observed. Comparison of the yields and features of selected events did not show significant discrepancy from the expectation of the null signal hypothesis, and we concluded that no significant data excess is found in the dataset, and the exclusion limits are set on the targeted slepton decay scenario. Furthermore, we explore possible future sensitivity improvements in this analysis in Chapter 11. Finally, Chapter 12 presents a summary of the conclusions derived from the results of this analysis.

Chapter 2

Theoretical Backgrounds

This chapter provides the backgrounds necessary to motivate the study in this thesis. A brief overview of the theoretical framework of the Standard Model and the Minimal Supersymmetric Standard Model is given.

2.1 The Standard Model of Elementary Particles

The Standard Model (SM) [1, 2] in particle physics is a theoretical framework that formulates the behavior of the six quarks and six leptons that consist matter and the strong, weak, and electromagnetic interactions that act among them. There are three types of particles: fermions, with spin $1/2$, which form matter; gauge bosons, with spin 1, which mediate the interaction between particles; and the Higgs boson, with spin 0, which feeds masses by Brout-Englert-Higgs (or BEH) mechanism [3, 4]. The fermion contents of the SM is shown in Table 2.1, and Table 2.2 lists the gauge bosons and Higgs boson.

Three types of gauge bosons, gluon (g), weak bosons (W^\pm, Z) and photon (γ) mediate strong, weak, and electromagnetic interaction, respectively. Fermions can be categorized into two families: quarks which interact through all three gauge interactions and leptons which feel only weak and electromagnetic interactions.

Table 2.1: Fermion contents in the SM. The quantum numbers Q , T^3 and Y are respectively electric charge, the third component of weak iso-spin and weak hyper charge. N_C represents the number of color states. The subscripts L , R indicate the chirality (left- or right-handed respectively), and the parentheses denote the $SU(2)_L$ doublet.

	Generation			Q	T^3	Y	N_C
	1st	2nd	3rd				
quarks	$\begin{pmatrix} u \\ d \end{pmatrix}_L$	$\begin{pmatrix} c \\ s \end{pmatrix}_L$	$\begin{pmatrix} t \\ b \end{pmatrix}_L$	$\begin{pmatrix} 2/3 \\ -1/3 \end{pmatrix}$	$\begin{pmatrix} 1/2 \\ -1/2 \end{pmatrix}$	$1/3$	3
	u_R	c_R	t_R	$2/3$	0	$4/3$	3
	d_R	s_R	b_R	$-1/3$	0	$-2/3$	3
leptons	$\begin{pmatrix} \nu_e \\ e^- \end{pmatrix}_L$	$\begin{pmatrix} \nu_\mu \\ \mu^- \end{pmatrix}_L$	$\begin{pmatrix} \nu_\tau \\ \tau^- \end{pmatrix}_L$	$\begin{pmatrix} 0 \\ -1 \end{pmatrix}$	$\begin{pmatrix} 1/2 \\ -1/2 \end{pmatrix}$	-1	0
	e_R	μ_R	τ_R	-1	0	-2	0

Table 2.2: Gauge bosons and Higgs in the SM. The notation for the quantum numbers is the same as in Table 2.1.

		Q	T^3	Y	N_C
gluon	g	0	0	0	8
weak bosons	W^\pm	± 1	± 1	0	0
	Z	0	0	0	0
photon	γ	0	0	0	0
Higgs boson	h	0	$-1/2$	1	0

2.1.1 The Gauge Principle and Interaction

The framework of the SM is formularized through the principles of relativistic and quantum field theory. It features a Lorentz-invariant Lagrangian, wherein particles are represented by wave functions that adhere to the Lorentz transformation laws corresponding to the spin characteristics of each particle. The free Lagrangian for a fermion is given by:

$$\mathcal{L} = i\bar{\psi}\gamma^\mu\partial_\mu\psi - m\bar{\psi}\psi, \quad (2.1)$$

where ψ is a spinor field with the mass of m , and γ^μ is the 4-dimensional gamma matrices. The first (second) term of Eq. 2.1 represents the kinetic (mass) term of the fermion.

Interactions among particles are governed by a local symmetry known as “gauge symmetry”. The terms related to these interactions are derived by enforcing invariance under gauge transformations on the free Lagrangian. For electromagnetic interaction, the gauge transformation is defined as follows:

$$\psi \rightarrow e^{i\theta(x)Q}\psi = e^{i\theta(x)q}\psi, \quad (2.2)$$

where Q represents the generator of the $U(1)$ transformation, q denotes the electrical charge of the fermion ψ , and $\theta(x)$ signifies an arbitrary phase. The free Lagrangian (Eq. 2.1) does not exhibit invariance under this gauge transformation; however, it can be rectified through a small adjustment in the differential (∂_μ), as follows:

$$\partial_\mu \rightarrow D_\mu := \partial_\mu - ieA_\mu(x), \quad (2.3)$$

where e represents the elementary charge and $A(x)$ denotes a field that has a transformation law:

$$A_\mu \rightarrow A_\mu + \frac{1}{e}\partial_\mu\theta(x). \quad (2.4)$$

The term representing electromagnetic interaction appears as an extra term within the Lagrangian.

$$\mathcal{L}_{\text{int.}} = e\bar{\psi}\gamma^\mu\psi A_\mu. \quad (2.5)$$

This interaction term characterizes the electromagnetic force exerted on the charged fermion, while A_μ represents the electromagnetic scalar and vector potential as defined in classical electromagnetism.

2.1.2 Perturbation and Renormalization

The effect of interaction is characterized by the transition amplitude:

$$\langle f | e^{-i\mathcal{H}_{\text{int.}}t} | i \rangle, \quad (2.6)$$

where i (f) represents the initial (final) state and $\mathcal{H}_{\text{int.}}$ is the interaction Hamiltonian. Phenomenological important predictions such as interaction cross-sections and decay branching fractions are calculated based on this amplitude. However, in many situations, the transition amplitude cannot be calculated analytically. As a result, a perturbative expansion based on the interaction's coupling constant is commonly employed, with $\alpha := e^2/4\pi$ typically used for electromagnetic interaction.

The small coupling constant of electromagnetic interaction ($\alpha \sim 1/137$) indicates a good convergence of the perturbative expansion with sufficiently small contributions from higher-order terms. However, it was found that higher-order terms in the perturbative expansion cause the cross-section calculations to diverge (infrared / ultraviolet divergences) which make the theory unreliable. This issue was addressed through a process called “renormalization”, where the parameters of the theory, such as masses and coupling constants, are redefined to eliminate these infinities.

Renormalization indicates that the values of theoretical parameters change depending on the energy scale at which interactions occur. The dynamics of these parameters are described by the renormalization group equation (RGE), which for the coupling constant is expressed as:

$$\frac{1}{\alpha(Q^2)} - \frac{1}{\alpha(Q_0^2)} = -\frac{b_0}{2\pi} \log\left(\frac{Q}{Q_0}\right), \quad (2.7)$$

at 1-loop level, where Q is the scale of the typical momentum transfer, and b_0 is related to the 1-loop beta function, β_0 , as $b_0 = 16\pi^2\beta_0/e^3$. This evolution is known as the “running” effect, which serves as a valuable proxy for examining the behavior of the theory at a high energy scale.

2.1.3 QED, QCD and Electroweak Theory

Electromagnetic Interaction The Lagrangian for Quantum Electrodynamics (QED) is described as:

$$\mathcal{L}_{\text{QED}} = -\frac{1}{4}F_{\mu\nu}F^{\mu\nu} + i\bar{\psi}\gamma^\mu\partial_\mu\psi - m\bar{\psi}\psi + e\bar{\psi}\gamma^\mu\psi A_\mu, \quad (2.8)$$

with $F_{\mu\nu}$ being the field strength:

$$F_{\mu\nu} := \partial_\mu A_\nu - \partial_\nu A_\mu. \quad (2.9)$$

Strong Interaction Similar to what is done in QED, the Lagrangian for strong interaction can be generated by considering the gauge group of $SU(3)$:

$$\psi \rightarrow e^{i\theta_a(x)\lambda^a}\psi, \quad a = 1, 2, \dots, 8, \quad (2.10)$$

with λ^a being the generators of the gauge group.

The Lagrangian for strong interaction is:

$$\begin{aligned} \mathcal{L}_{\text{QCD}} &= -\frac{1}{4}\hat{\mathbf{G}}_{\mu\nu}\hat{\mathbf{G}}^{\mu\nu} + \bar{q}(i\gamma^\mu D_\mu - m)q, \\ D_\mu &:= \partial_\mu + ig_s \sum_{a=1}^8 G_\mu^a \frac{\lambda_a}{2} \\ \hat{\mathbf{G}}_{\mu\nu} &:= \partial_\mu \mathbf{G}_\nu - \partial_\nu \mathbf{G}_\mu - g_s \mathbf{G}_\mu \times \mathbf{G}_\nu \\ \mathbf{G}_\mu &:= \{G_\mu^a; a = 1, 2, \dots, 8\} \end{aligned} \quad (2.11)$$

where G_μ^a and q represent the fields for gluons and quarks respectively. The strong coupling constant α_s is related to g_s by $\alpha_s = g_s^2/4\pi$. The theoretical framework is referred to Quantum

Chromodynamics (QCD) as the charge of strong interaction is called “color”. Quarks (gluons) are in the triplet (octet) expression with 3 (8) degenerated states. The RGE equation of α_s can be written as,

$$\alpha_s(Q^2) = \frac{4\pi}{b_s \log(Q^2/\Lambda_{\text{QCD}}^2)}, \quad (2.12)$$

at 1-loop level where $b_s = -(11 - 2n_f/3)$, with n_f representing the number of quark flavors that are active at the energy scale Q^2 , and Λ_{QCD} denotes the QCD cut-off scale (~ 200 MeV). A negative b_s value indicates that the coupling constant decreases as the energy scale increases. Although the strong interaction typically exhibits a large coupling, α_s is generally around 0.1 at the energy scales relevant to the LHC ($Q > 100$ GeV) which is sufficiently small to support a perturbative framework known as “asymptotic freedom”. Conversely, as one approaches Λ_{QCD} , the coupling constant increases. This behavior of strong coupling necessitates that colored particles combine to create a color singlet state, a phenomenon referred to as “color confinement”.

Electroweak Interaction Electroweak interaction is described by a larger gauge group $SU(2)_L \times U(1)_Y$ [5–7]. The fundamental concept is that the weak and electromagnetic interactions originate from a common source at a high energy scale and subsequently diverge into distinct interactions due to a process known as spontaneous symmetry breaking, represented as $SU(2)_L \times U(1)_Y \rightarrow U(1)_Q$. This unified interaction domain is termed as the electroweak (EW) scale.

To address the observed parity-violating characteristics of weak interactions, the gauge transformation differentiates the chirality of fermions, with $SU(2)_L$ specifically acting on the left-handed component.

$$\psi_L \rightarrow e^{i\theta T_3 + i\Theta Y} \psi_L, \quad (2.13)$$

$$\psi_R \rightarrow e^{i\Theta Y} \psi_R. \quad (2.14)$$

The Lagrangian arrives at:

$$\begin{aligned} \mathcal{L}_{\text{EW}} &= -\frac{1}{4} \hat{\mathbf{W}}_{\mu\nu} \hat{\mathbf{W}}^{\mu\nu} - \frac{1}{4} B_{\mu\nu} B^{\mu\nu} + \bar{\psi}(i\gamma^\mu D_\mu - m)\psi, \\ D_\mu &:= \partial_\mu + ig \sum_{a=1}^3 W_\mu^a \tau_a + ig' \frac{Y}{2} B_\mu, \\ \hat{\mathbf{W}}_{\mu\nu} &:= \partial_\mu \mathbf{W}_\nu - \partial_\nu \mathbf{W}_\mu - g_s \mathbf{W}_\mu \times \mathbf{W}_\nu, \\ \mathbf{W}_\mu &:= \{W_\mu^a; a = 1, 2, 3\}, \\ B_{\mu\nu} &= \partial_\mu B_\nu - \partial_\nu B_\mu, \end{aligned} \quad (2.15)$$

where W_μ^a and B_μ represent the fields of EW gauge bosons. The parameters g and g' denote the coupling constants for $SU(2)_L$ and $U(1)_Y$, respectively, while τ ($= \sigma/2$) corresponds to the generators of $SU(2)$.

2.1.4 Electroweak Symmetry Breaking and the Higgs boson

The EW Lagrangian successfully describes both weak and electromagnetic interactions; however, it cannot include mass terms for gauge bosons and fermions, as their presence would violate EW gauge invariance. To address this issue, the BEH mechanism is utilized, which involves the introduction of a $SU(2)$ doublet of scalar fields, $\phi = (\phi_1, \phi_2) = (\phi^+, \phi^0)$, with hypercharge $Y =$

-1 and isospin $T = 1/2$, along with a scalar potential $V(\phi)$ incorporated into the Lagrangian:

$$\begin{aligned}\mathcal{L}_{\text{Higgs}} &:= (D_\mu \phi)^\dagger (D^\mu \phi) - V(\phi), \\ V(\phi) &:= \mu^2 \phi^\dagger \phi + \lambda (\phi^\dagger \phi)^2.\end{aligned}\tag{2.16}$$

$\lambda > 0$ is required to have a minimum value in $V(\phi)$. The minimum of $V(\phi)$ is found in $\phi = (0, 0)$ in the ϕ_1 - ϕ_2 plane when $\mu^2 > 0$, while negative μ^2 leads to non-trivial minima in $v := |\phi|^2 = -\mu^2/2\lambda$. This causes a shift in the vacuum expectation value (VEV) : $\langle 0 | \phi | 0 \rangle = 0 \rightarrow v$ which is referred as “spontaneous symmetry breaking”.

ϕ can be redefined by the variation around the new vacuum $(0, v)$:

$$\phi = \begin{pmatrix} 0 \\ v + h(x) \end{pmatrix}.\tag{2.17}$$

Mass terms of gauge particles appear in the scalar kinetic energy term:

$$\begin{aligned}& \frac{1}{2}(0, v) \left(\frac{g'}{2} B_\mu + g W_\mu^a \tau_a \right) \begin{pmatrix} 0 \\ v \end{pmatrix} \\ &= \frac{g'^2 v^2}{8} (W^{1\mu} - i W^{2\mu}) (W_\mu^1 + i W_\mu^2) + \frac{v^2}{8} (g W^{3\mu} - g' B^\mu) (g W_\mu^3 - g' B_\mu) \\ &= \frac{1}{2} m_W^2 (W^{+\mu} W_\mu^- + W^{-\mu} W_\mu^+) + \frac{1}{2} m_Z^2 Z^\mu Z_\mu\end{aligned}\tag{2.18}$$

The quantities corresponding to the gauge fields W_μ^\pm, Z_μ and a mass-less gauge field for a photon A_μ which is defined as the orthogonal field with respect to Z_μ and masses m_W, m_Z are defined as follows:

$$W_\mu^\pm = \frac{1}{\sqrt{2}} (W_\mu^1 \mp i W_\mu^2), \quad Z_\mu = \frac{g W_\mu^3 - g' B_\mu}{\sqrt{g^2 + g'^2}}, \quad A_\mu = \frac{g W_\mu^3 + g' B_\mu}{\sqrt{g^2 + g'^2}},\tag{2.19}$$

$$m_W = \frac{gv}{2}, \quad m_Z = \frac{\sqrt{g^2 + g'^2} v}{2}.\tag{2.20}$$

The mass for scalar field h is determined to be:

$$m_h = \sqrt{-2\mu^2}.\tag{2.21}$$

As h has positive mass, h can be regarded as a physical mode and it is commonly referred as “Higgs boson”. Fermion masses are introduced by incorporating the following gauge invariant terms into the Lagrangian:

$$\begin{aligned}\mathcal{L}_{\text{Yukawa}} &:= -\bar{\psi}_{i,L} y_u^{ij} \phi \psi_{j,R} - \bar{\psi}_{i,R} y_u^{ij} \phi^\dagger \psi_{j,L} \\ &\quad - \bar{\psi}_{i,L} y_d^{ij} \phi^c \psi_{j,R} - \bar{\psi}_{i,R} y_d^{ij} \phi^{c\dagger} \psi_{j,L} \\ &\quad - \bar{\psi}_{i,L} y_e^{ij} \phi \psi_{j,R} - \bar{\psi}_{i,R} y_e^{ij} \phi^\dagger \psi_{j,L},\end{aligned}\tag{2.22}$$

where the indices $i, j = 1, 2, 3$ represent the different generations of fermions. The Yukawa matrices are 3×3 matrices that span the family space, with the Yukawa couplings for each fermion located in the diagonal elements. The off-diagonal elements facilitate the mixing between generations; these are set to zero for down-type leptons, while they take non-zero values for quarks, as characterized by the CKM matrix [8]. By utilizing the VEV of the complex scalar field, the electron part of Eq. 2.22 can be expressed as follows:

$$\begin{aligned}& -\frac{y_e^{11}}{\sqrt{2}} \left[(\bar{\nu}_L, \bar{e}_L) \begin{pmatrix} 0 \\ v \end{pmatrix} e_R + \bar{e}_R(0, v) \begin{pmatrix} \nu_L \\ e_L \end{pmatrix} \right] \\ &= -\frac{y_e^{11} v}{\sqrt{2}} (\bar{e}_L e_R + \bar{e}_R e_L) = -\frac{y_e^{11} v}{\sqrt{2}} \bar{e} e.\end{aligned}\tag{2.23}$$

Electron mass is related to Yukawa coupling by the following equation:

$$m_e = \frac{y_e^{11} v}{\sqrt{2}}. \quad (2.24)$$

2.2 Remained Problems for the Standard Model and the Supersymmetry Solution

Despite the enormous success of the SM, there are still a couple of problems left to be solved, ranging from phenomenological ones such as the absence of dark matter candidate, to conceptual ones towards the ultimate theory (e.g. the too many parameters, the naturalness as a theory etc.). This section will overview the most notable ones, enough motivating the beyond-the-SM (BSM) theories including supersymmetry (SUSY) [9–14]. A particular emphasis is put on the TeV-scale SUSY to be the solution of the problems.

2.2.1 The Fine-tuning Problem in Higgs Mass

Though divergences appearing in higher-order calculations in the SM are universally cured in renormalization by the cancellation with the counter terms, it has been pointed that the magnitude of the cancelling terms are unnaturally large in case of the radiation correction on the Higgs mass [15–18]. For instance, if the Higgs field couples to a Dirac fermion f with a term in the Lagrangian, $-\lambda_f h \bar{f} f$, then the 1-loop correction given by a fermion loop (Fig. 2.1(a)) before renormalization is:

$$\Delta m_h^2 = -\frac{|\lambda_f^2|}{8\pi^2} \Lambda_{\text{UV}}^2 + \mathcal{O}(\log \Lambda_{\text{UV}}), \quad (2.25)$$

where Λ_{UV} is an ultraviolet momentum cutoff used to regulate the loop integral. The largest correction comes when f is the top quark with $\lambda_f \approx 0.94$. The magnitude of the correction term Δm_h^2 can be an order of $10^{38} (\text{GeV})^2$ assuming the SM is valid upto the Planck scale around $\Lambda_{\text{UV}} \sim 10^{19} (\text{GeV})^2$, while the observed mass is 125 GeV. Naively thinking this implies that the bare mass $m_{h,\text{bare}}$ and the correction Δm_h^2 has to cancel in a precision of 10^{-17} (“fine tuning problem” or “naturalness problem”). It is unnatural for a complete theory to contain such extraordinary scale hierarchy in it.

The simplest solution is to add a partner particle yielding the opposite loop contribution to cancel it. For example, suppose there exists a heavy complex scalar particle S with mass m_S that couples to the Higgs with a Lagrangian term $-\lambda_S |h|^2 |S|^2$. Then the Feynman diagram in Fig. 2.1(b) gives a correction

$$\tilde{\Delta} m_h^2 = \frac{\lambda_S}{16\pi^2} [\Lambda_{\text{UV}}^2 - 2m_S^2 \log(\Lambda_{\text{UV}}/m_S) + \dots]. \quad (2.26)$$

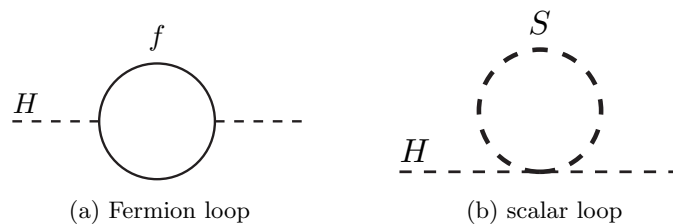


Figure 2.1: Feynman diagrams of 1-loop processes contributing to Higgs mass by (a) fermion and (b) scalar loop.

The quadratic term in Eq. 2.25 and Eq. 2.26 cancels out when there are two complex scalar fields for one Dirac fermion and the associated dimensional coupling have a specific relationship (e.g. $\lambda_S = |\lambda_f|^2$). This requirement is fulfilled in SUSY and the scalar partner of top quark, “stop”, plays the most important role in the cancellation. With the the existence of stop, the mass correction to Higgs will be

$$\Delta m_{h,\text{stop}}^2 = \Delta m_h^2 + \tilde{\Delta} m_h^2 = \mathcal{O}(\log \Lambda_{\text{UV}}), \quad (2.27)$$

where the 10^{-34} order of fine-tuning is no longer needed.

2.2.2 Grand Unification

One of the primary aspirations of physicists is to encapsulate all phenomena under a singular principle. The EW symmetry breaking in the SM, represented as $SU(2)_L \times U(1) \rightarrow U(1)_Q$, suggests a shared origin for both electromagnetic and weak interactions. This notion propels physicists toward the unification of these forces with the strong interaction at a more higher energy scale, a concept referred to as Grand Unification Theory (GUT).

Possibility of such unification can be analyzed through running coupling constants. The evolution of coupling constants is described by the RGE:

$$\frac{1}{\alpha_i(Q^2)} - \frac{1}{\alpha_i(Q_0^2)} = -\frac{b_i}{2\pi} \log \left(\frac{Q}{Q_0} \right), \quad (2.28)$$

at 1-loop level, with the indices $i = 1, 2, 3$ denote electromagnetic, weak and strong interaction respectively. The b_i is related to the 1-loop level beta function, β_i , as $b_i = 16\pi^2 \beta_i / g_i^3$. In the SM,

$$\begin{pmatrix} b_1 \\ b_2 \\ b_3 \end{pmatrix} = \begin{pmatrix} 1/10 \\ -43/6 \\ -11 \end{pmatrix} + n_{\text{gen}} \begin{pmatrix} 4/3 \\ 4/3 \\ 4/3 \end{pmatrix}, \quad (2.29)$$

where n_{gen} is the number of generation of fermions, which is equal to 3 for $Q > m_t$. In case of the grand unification, one naively expects a convergence of the three couplings at a certain scale (Q_{GUT}). However, as illustrated in Fig. 2.2, this does not happen in the SM. On the other hand, SUSY can realize the converge by changing the slope of the running where additional MSSM particles participate. For instance, the b_i for MSSM is,

$$\begin{pmatrix} b_1 \\ b_2 \\ b_3 \end{pmatrix} = \begin{pmatrix} 33/5 \\ 1 \\ -3 \end{pmatrix}, \quad (2.30)$$

and the coupling unification is achieved at $Q_{\text{GUT}} \sim 10^{16}$ GeV, as shown in Fig. 2.2. This is unexpected considering that even a slight variation in particle content can easily disrupt the convergence. This characteristic is one of the reasons why SUSY stands out as particularly significant and compelling among the BSM frameworks.

2.2.3 Dark Matter

Historically, the concept of dark matter (DM) emerged from studies of galaxy rotation velocities, which indicated that the mass present in the centers of galaxies exceeded what spectroscopy would predict [20, 21]. The non-baryonic dark matter hypothesis has received substantial backing from various observations, including mass tomography of the Bullet Cluster through gravitational lensing. At present, the prevailing framework for understanding DM is the Λ -CDM model (Cold Dark Matter), which posits that DM is characterized as follows.

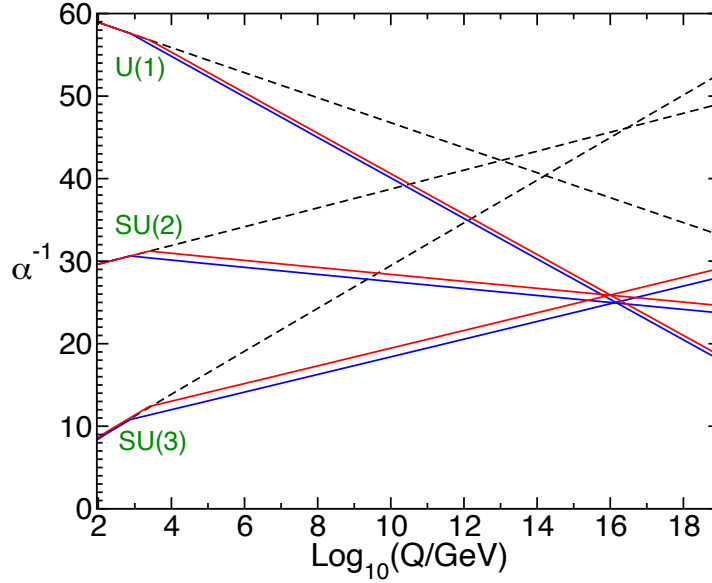


Figure 2.2: Two-loop renormalization group evolution of the inverse gauge coupling $1/\alpha_i$ in case of SM (dashed lines), and a scenario in MSSM (solid lines) where the masses of SUSY partners are set between 500 GeV and 1.5 TeV [19].

- Only sense very weak interaction such as gravity and the weak interaction.
- Be non-relativistic, to realize the large-scale structure of the universe.

One of the possible candidates for the CDM is the Weakly Interacting Massive Particles (WIMPs) [22–25]. The density abundance is dedicatedly measured via cosmic microwave background (CMB) by Planck [26] under the Λ -CDM regime:

$$\Omega_{\text{CDM}} h^2 = 0.120 \pm 0.001. \quad (2.31)$$

A series of DM direct direction searches have been conducted. The most stringent limits to the spin-independent dark matter-nucleon cross-section, denoted as σ_{SI} , have been set by the LUX-ZEPLIN (LZ) experiment [27] as shown in Fig. 2.3.

While the SM has no candidates for DM, SUSY provides several attractive candidates when assuming the R -parity conservation in which the lightest SUSY particle (LSP) becomes stable. It is worth noting that the LSP mass will be constrained by an upper bound about 3 TeV, when trying to explain the whole dark matter abundance by the LSP [32]. This makes SUSY as a phenomenologically important model rather than a purely theoretical framework, and is a strong motivation of considering TeV-scale SUSY.

2.2.4 The Muon $g - 2$ Anomaly

The magnetic moment of the muon plays a special role in the establishment of the SM. For an elementary particle with intrinsic angular momentum (spin, \mathbf{S}), mass m and charge q , its magnetic moment $\boldsymbol{\mu}$ is given by

$$\boldsymbol{\mu} = g \frac{q}{2m} \mathbf{S}, \quad (2.32)$$

where g is the gyromagnetic ratio. The original formulation of quantum mechanics by Dirac anticipated a value of $g = 2$ for all spin-1/2 elementary particles [33]. Nevertheless, in the context of relativistic quantum field theories, this value is influenced by radiative corrections, as

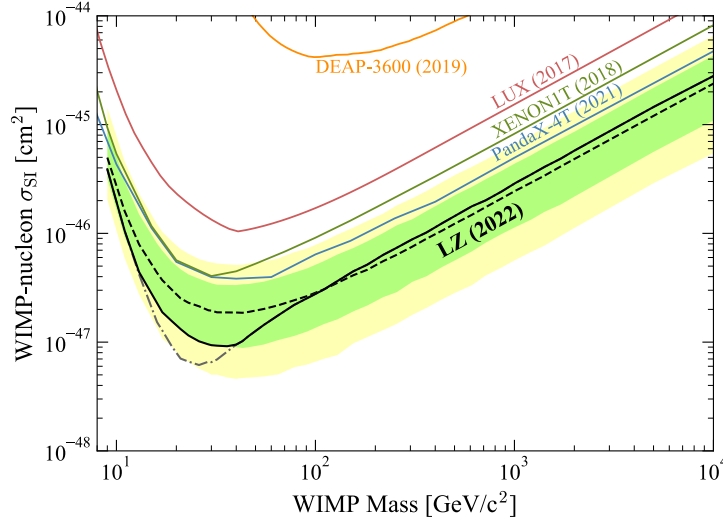


Figure 2.3: The 90% confidence limit (black line) for the spin-independent WIMP cross-section vs. WIMP mass from the LZ experiment [27]. The green and yellow bands are the 1σ and 2σ sensitivity bands. Also shown are the PandaX-4T [28], XENON1T [29], LUX [30], and DEAP-3600 [31] limits.

interactions with virtual particles alter the way the elementary particle interacts with a photon. The first order correction from QED was found to be an increase of exactly α_1/π [34]. For the charged leptons ($l = e, \mu, \tau$), the anomalous magnetic momentum a_l is defined as the deviation of g_l from 2:

$$a_l := (g_l - 2)/2. \quad (2.33)$$

This quantity continues to remain as a long-standing test of the SM to this day. Comparisons with experimental measurements, a_l^{exp} , result in a powerful indirect search for new physics. The SM prediction, a_l^{SM} , require calculating the modifications to g from virtual SM particles up to a sufficient order. If disagreement between precise calculations of a_l^{SM} and measurements of a_l^{exp} is observed, it could indicate BSM contributions, where BSM virtual particles or forces provide additional contributions to a_l . Among the three values a_l (a_e, a_μ, a_τ), the muon a_μ is the most appropriate for observing the effects of new physics. Based on mass scaling arguments, it can be found that the muon is generally $(m_\mu/m_e)^2 \sim 4 \times 10^4$ times more sensitive to BSM effects compared to the electron. Additionally, the current status of a_τ is relatively minor due to the lack of sufficient accuracy in the experimental measurement of a_τ^{exp} .

In modern muon $g-2$ experiments, spin-polarized muons are injected into a magnetic storage ring where their spin evolution is monitored. The value of a_μ^{exp} is determined by assessing the anomalous precession frequency ω_a , which is defined as the difference between the spin precession frequency ω_s and the cyclotron frequency ω_c for muons moving within a highly uniform magnetic field \mathbf{B} at a velocity of β :

$$\omega_a := \omega_s - \omega_c = -\frac{q}{m_\mu} \left[a_\mu \mathbf{B} - a_\mu \left(\frac{\gamma}{\gamma + 1} \right) (\boldsymbol{\beta} \cdot \mathbf{B}) \boldsymbol{\beta} - \left(a_\mu - \frac{1}{\gamma^2 - 1} \right) \frac{\boldsymbol{\beta} \times \mathbf{E}}{c} \right]. \quad (2.34)$$

The Fermilab Muon $g-2$ experiment utilizes a methodology same as that of BNL [35]. The superconducting storage ring, with a radius of 7.112 m and a magnetic field strength of 1.45 T, was transferred from BNL to Fermilab. The determination of ω_a is carried out by 24 calorimeter stations, which are evenly positioned around the inner circumference of the storage ring.

The latest result by the Run-2 and Run-3 data is reported to be $a_\mu^{\text{exp-FNAL}} = (11659205.7 \pm 2.5) \times 10^{-10}$ [36] which is being compatible with the previous experimental result using Run-1

data [37] and at BNL [38]. The combined world average is:

$$a_\mu^{\text{exp}} = (11659205.9 \pm 2.2) \times 10^{-10}. \quad (2.35)$$

The SM prediction for the muon anomalous magnetic moment is derived from the cumulative contributions of all sectors within the SM:

$$a_\mu^{\text{SM}} = a_\mu^{\text{QED}} + a_\mu^{\text{EW}} + a_\mu^{\text{HVP}} + a_\mu^{\text{HLbL}}, \quad (2.36)$$

where a_μ^{QED} represents the contribution from QED, a_μ^{EW} denotes the contribution from EW interactions, a_μ^{HVP} refers to the contribution arising from hadronic vacuum polarization (HVP), and a_μ^{HLbL} is associated with the contribution from hadronic light-by-light (HLbL) scattering. Illustrative examples of these processes can be found in Fig. 2.4. The uncertainty in a_μ^{SM} is dominated by the hadronic contributions, a_μ^{HVP} and a_μ^{HLbL} , which stem from the non-perturbative characteristics of the low-energy strong interaction.

QED contributions The contributions from QED to a_μ encompass all contributions from leptons and photons, with calculations completed up to the five-loop order. Contributions up to the four-loop order have been established through both numerical and analytical methods [39, 40]. The complete five-loop contribution, which consists of 12,672 Feynman diagrams illustrated in Fig. 2.5, has been computed numerically [41–46]. The value for the QED contributions is given as

$$a_\mu^{\text{QED}} = 116\,584\,718.931(104) \times 10^{-11}. \quad (2.37)$$

EW contributions The EW contributions encompass all diagrams containing at least one of the EW bosons, with the one-loop Feynman diagrams illustrated in Fig. 2.6. The presence of the masses of the EW bosons results in a significant suppression of the EW contributions to a_μ . These contributions have been computed up to the two-loop order, while the three-loop contributions have been approximated [47, 48]. The value for a_μ^{EW} is determined to be

$$a_\mu^{\text{EW}} = 153.6(1.0) \times 10^{-11}. \quad (2.38)$$

HVP contributions The contributions from the HVP, as illustrated in the third diagram of Fig. 2.4, can be derived through data-driven methodologies that employ $e^+e^- \rightarrow \text{hadrons}$ data within dispersion relation:

$$a_\mu^{\text{LO HVP}} = \frac{1}{4\pi^3} \int_{s_{th}}^{\infty} ds K(s) \sigma_{\text{had}}(s), \quad (2.39)$$

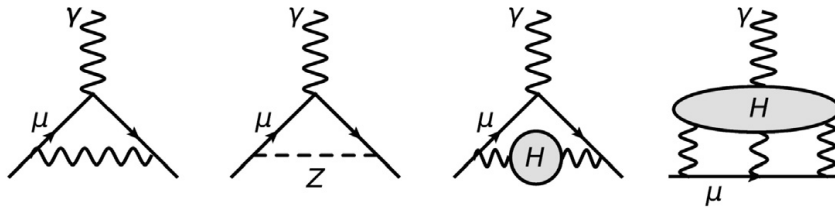


Figure 2.4: Feynman diagrams of SM contributions to a_μ . The diagrams shown (from left to right) are the one-loop QED diagram, the one-loop EW process involving Z boson exchange, the leading-order HVP diagram and HLbL contributions.

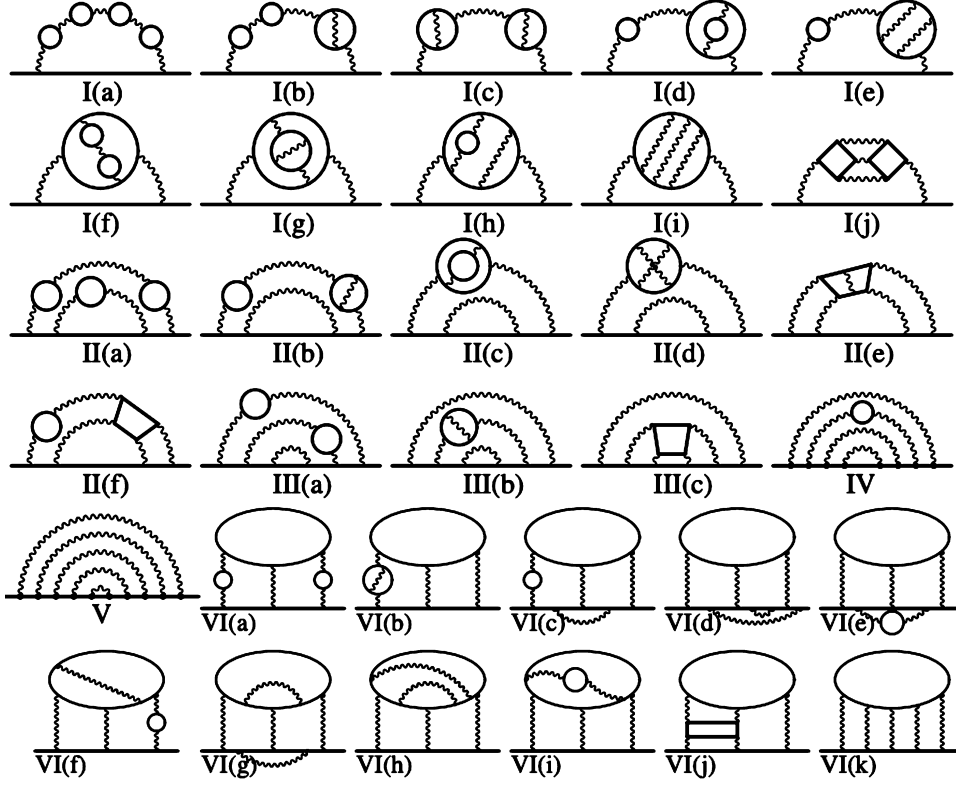


Figure 2.5: Five-loop QED diagrams. There are, in total, 12,672 diagrams contributing to a_μ^{QED} [41]. The straight and wavy lines represent lepton and photon propagators, respectively.

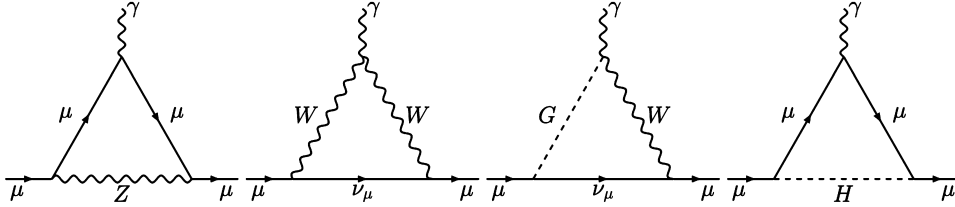


Figure 2.6: One-loop EW Feynman diagrams [49].

where $s_{th} = m_{\pi^0}^2$. $K(s)$ is a kernel function [50, 51] which gives larger weight to contributions from lower energies. NLO and NNLO contributions are determined from similar dispersion integrals. Combining several experimental results in an estimate of the total HVP contribution of Ref. [49],

$$a_\mu^{\text{HVP}} = 6845(40) \times 10^{-11}. \quad (2.40)$$

HLbL contributions Contributions from HLbL scattering, shown in the furthest-right diagram of Fig. 2.4, describe the process where an external soft and on-shell photon interacts through a hadronic blob with three off-shell photons. The HLbL contributions arise from single mesons, axial-vector mesons, tensor mesons and charged pion or kaon loops. For the calculation, experimental data are used as input for various hadronic insertions where available, and theoretical calculations of the amplitudes are employed where not. The sum of the values from the different contributions results in the estimation for a_μ^{HLbL} [52–62],

$$a_\mu^{\text{HLbL}} = 92(19) \times 10^{-11}. \quad (2.41)$$

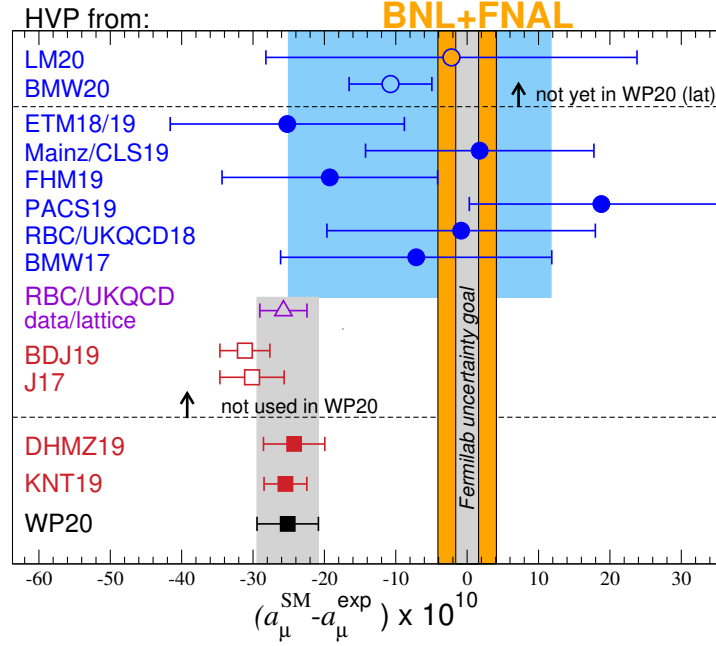


Figure 2.7: Results for $(a_\mu^{\text{SM}} - a_\mu^{\text{exp}}) \times 10^{10}$ when is $a_\mu^{\text{LO HVP}}$ is taken from various lattice [65–77] and data-driven results [78–81]. The filled dark blue circles are lattice results [65–72] that are included in the lattice average advocated in [49], which is given indicated by the light-blue band. The unfilled dark blue circles are those results not included in the average [73–77, 82]. The red squares show results from data-driven determinations of $a_\mu^{\text{LO HVP}}$, where filled squares are those included in the merged data-driven result [49, 79] (given by the black square marker and grey band) and unfilled squares are not [80, 81]. The purple triangle shows a hybrid result where noisy lattice data at very short and long distances are replaced by $e^+e^- \rightarrow \text{hadrons}$ cross-section data [71]. The yellow band indicates the “no new physics” scenario, where HVP results are large enough to bring the SM prediction of a_μ into agreement with the experimental value. The grey band in the center of this indicates the projected experimental uncertainty from the Fermilab Muon $g - 2$ experiment. This figure has been adapted from [49, 83].

The Lattice QCD calculation for HLbL contributions [63, 64] is also available and the result is found to be consistent within uncertainties with the data-driven calculation (Eq. 2.41).

The current recommended value for the SM prediction of the muon’s anomalous magnetic moment is obtained by combining each contribution as Eq. 2.36 [49]:

$$a_\mu^{\text{exp}} = 116\,591\,810(43) \times 10^{-11}. \quad (2.42)$$

Comparing with the experimental result (Eq. 2.35) results in a deviation of

$$\Delta a_\mu^{\text{exp}} := a_\mu^{\text{exp}} - a_\mu^{\text{SM}} = (24.9 \pm 5.0) \times 10^{-10}, \quad (2.43)$$

corresponding to a 5.0σ discrepancy, which may imply the need of SM extention. This anomaly is known as the “**muon $g - 2$ anomaly**”. For the HVP contribution, several lattice calculation results exists, which are summarized in Fig. 2.7. These results have values which span across the data-driven approaches and a no-new-physics scenario but generally with too large errors to have a definitive statement. For example, although not shown in Fig. 2.7, the latest result from BMW [84] leads to a prediction of the muon anomalous magnetic momentum that differs from

the measurement by only 0.9 standard deviations. As the lattice evaluations are still not precise enough to be compared to those from dispersive approaches for HVP, Lattice QCD results are not included in the a_μ^{SM} recommended value.

If we take the recommended a_μ^{SM} value, Eq. 2.42, and assume that the muon $g - 2$ anomaly is true, TeV-scale SUSY with light scalar-muons and gauginos is a good candidate to explain the anomaly which would be further discussed in Section 2.5.

2.3 Supersymmetry and the MSSM

The Minimal Supersymmetric Standard Model (MSSM) is a framework of SUSY that incorporates the minimum of number of supersymmetric particles and degrees of freedom in addition to the SM such as:

- A single set of SUSY particles is introduced ($\mathcal{N}_{\text{SUSY}} = 1$).
- The SUSY partners of the SM fermions have a spin of 0, while those of bosons, including gauge and Higgs bosons, have a spin of 1/2.
- The Higgs sector is described using two Higgs doublets.

Although referred to as “minimal,” the MSSM serves as a sufficiently broad framework to encapsulate the characteristic features of SUSY at the phenomenological level. Consequently, this thesis will limit its focus to the MSSM.

2.3.1 Particle Contents in MSSM

The particle content of MSSM is shown in Table 2.3. Scalar-fermions (sfermions) have two types, labeled L and R , which represent their roles as SUSY partners for left-handed or right-handed SM fermions. Gauginos are all Majorana particles to ensure that their degrees of freedom match those of the partner gauge bosons or Higgs bosons.

Table 2.3: Particle content of MSSM. The left column describes the naming convention for SUSY particles. $n[SU(3)_C]$ ($n[SU(2)_L]$) represents the degree of freedom of the $SU(3)_C$ ($SU(2)_L$) multiplet that the field(s) belongs to. The $U(1)$ charge Y is shown as all particles belongs to the singlet of $U(1)_Y$.

Super-multiplet		SM sector	SUSY partner	$n[SU(3)_C]$	$n[SU(2)_L]$	Y
gluon / gluino	G	g	\tilde{g}	8	1	0
EW gauge boson /	W	W^\pm, W^0	$\tilde{W}^\pm, \tilde{W}^0$	1	3	0
EW gaugino	B	B^0	\tilde{B}^0	1	1	0
lepton / slepton	L	$(\nu_e, e)_L$	$(\tilde{\nu}_e, \tilde{e})_L$	1	2	-1
	E	e_R	\tilde{e}_R	1	1	-2
quark / squark	Q	$(u, d)_L$	$(\tilde{u}, \tilde{d})_L$	3	2	1/3
	U	u_R	\tilde{u}_R	3	1	4/3
	D	d_R	\tilde{d}_R	3	1	-2/3
Higgs boson /	H_u	(H_u^+, H_u^0)	$(\tilde{H}_u^+, \tilde{H}_u^0)$	1	2	1
	H_d	(H_d^0, H_d^-)	$(\tilde{H}_d^0, \tilde{H}_d^-)$	1	2	-1

The MSSM Higgs sector includes two Higgs doublets, $\mathbf{H}_u := (H_u^+, H_u^0)$, $\mathbf{H}_d := (H_d^0, H_d^-)$, each with its own VEV:

$$v_u := \langle H_u^0 \rangle, \quad v_d := \langle H_d^0 \rangle. \quad (2.44)$$

These doublets give masses to up-type and down-type fermions, respectively. Their ratio is parametrized using a mixing angle β as:

$$\tan \beta := v_u/v_d. \quad (2.45)$$

Consistency with the SM is guaranteed by relating VEVs as:

$$v_{\text{SM}}^2 = v_u^2 + v_d^2. \quad (2.46)$$

If gravity is quantized in the framework of Quantum Field Theory (QFT), there must exist a corresponding gauge boson known as the “graviton”, along with its supersymmetric partner referred to as the “gravitino”. Gravitinos play a significant role in certain SUSY scenarios, such as in GMSB (Gauge-Mediated SUSY Breaking) [85], however, they are not considered in this thesis.

2.3.2 The MSSM Lagrangian

A supersymmetric Lagrangian can be systematically constructed using super-potential and super-space techniques. The Lagrangian of the MSSM can be separated into two parts:

$$\mathcal{L}^{\text{MSSM}} = \mathcal{L}_{\text{SUSY}}^{\text{MSSM}} + \mathcal{L}_{\text{soft}}^{\text{MSSM}}. \quad (2.47)$$

The first term is the SUSY invariant part which is given by:

$$\mathcal{L}_{\text{SUSY}}^{\text{MSSM}} = -\frac{1}{4}F_{\mu\nu}^a F^{a\mu\nu} - D^\mu \phi^{*i} D_\mu \phi_i + i\psi^{\dagger i} \bar{\sigma}^\mu D_\mu \psi_i + i\lambda^{\dagger a} \bar{\sigma}^\mu D_\mu \lambda^a \quad (\text{Kinetic terms}) \quad (2.48)$$

$$- \frac{1}{2}W^{ij}\psi_i\psi_j + \text{h.c.} \quad (\text{Yukawa interaction terms}) \quad (2.49)$$

$$- \sqrt{2}g_a(\phi^* T^a \psi)\lambda^a + \text{h.c.} \quad (\text{Gaugino interaction terms}) \quad (2.50)$$

$$- W^i W_i^* - \frac{1}{2}g_a^2(\psi^* T^a \phi)^2 \quad (\text{scalar potential}), \quad (2.51)$$

$$(2.52)$$

where ψ represents the SM fermions, and ϕ denotes their associated spin-0 SUSY partners. The λ represent gauginos which are the SUSY partners of gauge bosons in $F_{\mu\nu}^a$ and D_μ . W_i (W_{ij}) is the first (second) derivative of super-potential W , where W is defined by:

$$W^i := \frac{\delta W}{\delta \phi_i}, \quad W^{ij} := \frac{\delta^2 W}{\delta \phi_i \delta \phi_j}, \quad (2.53)$$

$$W := \bar{U} \mathbf{y}_u Q H_u - \bar{D} \mathbf{y}_d Q H_d - \bar{E} \mathbf{y}_d Q H_d + \mu H_u H_d.$$

$\mathbf{y}_u, \mathbf{y}_d, \mathbf{y}_e$ are the Yukawa matrices as in Eq. 2.22. It has to be noted that no new theory parameters are introduced in addition to the SM in $\mathcal{L}_{\text{SUSY}}^{\text{MSSM}}$.

On the other hand, the soft SUSY breaking term $\mathcal{L}_{\text{soft}}^{\text{MSSM}}$ is the SUSY variant part of the Lagrangian.

SUSY breaking An exact SUSY necessitates that the SUSY partners possess masses identical to those of the SM particles. However, this condition has not been met, at least within the energy scales observable in our current universe, as no SUSY particles have yet been discovered. Consequently, a viable SUSY model must incorporate terms that account for SUSY breaking within its Lagrangian framework. Simultaneously, it is essential to preserve the advantageous characteristics of SUSY, particularly its potential to address the fine-tuning issue associated with the Higgs mass (Section 2.2.1). As a result, the SUSY breaking terms are typically constrained to a form known as “soft breaking”, which ensures the cancellation of quadratic divergences as outlined in Eq. 2.27.

The most general form of the soft breaking terms is given by:

$$\mathcal{L}_{\text{soft}}^{\text{MSSM}} = -\frac{1}{2} \left(M_3 \tilde{g} \tilde{g} + M_2 \tilde{W} \tilde{W} + M_1 \tilde{B} \tilde{B} + \text{c.c.} \right) \quad (\text{Gaugino mass terms}) \quad (2.54)$$

$$- \tilde{Q}^\dagger \mathbf{m}_{\tilde{Q}}^2 \tilde{Q} - \tilde{L}^\dagger \mathbf{m}_{\tilde{L}}^2 \tilde{L} - \tilde{U}^\dagger \mathbf{m}_{\tilde{U}}^2 \tilde{U} - \tilde{D}^\dagger \mathbf{m}_{\tilde{D}}^2 \tilde{D} - \tilde{E}^\dagger \mathbf{m}_{\tilde{E}}^2 \tilde{E} \quad (\text{Sfermion mass terms}) \quad (2.55)$$

$$- \left(\tilde{U} \mathbf{a}_u \tilde{Q} H_u - \tilde{D} \mathbf{a}_d \tilde{Q} H_d - \tilde{E} \mathbf{a}_e \tilde{L} H_d + \text{c.c.} \right) \quad (\text{Trilinear coupling terms}) \quad (2.56)$$

$$- m_{H_u}^2 H_u^* H_u - m_{H_d}^2 H_d^* H_d - (b H_u H_d + \text{c.c.}). \quad (\text{Higgs potential}) \quad (2.57)$$

The notation $(\tilde{Q}, \tilde{L}, \tilde{U}, \tilde{D}, \tilde{E})$ represent the supersymmetric part of the super-multiples (Q, L, U, D, E) . In the first line (Eq. 2.54), M_1, M_2 and M_3 are the bino, wino, and gluino mass terms. Eq. 2.55 incorporates the mass terms of sfermions, and the trilinear terms in Eq. 2.56 characterize the Yukawa interaction between left-handed and right-handed sfermions. Additionally, the last terms represent the MSSM Higgs potential, which governs the EW symmetry breaking. While this thesis does not focus on a specific model, several models provide explicit mechanisms for soft SUSY breaking. The most basic models are referred to as GMSB, AMSB (Anomaly-mediated SUSY breaking [86, 87]) or mSUGRA (minimal Super Gravity [88]).

R-parity A quantum number P_R , linked to the number of SUSY partners (similar to lepton number or baryon number etc.), can be defined using spin, baryon number, and lepton number as follows:

$$P_R := (-1)^{-3(B-L)+2s}. \quad (2.58)$$

The first half of Eq. 2.58, $(-1)^{3(B-L)}$, is known as matter parity, P_M . Quark and lepton supermultiplets all have $P_M = -1$, while the Higgs supermultiplets, gauge bosons and gauginos have $P_M = +1$. Because of the second half of Eq. 2.58, $(-1)^{2s}$, the SM particle and its superpartner within the same supermultiplet do not have the same P_R . All of the SM particles and the Higgs bosons have $P_R = +1$, while all of the squarks, sleptons, gauginos, and higgsinos have $P_R = -1$. The associated symmetry is known as R -parity, a conservation law that forbids the single production of SUSY particles, as well as the annihilation of the SM particles into a resonance of SUSY particles.

This results in a series of phenomenological advantages:

- The LSP can be a candidate for dark matter if it has no electric charge. The lightest neutralino is typically regarded as the most common candidate.
- Proton decay as illustrated in Fig. 2.8 is not allowed, which aligns well with the constraints established by experiments [89].

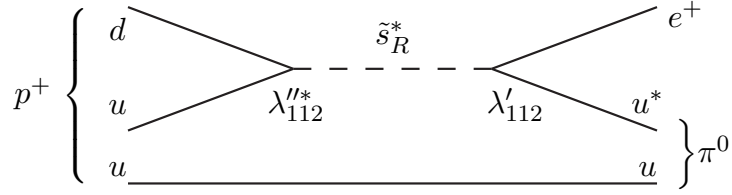


Figure 2.8: An example process of a proton decay triggered by intermediate SUSY particles (scalar-strange quark here). λ''_{112} and λ'_{112} are couplings for corresponding interaction vertices which violate R -parity.

In the context of the MSSM, the conservation of R -parity is explicitly postulated, which entails the exclusion of following terms from the most general superpotential:

$$\begin{aligned} W_{\Delta L=1} &= \frac{1}{2} \lambda^{ijk} L_i L_j \bar{e}_k + \lambda'^{ijk} L_i Q_j \bar{d}_k + \mu^i L_i H_u, \\ W_{\Delta B=1} &= \frac{1}{2} \lambda^{ijk} \bar{u}_i \bar{d}_j \bar{d}_k. \end{aligned} \quad (2.59)$$

2.3.3 Mass Spectra

The masses of SUSY particles are determined by the coefficient associated with mass terms (e.g. m in $m\phi\phi$) in the Lagrangian (Eq. 2.47). This involves extracting relevant terms and diagonalizing the mass matrices, accounting for the mixing of interaction eigenstates.

Squarks and sleptons Sfermion mass terms are sourced by the soft Lagrangian, $\mathcal{L}_{\text{soft}}^{\text{MSSM}}$. They are generally allowed to mix between different generations via the off-diagonal components either in the sfermion mass or trilinear coupling terms. However, these mixings lead to a significant rate of flavor changing natural current which is experimentally highly disfavored. Thus the off-diagonal components in the sfermion mass and trilinear coupling terms are usually set to zero:

$$\mathbf{m}_{\tilde{Q}} = m_{\tilde{Q}}^2 \mathbf{1}, \quad \mathbf{m}_{\tilde{U}} = m_{\tilde{U}}^2 \mathbf{1}, \quad \mathbf{m}_{\tilde{D}} = m_{\tilde{D}}^2 \mathbf{1}, \quad \mathbf{m}_{\tilde{L}} = m_{\tilde{L}}^2 \mathbf{1}, \quad \mathbf{m}_{\tilde{E}} = m_{\tilde{E}}^2 \mathbf{1}, \quad (2.60)$$

$$\mathbf{a}_u = A_{u0} \mathbf{y}_u, \quad \mathbf{a}_d = A_{d0} \mathbf{y}_d, \quad \mathbf{a}_e = A_{e0} \mathbf{y}_e. \quad (2.61)$$

Since the top quark, bottom quark and tau lepton are the heaviest fermions in the SM, it is useful to make an approximation that only the (3,3) family components of each \mathbf{y}_u , \mathbf{y}_d and \mathbf{y}_e are important. In this approximation, squared-mass matrix for the stop reduces to:

$$\begin{pmatrix} m_{Q_3}^2 + m_t^2 + (T_{3,t_L} - Q_t \sin^2 \theta_W) \cos(2\beta) m_Z^2 & v(A_{u0}^* y_t \sin \beta - \mu y_t \cos \beta) \\ v(A_{u0} y_t \sin \beta - \mu^* y_t \cos \beta) & m_{U_3}^2 + m_t^2 + Q_t \sin^2 \theta_W \cos(2\beta) m_Z^2 \end{pmatrix}. \quad (2.62)$$

As the magnitude of the off-diagonal component of this mass matrix scales with the Yukawa coupling, the effect of the mixing between left- and right-handed squarks can be only sizable in case of third generation sfermions (stop, sbottom and stau). Since the masses of lighter eigenstates of the third generation sfermions can be significantly lowered, the third generation sfermions are particularly phenomenologically important.

Gauginos and higgsinos EW gauginos and higgsinos masses are fed solely from $\mathcal{L}_{\text{soft}}^{\text{MSSM}}$. The gauge eigenstate of charged EW gauginos (charginos; $\tilde{W}^\pm, \tilde{H}_u^\pm, \tilde{H}_d^\pm$) with same electric charges will mix each other. The mass matrices are described as,

$$\begin{pmatrix} M_2 & \sqrt{2}m_W \sin \beta \\ \sqrt{2}m_W \cos \beta & \mu \end{pmatrix}. \quad (2.63)$$

The diagonalized mass eigenvalues are then,

$$m_{\tilde{\chi}_{1,2}^\pm}^2 = \frac{1}{2} \left[|M_2|^2 + |\mu|^2 + 2m_W^2 \mp \sqrt{(|M_2|^2 + |\mu|^2 + 2m_W^2)^2 - 4|\mu M_2 - m_W^2 \sin 2\beta|^2} \right]. \quad (2.64)$$

The conventional notation for charginos masses $m(\tilde{\chi}_{1,2}^\pm)$ are defined by sorting these eigenvalues as $m(\tilde{\chi}_1^\pm) < m(\tilde{\chi}_2^\pm)$. The mass matrix for neutral EW gauginos (neutralinos; $\tilde{B}, \tilde{W}^0, \tilde{H}_u^0, \tilde{H}_d^0$) are given as,

$$\begin{pmatrix} M_1 & 0 & -\cos \beta \sin \theta_W m_Z & \sin \beta \sin \theta_W m_Z \\ 0 & M_2 & \cos \beta \cos \theta_W m_Z & -\sin \beta \cos \theta_W m_Z \\ -\cos \beta \sin \theta_W m_Z & \cos \beta \cos \theta_W m_Z & 0 & -\mu \\ \sin \beta \sin \theta_W m_Z & -\sin \beta \cos \theta_W m_Z & -\mu & 0 \end{pmatrix}. \quad (2.65)$$

The eigenvalues are,

$$m_1 = M_1 - \frac{m_Z^2 \sin^2 \theta_W (M_1 + \mu \sin 2\beta)}{\mu^2 - M_1^2} + \dots, \quad (2.66)$$

$$m_2 = M_2 - \frac{m_W^2 (M_2 + \mu \sin 2\beta)}{\mu^2 - M_2^2} + \dots, \quad (2.67)$$

$$m_3 = |\mu| + \frac{m_Z^2 (1 - \sin 2\beta) (\mu + M_1 \cos^2 \theta_W + M_2 \sin^2 \theta_W)}{2(\mu + M_1)(\mu + M_2)} + \dots, \quad (2.68)$$

$$m_4 = |\mu| + \frac{m_Z^2 (1 + \sin 2\beta) (\mu - M_1 \cos^2 \theta_W - M_2 \sin^2 \theta_W)}{2(\mu - M_1)(\mu - M_2)} + \dots \quad (2.69)$$

As charginos, the conventional notation for neutralino masses $m(\tilde{\chi}_{1-4}^0)$ are defined by sorting these eigenvalues as $m(\tilde{\chi}_1^0) < m(\tilde{\chi}_2^0) < m(\tilde{\chi}_3^0) < m(\tilde{\chi}_4^0)$.

Finally, gluinos are color-octet fermions and do not mix to any other gauginos.

The MSSM Higgs sector In the MSSM, the description of EW symmetry breaking is slightly complicated by the fact that there are two complex Higgs doublets rather than just one in the ordinary SM. The MSSM Higgs potential is given by,

$$\begin{aligned} V = & (|\mu|^2 + m_{H_u}^2)(|H_u^0|^2 + |H_u^\pm|^2) + (|\mu|^2 + m_{H_d}^2)(|H_d^0|^2 + |H_d^\pm|^2) \\ & + [b(H_u^+ H_d^- - H_u^0 H_d^0) + \text{c.c.}] \\ & + \frac{1}{8}(g^2 + g'^2)(|H_u^0|^2 + |H_u^\pm|^2 - |H_d^0|^2 - |H_d^\pm|^2)^2 \\ & + \frac{1}{2}g^2 |H_u^+ H_d^{0*} + H_u^0 H_d^{-*}|^2. \end{aligned} \quad (2.70)$$

Similarly to the case in SM, implementing the spontaneous symmetry breaking and requiring $\partial V / \partial H_u^0 = \partial V / \partial H_d^0 = 0$, one arrives:

$$\sin(2\beta) = \frac{2b}{m_{H_u}^2 + m_{H_d}^2 + 2|\mu|^2}, \quad (2.71)$$

$$m_Z^2 = \frac{|m_{H_d}^2 - m_{H_u}^2|}{\sqrt{(1 - \sin^2(2\beta))}} - m_{H_u}^2 - m_{H_d}^2 - 2|\mu|^2. \quad (2.72)$$

The Higgs masses are found by the mass terms:

$$m_{A^0}^2 = 2|\mu|^2 + m_{H_u}^2 + m_{H_d}^2, \quad (2.73)$$

$$m_{H^\pm}^2 = m_{A^0}^2 + m_W^2, \quad (2.74)$$

$$m_{h,H^0}^2 = \frac{1}{2} \left(m_{A^0}^2 + m_Z^2 \mp \sqrt{(m_{A^0}^2 - m_Z^2)^2 + 4m_Z^2 m_{A^0}^2 \sin^2(2\beta)} \right), \quad (2.75)$$

where H^\pm represents the mass eigenstate of the charged Higgs boson, while A^0 denotes the CP-odd Higgs boson. The mass eigenstates of the \mathcal{CP} -even neutral Higgs bosons are denoted as H^0 and h , with the lighter one h typically associated with the SM Higgs boson. Given that H^0 has not been observed up to a mass of 400 GeV-1 TeV, a large mass difference between h and H^0 is generally favored, suggesting a large value of $\tan \beta$.

2.3.4 Running Masses and GUT

Although the masses of SUSY particles are primarily treated as free parameters within the MSSM framework, a quick analysis can be conducted. In the context of SUSY, it is frequently assumed that mass unifications occur, particularly in the regime where:

- all sfermions masses converge to $m_{1/2}$
- all gaugino masses converge to m_0
- all Higgs boson H_u, H_d masses converge to $(\mu^2 + m_0^2)^{1/2}$

This configuration is particularly advantageous as it is available to cause EW symmetry breaking naturally at the EW scale, and is adopted in many minimal models including mSUGRA. Using the general condition satisfied in the 1-loop renormalization of gaugino masses:

$$\frac{d}{dt} \left(\frac{M_i}{\alpha_i} \right) = 0, \quad (i = 1, 2, 3). \quad (2.76)$$

it turns that M_i/α_i is constant in arbitrary scales. Therefore, one obtains:

$$\left. \frac{M_i}{\alpha_i} \right|_{Q=Q_{\text{EW}}} = \left. \frac{M_i}{\alpha_i} \right|_{Q=Q_{\text{GUT}}} = \frac{m_{1/2}}{\alpha_{\text{GUT}}}, \quad (2.77)$$

which is rewritable to

$$M_3 = \frac{\alpha_3}{\alpha_1} \sin^2 \theta_W M_2 = \frac{3}{5} \frac{\alpha_3}{\alpha_1} \cos^2 \theta_W M_1, \quad (2.78)$$

resulting in a rough prediction of gaugino masses near the TeV scale:

$$M_1 : M_2 : M_3 \sim 1 : 2 : 6. \quad (2.79)$$

The mass hierarchy between gluino, wino, and bino is primarily driven by this relationship and is a common assumption in SUSY phenomenology. However, it is important to acknowledge that the assumption of mass unification might be overly stringent.

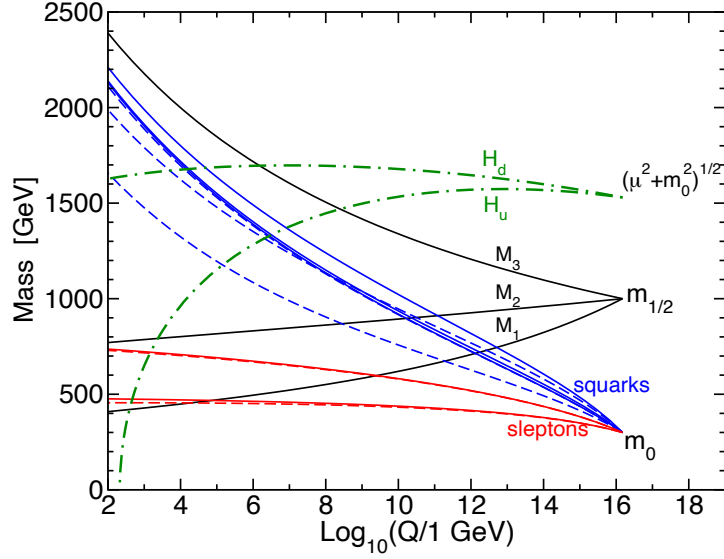


Figure 2.9: RG evolution of scalar and gaugino mass parameters in the MSSM with mSUGRA boundary conditions imposed at $Q_0 = 1.5 \times 10^{16}$ GeV [19]. The parameter $\mu^2 + m_{H_u}^2$ runs negative, provoking EW symmetry breaking. The parameters are $m_0 = 300$ GeV, $m_{1/2} = -A_0 = 1000$ GeV, $\tan\beta = 15$, and $\text{sign}(\mu) = +$.

The running masses of sfermions offer insights into the mass spectra at the EW scale. These masses can be determined clearly through the application of RGE:

$$m_{\tilde{d}_L}^2 = m_0^2 + K_3 + K_2 + \frac{1}{36}K_1 + \Delta_{\tilde{d}_L}, \quad (2.80)$$

$$m_{\tilde{u}_L}^2 = m_0^2 + K_3 + K_2 + \frac{1}{36}K_1 + \Delta_{\tilde{u}_L}, \quad (2.81)$$

$$m_{\tilde{d}_R}^2 = m_0^2 + K_3 + \frac{1}{9}K_1 + \Delta_{\tilde{d}_R}, \quad (2.82)$$

$$m_{\tilde{u}_R}^2 = m_0^2 + K_3 + \frac{4}{9}K_1 + \Delta_{\tilde{u}_R}, \quad (2.83)$$

$$m_{\tilde{e}_L}^2 = m_0^2 + K_2 + \frac{1}{4}K_1 + \Delta_{\tilde{e}_L}, \quad (2.84)$$

$$m_{\tilde{\nu}_L}^2 = m_0^2 + K_2 + \frac{1}{4}K_1 + \Delta_{\tilde{\nu}_L}, \quad (2.85)$$

$$m_{\tilde{e}_R}^2 = m_0^2 + K_1 + \Delta_{\tilde{e}_R}, \quad (2.86)$$

with identical formulas for the second-family squarks and sleptons. K_1 , K_2 , and K_3 respectively denote the contribution from the interaction of $U(1)_Y$, $SU(2)_L$ and, $SU(3)_L$ which are approximately:

$$K_1 \sim 0.15m_{1/2}^2, \quad K_2 \sim 0.5m_{1/2}^2, \quad K_3 \sim 6m_{1/2}^2. \quad (2.87)$$

and the correction factors $\Delta_{\tilde{f}}$ are given by the third component of weak isospin, T_3 , and the electric charge, q , as

$$\begin{aligned} \Delta_{\tilde{f}_L} &= (T_3 - q \sin^2 \theta_W) m_Z^2 \cos(2\beta), \\ \Delta_{\tilde{f}_R} &= q \sin^2 \theta_W m_Z^2 \cos(2\beta), \end{aligned} \quad (2.88)$$

which split apart the components of the $SU(2)_L$ -doublet sleptons and squarks. The mass splittings for the left-handed squarks and sleptons are governed by model-independent sum rules

$$m_{\tilde{e}_L}^2 - m_{\tilde{\nu}_e}^2 = m_{\tilde{d}_L}^2 - m_{\tilde{u}_L}^2 = g^2(v_u^2 - v_d^2)/2 = -\cos(2\beta)m_W^2. \quad (2.89)$$

The effect of running masses tends to be greater for squarks compared to sleptons because of the $SU(3)_L$ interaction, which generally results in lighter masses for sleptons. The typical running mass spectra is illustrated in Fig. 2.9.

2.4 MSSM and the Dark Matter Direct Detection

As mentioned in Section 2.2.3, MSSM with R -parity conservation provides good DM candidates, especially neutralinos. The process of Higgs boson exchange between neutralinos and nuclei induces the spin independent (SI) elastic scattering, as illustrated in Fig. 2.10(a). The corresponding $h\tilde{\chi}_1^0\tilde{\chi}_1^0$ coupling is given at tree level for higgsino-like LSP by [91],

$$c_{h\tilde{\chi}\tilde{\chi}} \simeq -\frac{1}{2}\text{sign}(\mu)(1 + \text{sign}(\mu)\sin 2\beta) \left(\tan^2 \theta_W \frac{g_1 m_W}{M_1 - |\mu|} + \frac{g_2 m_W}{|M_2| - |\mu|} \right), \quad (2.90)$$

for wino-like LSP by,

$$c_{h\tilde{\chi}\tilde{\chi}} \simeq -\frac{g_2}{2} \frac{m_W}{M_2^2 - \mu^2} (M_2 + \mu \sin 2\beta), \quad (2.91)$$

and for bino-like LSP by,

$$c_{h\tilde{\chi}\tilde{\chi}} \simeq -\frac{g_1}{2} \frac{m_W \tan \theta_W}{M_1^2 - \mu^2} (M_1 + \mu \sin 2\beta). \quad (2.92)$$

One can see that the coupling becomes large for $|\mu| \sim M_1$ or $|\mu| \sim |M_2|$. As the DM direct detection pushes the allowed parameter space into small $c_{h\tilde{\chi}\tilde{\chi}}$, large mixing between higgsino/bino and higgsino/wino, which is equivalent to a small mass difference between them, is disfavored. On the other hand, the completely pure Higgsino DM has already been ruled out, as the DM is a Dirac fermion and the scattering cross-section for the spin dependent (SD) elastic scattering, which is shown in Fig. 2.10(b), significantly exceeds the existing DM direct detection limits [92, 93].

2.5 MSSM and the Muon $g - 2$ Anomaly

The MSSM dominant contribution to muon magnetic moment is the one-loop diagram with chargino-sneutrino and the neutralino-smuon loop, as summarized in Fig. 2.11. Numerically,

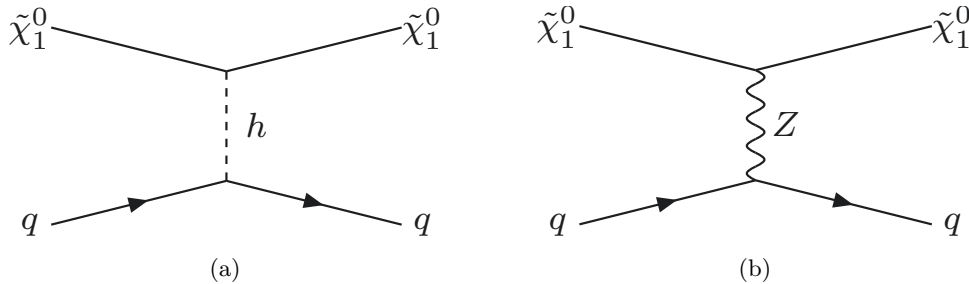


Figure 2.10: Diagrams inducing (a) spin independent and (b) spin dependent elastic scattering between neutralinos and quarks. The figure is taken from [90].

various loop contributions can be approximated as Ref. [94],

$$\Delta a_\mu(\tilde{W}^\pm, \tilde{H}^\pm, \tilde{\nu}_\mu) \simeq 15 \times 10^{-9} \left(\frac{\tan \beta}{10} \right) \left[\frac{(100 \text{ GeV})^2}{M_2 \mu} \right] \left[2 \cdot f_C \left(\frac{M_2^2}{m(\tilde{\nu}_\mu)^2}, \frac{\mu^2}{m(\tilde{\nu}_\mu)^2} \right) \right], \quad (2.93a)$$

$$\Delta a_\mu(\tilde{W}^0, \tilde{H}^0, \tilde{\mu}_L^\pm) \simeq -2.5 \times 10^{-9} \left(\frac{\tan \beta}{10} \right) \left[\frac{(100 \text{ GeV})^2}{M_2 \mu} \right] \left[6 \cdot f_N \left(\frac{M_2^2}{m(\tilde{\mu}_L)^2}, \frac{\mu^2}{m(\tilde{\mu}_L)^2} \right) \right], \quad (2.93b)$$

$$\Delta a_\mu(\tilde{H}^0, \tilde{B}^0, \tilde{\mu}_L^\pm) \simeq 0.76 \times 10^{-9} \left(\frac{\tan \beta}{10} \right) \left[\frac{(100 \text{ GeV})^2}{M_1 \mu} \right] \left[6 \cdot f_N \left(\frac{M_1^2}{m(\tilde{\mu}_L)^2}, \frac{\mu^2}{m(\tilde{\mu}_L)^2} \right) \right], \quad (2.93c)$$

$$\Delta a_\mu(\tilde{H}^0, \tilde{B}^0, \tilde{\mu}_R^\pm) \simeq -1.5 \times 10^{-9} \left(\frac{\tan \beta}{10} \right) \left[\frac{(100 \text{ GeV})^2}{M_1 \mu} \right] \left[6 \cdot f_N \left(\frac{M_1^2}{m(\tilde{\mu}_R)^2}, \frac{\mu^2}{m(\tilde{\mu}_R)^2} \right) \right], \quad (2.93d)$$

$$\Delta a_\mu(\tilde{\mu}_L^\pm, \tilde{\mu}_R^\pm, \tilde{B}^0) \simeq 1.5 \times 10^{-9} \left(\frac{\tan \beta}{10} \right) \left[\frac{(100 \text{ GeV})^2 M_1 \mu}{m(\tilde{\mu}_L)^2 m(\tilde{\mu}_R)^2} \right] \left[6 \cdot f_N \left(\frac{m(\tilde{\mu}_L)^2}{M_1^2}, \frac{m(\tilde{\mu}_R)^2}{M_1^2} \right) \right], \quad (2.93e)$$

where f_C, f_N are the charged and neutral loop functions respectively,

$$f_C(x, y) = xy \left[\frac{5 - 3(x + y) + xy}{(x - 1)^2(y - 1)^2} - \frac{2 \log x}{(x - y)(x - 1)^3} + \frac{2 \log y}{(x - y)(y - 1)^3} \right], \quad (2.94a)$$

$$f_N(x, y) = xy \left[\frac{-3 + x + y + xy}{(x - 1)^2(y - 1)^2} + \frac{2x \log x}{(x - y)(x - 1)^3} - \frac{2y \log y}{(x - y)(y - 1)^3} \right]. \quad (2.94b)$$

The arguments in the left-hand side of Eq. 2.93 show the SUSY particles which propagate in each loop diagram. For a certain loop to have sufficient contribution to the muon anomalous magnetic

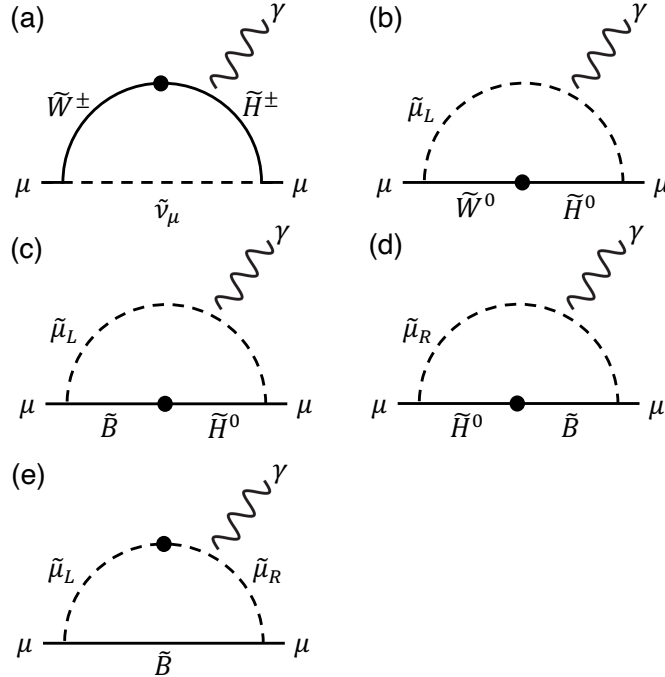


Figure 2.11: One-loop Feynman diagrams that contribute to the muon anomalous magnetic momentum.

momentum, all three SUSY particles in the loop must be light. The SUSY contributions to the muon anomalous magnetic momentum are enhanced when $\tan\beta$ is large or masses of SUSY particles in the loop are light. When masses of SUSY particles in the loop are $\mathcal{O}(100)$ GeV and $\tan\beta$ is $\mathcal{O}(10)$, Eq. 2.93 become $\mathcal{O}(10^{-9})$ which can explain the muon $g - 2$ anomaly.

Chapter 3

SUSY Mass Hierarchy Motivated by Muon $g - 2$ Anomaly and Dark Matter

In this chapter, a class of SUSY scenarios which are motivated by the muon $g - 2$ anomaly and dark matter is analyzed and the target scenario is specified.

3.1 Muon $g - 2$ Anomaly and Dark Matter Motivated SUSY scenarios

There are four major SUSY scenarios, depending on which diagram in Fig. 2.11 dominates the contribution to the muon anomalous magnetic momentum. Here we assume that only one type of loop in Fig. 2.11 dominates the contribution.¹

(A) scenario : $M_2, \mu, m(\tilde{\mu}_L) \ll M_1, m(\tilde{\mu}_R)$. Fig. 2.11(a)(b) dominates.

(B) scenario : $M_1, \mu, m(\tilde{\mu}_L) \ll M_2, m(\tilde{\mu}_R)$. Fig. 2.11(c) dominates.

(C) scenario : $M_1, \mu, m(\tilde{\mu}_R) \ll M_2, m(\tilde{\mu}_L)$. Fig. 2.11(d) dominates.

(D) scenario : $M_1, m(\tilde{\mu}_L), m(\tilde{\mu}_R) \ll M_2, \mu$. Fig. 2.11(e) dominates.

By permutation of the three SUSY particles in each loop, six different mass hierarchy sub-scenarios are possible in each scenario, resulting in a total of 24 ($= 4 \times 3!$) possible sub-scenarios. We systematically analyze each of these sub-scenarios and summarize which sub-scenarios is viable in terms of the DM and study the constraints from the LHC.

Table 3.1 lists the nature of the DM for all sub-scenarios. The naming convention of the sub-scenario follows “ $S_{\text{heavy}}\text{-}S_{\text{middle}}\text{-}S_{\text{light}}$ ” format where the symbols S_{heavy} , S_{middle} , and S_{light} represent single SUSY particle, or collectively a bunch of approximately mass degenerate SUSY particles. Symbol “W” stands for wino, “H” stands for higgsino, “B” stands for bino, and “L” (“R”) stands for left-handed (right-handed) smuon. The symbol “H” collectively represents the charged and two neutral higgsinos, and the “W” represents the charged and neutral wino. For

¹We could consider the case where multiple loops contribute to the muon anomalous magnetic momentum, but that would be too complicated, and we will not consider that case. In that case, however, it is expected that constraints will become tighter as the number of light SUSY particles increase and search becomes easier in general.

Table 3.1: The nature and faced constraints of the DM (“DM condition”). Line in gray indicates a sub-scenario that does not satisfy the dark matter condition.

(A) scenario	DM condition
W-H-L	(a) : Sneutrino LSP
W-L-H	(c) : Underabundant
H-W-L	(a) : Sneutrino LSP
H-L-W	(c) : Underabundant
L-W-H	(c) : Underabundant
L-H-W	(c) : Underabundant
(B) scenario	
H-B-L	(a) : Sneutrino LSP
H-L-B	(d) : Fulfill DM relic density with slepton-bino coannihilation
B-H-L	(a) : Sneutrino LSP
B-L-H	(c) : Underabundant
L-H-B	(e) : Overabundant or excluded by DM direct detection
L-B-H	(c) : Underabundant
(C) scenario	
H-B-R	(b) : Charged LSP
H-R-B	(d) : Fulfill DM relic density with slepton-bino coannihilation
B-H-R	(b) : Charged LSP
B-R-H	(c) : Underabundant
R-H-B	(e) : Overabundant or excluded by DM direct detection
R-B-H	(c) : Underabundant
(D) scenario	
B-L-R	(b) : Charged LSP
B-R-L	(a) : Sneutrino LSP
L-B-R	(b) : Charged LSP
L-R-B	(d) : Fulfill DM relic density with slepton-bino coannihilation
R-B-L	(a) : Sneutrino LSP
R-L-B	(d) : Fulfill DM relic density with slepton-bino coannihilation

example the W-H-L stands for the sub-scenario where wino, higgsino, left-handed smuon are heavy in that order.

The nature of the DM and the constraints can be summarized into five categories depending on the species of S_{light} and S_{middle} . (a) The case when S_{light} is the left-handed smuon and the sneutrino is the LSP. The sneutrino couples to Z boson with gauge strength and is strongly constrained by DM direct detection up to a very heavy mass, beyond which it becomes overabundant [26, 95]. (b) When S_{light} is the right-handed smuon, the LSP is charged and unsuitable for DM. (c) When S_{light} is the wino or higgsino, the LSP will be the lightest neutralino $\tilde{\chi}_1^0$, and constitutes only a part of DM. Wino (higgsino) DM fulfills the DM relic density when $m(\tilde{\chi}_1^0) \sim 3$ TeV (1 TeV), which tends to be too heavy to explain muon $g - 2$ anomaly. (d) When the LSP is bino and NLSP is the smuon, bino LSP fulfills the DM relic density when $\Delta m(\tilde{\ell}, \tilde{\chi}_1^0) \lesssim 100$ GeV [96]. (e) When the LSP is bino and NLSP is the higgsino, mixing between the bino and higgsino tends to be large to explain the correct DM relic density, and almost all

region is excluded already by the DM direct detection search [97, 98].

The discussion of DM conditions indicates that smuon LSP : case (a)(b), bino LSP with higgsino NLSP : case (e) are not promising, and we are left with twelve mass hierarchies where the LSP is wino/higgsino : case (c) or the LSP is bino and the NLSP is smuon: case (d).

Table 3.2 summarizes the relevant collider signatures which have competitive sensitivities at LHC for mass hierarchies case (c) and case (d). The production cross-section of bino like neutralino is too small to aim at LHC with respect to the available integrated luminosity, and the bino production channel can be ignored.²

For the S_{light} production mode, we have to consider wino or higgsino pair production. The collider signature for the wino production will be disappearing tracks [99]. The disappearing track signature is important when the mass splittings between the lightest chargino and lightest neutralino is below 200 MeV. Charged and neutral winos tend to have mass splitting of this order due to radiative corrections. Pure-higgsino also has mass splitting of this order, but in the models motivated by muon $g - 2$ anomaly, the mass of wino or bino should be close to that of higgsino, resulting in a mixing of higgsino with wino or bino and a higgsino mass splitting of $\mathcal{O}(1 \text{ GeV})$. Therefore the collider signature for the higgsino production will be soft leptons or displaced tracks [100]. These disappearing/displaced track and soft lepton signatures are well covered by ATLAS and CMS experiments [101–110] at LHC.

For the S_{middle} and S_{heavy} production which decays directly to S_{light} , the signatures which

Table 3.2: The expected collider signatures including the four different modes in terms of the productions and decays as described in the main text and Fig. 3.1. The prohibited modes are indicated by “N/A”, and the modes with negligible experimental sensitivity is labeled as “-”. The collider signature of the cascade decay in W-L-H (L-B-H/R-B-H) sub-scenario is shown in blue (red), which may have unique sensitivity to the corresponding sub-scenario.

(A) scenario	Relevant collider signatures			
	S_{light} prod.	S_{middle} prod.	S_{heavy} prod. + direct	S_{heavy} prod. + cascade
W-L-H	soft lepton/ displaced track	$2\ell + E_{\text{T}}^{\text{miss}}$	di-boson + $E_{\text{T}}^{\text{miss}}$	4ℓ/3ℓ/2ℓ + $E_{\text{T}}^{\text{miss}}$
H-L-W	disappearing track	-	-	-
L-W-H	soft lepton/ displaced track	di-boson + $E_{\text{T}}^{\text{miss}}$	-	-
L-H-W	disappearing track	di-boson + $E_{\text{T}}^{\text{miss}}$	-	-
(B) scenario				
H-L-B	N/A	$2\ell + E_{\text{T}}^{\text{miss}}$	di-boson + $E_{\text{T}}^{\text{miss}}$	-
B-L-H	soft lepton/ displaced track	$2\ell + E_{\text{T}}^{\text{miss}}$	N/A	N/A
L-B-H	soft lepton/ displaced track	N/A	-	di-boson + 2ℓ/1ℓ + $E_{\text{T}}^{\text{miss}}$
(C) scenario				
H-R-B	N/A	$2\ell + E_{\text{T}}^{\text{miss}}$	di-boson + $E_{\text{T}}^{\text{miss}}$	-
B-R-H	soft lepton/ displaced track	$2\ell + E_{\text{T}}^{\text{miss}}$	N/A	N/A
R-B-H	soft lepton/ displaced track	N/A	-	di-boson + 2ℓ + $E_{\text{T}}^{\text{miss}}$
(D) scenario				
L-R-B	N/A	$2\ell + E_{\text{T}}^{\text{miss}}$	$2\ell + E_{\text{T}}^{\text{miss}}$	N/A
R-L-B	N/A	$2\ell + E_{\text{T}}^{\text{miss}}$	-	N/A

²There exists a bino-higgsino-Higgs vertex, therefore if both bino and higgsino were light, it could be possible to have bino+higgsino production through s-channel Higgs. However since Higgs which have a narrow width must be very off-shell, bino can be considered not to be directly produced.

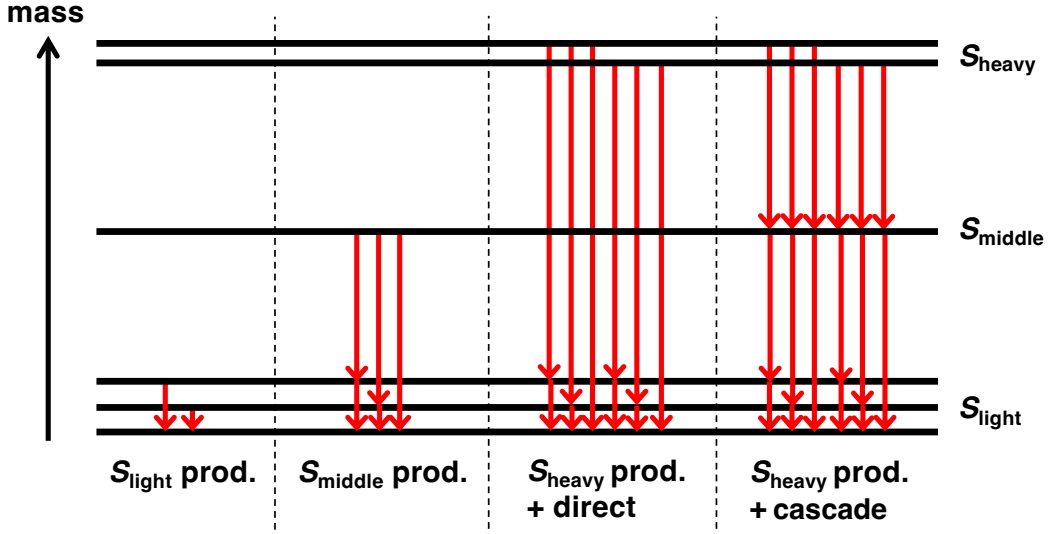


Figure 3.1: A schematic diagram for the production and decay modes. The number of particles with close masses is just one example.

have sufficient sensitivities are typically two charged lepton + E_T^{miss} (“ $2\ell + E_T^{\text{miss}}$ ”) or two bosons (W, Z, h) + E_T^{miss} (“di-boson + E_T^{miss} ”) where E_T^{miss} represents the missing transverse momentum imbalance. We do not show the soft production which occurs when S_{light} decays into the pseudo-degenerate LSP. These $2\ell + E_T^{\text{miss}}$ and di-boson + E_T^{miss} signatures are also well covered by several optimized analyses [104, 105, 111–121].

In the S_{heavy} production, cascade decay through S_{middle} is also possible. However, the number of the promising collider signatures is limited. For example, the wino pair production cross-section is generally large and in the H-L-W and L-W-H sub-scenarios, the heavier higgsino or smuon pair production tends to have less sensitivity compared to the wino search. In the H-L-W, L-H-W, H-L-B, H-R-B sub-scenarios, higgsino decay through smuon or smuon decay through higgsino have usually negligible branching ratios due to small coupling between the smuon and higgsino which is mainly determined by the Yukawa coupling. These discussions leave us with three sub-scenarios with potentially promising cascade decay signatures. A cascade decay of the W-L-H sub-scenario leads to the signature of four/three/two charged leptons + E_T^{miss} (“ $4\ell/3\ell/2\ell + E_T^{\text{miss}}$ ”) for which diagram is shown in Fig. 3.2(a). On the other hand, cascade decays of L-B-H and R-B-H sub-scenarios lead to the signature of two bosons (W, Z, h) + two/one charged leptons + E_T^{miss} (“di-boson + $2\ell/1\ell + E_T^{\text{miss}}$ ”) for which diagram is shown in Fig. 3.2(b). For these sub-scenarios, there are analyses that cover the S_{heavy} direct decay, S_{middle} (for W-L-H sub-scenario) and S_{light} production, but there are no analysis dedicated to the S_{heavy} cascade decay. Since unique sensitivity may be obtained by focusing on S_{heavy} cascade decay, we will discuss W-L-H and L-B-H sub-scenarios below. Although the situation for the R-B-H sub-scenario is same as the L-B-H sub-scenario, the right-handed smuon pair production cross-section is an order of magnitude smaller than that of the left-handed smuon and therefore we do not include it here.

3.2 Identification of Viable MSSM Mass Space

To identify the viable MSSM mass space, we perform the MSSM parameter scan and the re-interpretation of the relevant ATLAS SUSY searches. We investigate the two sub-scenarios, W-L-H and L-B-H, given by the mass orderings of $M_1, M_2, \mu, m(\tilde{\ell}_L)$, and $m(\tilde{\ell}_R)$. The sign of

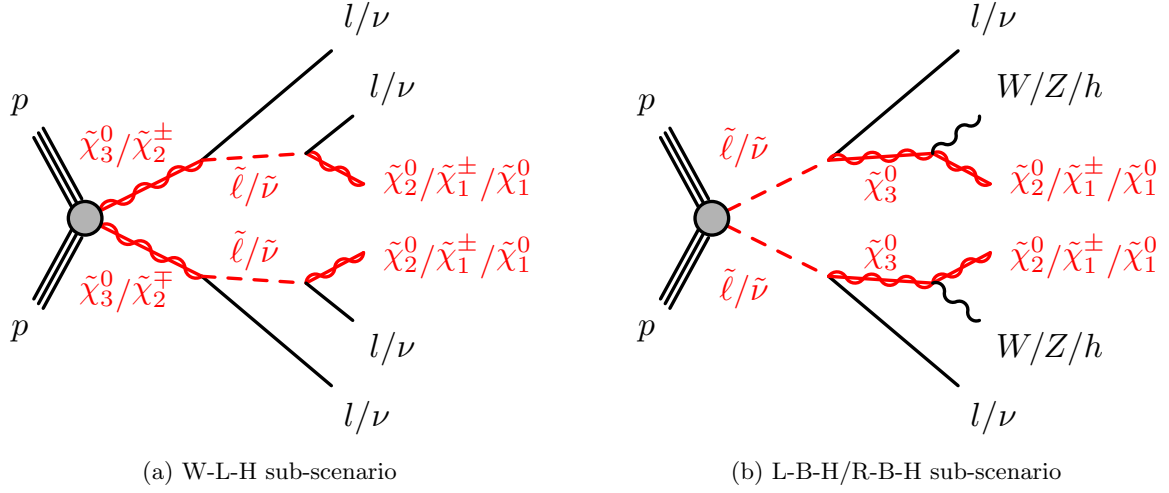


Figure 3.2: Feynman diagrams of the cascade decay signatures in the W-L-H sub-scenario and L-B-H/R-B-H sub-scenario. The decays of $\tilde{\chi}_2^0$ and $\tilde{\chi}_1^\pm$ are ignored as they only result in low-momentum particles that are almost never reconstructed.

M_1 is fixed to positive and all combinations of the signs of M_2 and μ are scanned. Since the sign of M_1 can be freely chosen, this setting does not lose any generality. We assume that the colored sector is heavy, M_A to be large, and take the slepton trilinear coupling $a_{\tilde{l}}$ to be zero. We also assume that the stau is decoupled. This is to ensure the stability of the EW vacuum [122] which is related to the stau-Higgs potential.

Here, we briefly review the experimental constraints that are relevant for the EW sector of the MSSM, which are the deviation of the muon anomalous magnetic moment from its SM prediction, W boson mass, the measurement of the DM relic density, and the limits from DM direct detection experiments. For the Higgs boson mass, we assume that the radiative corrections to the light \mathcal{CP} -even Higgs boson, largely originating from the top/stop sector, yield a value in agreement with the experimental data, $m_h = 125$ GeV, and therefore is not included in the parameter scan constraints.

1. **Muon $g - 2$ constraint:** We use the experimental result $\Delta a_\mu^{\text{exp}} = (24.9 \pm 5.0) \times 10^{-10}$ as a selection at the 2σ level, and models that are not consistent with $\Delta a_\mu^{\text{exp}}$ within 2σ are discarded. MSSM contribution to muon anomalous magnetic moment up to two-loop order is calculated using `GM2Calc v2.1.0` [123], implementing two-loop corrections from Ref. [124–126].
2. **W boson mass constraint:** EW SUSY particles can induce shifts in W boson mass, m_W [127–129]. We use the experimental world average, $m_W^{\text{exp}} = 80.379 \pm 0.012$ GeV, and the models are required to predict the m_W within 2σ from the central value. It has to be noted that in this average, the newest result by CDF collaboration, $m_W^{\text{CDF-new}} = 80.4335 \pm 0.0094$ GeV [130], is not included.
3. **Dark matter relic density constraint:** For the experimental data, we use the latest result from Planck [26] as an upper bound, $\Omega_{\text{CDM}} h^2 \leq 0.120$. The relic density in the MSSM is calculated with `MicroOMEGAs v5.0.8` [131–133].
4. **Dark matter direct detection constraint:** We use the constraint on the spin-independent DM scattering cross-section, σ_p^{SI} , from LZ experiment and discard models with larger DM

scattering cross-section compared to the 90% confidence limit. The theoretical calculation is performed using `MicroOMEGAs v5.0.8` [131–133]. We scale the spin-independent DM scattering cross-section by a factor of $\Omega_{\tilde{\chi}_1^0} h^2 / 0.120$ to account for the fact that $\tilde{\chi}_1^0$ provides only a fraction of the total DM relic density of the universe.

For each sub-scenario, the mass hierarchy and the range of parameters are set as follows.

W-L-H sub-scenario

$$\begin{aligned} 100 \text{ GeV} \leq |\mu| \leq 1000 \text{ GeV}, \quad |\mu| \leq m(\tilde{\ell}_L), \\ m(\tilde{\ell}_L) \leq |M_2|, \quad 1 \leq \tan \beta \leq 62. \end{aligned} \quad (3.1)$$

$M_1, m(\tilde{\ell}_R)$ are assumed to be decoupled.

L-B-H sub-scenario

$$\begin{aligned} 100 \text{ GeV} \leq |\mu| \leq 1000 \text{ GeV}, \quad |\mu| \leq M_1, \\ M_1 \leq m(\tilde{\ell}_L), \quad 1 \leq \tan \beta \leq 62. \end{aligned} \quad (3.2)$$

$|M_2|, m(\tilde{\ell}_R)$ are assumed to be decoupled.

The lower (upper) limit on $\tan \beta$ is obtained by requiring that $y_t(y_b \text{ and } y_\tau)$ not be non-perturbatively large above the EW scale [19].

The mass points are generated by scanning randomly over the input parameter ranges which is specified above. We employ the `Multinest v3.10` [134–136] package for the scan, using flat priors for all parameters. The Markov Chain Monte Carlo method based on the Metropolis-Hastings algorithm is adopted to perform the scan of MSSM parameter space. The Gaussian distributed constraints are implemented in the likelihood, \mathcal{L} , to guide the scan which take the form

$$-\log \mathcal{L} = \sum_i \frac{(\hat{\mu}_i - \mu_i)^2}{2(\sigma_i^2 + \tau_i^2)}, \quad (3.3)$$

where i runs over the constraints mentioned above. The $\hat{\mu}_i$ denotes the predicted value of observable i , μ_i is the corresponding central value of experimental measurement, and σ_i (τ_i) is the experimental (theory) uncertainty. As the MSSM spectrum and SLHA file generator, we use `Spheno v4.0.4` [137, 138]. The SLHA output files are then passed as input files to `GM2Calc v2.1.0` and `MicroOMEGAs v5.0.8` for the calculation of the muon anomalous magnetic momentum and the DM observables, respectively. Finally mass points are checked whether they satisfy the muon $g - 2$ constraint, the W boson mass constraint, the DM relic density, and the DM direct detection constraint.

3.2.1 W-L-H sub-scenario

In Fig. 3.3, we show the result of the parameter scan for the W-L-H sub-scenario. Only the points with $M_2 \times \mu > 0$ survive all scan constraints since the muon $g - 2$ experimental value is positive. Fig. 3.3(a) shows the scan result in $m(\tilde{\chi}_3^0)$ vs. $m(\tilde{\chi}_1^0)$ plane and the color code represents the $\Delta a_\mu^{\text{MSSM}} - \Delta a_\mu^{\text{exp}}$. The allowed LSP mass, $m(\tilde{\chi}_1^0)$, ranges from 100 GeV to 500 GeV, where wino mass, $m(\tilde{\chi}_3^0)$, is found in the range between 500 GeV and 4500 GeV. For the constraints from DM direct detection, it can be seen from Eq. 2.90 that the $h\tilde{\chi}_1^0\tilde{\chi}_1^0$ coupling becomes large for $|\mu| \sim |M_2|$ or $|\mu| \sim M_1$. Consequently, the LZ direct detection bound [27] pushes the allowed parameter space into the almost pure higgsino-LSP region, namely, to larger values for $|M_2/\mu|$ and $M_1/|\mu|$. Fig. 3.3(b) shows the $\sigma_{\text{SI}} \times \Omega_{\tilde{\chi}_1^0} h^2 / 0.120$ vs. $m(\tilde{\chi}_1^0)$ plane, and the color code represents

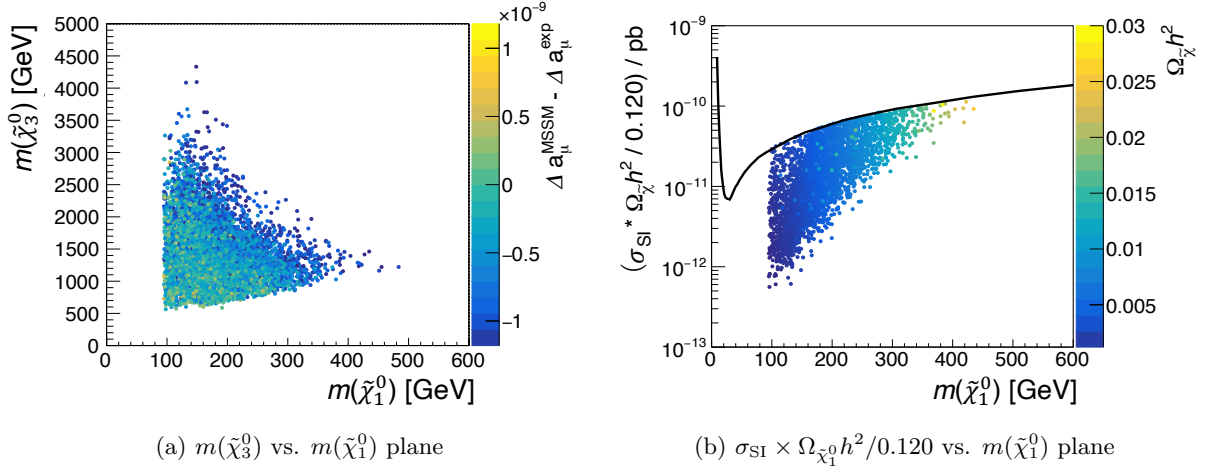


Figure 3.3: Scan result for the W-L-H sub-scenario. (a) The color code represents the $\Delta a_\mu^{\text{MSSM}} - \Delta a_\mu^{\text{exp}}$. (b) The color code represents the DM relic density. Black line shows the LZ direct detection bound [27].

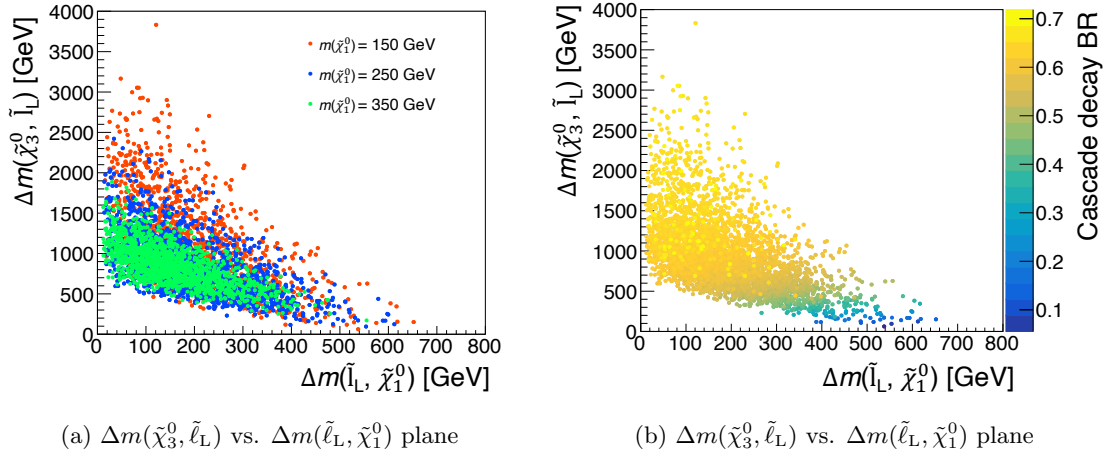


Figure 3.4: Scan result for the W-L-H sub-scenario. (a) Red, blue, and green dots represent the case with $m(\tilde{\chi}_1^0) = 150$ GeV, 250 GeV, and 350 GeV, respectively. (b) The color code represents the wino cascade decay branching ratio.

the DM relic density. The points are bounded by the LZ limit from above. It can be seen that a two order of magnitude improvement in the LZ limit is required to eliminate all points. The mass difference of each SUSY particle dictate the kinematics of collider signatures. Fig. 3.4(a) is the scan result in the $\Delta m(\tilde{\chi}_3^0, \tilde{l}_L)$ vs. $\Delta m(\tilde{l}_L, \tilde{\chi}_1^0)$ plane. Region satisfying the scan constraints becomes smaller as the LSP mass increases.

The importance of considering the cascade decay is not only because the signal signature is distinctive, but also because the branching ratio of the wino cascade decay is large enough to consider when this W-L-H sub-scenario is realized. Fig. 3.4(b) shows the wino cascade decay branching ratio on the $\Delta m(\tilde{\chi}_3^0, \tilde{l}_L)$ vs. $\Delta m(\tilde{l}_L, \tilde{\chi}_1^0)$ plane. Wino cascade branching ratio is obviously not negligible and it reaches 70 % when $\Delta m(\tilde{\chi}_3^0, \tilde{l}_L) > 500$ GeV. The cascade branching ratio decreases as the $\Delta m(\tilde{\chi}_3^0, \tilde{l}_L)$ becomes smaller due to phase space suppression.

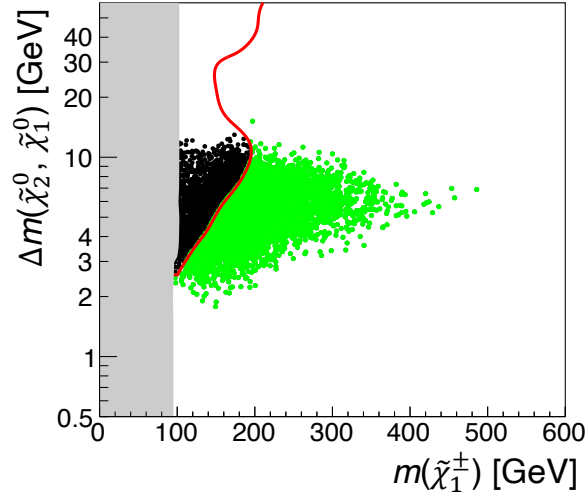


Figure 3.5: Overlay of the SUSY scan results for the W-L-H sub-scenario and the sensitivity of the current higgsino analyses. Gray area denotes the lower $\tilde{\chi}_1^\pm$ mass limit obtained by LEP (Large Electron-Positron collider) [139]. Red line represents the exclusion contour of the current ATLAS higgsino analyses [104, 105], and the existing analyses are sensitive to the region left to the red line. Black points are the mass points that are sensitive to current higgsino analyses, while green points are the mass points which are not.

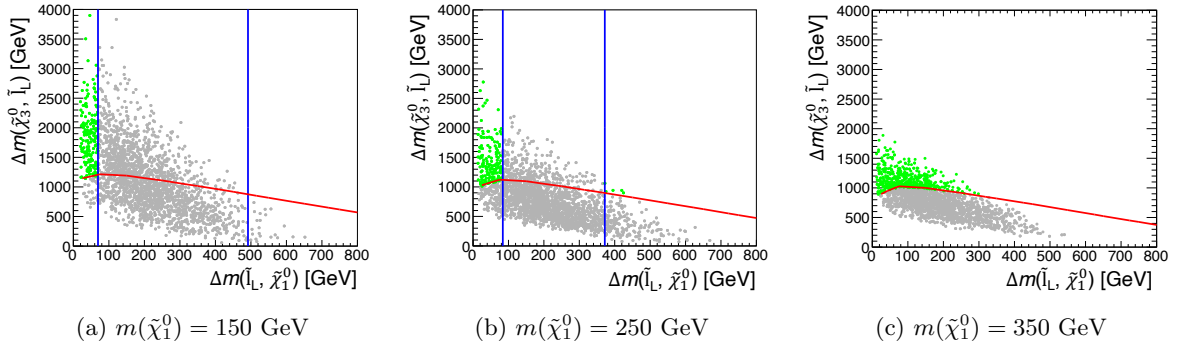


Figure 3.6: Overlay of the SUSY scan results for the W-L-H sub-scenario and the sensitivity of the current analyses. Red line represents the exclusion contour for wino pair production, and the existing analyses are sensitive to the region below the red line. Blue lines represent the exclusion contour for smuon pair production, and the existing analysis is sensitive to the region between the blue lines. Gray points are the mass points that are already sensitive to current analyses, while green points are the mass points that are not yet explored.

To account for the current ATLAS sensitivity to the W-L-H sub-scenario, we need to consider wino pair production, left-handed smuon pair production, and also higgsino pair production. Fig. 3.5 shows the current sensitivity to the higgsino pair production. Due to the non-negligible wino component in higgsino, $\Delta m(\tilde{\chi}_2^0, \tilde{\chi}_1^0)$ spreads to about 2-10 GeV (while $\Delta m(\tilde{\chi}_2^0, \tilde{\chi}_1^0)$ would be about ~ 300 MeV for pure higgsino [140]). This mass difference region is covered in LHC analyses designed to search higgsinos (soft lepton analyses), but it is difficult to cover up to 500 GeV by direct higgsino search using the current LHC data statistics due to the small higgsino

pair production cross-section and low signal acceptance. On the other hand, for wino pair production and left-handed smuon pair production sensitivity, re-interpretation of the ATLAS results is necessary. Here, we assume that wino ($\tilde{\chi}_3^0, \tilde{\chi}_2^\pm$) always decays in one-step. Note that this assumption makes the exclusion a bit stronger than it would be with the actual branching ratios. Three ATLAS multi-lepton searches [105, 111, 141] are taken into account and the sensitivity of these analyses are estimated using **SimpleAnalysis** framework [142]. Among the three analyses, the $3\ell + E_T^{\text{miss}}$ analysis [105] is found to be the most sensitive analysis to the wino pair production. Combined sensitivity of the three analyses reaches up to wino mass $m(\tilde{\chi}_3^0) = 1450$ GeV. For the left-handed smuon pair production, the $2\ell + E_T^{\text{miss}}$ analysis [111] is relevant. It was found that smuon between 220 GeV and 640 GeV is covered by the $2\ell + E_T^{\text{miss}}$ analysis when $m(\tilde{\chi}_1^0) = 150$ GeV. Fig. 3.6 is the overlay of the SUSY scan results and the sensitivity of the current ATLAS analyses. ATLAS SUSY analyses well cover the parameter space for this scenario, and only the region where $\Delta m(\tilde{\ell}_L, \tilde{\chi}_1^0)$ is small (< 70 GeV) and $\Delta m(\tilde{\chi}_3^0, \tilde{\ell}_L)$ is large (> 1200 GeV), is yet unexplored when $m(\tilde{\chi}_1^0) = 150$ GeV.

3.2.2 L-B-H sub-scenario

Fig. 3.7 is the result of the parameter scan. Only the points with $M_2 \times \mu > 0$ survive all constraints. Fig. 3.7(a) shows the results in the $m(\tilde{\ell}_L)$ vs. $m(\tilde{\chi}_1^0)$ plane and the color code represents the $\Delta a_\mu^{\text{MSSM}} - \Delta a_\mu^{\text{exp}}$. The allowed LSP mass, $m(\tilde{\chi}_1^0)$, ranges from 100 GeV to 400 GeV, where left-handed smuon mass, $m(\tilde{\ell}_L)$, is found in the range between 250 GeV and 950 GeV. Fig. 3.7(b) shows the $\sigma_{\text{SI}} \times \Omega_{\tilde{\chi}_1^0} h^2 / 0.120$ vs. $m(\tilde{\chi}_1^0)$ plane, and the color code represents the DM relic density. The points are bounded from above by the LZ limit [27], and it can be seen that an improvement of more than two orders of magnitude in the LZ limit is needed to eliminate all points. Fig. 3.8(a) is the scan result in the $\Delta m(\tilde{\ell}_L, \tilde{\chi}_3^0)$ vs. $\Delta m(\tilde{\chi}_3^0, \tilde{\chi}_1^0)$ plane. Each color corresponds to LSP masses of 200 GeV, 250 GeV, and 300 GeV. It can be seen that the region satisfying the constraints in the $\Delta m(\tilde{\ell}_L, \tilde{\chi}_3^0)$ vs. $\Delta m(\tilde{\chi}_3^0, \tilde{\chi}_1^0)$ plane becomes slightly smaller as the LSP mass increases. Since the coupling between smuon and higgsino is determined by the Yukawa coupling and is very small, the importance of considering the cascade decay in the L-B-H sub-scenario is significantly high. This can be seen from Fig. 3.8(b) which shows the left-handed smuon cascade branching ratio. This branching ratio reaches 80 % when $\Delta m(\tilde{\ell}_L, \tilde{\chi}_3^0) \gtrsim 50$ GeV

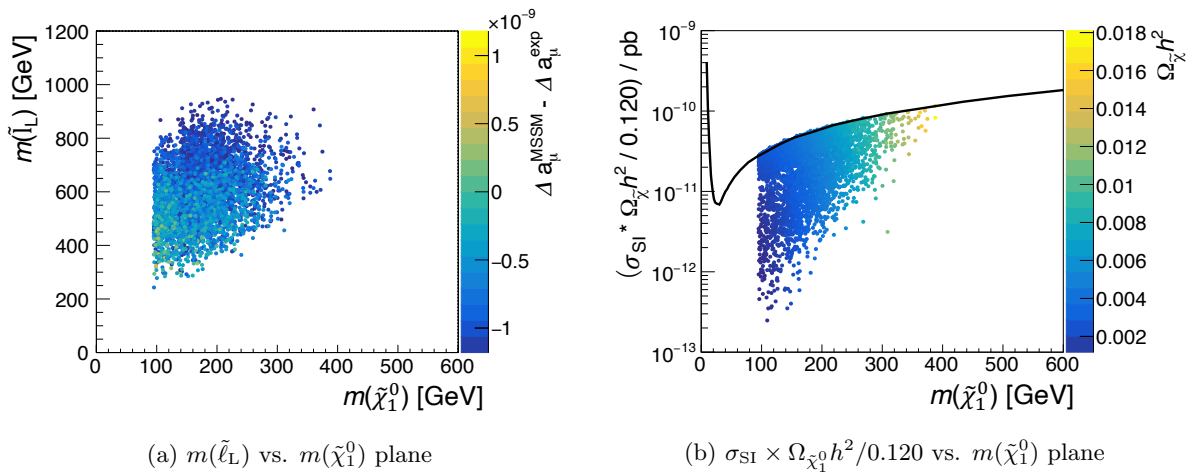


Figure 3.7: Scan result for the L-B-H sub-scenario. (a) The color code represents the $\Delta a_\mu^{\text{MSSM}} - \Delta a_\mu^{\text{exp}}$. (b) The color code represents the DM relic density. Black line shows the LZ bound [27].

and 90 % when $\Delta m(\tilde{\ell}_L, \tilde{\chi}_3^0) \gtrsim 100$ GeV and decreases rapidly as the $\Delta m(\tilde{\ell}_L, \tilde{\chi}_3^0)$ becomes smaller due to phase space suppression.

To account for the current ATLAS sensitivity to the L-B-H sub-scenario, we need to consider left-handed smuon pair production and higgsino pair production. Fig. 3.9 shows the current sensitivity to the higgsino pair production. Due to the non-negligible bino component in higgsino, $\Delta m(\tilde{\chi}_2^0, \tilde{\chi}_1^0)$ spreads to about 7-25 GeV. This region of $\Delta m(\tilde{\chi}_2^0, \tilde{\chi}_1^0)$ should be covered by the soft lepton analyses, but it is difficult to cover up to 400 GeV by direct higgsino search using the current LHC data statistics by the same reason mentioned in the W-L-H sub-scenario section. For the L-B-H sub-scenario cascade decay, several ATLAS multi-lepton analyses [105, 111, 143] were found to have sensitivity to some extent. Fig. 3.10 shows the reinterpreted sensitivity of the ATLAS analyses to the L-B-H sub-scenario which assumes the same mass for the selectron and smuon and 100% cascade branching ratio of sleptons. Sensitivities are estimated using the ATLAS official reconstructed signal samples. In Fig. 3.10, green mass points which are obtained in the SUSY parameter scan are also drawn. These mass points explain the muon $g - 2$ anomaly within 2σ , W boson mass ($m_W^{\text{exp}} = 80.379 \pm 0.012$ GeV [144]) within 2σ , and satisfy the dark matter relic density constraint ($\Omega_{\tilde{\chi}_1^0} h^2 \leq 0.120$) [26], the dark matter direct detection constraint by the latest LZ experiment [27], and the ATLAS higgsino search constraints [101, 104, 105]. It can be seen that the green points are mainly in the region where $\Delta m(\tilde{\chi}_3^0, \tilde{\chi}_1^0) > 90$ GeV. This is because the spin-independent DM scattering cross-section is heavily enhanced by the bino component in LSP [91] (Eq. 2.90), and the region not excluded by DM direct detection are with (almost) pure higgsino LSP by large $\Delta m(\tilde{\chi}_3^0, \tilde{\chi}_1^0)$. Existing analysis barely exclude the region which can explain the muon $g - 2$ anomaly and satisfy the DM direct detection constraints, which motivates a new dedicated search for the L-B-H sub-scenario. The reason why the current gaugino and slepton searches do not have sensitivities to L-B-H sub-scenario is that it tends to have a hadronic jet veto, while L-B-H sub-scenario signals can have hadronic jets from bosons even in the multi-lepton channel. On the other hand, gluino and squark searches lose sensitivities to L-B-H sub-scenario because these searches have a too strict E_T^{miss} selection (typically > 300 GeV). Low mass smuon which is the main target of the LHC search has small E_T^{miss} , and from this point of view it is important to reduce backgrounds by not relying on the

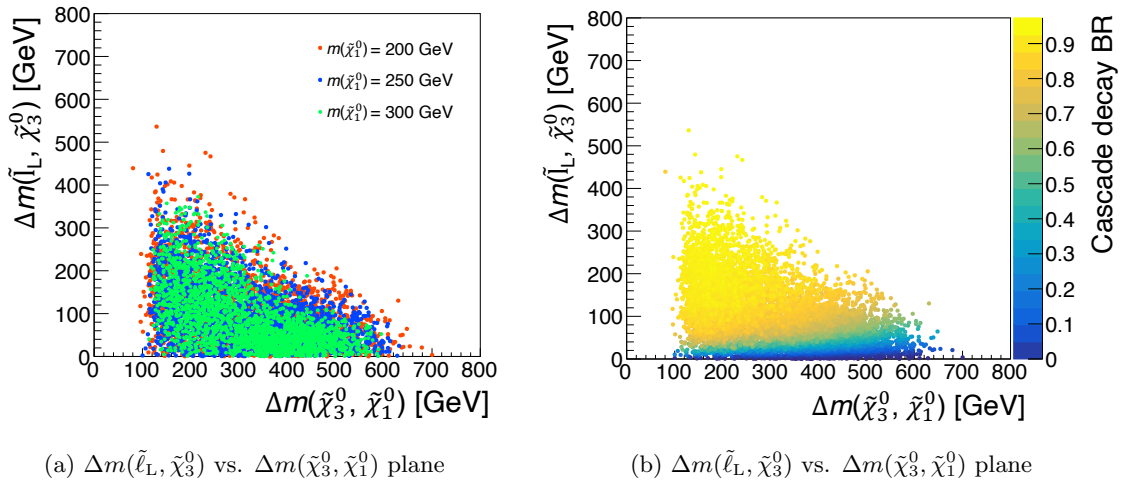


Figure 3.8: Scan result for the L-B-H sub-scenario. (a) Red, blue, and green dots represent the case with $m(\tilde{\chi}_1^0) = 200$ GeV, 250 GeV, and 300 GeV, respectively. (b) The color code represents the left-handed smuon cascade decay branching ratio.

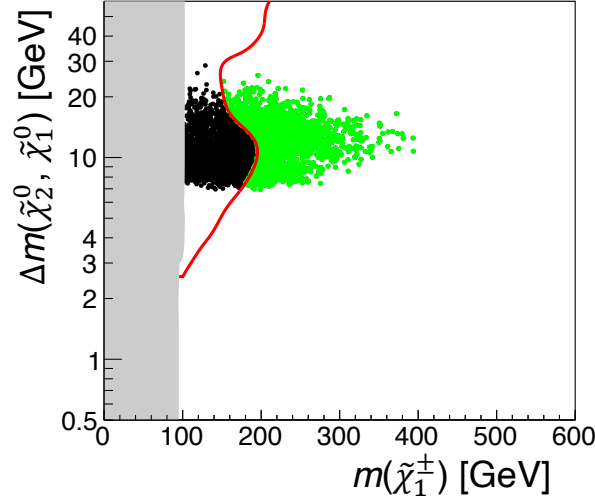


Figure 3.9: Overlay of the SUSY scan results for the L-B-H sub-scenario and the sensitivity of the current higgsino analyses. Gray area denotes the lower $\tilde{\chi}_1^\pm$ mass limit obtained by LEP [139]. Red line represents the contour of the current ATLAS higgsino analyses [104, 105], and the existing analyses are sensitive to the region left to the red line. Black points are the mass points that are sensitive to current higgsino analyses, while green points are the mass points which are not.

strict E_T^{miss} selection.

3.3 Target SUSY Scenario

This thesis focuses on the MSSM scenarios where the light-flavored left-handed slepton ($\tilde{\ell}_L$; \tilde{e}_L or $\tilde{\mu}_L$) together with a degenerated sneutrino ($\tilde{\nu}$) are the heaviest states, the bino-dominated state ($\tilde{\chi}_3^0$) is in the intermediate mass range, and the higgsino consists the LSP ($\tilde{\chi}_1^0/\tilde{\chi}_1^\pm/\tilde{\chi}_2^0$). We call this model as the slepton-bino-higgsino model. While the slepton-bino-higgsino model involving smuons drive more motivation in light of muon $g - 2$ anomaly, slepton-bino-higgsino model with selectrons are also considered in this analysis. Though the SM prediction of electron anomalous magnetic moment [145–148] has not yet been established, the measured value [149, 150] indicate a deviation from the prediction, providing some motivation for light selectrons. Cascade decay of the left-handed sleptons is targeted, of which feynman diagram is shown in Fig. 3.11. A benchmark model in which model parameters other than masses are fixed for convenience is considered in this thesis. This model, also referred to as the “simplified model” [151], serves as a benchmark model, allowing one to establish the criteria for selecting events in this analysis and for comparing the search sensitivity with the other previous searches. Although certain assumptions, such as the branching ratio, are necessary for constructing the model, the resultant simplified model is considered realistic enough in this case. This section outlines the configuration for building the simplified model in this thesis.

Production mode This thesis considers the direct production of sleptons and sneutrinos mediated by the off-shell W and Z bosons. Only $\tilde{\ell}_L$, $\tilde{\nu}$, $\tilde{\chi}_3^0$, and $\tilde{\chi}_1^0/\tilde{\chi}_1^\pm/\tilde{\chi}_2^0$ are assumed to be

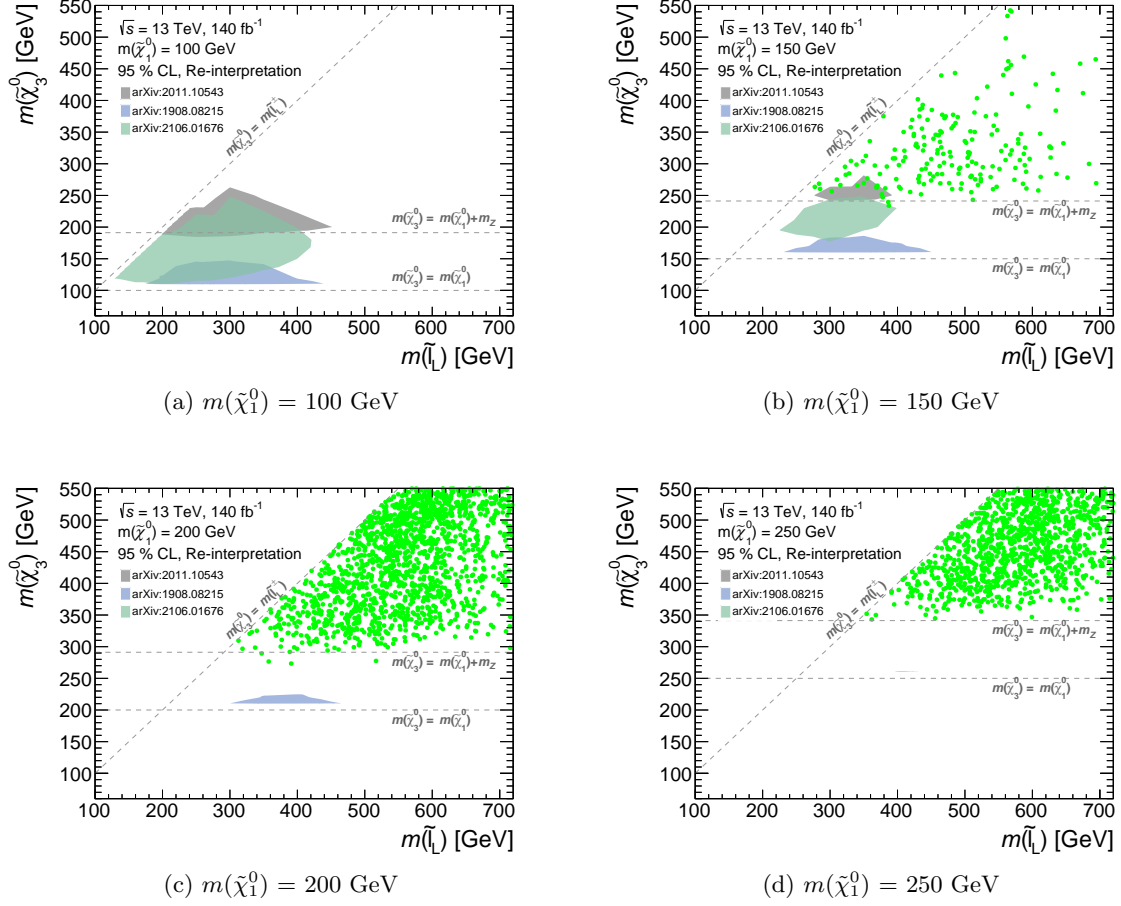


Figure 3.10: Reinterpreted sensitivity of the ATLAS analyses to the L-B-H sub-scenario which assumes the same mass for the selectron and smuon. The observed limits obtained by the previous searches in ATLAS are also shown in the shaded areas [105, 111, 143]. Green mass points explain the muon $g - 2$ [36] anomaly within 2σ , W boson mass [144] within 2σ , and satisfy the dark matter relic density constraint [26], the dark matter direct detection constraint by the LZ experiment [27] and the ATLAS higgsino search constraints [101, 104, 105].

light enough to be produced in LHC and the focus is on the following production modes:

$$pp \rightarrow \tilde{\ell}_L^+ \tilde{\ell}_L^-, \quad \tilde{\ell}_L^\pm \tilde{\nu}, \quad \tilde{\nu} \tilde{\nu}. \quad (3.4)$$

The slepton and sneutrino states are assumed to be degenerate:

$$m(\tilde{\ell}_L^\pm) = m(\tilde{\nu}). \quad (3.5)$$

Since $\tilde{\nu} \tilde{\nu}$ production results in the di-boson + E_T^{miss} signature which is already widely targeted, the main target in this thesis is the $\tilde{\ell}_L^+ \tilde{\ell}_L^-$ and $\tilde{\ell}_L^\pm \tilde{\nu}$ production.

Decay mode The cascade decay branching ratio is assumed to be 100%.³ S sleptons (sneutrinos) decay into leptons (neutrinos) and $\tilde{\chi}_3^0$:

$$\tilde{\ell}_L^\pm \rightarrow \ell^\pm \tilde{\chi}_3^0, \quad \tilde{\nu} \rightarrow \nu \tilde{\chi}_3^0. \quad (3.6)$$

³As seen from Fig. 3.8(b), this assumption results in stronger exclusions than actual branching ratios, especially in the small $\Delta m(\tilde{\ell}_L, \tilde{\chi}_3^0)$ region.

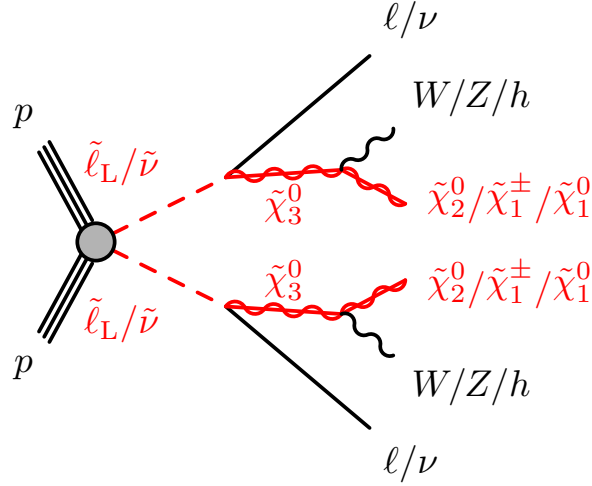


Figure 3.11: Feynman diagram of the targeted signal. The decays of $\tilde{\chi}_2^0$ and $\tilde{\chi}_1^\pm$ are ignored as they only result in low-momentum particles that are almost never reconstructed.

Table 3.3: $\tilde{\chi}_3^0$ branching ratio for the signal.

Process	$\Delta m(\tilde{\chi}_3^0, \tilde{\chi}_1^0) < m_h$	$\Delta m(\tilde{\chi}_3^0, \tilde{\chi}_1^0) \geq m_h$
$\tilde{\chi}_3^0 \rightarrow W^\pm \tilde{\chi}_1^\mp$	50%	50%
$\tilde{\chi}_3^0 \rightarrow Z \tilde{\chi}_2^0$	25%	12.5%
$\tilde{\chi}_3^0 \rightarrow Z \tilde{\chi}_1^0$	25%	12.5%
$\tilde{\chi}_3^0 \rightarrow h \tilde{\chi}_2^0$	—	12.5%
$\tilde{\chi}_3^0 \rightarrow h \tilde{\chi}_1^0$	—	12.5%

The $\tilde{\chi}_3^0$ have several decay modes via weak bosons and Higgs:

$$\tilde{\chi}_3^0 \rightarrow W^\pm \tilde{\chi}_1^\mp, \quad \tilde{\chi}_3^0 \rightarrow Z \tilde{\chi}_2^0, \quad \tilde{\chi}_3^0 \rightarrow Z \tilde{\chi}_1^0, \quad \tilde{\chi}_3^0 \rightarrow h \tilde{\chi}_2^0, \quad \tilde{\chi}_3^0 \rightarrow h \tilde{\chi}_1^0, \quad (3.7)$$

where decay through Higgs is only allowed when $\Delta m(\tilde{\chi}_3^0, \tilde{\chi}_1^0) \geq m_h$. The $\tilde{\chi}_3^0$ branching ratio depends on the mass splitting of $\tilde{\chi}_3^0$ and $\tilde{\chi}_1^0$. Table 3.3 shows the assumed branching ratios for $\tilde{\chi}_3^0$. The branching ratios for $\Delta m(\tilde{\chi}_3^0, \tilde{\chi}_1^0) \geq m_h$ are set to its typical value [152], while the branching ratios for $\Delta m(\tilde{\chi}_3^0, \tilde{\chi}_1^0) < m_h$ are assumed for convenience, since they vary considerably depending on the phase space. Higgsinos are assumed to be mass degenerated,⁴

$$m(\tilde{\chi}_2^0) = m(\tilde{\chi}_1^\pm) = m(\tilde{\chi}_1^0) + 0.5 \text{ GeV}. \quad (3.8)$$

While the muon $g - 2$ anomaly and the dark matter direct detection motivated models have a higgsino mass splitting of $\Delta m(\tilde{\chi}_2^0, \tilde{\chi}_1^0) \sim 10 \text{ GeV}$ (Fig. 3.9), assuming the higgsinos to be degenerate will make the SUSY search generally more difficult as the number of decay objects with enough momentum to be reconstructed in the detector decreases. SUSY particles that are not involved in the decay chains are set decoupled.

This thesis focuses on the final state with exactly three leptons. Since the final state with three leptons require at least one boson to decay leptonically, the signal is reduced because of the boson branching ratio, but the backgrounds can be efficiently reduced by requiring multiple-leptons.

⁴A mass splitting of 0.5 GeV is used to avoid potential technical issues when setting it exactly to zero. This choice is arbitrary and has no impact on the analysis.

Chapter 4

Experimental Apparatus: The ATLAS Detector at the LHC

4.1 The Large Hadron Collider

The Large Hadron Collider (LHC) [153] is a 27 km long circular proton accelerator embedded underground of the Geneva area. It is designed to collide protons at a center-of-mass energy of $\sqrt{s} = 14$ TeV, at four detector sites (ATLAS [154], CMS [155], ALICE [156], and LHCb [157]) built on the accelerator ring. ATLAS and CMS are general purpose detectors designed to study a vast range of physics programs, while LHCb and ALICE are specialized in studying b -hadrons and heavy-ion collisions respectively.

Fig. 4.1 provides an overall view of the LHC accelerator system. The operation started in 2010, offering proton-proton (pp) collisions at a center-of-mass energies of 7 TeV and 8 TeV with 4.7 fb^{-1} and 20.3 fb^{-1} of integrated luminosity until 2012 (Run 1). The center-of-mass energies has been almost doubled to 13 TeV in the runs starting from 2015 (Run 2). In the initial stage of the acceleration system, protons extracted from hydrogen gas are accelerated to 50 MeV in the linear accelerator 2 (LINAC 2). The protons progress through further acceleration stages, reaching energies of 1.4 GeV in the Proton Synchrotron Booster (PSB), 26 GeV in the Proton Synchrotron (PS), and finally, 450 GeV in the Super Proton Synchrotron (SPS). Protons entering the LHC are divided into two beam pipes and accelerated to 6.5 TeV in opposite directions.

The instantaneous luminosity is defined as [159]:

$$L = \frac{f_{\text{rev}} n_b N_b^2 \gamma}{4\pi\epsilon\beta^*} F, \quad (4.1)$$

where f_{rev} is the revolution frequency, n_b is the number of bunches per beam colliding at the interaction point (IP), N_b is the bunch population, γ is the relativistic gamma factor, ϵ is the transverse normalized emittance, β^* is the value of the β function at the IP, and F is the geometric luminosity reduction factor. The typical values of these parameters for each year are shown in Table 4.1.

4.2 The ATLAS detector

4.2.1 Overview

ATLAS (A Toroidal LHC Apparatus) is a general purpose detector, aiming to a wide range of physics programs from precision measurements to the energy frontier experiments, through a dedicated measurement of particles produced in the pp collisions. The detector extends over

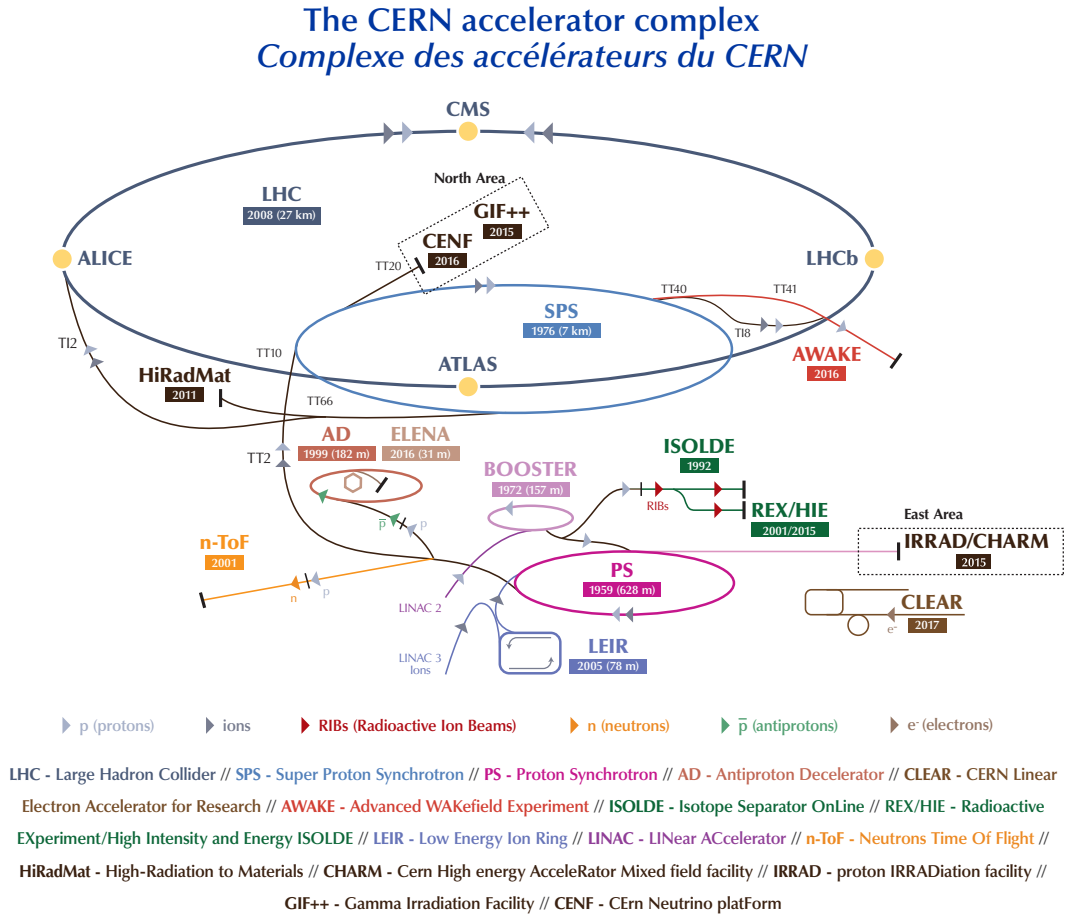


Figure 4.1: The LHC and associated booster accelerator system [158].

Table 4.1: Selected LHC parameters of pp collisions at $\sqrt{s} = 13$ TeV in 2015-2018 [160]. The values are representative of the best accelerator performance during normal physics operation. In 2017 run, two different conditions were applied. “8b4e” denotes a pattern of eight bunches separated by 25 ns followed by a four bunch-slot gap.

Parameter	2015	2016	2017	2018
Frequency (f_{rev} [Hz])	11253	11253	11253	11253
Bunch spacing [ns]	25	25	25/8b4e	25
Maximum number of colliding bunch pairs (n_b)	2232	2208	2544/1909	2554
Typical proton bunch population ($N_b/10^{11}$ protons)	1.1	1.1	1.1/1.2	1.1
β^* [m]	0.8	0.4	0.3	0.3-0.25
Geometric luminosity reduction factor (F)	0.94	0.94	0.94	0.94

44 m in width and 25 m in height weighing 7000 tons in total, covering the IP by a cylindrical barrel and two end-caps, achieving a nearly full solid angle coverage. The cut-away image is shown in Fig. 4.2.

The purpose of the detector is to identify the particle species and to determine the particle’s energy and momentum with two complementary concepts of measurement, the fast measurement to provide triggers and the precision measurement for physics analyses. To satisfy these

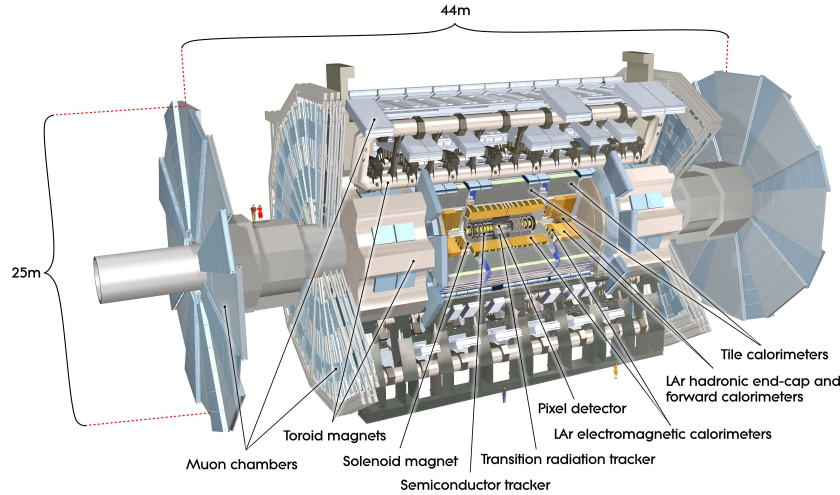


Figure 4.2: Cut-away view of the ATLAS detector. The dimensions of the detector are 25 m in height and 44 m in length. The overall weight of the detector is approximately 7000 tons [154].

functionalities at the same time, following sub-detectors are arranged in a designed order from the inner to the outer with respect to the IP.

- **Inner detector** is placed to identify and measure electrically charged particles, as well as to reconstruct primary vertices. Charged particles interact with materials by ionizing the atoms inside. The path of flight can be reconstructed as a track, by recording the position of ionization. In ATLAS, a complex of discrete layers of silicon sensors and a continuously volumed gas chambers are placed in the innermost part. The momentum can be measured by applying a magnetic field, and quantifying the curvature of the trajectory.
- **Calorimeter** is installed to measure the energy of electrons, photons, and hadrons. Electrons and photons traveling inside materials lose their energy through electromagnetic showering; photons create e^+e^- pairs and electrons emit bremsstrahlung photons; the daughter electrons and photons are multiplied by the recursive splitting; ending up in a particle shower. Most of the energy is absorbed after traversing about 20 radiation lengths (X_0) of material. Hadrons (mostly pions) also cause similar cascade reactions. The shower branch evolves by interacting with nuclei in the material via strong interaction, meanwhile produced π_0 's promptly decay into two photons which shower electromagnetically. This results in a shower with a combination of a long hadronic shower and small local EM clusters in it.
- **Muon Spectrometer** is placed to measure the muons penetrating the detector. Among all the SM particles that interact with material, only muons penetrate the calorimeter. This is due to muons have a sufficiently long lifetime and a mass realizing the minimum electromagnetic interaction with material (Minimum ionizing particle; MIP). The muon spectrometer located the outermost serves for identifying such muons as well as measuring the tracks together with the information from the inner tracker.

In the following sections, each of the sub-detector system is overviewed, comprehensively based on references [154] and [161].

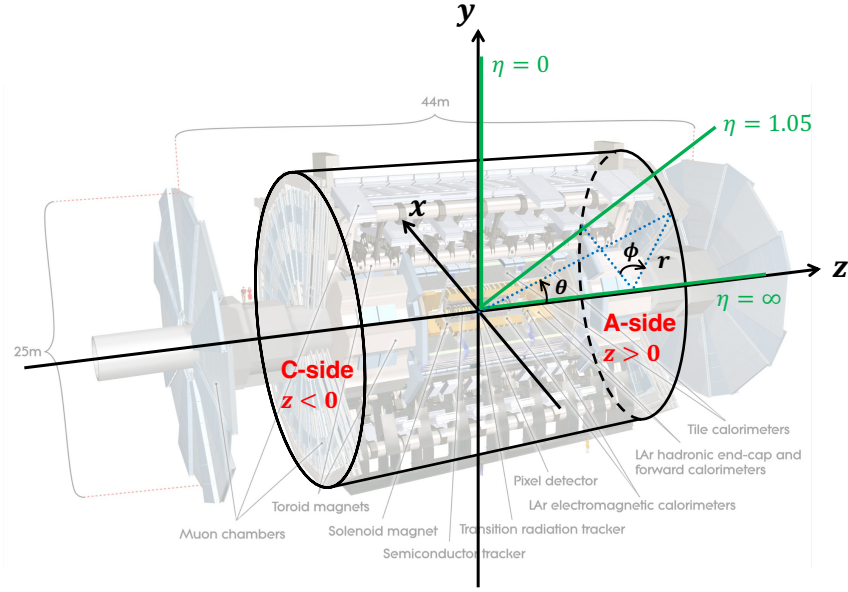


Figure 4.3: The coordinate system of the ATLAS detector, with the x -axis pointing toward the center of the LHC and the y -axis pointing toward the sky. $z > 0$ is called A-side and $z < 0$ is called C-side. Polar angle θ and azimuthal angle ϕ are defined by the cylindrical representation (θ, ϕ, z) . The distance from the z -axis is represented by r . The pseudorapidity η is used to describe the area covered by each detector.

4.2.2 Coordinate System

For referencing the position in the detector as well as the orientation of particles, a right-handed Cartesian coordinate system is defined where the IP is the origin; the x -axis pointing to the center of the LHC ring; the y -axis and z -axis are accordingly the direction of sky and the beam direction, respectively. Polar angle θ and azimuthal angle ϕ are defined by the cylindrical representation (θ, ϕ, z) : θ ranges from 0 to π with respect to the z -axis, and ϕ runs from $-\pi$ to π from the x -axis. The two end-caps in the ATLAS detector are referred to as “A-side” and “C-side”, corresponding to the position of positive and negative coordinate in the z -axis. The distance from the z -axis is represented by r .

Since the pp collision vertices are approximately at the IP, the angles of the generated particles or their systems are defined in the same manner. The rapidity y is defined as

$$y := \operatorname{artanh} \beta_z = \frac{1}{2} \log \frac{E + p_z}{E - p_z}, \quad (4.2)$$

where the velocity is $\boldsymbol{\beta} = (\beta_x, \beta_y, \beta_z)$, E is the energy, and the momentum is $\mathbf{p} = (p_x, p_y, p_z)$. The pseudorapidity is then defined as the massless limit of the rapidity,

$$\eta := \frac{1}{2} \log \frac{E + E \cos \theta}{E - E \cos \theta} = -\log \left(\tan \frac{\theta}{2} \right). \quad (4.3)$$

In addition, the transverse energy $E_T := E \sin \theta$ and transverse momentum $p_T = \sqrt{p_x^2 + p_y^2}$ are often used in the analysis.

Angular distance between two particles are commonly expressed by ΔR , defined as:

$$\Delta R := \sqrt{(\Delta \eta)^2 + (\Delta \phi)^2}. \quad (4.4)$$

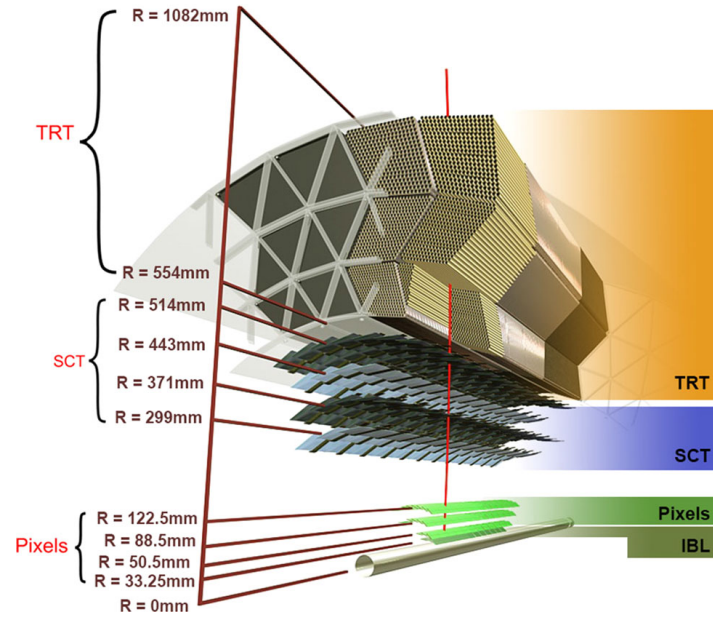


Figure 4.4: Cross-section of the ATLAS inner detectors [162].

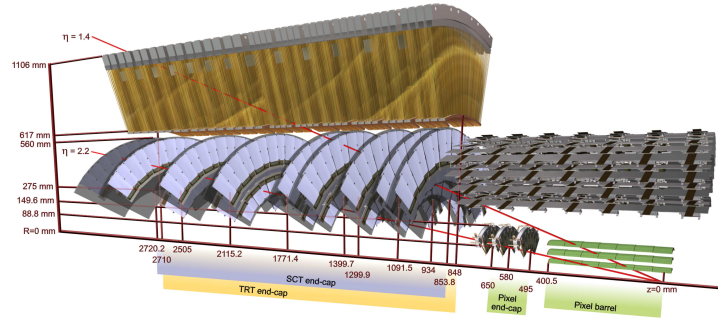


Figure 4.5: Schematic of the ID in the end-cap region. The two red lines show the trajectory of charged particles with p_T of 10 GeV traversing the ID. The charged particle passing through $\eta = 1.4$ penetrates the beam pipe, three layers of pixel detectors, four layers of SCTs, and about 40 tubes of the TRT detector. The IBL is omitted from this picture. The figure is taken from [154].

4.2.3 Inner Detectors

The inner detector (ID) is placed in the innermost part of the ATLAS detector, designed to measure the tracks of charged particles, as well as precisely determining the position of vertices of the hardest scattering in interest. It consists of a silicon tracker (the Pixel detector and the Semiconductor Tracker) and the Transition Radiation Tracker for continuous tracking. The detector arrangement is illustrated in Fig. 4.4 and Fig 4.5. The outer radius is surrounded by the central solenoid, providing a magnetic field of 2 T along the z -axis, to bend the tracks traveling inside the ID volume.

Insertable B-Layer and Pixel detector The innermost layer of the ID, called the Insertable B-layer (IBL), was installed during the long shutdown period (2013-2015) before Run 2. The pixel size of IBL is $\Delta\phi \times \Delta z = 50 \mu\text{m} \times 250 \mu\text{m}$. The IBL covers the entire ϕ region by tilting

the modules by about 26 degrees in the ϕ direction relative to beam axis. The IBL provides hit information near the beam pipe $r = 33.25$ mm, which improves the tracking and vertexing performance. Three pixel layers of the Pixel detector are installed in the barrel and end-cap region. The pixel size of the Pixel detector is $\Delta\phi \times \Delta z = 50 \mu\text{m} \times 600 \mu\text{m}$.

Semiconductor Tracker The Semiconductor Tracker (SCT) module consists of two strips with a pitch of $80 \mu\text{m}$, mounted back to back with a 40 mrad stereo angle. The two-dimensional position information of the particle can be measured from the intersection of two readout strips. The barrel region has four layers of SCT modules, and the end-cap region has nine layers of SCT modules.

Transition Radiation Tracker The Transition Radiation Tracker (TRT) consists of 73 (160) layers of drift tubes with a diameter of 4 mm in the barrel (end-cap) region, aligned along the beam axis. The drift tubes are filled with Xe (or Ar)-rich gas and operated as drift chambers. The space between the tubes is filled with polypropylene fibers, and transition radiation, which occurs when a charged particle traverses the tubes, is used for particle identification, particularly for the e/π separation. The signal produced by transition radiation generally exhibits greater amplitude than the standard gas ionization. Consequently, two distinct thresholds are established in the TRT: a lower threshold to capture the ionization signal generated by a particle's passage, and a higher threshold that captures the signal associated with the transition radiation.

4.2.4 Calorimeter

The ATLAS Calorimeter located outside the ID is composed of the electromagnetic calorimeter (EM calorimeter), the hadronic calorimeter (HC), and the forward calorimeter. The whole view is given by Fig. 4.6. Electromagnetic calorimeters measure the energy of electrons and photons using electromagnetic showers, while hadronic calorimeters measure the energy of hadrons using hadronic showers.

Electromagnetic calorimeter The electromagnetic calorimeter is a sampling calorimeter with a lead absorber, filling its gap with liquid argon (LAr). Charged particles entering the lead

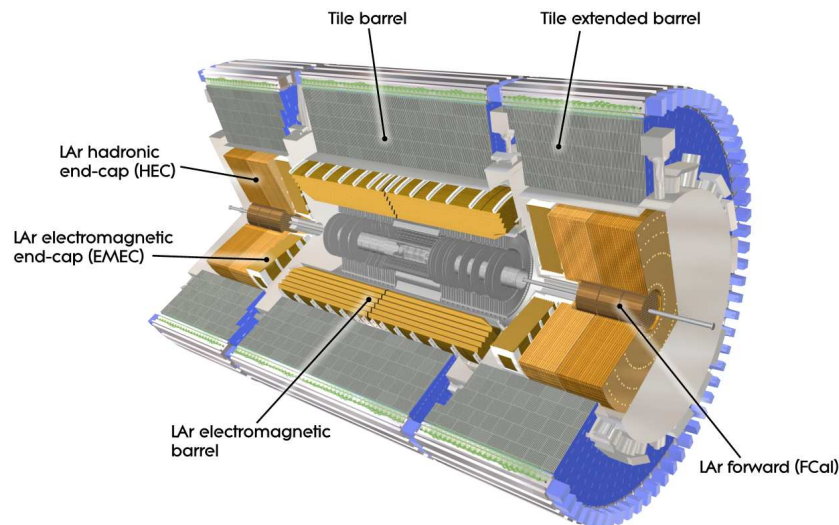


Figure 4.6: Cut-away view of the ATLAS calorimeter [154].

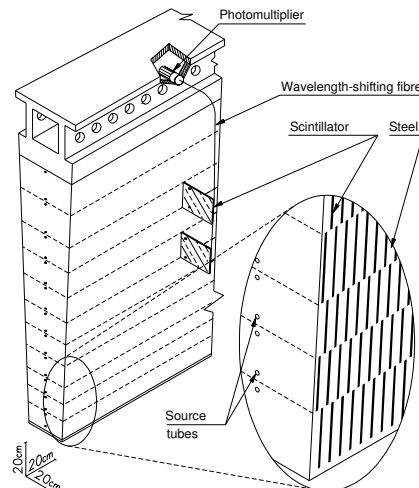


Figure 4.7: Illustration of a Tile HC module [154].

absorber lose their energy through electromagnetic showering, and ionized free electrons in LAr drift to the electrodes by the electric field. The long drift time (600 ns) leads to a significant contribution from other bunch crossings. The readout signal is amplified by a pre-amplifier, and shaped into a 13 ns width signal pulse by a bi-polar shaper to manage the 25 ns width bunch crossings.

Hadronic calorimeter The ATLAS hadronic calorimeter consists of the barrel Tile HC ($|\eta| < 1.7$) and end-cap LAr HC ($1.5 < |\eta| < 3.2$). Barrel Tile HC is segmented into three sections, the central barrel section ($|\eta| < 1.0$) and the two extended barrel sections ($1.0 < |\eta| < 1.7$), using different channel dimensions. Fig. 4.7 schematizes one module in the Tile HC. Generated scintillation photons are read out by the photo-multiplier tubes equipped at the ends of the module via wavelength shifting fibers. The end-cap HC is the sampling calorimeter with layers of liquid-argon sensor and copper absorber.

Forward calorimeter A set of LAr calorimeter layers are arranged in a very forward region close to the beam axis covering ($3.1 < |\eta| < 4.9$), designed to capture the full content of highly boosted jets or particles. Forward calorimeter is made by three sampling layers in which both functions of EM calorimeter and hadronic calorimeter are integrated. The overlap region with respect to the end-cap HC is deliberated to realize smooth transition.

4.2.5 Muon Spectrometer

Muon spectrometers (MS) are located outermost in the ATLAS, consisting of four sub-detectors; Monitored Drift Tubes (MDT); Cathode Strip Chamber (CSC); Resistive Plate Chamber (RPC); and the Thin Gap Chamber (TGC). The former two are dedicated to precision measurement of muon tracks and the latter two are to triggering. The whole view is given in Fig. 4.8.

The magnetic field for tracking is sourced by the three pieces of toroidal superconducting magnets: two end-cap toroids and a barrel toroid embedded inside the MS. The internal volume of toroidal coils are vacant (“air-core”), in order to reduce the material with which muons experience the multiple scattering. The global schematic of the magnet system is given in Fig. 4.9(a), while the integrated magnetic filed profile at the position of MDT is shown in Fig. 4.9(b).

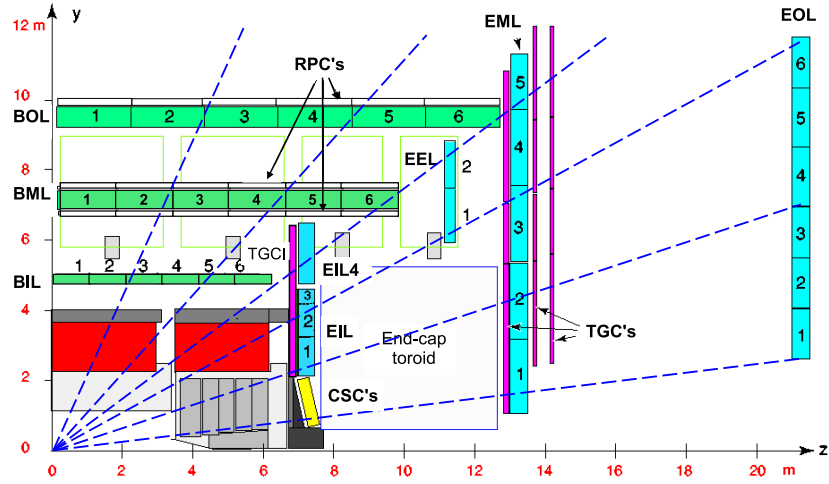
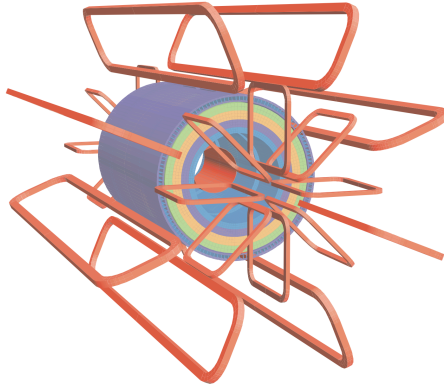
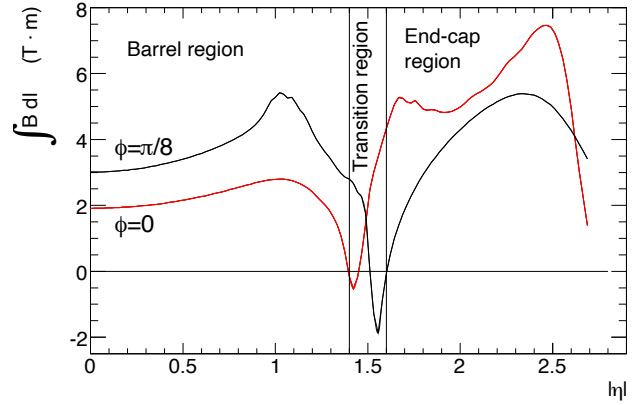


Figure 4.8: Cross-section of the ATLAS Muon spectrometer [154]. The cyan chambers represent the MDT detector. The yellow chamber represents the CSC detector. The green chambers represent the RPC detector and the magenta chambers represent the TGC detector. Infinite-momentum muons would propagate along straight trajectories which examples are illustrated by the blue dashed lines.



(a)



(b)

Figure 4.9: (a) Schematic of the ATLAS magnet system with one central solenoid and three toroidals (one in barrel and two in end-cap). (b) Simulated magnetic field integral provided by a single troid octant [154].

Monitored Drift Tubes The MDT consists of six or eight layers of drift tubes of 30 mm diameter filled with Ar/CO₂ mixture gas. Electrons produced by ionization are multiplied by the electron avalanche effect and collected by the anode wire placed at the center of the drift tube. The maximum drift time from the wall to the wire is about 700 ns. The MDT measures the position of tracks based on the drift time of the electrons.

Cathode Strip Chamber The CSC is a Multi Wire Proportional Chamber (MWPC) placed in the $|\eta| > 2.0$ region, where hit rates are expected to be too high for the MDTs to be sufficiently tolerant. The detector is filled with Ar/CO₂ mixture gas. Electron drift times of less than 40 ns

results in a timing resolution of about 7 ns per plane. Two cathode strips are placed orthogonally, allowing for the measurement of the r and ϕ coordinates.

Resistive Plate Chamber The RPC consists of two high resistive plates with a 2 mm insulator inserted. The gas volume between the two plates is filled with $\text{C}_2\text{H}_2\text{F}_4$ based gas mixture. The high voltage application of 9.8 kV and thin gap widths produce a sharp signal rise. Strips are placed orthogonally to calculate positions in the η and ϕ coordinates.

Thin Gap Chamber The TGC is a MWPC filled with $\text{CO}_2/\text{n-C}_5\text{H}_{12}$ mixture gas, which determines the r and ϕ position from a two-dimensional readout by wires and strips. The wires and strips are placed with a pitch of 1.4 mm, shorter than the pitch between the wires, resulting in a high detector time response and rate tolerance.

4.2.6 Trigger and Data Acquisition System

In the ATLAS detector, beam collisions occur at 40 MHz, resulting in a data acquisition rate up to $\mathcal{O}(1)$ PB/s in case of acquiring every event. On the other hand, the cross-section of events that produce weak bosons, Higgs bosons, or top quarks of our interest is 6-8 orders of magnitude smaller compared to the total inelastic scattering cross-section that occurs in pp collisions. Therefore, in the ATLAS experiment, the detector signals are used to quickly determine the events whether to be recorded which is called the “trigger system”, and the system that temporarily holds the data and records them when an event is triggered is called the “data acquisition system”. Fig. 4.10 illustrates the trigger and data acquisition system in Run 2.

Level-1 Trigger (L1 Trigger) The L1 Trigger consists of calorimeter-based Level-1 Calo (L1Calo), muon-spectrometer-based Level-1 Muon (L1Muon), and Central Trigger, which combines trigger decision from L1Calo and L1Muon. The trigger rate is reduced to ~ 100 kHz by the L1 Trigger. The L1 Trigger sends the η and ϕ information of issued triggers, called Region of Interest (RoI), to the High-Level Trigger for more precise trigger decisions.

High-Level Trigger (HLT) The HLT uses the detector information around the RoI to reconstruct objects with an algorithm similar to an offline algorithm to perform more precise trigger decisions. The trigger rate is reduced to ~ 1 kHz by the HLT.

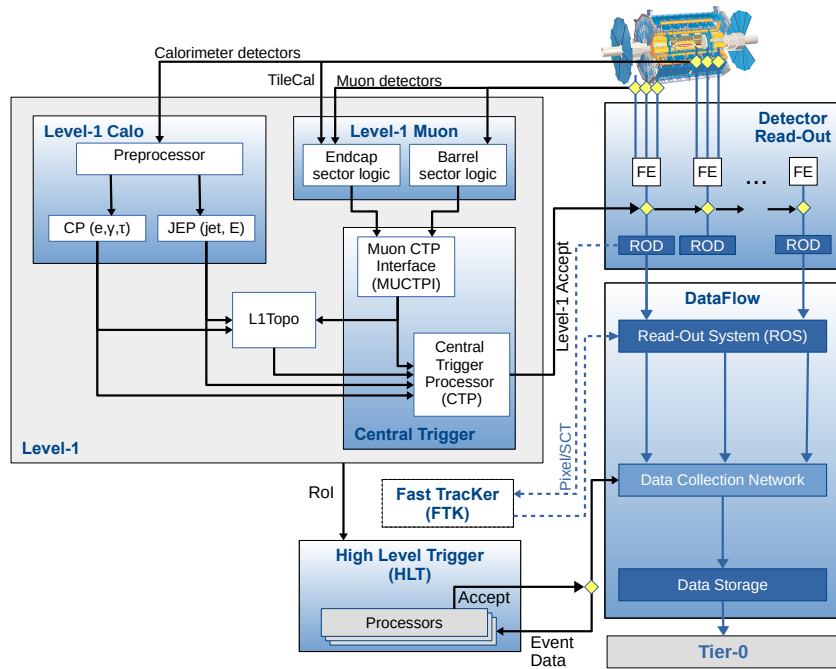


Figure 4.10: The logic of ATLAS trigger system [163]. Trigger detectors have separated readout line for trigger, sending input information for trigger decision to Central Trigger Processors (CTP). The CTP reconstructs L1 objects and issue a global accept signal relieving the buffered data, once the trigger criteria are satisfied. The η , ϕ position of identified trigger object is sent to downstream HLT, in which offline-like software-based triggers run to further filter events.

Chapter 5

Dataset and Monte Carlo Samples

This thesis uses data collected by the ATLAS detector in pp collisions at the LHC. In addition, Monte Carlo (MC) simulations to describe the signal and background processes are used. Details of the data and MC simulations are discussed in this chapter.

5.1 Actual collision data used for this work

During Run 2 (2015-2018), LHC has delivered $\sqrt{s} = 13$ TeV pp collision data with integrated luminosity of 156 fb^{-1} , of which 147 fb^{-1} were recorded by the ATLAS detector. As physics analyses require that the recorded data pass standard data quality requirements in ATLAS [164], the actual data used in the physical analysis corresponds to $140.1 \pm 1.2 \text{ fb}^{-1}$ with uncertainty of 0.83% [165], obtained primarily using the luminosity measurements of the LUCID-2 (LUMinosity CHerenkov Integrating DETector) [160]. The integrated luminosity of the data for physics analyses during 2015, 2016, 2017, and 2018 is 3.24, 33.40, 44.63, and 58.79 fb^{-1} , respectively.

Important parameter related to the instantaneous luminosity is the average number of inelastic interactions per bunch crossing, known as the “pile-up”. The pile-up degrades the performance of the reconstructed physics objects and makes the identification of vertices and the reconstruction of tracks more difficult. The evolution of the integrated luminosity, delivered by

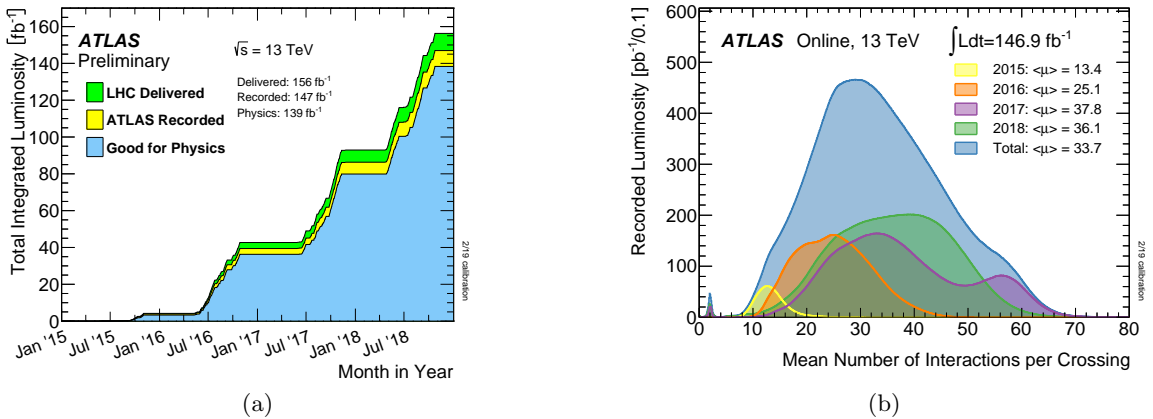


Figure 5.1: (a) The integrated luminosity which LHC delivered (green), ATLAS recorded (yellow), and is good for physics analysis in ATLAS (light blue) during Run 2 period [164]. (b) The luminosity recorded by ATLAS as a function of mean number of proton interactions per bunch crossing in Run 2 period [164].

the LHC, recorded by ATLAS, good for physics analysis, and the luminosity as a function of pile-up are shown in Fig. 5.1.

5.2 Monte Carlo Samples

At the LHC, multiple pp collisions occur at every bunch crossing. Also, depending on the time resolution of the detector, signals from other bunch crossings may affect the measurement. To accurately estimate the number of background and signal yields, it is necessary to simulate all the physical processes that contribute to the analysis. Section 5.2.1 briefly overviews the simulated physics processes in pp collisions. Sections 5.2.2 and 5.2.3 provide details of the configurations to generate simulation samples for the SM background and signal processes, respectively. In addition to estimating the SM background and signal yields, samples generated by MC simulations are used to assess the impact of systematic uncertainties. The systematic uncertainties considered in this thesis will be further discussed in Chapter 9.

5.2.1 General Description

Event Generation The main physics processes from pp collisions can be estimated by factorizing the calculation into two components: the perturbatively calculable part, corresponding to the Matrix Element, and the perturbatively non-calculable part, corresponding to the parton shower and fragmentation. Parton shower and fragmentation are predicted by phenomenological models with parameters turned to match observations. The differential cross-section of an observable \mathcal{O} can be described as Ref. [166]

$$\frac{d\sigma}{d\mathcal{O}} = \sum_{a,b} \int_0^1 dx_a dx_b \sum_F \int d\Phi_F f_a^{h_1}(x_a, \mu_F) f_b^{h_2}(x_b, \mu_F) \frac{d\hat{\sigma}_{ab \rightarrow F}}{d\hat{\mathcal{O}}} D_F(\hat{\mathcal{O}} \rightarrow \mathcal{O}, \mu_F), \quad (5.1)$$

where indices a and b represents the partonic constituents in the colliding hadrons h_1, h_2 , and $d\Phi_F$ is the standard phase space differential in the final state. The energy scale at which the perturbatively calculable and non-calculable parts are separated is called the “factorization scale” and is denoted as μ_F . The Parton Density Function (PDF) $f_j^h(x_j, \mu_F)$ describes the momentum fraction that a parton of type j carries within the hadron h at the factorization scale. The partonic scattering cross-section $d\hat{\sigma}_{ab \rightarrow F}$ can be calculated as

$$d\hat{\sigma}_{ab \rightarrow F} = \frac{1}{2\hat{s}_{ab}} |\mathcal{M}_{ab \rightarrow F}(\Phi_F; \mu_F, \mu_R)|^2, \quad (5.2)$$

where $1/2\hat{s}_{ab}$ represents the parton flux factor. The strong coupling constant in the Matrix Element is subject to quantum corrections, such as corrections to the quark and gluon self-energies, with values varying with the energy scale, referred to as the renormalization scale. The \mathcal{M} is the Matrix Element, summed over all possible intermediate states and phase space of $ab \rightarrow F$ at the factorization scale μ_F and the renormalization scale μ_R . The following soft parton emissions of particles described in the Matrix Element are complemented by the parton shower approximation. Since the probability of one parton splitting into two can be calculated using the Dokshitzer-Gribov-Lipatov-Altarelli-Parisi (DGLAP) evolution equations [167–169], the parton shower approximation predicts the partonic final state by repeating the parton splitting process until the momentum of the parton reaches $\mathcal{O}(1)$ GeV.

The final part of the Eq. 5.1 is the fragmentation function D_F , which represents the evolution from the partonic final state to the color-neutral final state, and $\hat{\mathcal{O}}$ represents an observable at the partonic final state. The fragmentation process is modeled by the Lund string model [170].

Pile-up Simulation Pile-up arises from relatively soft pp inelastic scattering in the same bunch crossing or from surrounding bunch crossings, which is complex and requires intensive CPU consumption for simulation. The pile-up events produced with PYTHIA 8.186, A3 tune [171], and MSTW2008LO PDF set [172] are overlaid to the main physics process' simulation samples to match the pile-up distribution shown in Fig. 5.1(b).

Detector Simulation Events from all generators, except SUSY signals and 4-top processes, are propagated through a full simulation of the ATLAS detector [173] based on GEANT4 [174] to model the interactions of particles with the detector. SUSY signals and 4-top processes undergo simulation using the Atfast3 (AF3) [175] fast simulation package. This package effectively reduces simulation CPU costs in the detector simulation by parameterizing the detector response against shower activities in detector materials.

5.2.2 SM Background Simulation Samples

This section outlines the configuration details for generating SM background processes. This analysis relies on multi-lepton signatures and the background processes which contribute to the targeted phase space are listed below. Vector boson processes, especially the multi-boson processes are the main backgrounds for this analysis, with top and Higgs processes being secondary contributions.

Vector boson production The production of single, two, and three vector bosons, known as single boson (W/Z +jets), di-boson (WW, WZ, ZZ), and tri-boson (WWW, WWZ, WZZ, ZZZ) processes are the main SM backgrounds in the targeted phase space in this analysis. For the single boson production, the t -channel production dominates over the s -channel production induced by pure EW interactions.

The full-leptonically decaying di-boson events are generated using SHERPA 2.2.12 [176]. Events of $Z \rightarrow ee$, $Z \rightarrow \mu\mu$, W +jets, and semi-leptonically decaying di-boson processes are simulated with SHERPA 2.2.11. $Z \rightarrow \tau\tau$ samples are simulated with SHERPA 2.2.14 and tri-boson processes are simulated with SHERPA 2.2.2. The NNPDF3.0NNLO [177] set of parton distribution functions (PDFs) is used together with a dedicated set of tuned parton shower parameters developed by the SHERPA authors [178]. Since the cross-section is calculated at next-to-next-to leading order (NNLO) accuracy for single boson productions, the total cross-section calculated by SHERPA is normalized to NNLO accuracy.

Electroweak corrections to single boson and di-boson production [179] can play a significant role in phase space where the boson is recoiled with large transverse momentum. The higher order EW corrections contain contributions from virtual loops and from real emission of gauge bosons. The SHERPA configuration only contains the virtual-loop terms, since applying the full NLO EW corrections is not currently possible. Moreover, the real emission of a gauge boson leads to a fundamentally different experimental signature that is typically produced in separate samples. Amplitudes for the EW virtual corrections are calculated by OPENLOOPS [180–183] and implemented in the SHERPA event generator for multi-jet merged set-ups. The cross-section calculated at NLO QCD and NLO EW accuracy, where the higher-order terms in QCD and EW couplings are summed (*additive* scheme), can be expressed as:

$$\sigma_{n,\text{QCD+EW}}^{\text{NLO}} = \sigma_{n,\text{LO}} + \Delta\sigma_{n,\text{QCD}}^{\text{NLO}} + \Delta\sigma_{n,\text{EW}_{\text{virt}}}^{\text{NLO}}, \quad (5.3)$$

where $\sigma_{n,\text{LO}}$ denotes the Born-level cross-section and $\Delta\sigma_{n,\text{QCD}}^{\text{NLO}}$ the NLO QCD corrections to the Born process. The $\Delta\sigma_{n,\text{EW}_{\text{virt}}}^{\text{NLO}}$ term only contains the virtual-loop components. Two additional

NLO QCD and NLO EW combination schemes are provided by the SHERPA framework. The first is the *multiplicative* scheme, which is defined as:

$$\sigma_{n,\text{QCD}\times\text{EW}}^{\text{NLO}} = (\sigma_{n,\text{LO}} + \Delta\sigma_{n,\text{QCD}}^{\text{NLO}}) \times (1 + \Delta\sigma_{n,\text{EW}_{\text{virt}}}^{\text{NLO}}). \quad (5.4)$$

The second scheme is referred to as the *exponentiated* scheme, and is defined as:

$$\sigma_{n,\text{QCD}\times e^{\text{EW}_{\text{virt}}}}^{\text{NLO}} = (\sigma_{n,\text{LO}} + \Delta\sigma_{n,\text{QCD}}^{\text{NLO}}) \times e^{\Delta\sigma_{n,\text{EW}_{\text{virt}}}^{\text{NLO}}}. \quad (5.5)$$

In this thesis, the *additive* scheme is used as nominal and *multiplicative* and *exponentiated* scheme are used for the theoretical systematic uncertainties evaluation which will be also discussed in Section 9.1.

Top production In the LHC, about 90% of the top-quark production is generated by gluon-initiated production, and the remaining 10% is generated by quark-initiated production. Single-top production can be classified into three processes: t -channel production, associated Wt -channel, and s -channel production.

The Matrix Element part of $t\bar{t}$, single-top tW , t -channel, and s -channel processes is calculated by POWHEG [184–187] at next-to-leading order (NLO) accuracy with NNPDF3.0NNLO PDF set. The output from POWHEG is passed to PYTHIA 8 [188] to simulate the parton shower and hadronization step, using the A14 tune [189]. The A14 tune is a set of parameters tuned to match observables sensitive to underlying events, jet structure, and additional jet emissions. Parameters are tuned using data measured by ATLAS during the LHC Run 1 period. The decay of heavy-flavor particles is simulated with EVTGEN 1.6.0 [190]. The total cross-section calculated by POWHEG is normalized to the NNLO+NNLL accuracy. Other top-quark-involved processes ($t\bar{t}Z$, tZ , tWZ , $t\bar{t}WW$, 3-top and 4-top) are modelled using MADGRAPH5_AMC@NLO 2 [191] + PYTHIA 8.

Higgs production Though small cross-section in LHC, Higgs processes could be a important background for SUSY searches. Several production modes (ggF : gluon-gluon fusion, Vh : associated production with W/Z , and $t\bar{t}h$ production) are included.

The Matrix Element part is simulated by POWHEG at NNLO+NNLL (NLO) accuracy for ggF (Vh , $t\bar{t}h$) and with NNPDF3.0NNLO PDF set. The output from POWHEG is passed to PYTHIA 8 to simulate the parton shower and hadronization step, using the A14 or AZNLO tune.

The MC generator setup for the SM backgrounds used in this thesis is summarized in Table 5.1.

5.2.3 Signal Simulation Samples

This section describes the simulation samples of the signal model described in Section 3.3. Signal simulation samples are produced for each production mode, $\tilde{\ell}_L^+ \tilde{\ell}_L^-$, $\tilde{\ell}_L^\pm \tilde{\nu}$, and $\tilde{\nu} \tilde{\nu}$ via the off-shell W and Z bosons.

The samples are generated from leading-order (LO) matrix elements with up to two extra partons using MADGRAPH5_AMC@NLO 3.3.1 interfaced with PYTHIA 8.307, with the A14 tune, for the modeling of the SUSY decay chain, parton showering, hadronization and the description of the underlying event. Parton luminosities are provided by the NNPDF2.3LO PDF set. Jet-parton matching has been done following the CKKW-L prescription [192, 193] with a matching scale set to one quarter of the pair-produced SUSY particle mass. An overview of the signal grid is shown in Fig. 5.2, together with the total number of generated MC events after the generator level selections which require events to have two or more leptons. The cross-sections and their

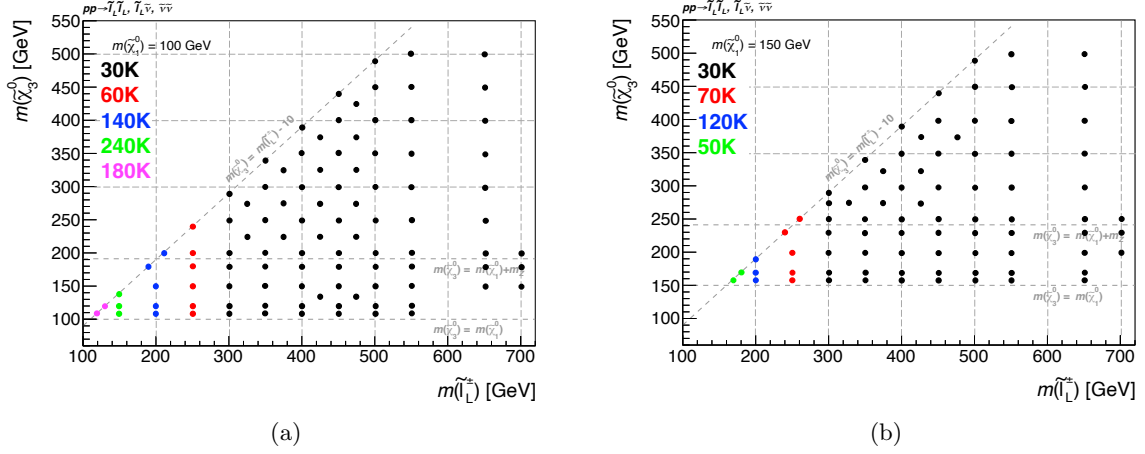


Figure 5.2: An overview of the signal grid used in this analysis for $m(\tilde{\chi}_1^0)$ of (a) 100 GeV and (b) 150 GeV. The color of the dots indicates the total number of generated MC events as written in the figure.

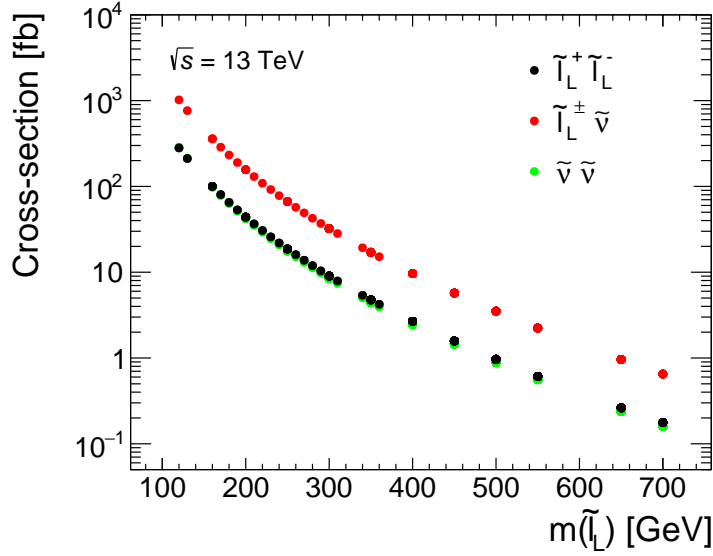


Figure 5.3: Production cross-section as a function of slepton mass for each production process, at the NNLO+NNLL accuracy.

uncertainties are calculated to NLO+NLL accuracy using the Resummino [194] package which are summarized in Fig. 5.3. Since the decay of electroweakinos is calculated by PYTHIA, the polarization of the W/Z boson produced by the chargino or neutralino decay is not considered. We have checked that even if MADSPIN [195, 196] which takes spin into account is used in the event generation, there is no significant difference in the kinematics between MADSPIN and PYTHIA.

The MC generator setup for signal samples used in this thesis is also summarized in Table 5.1.

Table 5.1: Summary of generator setup for the SM backgrounds and signal samples. The corresponding event generator, parton shower, set of tuned parameters, PDF set, and cross-section normalization are shown for each sample.

Process	Matrix Element	Parton Shower	Tune	PDF set	Cross-section
SUSY processes	MADGRAPH5_AMC@NLO 3.3.1	PYTHIA 8.307	A14	NNPDF2.3LO	NLO+NNL
W/Z+jets	SHERPA 2.2.11/2.2.14		standard	NNPDF3.0NNLO	NNLO
Di-bosons	SHERPA 2.2.11/2.2.12		standard	NNPDF3.0NNLO	Generator NLO
Tri-bosons	SHERPA 2.2.2		standard	NNPDF3.0NNLO	Generator NLO
$t\bar{t}$	POWHEG BOX 2	PYTHIA 8.230	A14	NNPDF2.3LO	NNLO+NNL
Single-top	POWHEG BOX 2	PYTHIA 8.230	A14	NNPDF2.3LO	NNLO+NNL
$t\bar{t}W$	SHERPA 2.2.10		standard	NNPDF3.0NNLO	Generator NLO
$t\bar{t}Z, tZ, tWZ$	MADGRAPH5_AMC@NLO 2.3	PYTHIA 8.210	A14	NNPDF3.0NNLO	Generator NLO
$t\bar{t}WW, 3\text{-top}, 4\text{-top}$	MADGRAPH5_AMC@NLO 2.2	PYTHIA 8.186	A14	NNPDF2.3NNLO	Generator LO
Higgs (ggF)	POWHEG BOX 2	PYTHIA 8.212	AZNLO	CTEQ6L1	NNLO+NLO(EWK)
Higgs (Vh)	POWHEG BOX 2	PYTHIA 8.230	AZNLO	CTEQ6L1	NNLO+NLO(EWK)
Higgs ($t\bar{t}h$)	POWHEG BOX 2	PYTHIA 8.230	A14	NNPDF2.3LO	Generator NLO

Table 5.2: A summary of trigger requirements. A logical OR is performed for a given year.

Electron Triggers	Muon Triggers
2015	
HLT_e24_lhmedium_L1EM20VH	HLT_mu20_iloose_L1MU15
HLT_e60_lhmedium	HLT_mu50
HLT_e120_lhloose	
2016, 2017, 2018	
HLT_e26_lhtight_nod0_ivarloose	HLT_mu26_ivarmedium
HLT_e60_lhmedium_nod0	HLT_mu50
HLT_e140_lhloose_nod0	

5.3 Trigger Selection

Since the signal event has isolated leptons from the decay of sleptons, the direct decay of W , Z bosons, or the indirect decay of a Higgs boson, such a lepton is used to trigger events in data taking. Single-lepton trigger chains listed in Table 5.2 are used to maximize the data statistics.

The numbers following “HLT_e” or “HLT_mu” indicate the E_T or p_T threshold in GeV at HLT. The “lhtight”, “lhmedium”, and “lhloose” denote the requirement of an electron identification using the likelihood discriminant of the multivariate techniques. “L1EM20” stands for the L1 trigger imposing a 20 GeV transverse energy threshold on electron objects. “V” and “H” indicate that the E_T correction is made for the η direction and the hadron calorimeter information is not used in the construction of the electron objects, respectively. The “nod0” means no information on the impact parameter is used. “iloose” and “ivarmedium” represent the additional requirements of the muon isolation. On the other hand, “L1MU15” means that muon p_T above 15 GeV is required in the L1 trigger. The efficiency curve as a function of offline lepton p_T is shown in Fig. 5.4 and 5.5 [197, 198].

Events are required to have at least one signal lepton, whose definition is described in Section 6.10, matched to the trigger fired in that event. This lepton is not required to be the leading lepton in an event, but it must exceed the offline p_T threshold for the trigger to assure the plateau efficiency. For electrons, the offline threshold is 1 GeV larger than the HLT trigger threshold. For muons, this is 1.05 times the HLT trigger threshold. The trigger is simulated in MC, and selection is applied in the same way as actual collision data.

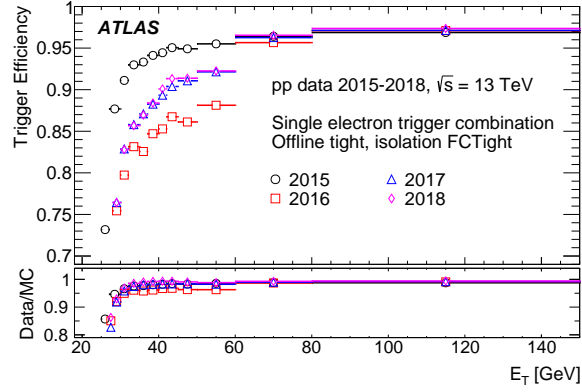


Figure 5.4: Evolution of the single-electron trigger combination efficiency as a function of the offline electron E_T during Run 2 [197]. Efficiency is given with respect to offline tight identification and the FCTight isolation working point. The ratios of data to MC simulation efficiencies are also shown. The error bars indicate statistical and systematic uncertainties combined in quadrature.

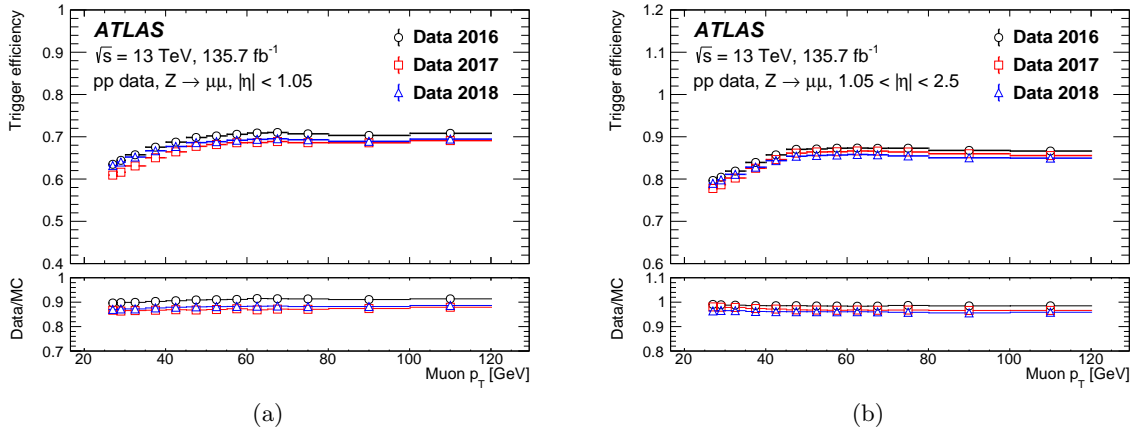


Figure 5.5: Efficiency of passing either the HLT_mu26_ivarmedium or the HLT_mu50 trigger in the (a) barrel and (b) end-cap as a function of the muon p_T , computed using data taken in 2016-2018 [198]. The error bars show the statistical uncertainties only.

Chapter 6

Object Reconstruction and Identification

Particles produced in pp collisions leave characteristic signals in the detector unique to their respective particle types, as illustrated in Fig. 6.1. These signals are used to reconstruct four vectors representing the produced particles, referred to as “objects”. In the first step, tracks, vertices, and calorimeter clusters called the “Topo-clusters” are reconstructed as fragmentary information of the produced particles. These objects are further combined to reconstruct objects that closely resemble the true information of the produced particles. These reconstructed objects called “physics objects” include jets, leptons, photons, and missing transverse momentum. This chapter describes the reconstruction algorithm used in the analysis.

6.1 Overview of Event Reconstruction

Fig. 6.2 illustrates the event reconstruction flow used in this thesis. Raw detector information is combined to form tracks, vertices, and topo-clusters, referred to as “low-level objects”. Section 6.2, 6.3, and 6.4 discusses the algorithms for reconstructing low-level objects. The low-level objects are combined to reconstruct physics objects, such as jets, muons, and electrons. These physics objects must meet specific “identification” criteria and kinematic selections to form “baseline” objects, which will be further discussed in Section 6.5, 6.6, and 6.7. To resolve the potential ambiguity arising from the reconstruction of multiple baseline objects from a single particle, a procedure called “overlap removal” is implemented, which will be further discussed in Section 6.8. The missing transverse momentum is calculated using all baseline objects, which will be described in Section 6.9. The baseline objects are subject to more stringent quality and “isolation” requirements to ensure a higher purity of the objects, which are referred to as “signal” objects. The definitions of the baseline and signal objects used in this analysis are summarized in Section 6.10.

6.2 Tracks

Charged tracks are the fundamental units seeding various offline particle reconstruction and calibration. Standard tracks used in ATLAS refers to ID tracks, reconstructed by the hits created in the ID. The reconstruction algorithm consists of the following five main steps (the detail can be found in Ref. [200]):

1. **Space Point Creation :** Adjacent hits in each layer of the Pixel and SCT detectors are merged to form “clusters”. The clusters are then converted to three-dimensional position

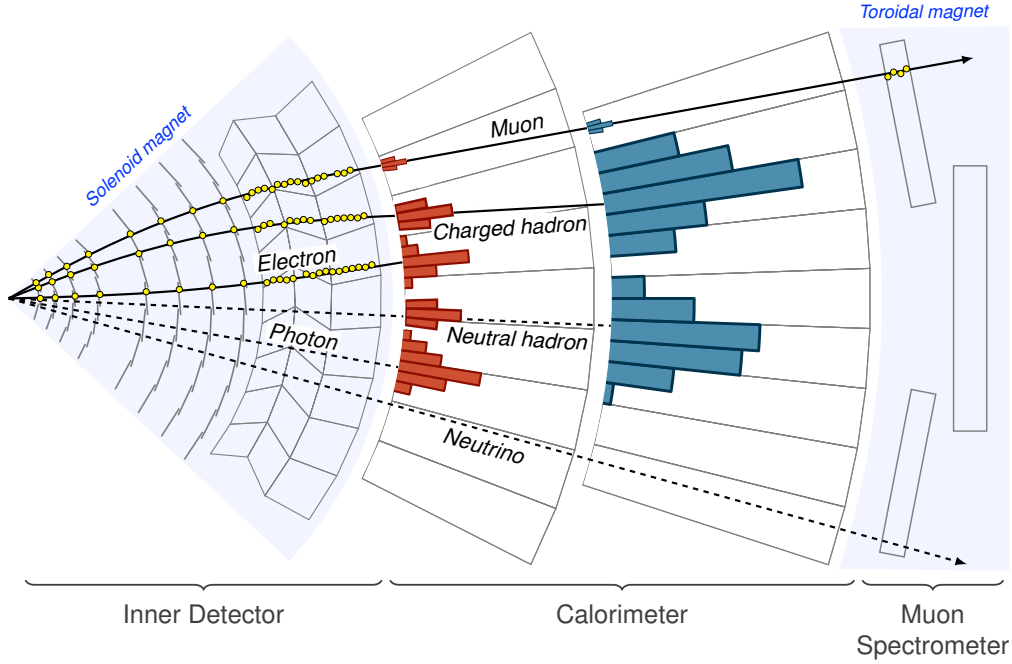


Figure 6.1: Schematic view of various particles passing through the ATLAS detector, leaving characteristic signals in the detector [199]. The figure shows hit information represented by yellow dots and energy deposits displayed through red and blue bars in the electromagnetic and hadronic calorimeters, respectively.

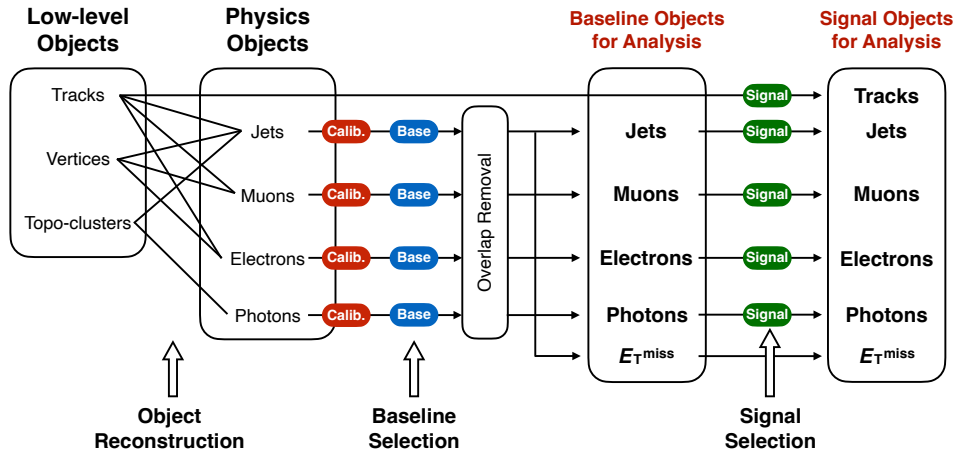


Figure 6.2: Schematic diagram of the event reconstruction flow utilized in this thesis [199]. The low-level objects are combined to form physics objects. The energy or momentum of physics objects is calibrated and required to pass baseline selections to form baseline objects. The overlap removal step resolves the ambiguity of baseline objects. The missing transverse momentum is calculated using all baseline objects. Finally, all physics objects must pass more stringent quality and isolation requirements to form signal objects. In this thesis, signal tracks are not used as physics objects.

information called “space points”.

2. **Pixel & Strip Seed Finding** Track seeds are formed by combining three space points from the pixel or the SCT detector.⁵ Selections on longitudinal impact parameters of track seeds are applied at this point to suppress low-quality track seeds and reduce computational time. From Run 2, fake track seeds are further suppressed by requiring an additional space point in another layer called the “confirmation space point”.
3. **Track Finding** : Track seeds are extrapolated and fitted by the combinatorial Kalman filter method [201] to determine the pixel and SCT modules through which the track could pass.
4. **Ambiguity Resolving** : During the track finding step, multiple track candidates can be reconstructed with overlap, and the ambiguity among them must be resolved. To resolve the overlap between tracks, “track scores” are calculated based on the number of hits and holes, the track p_T , and other criteria. Tracks with low scores are considered as fake and discarded at this point. When multiple tracks share the same clusters, called “shared hits”, they are assigned to the track with lower scores. Tracks with multiple shared hits are also considered fake tracks and are discarded.
5. **TRT Extended Track Refit** : Tracks are extended to the TRT detector, and if hits are found successfully, the fitting procedure and track scoring are repeated. If the track score is higher than the Pixel and SCT detector only fit, the TRT hit is added to the track. If the track score is lower, the TRT hit is recorded as an “outlier” of the track.

The reconstructed tracks are described with five parameters ($d_0, z_0, \phi, \theta, q/p$) as illustrated in Fig. 6.3. The transverse impact parameter, denoted by d_0 , refers to the closest transverse distance between the z -axis and the track. On the other hand, the longitudinal impact parameter,

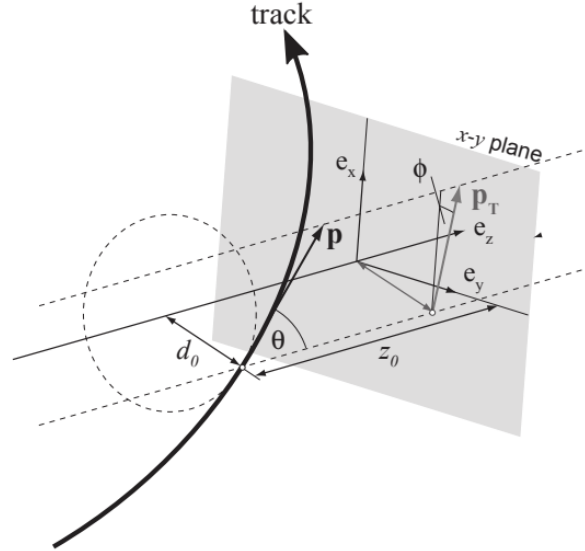


Figure 6.3: Schematic view of the track parameters. The track parameters are calculated based on the closest point of the track to the beam axis in the x - y plane, referred to as the “perigee” point [202]. The hard-scatter primary vertex lies on the gray x - y plane.

⁵A seed is composed of space points purely from either the Pixel detector or the SCT, or two from the Pixel detector (SCT) and one from the SCT (Pixel detector).

denoted by z_0 , refers to the distance between the hard-scatter primary vertex, which definition is mentioned in Section 6.3, and the nearest point of contact between the beam position and the track along the longitudinal axis. ϕ and θ are the azimuthal and polar angles of the tracks. q/p is the ratio between the charge and the momentum of the track.

6.3 Primary Vertices

The positions of pp collisions are identified using the reconstructed ID tracks. These vertices called “primary vertices” (PV)⁶ are important for providing reference point of re-tracking and object calibrations. PVs are reconstructed by calculating the intersection of reconstructed tracks. Tracks used to reconstruct the PV along the beam axis must pass the selection criteria in Ref. [203]. The PVs are reconstructed through the following steps.

1. **Vertex Finding :** A vertex seed is defined by taking the beam spot position as the x, y position and the closest point between the track and the beam spot as the z position.
2. **Vertex Fitting :** After defining a vertex seed, the seed and the tracks are used as inputs to the adaptive vertex fitting algorithm [204]. After each fit, the tracks are reweighted depending on the compatibility with the vertex position, and the fitting procedure is repeated. After reaching the minima of the fit, tracks incompatible with the final vertex position are used as inputs for the new vertex reconstruction procedure.

The above two steps are repeated until all input tracks are associated with PVs or no additional PVs are reconstructed. Though 10-30 PVs are reconstructed per bunch crossing, usually there is only one PV causing the meaningful scattering. Such a “hard-scatter” vertex is identified as a PV with the highest sum of associated track p_T , and the position is used as the origin for object calibrations.

6.4 Topo-clusters

Energy deposits in the calorimeter cells are combined to form “topo-clusters”. Topo-clusters are used to reconstruct jets, electrons, and photons and quantify hadron activity around leptons. To discriminate energy deposits from noise (electronic noise, pile-up, etc.) in the calorimeter cells, the calorimeter cell significance is defined by dividing the measured energy deposit by the average noise level in the electromagnetic scale. Topo-clusters are reconstructed by finding a seed cell with 4σ significance and merging neighboring cells which are above 2σ significance. The above process is repeated, and once no more cells can be merged, all adjacent cells are merged to define the boundary. If two seed cells are connected to each other by the cells above 2σ significance, they are merged to form a single topo-cluster.

6.5 Electrons

Electron objects are formed with the following four steps described briefly. More details can be found in Ref. [205].

⁶The “primary” is meant to distinguish against the vertices generated by late decaying particles known as “secondary vertices”.

Reconstruction The electron reconstruction algorithm proceeds as following.

1. **Supercluster reconstruction** : “Superclusters” with variable sizes are formed by combining topo-clusters. The clusters are formed around the electron cluster seeds using a clustering algorithm [206] that allows for duplicates to be removed.
2. **Track and supercluster matching** : The supercluster is loosely matched with an ID track reconstructed based on the angular distance ΔR . The loosely matched track receives further correction by a re-tracking using the Gaussian Sum Fitter (GSF) [207] to account for the energy loss by bremsstrahlung. Closest track in ΔR with respect to the supercluster is chosen as “primary” track.
3. **Energy determination** : The information from track momentum and calibrated supercluster energy are combined using a multivariate algorithm [208].

Identification Electron identification is performed using a likelihood discriminant with the following inputs.

- Variables of the primary track associated with the electron
- Lateral and longitudinal shower shape in the electromagnetic calorimeter
- Information regarding the alignment of the track and calorimeter

The likelihood discriminant is modeled by probability density functions (pdfs) with $Z \rightarrow ee$ ($E_T > 15$ GeV) and $J/\psi \rightarrow ee$ ($E_T < 20$ GeV) events as signals and di-jet events as backgrounds. Separate pdfs are derived from electrons in data events for each E_T and η range to incorporate the energy and position dependence. This thesis uses the *LooseAndBLayerLLH* and *TightLLH* working points for electron identification. The *LooseAndBLayerLLH* working point requires a threshold to the likelihood discriminant to achieve a detection efficiency of 93% for electrons with $E_T = 40$ GeV, and additionally requires a hit in the Insertable B-Layer (IBL) to suppress electrons from photon conversions. The *TightLLH* working point requires a slightly stricter threshold to the likelihood discriminant to achieve a detection efficiency of 77% for electrons with $E_T = 40$ GeV.

Isolation This thesis uses the *Tight_VarRad* working point for electron isolation. The track-based isolation variable for electrons, denoted as $p_T^{\text{varcone30}}$, is defined as the scalar sum of the p_T of tracks with $p_T > 1$ GeV and within a variable cone size around the electron. The radius of the cone is adjusted based on the momentum of the electrons, as electrons decaying from high-momentum hadronic sources tend to be closely aligned with other decay particles. The radius used for $p_T^{\text{varcone30}}$ is defined as $\Delta R = \min(0.3, 10/p_T [\text{GeV}])$. The calorimeter-based isolation variable for electrons, denoted as $E_T^{\text{topoetcone20}}$, is defined as the scalar sum of topo-clusters within $\Delta R < 0.2$ of the electron. Combining the track-based and calorimeter-based isolation variables, electrons are required to pass the selection,

$$p_T^{\text{varcone30}}/p_T < 0.06, \quad E_T^{\text{topoetcone20}}/p_T < 0.06. \quad (6.1)$$

Energy Calibration The energy scale and resolution of electrons are calibrated using the $Z \rightarrow ee$ process. The correction factor for the energy scale applied to the data is denoted as α_i ,

where i represents the η region. Similarly, the correction factor for the energy resolution applied to the simulation is denoted as c_i . The two correction factors are defined as

$$E^{\text{data, corr}} = \frac{E^{\text{data}}}{(1 + \alpha_i)}, \quad (6.2)$$

$$\left(\frac{\sigma_E}{E}\right)^{\text{MC, corr}} = \left(\frac{\sigma_E}{E}\right)^{\text{MC}} \oplus c_i, \quad (6.3)$$

where α_i and c_i are derived by minimizing the difference between the invariant mass distribution in data and simulation.

In addition, electrons which are reconstructed with an incorrect charge assignment are suppressed using electron cluster and track properties, such as $q \times d_0$, E/p , q_{AVG} , and $\Delta\Phi_{\text{res}}$ [209]. q_{AVG} is the average charge of the candidates to match the calorimeter energy cluster and $\Delta\Phi_{\text{res}}$ is the $\Delta\phi$ between the cluster position in the second layer of the EM calorimeter and the momentum-rescaled track, extrapolated from the perigee point. These variables, as well as the electron p_T and η , are combined into a single classifier using a boosted decision tree (BDT). A selection requirement on the BDT output is chosen to achieve a rejection factor for wrong sign electrons of around 6.33, while selecting properly measured electrons with an efficiency of 98.27% in $Z \rightarrow ee$ MC. This selection is applied using the `ElectronChargeIDSelector` (ECIDS) package.

Two additional variables exist to help rejecting electrons from converted photons and photons mis-reconstructed as electrons. The electron “AmbiguityType” variable tells if an electron has also been reconstructed as a photon. The “AddAmbiguity” variable has been implemented to offer further rejection of *material* and *internal* conversions. Material (internal) conversions have a reconstructed displaced vertex with radius $r > 20$ mm ($r < 20$ mm) with respect to the beamline. $\text{AmbiguityType} = 0$ and $\text{AddAmbiguity} \leq 0$ ensures that the electron candidate is certainly not a photon, and is not a material or an internal conversion candidate.

6.6 Muons

Muon objects are formed with the following four steps, which are briefly described. More details can be found in Ref. [210].

Reconstruction Muons are reconstructed using the ID and MS information. Track candidates in ID and MS are reconstructed independently and are combined to form muons called “combined” muons (CB muons).

Identification Additional selection criteria are applied to suppress muon candidates from in-flight decays of charged mesons, such as strange mesons or pions. Muons from in-flight decays are expected to have a “kink” topology, and this characteristic can be discerned by assessing the compatibility between the momentum measurements obtained from the ID and the MS. For CB muons, the “ q/p significance” is used to quantify the “kink” topology, defined as

$$\frac{|(q/p)_{\text{ID}} - (q/p)_{\text{MS}}|}{\sqrt{\sigma_{\text{ID}}^2 + \sigma_{\text{MS}}^2}}, \quad (6.4)$$

where σ corresponds to the momentum resolution and subscripts represent the detectors used for measurement.

In this thesis, the *Medium* working point is used for muon identification. Additional requirements on the number of MDT or CSC stations with at least three hits, denoted as “precision stations”, are applied. In the $|\eta| < 0.1$ region, where the MS is not fully equipped, the number of MDT or CSC stations with less than three hits anticipated based on its trajectory, denoted as “precision hole station”, is also used. The *Medium* working point is defined to achieve a detection efficiency of 97% for muons with $p_T = 20$ GeV, CB muons are required to pass q/p significance < 7 and at least two precision stations, except for the $|\eta| < 0.1$ region. In the $|\eta| < 0.1$ region, CB muons with at least one precision station and at most one precision hole station are also allowed.

Isolation Muons from semi-leptonic decays of hadronic sources can be suppressed by measuring hadronic activities around the muons using track and calorimeter information. The PFlow algorithm [211] is used to remove the overlap of activities of charged particles, as discussed in Section 6.7.

In this thesis, the *PflowTight_VarRad* working point is used for muon isolation. The track-based isolation variable, denoted as $p_T^{\text{varcone30}}$, is defined in the same way as for electrons. The calorimeter-based isolation variable, denoted as E_T^{neflow20} , is defined as the scalar sum of neutral particle-flow objects within $\Delta R < 0.2$ of the muon. Combining the track-based and calorimeter-based isolation variables, muons are required to pass the selection described as

$$\left(p_T^{\text{varcone30}} + 0.4 \times E_T^{\text{neflow20}}\right) / p_T < 0.045. \quad (6.5)$$

Momentum calibration The momentum distribution of muons in data and simulation samples do not match perfectly due to incomplete knowledge of the alignment of detectors and energy deposits in calorimeters or detector material. Therefore, the momenta are calibrated using the invariant mass of $J/\psi \rightarrow \mu\mu$ and $Z \rightarrow \mu\mu$ processes for low and high p_T , respectively. Correction factors are measured for the momentum of the CB muons, as well as the ID and MS tracks associated with the CB muon. The calibration step is validated by comparing the corrected CB muon momentum with the momentum combined from measurements in the ID and MS.

6.7 Jets

Hadron jets emerge as focused clusters of particles originating from the hadronization process of quarks and gluons produced in high-energy pp collisions. Tracks and topo-clusters are combined to form hadron jets following the procedures described briefly below. In the following, hadron jets will be abbreviated as “jets”. More details can be found in Ref. [211].

Particle Flow (PFlow) algorithm Individual hadrons in a jet typically have an energy as low as a few GeV. In this low-energy range, the resolution of tracks is much better than that of calorimeter clusters. Therefore, the energy resolution of reconstructed jets is improved by prioritizing the use of track information for the energies from charged hadrons. However, since charged hadrons interact with both the ID and the calorimeters, it is essential to remove the overlap. In the PFlow algorithm [211], the energy deposit of charged particles which is estimated from tracks is subtracted from the matched topo-clusters.

Reconstruction A new set of tracks and topo-clusters, provided by the PFlow algorithm, is combined by the Anti- k_t algorithm [212] to form jets. Tracks must be associated with the primary vertex, and positions of the topo-clusters are recalculated relative to the primary vertex.

Jet Vertex Tagger (JVT) Significant fraction of reconstructed jets are originated from pile-up, particularly when they are low- p_T . In order to suppress the contamination, a pile-up jet rejection is applied using the Jet Vertex Tagger (JVT) discriminant [213] exploiting the vertex information. The initial step is to classify tracks in the jet as either originating from the hard-scatter vertex or pile-up vertices. Subsequently, the ratio of the total momentum of the tracks to the jet energy is computed for each classification and used for discrimination. The sum of the track p_T from the pile-up vertices is proportional to the number of pp collisions in each event. The sum of the track p_T is divided by the number of tracks to eliminate this dependency. The ratio between the sum of the track p_T from the hard-scatter vertex and pile-up vertices is called the corrected Jet Vertex Fraction (corrJVF). Since the corrJVF becomes smaller when the number of tracks from the hard-scatter vertex is small, the selection for the corrJVF is adjusted according to the sum of the p_T of the tracks relative to the jet energy. Jets with $p_T < 60$ GeV and within the ID acceptance ($|\eta| < 2.5$) are required to pass the *FixedEffPt* working point of the JVT.

Flavor tagging Jets containing b -hadrons, referred to as b -jets, are characterized by the long lifetime of the b -hadrons and multiplicity of decay objects from b -hadrons. Identifying b -jets involves a two-stage approach: low-level algorithms that produce discriminants based on track inputs and a high-level algorithm that combines the output from low-level algorithms to maximize performance. The low-level algorithm is broadly categorized into two methods: one utilizes the impact parameters of individual tracks associated with jets, while the other reconstructs secondary vertices using tracks. In this thesis, the *DL1dv01FixedCutBeff85%* working point is used for b -jet flavor tagging. The identification criteria are tuned to an average identification efficiency of 85% as obtained for b -jets in simulated $t\bar{t}$ events, corresponding to rejection factors of 29, 2.6, and 3.9 for jets originating from light quarks and gluons, c -quarks, and τ -leptons, respectively [214].

Energy Reconstruction The measurement from reconstructed jets in sampling calorimeters represents only a fraction of the total energy. To obtain the complete energy, it is necessary to scale the measured energy and calibrate the measured energy resolution. The energy scale and resolution of the jets, referred to as Jet Energy Scale (JES) and Jet Energy Resolution (JER), are calibrated through the following steps.

1. **Pile-up correction** : The energy deposit from pile-up contributions is subtracted from the measured energy in the first step. The medium transverse energy density ρ is calculated from topo-clusters using k_t jets [215, 216] and multiplied by the area of the jet for subtraction [217].
2. **MC-based calibration** : The energy response in simulations is corrected to match the response measured in the data. The energy response, denoted as $R = E_{\text{reco}}/E_{\text{truth}}$, is measured as a function of η and the energy of the jets and then applied to the simulations.
3. **Global sequential calibration** : The energy response between the truth jet and the reconstructed jet may differ depending on other sources, such as the flavor of the jets. To account for these variations, additional variables that characterize the jets are used to correct the energy response, such as the fraction of the measured energy from tracks associated with the jet.
4. **In-situ calibration** : The final calibration step is applied exclusively to the data to address the residual difference between the reconstructed jets in the data and the truth jets in the simulations. The energy ratio between jets and well-measured reference objects, such

as Z bosons, photons, and low- p_T jets, is measured in both the data and the simulation. The calibration process consists of three steps. In the first step, using the multijet process, the “ η intercalibration” is applied to calibrate the jets in the forward regions ($0.8 \leq |\eta| \leq 4.5$). The second step involves using Z + jets and γ + jets processes to calibrate jets with p_T in the range of $17 < p_T < 1000$ GeV and $25 < p_T < 1200$ GeV, respectively. Finally, the calibration step using the multijet process is applied to calibrate jets with high p_T up to 2.4 TeV.

6.8 Overlap Removal between the Reconstructed Objects

The overlap removal procedure utilizes collections of electrons, muons, and jets to eliminate overlapping objects based on the ΔR between two objects or whether the objects share ID tracks. When high-momentum hadronic sources undergo semi-leptonic decays, the alignment between jets and leptons becomes very close. The ΔR is adjusted with the lepton p_T to avoid overlap between these objects. The sequence of removing overlap between the reconstructed objects is detailed in Table 6.1. First, the electron-electron overlap removal⁷ and electron-muon overlap removal aim to remove electrons from the bremsstrahlung photon radiated from the original lepton. Next, as an electron is usually clustered as well as a jet, jets in proximity to electrons are removed in the jet-electron overlap removal. Then, electrons from semi-leptonic decays of heavy flavored hadrons is suppressed by the electron-jet overlap removal. Subsequently, to reduce “jets” reconstructed from bremsstrahlung photon energy deposit in the EM calorimeter and ID track of the muon, jet-muon overlap removal is performed. Finally, the muon-jet overlap removal is performed to suppress muons from semi-leptonic decays of heavy flavored hadrons.

6.9 Missing Transverse Energy

In the LHC, the transverse energy of particles produced from the pp collision is conserved and equals to zero. The total transverse momentum of particles that do not leave signals in the detector, such as neutrinos or neutralinos, can be calculated by taking the negative vector sum of the transverse momentum of the reconstructed physics objects and the “soft term” [218]. The soft term consists of tracks associated with the primary vertex but not with the baseline objects. The vector sum is called the missing transverse momentum ($\mathbf{p}_T^{\text{miss}}$), and its magnitude is called

Table 6.1: The order of overlaps removed between reconstructed objects. The sequence is done from top to bottom. “Target” refers to the object that will either be discarded or kept based on each criterion between “Reference” object. ΔR is calculated as the positional difference between the reference and target object.

Target	Reference	Criterion
Electron	Electron	Reject an electron if they share a track with a electron with higher p_T
Electron	Muon	Reject an electron if associated ID track is shared with a muon
Jet	Electron	Reject a jet if not a b -jet and $\Delta R < 0.2$ with a electron
Electron	Jet	Reject an electron if $\Delta R < \min(0.4, 0.04 + 10 \text{ GeV}/p_T^e)$ with a jet
Jet	Muon	Reject a jet if not a b -jet and $\Delta R < 0.2$ with a muon
Muon	Jet	Reject a muon if $\Delta R < \min(0.4, 0.04 + 10 \text{ GeV}/p_T^\mu)$ with a jet

⁷“ A - B overlap removal” refers to the overlap removal where A is the target object and B is the reference object.

Table 6.2: Summary of object definitions utilized in this thesis.

Property	Signal	Baseline
Jets		
Kinematic	$p_T > 20 \text{ GeV}, \eta < 2.8$	$p_T > 20 \text{ GeV}, \eta < 4.5$
Pile-up mitigation	JVT FixedEffPt for $p_T < 60 \text{ GeV}, \eta < 2.5$	
b -tagging	DL1dv01FixedCutBeff85% for $p_T > 20 \text{ GeV}, \eta < 2.5$	
Electrons		
Kinematic	$p_T > 4.5 \text{ GeV}, \eta < 1.37 \text{ or } 1.52 < \eta < 2.47$	
Identification	TightLLH	LooseAndBLayerLLH
Isolation	Tight_VarRad	–
Impact parameter	$ d_0/\sigma(d_0) < 5, z_0 \sin \theta < 0.5 \text{ mm}$	$ z_0 \sin \theta < 0.5 \text{ mm}$
Quality	pass ECIDS	–
	AmbiguityType = 0, AddAmbiguity ≤ 0	–
Muons		
Kinematic	$p_T > 3 \text{ GeV}, \eta < 2.5$	
Identification	Medium	Medium
Isolation	PflowTight_VarRad	–
Impact parameter	$ d_0/\sigma(d_0) < 3, z_0 \sin \theta < 0.5 \text{ mm}$	$ z_0 \sin \theta < 0.5 \text{ mm}$

the missing transverse energy (E_T^{miss}). It is constructed by four independent terms as:

$$\mathbf{p}_T^{\text{miss}} := - \sum \mathbf{p}_T^e - \sum \mathbf{p}_T^\mu - \sum \mathbf{p}_T^{\text{jet}} - \mathbf{p}_T^{\text{soft}}, \quad (6.6)$$

where the first three terms (electron term / muon term / jet term) are the vectoral sum of \mathbf{p}_T of the objects after the calibration and the overlap removal. The last term is the soft term accounting for the residual visible momentum mainly from soft jets and mis-identified muons. This thesis uses the *Tight* working point for the E_T^{miss} to minimize pile-up dependence in the soft term. The *Tight* working point calculates the E_T^{miss} without forward jets with $|\eta| > 2.4$ and $20 < p_T < 30 \text{ GeV}$, where more pile-up jets fall in.

6.10 Object Definition in the Analysis

The selection criteria for kinematics, identification, and isolation of physics objects are summarized in Table 6.2. For electrons and muons, two working points are defined. The “baseline” working point refers to a set of relaxed selection criteria designed to suppress additional prompt leptons from the event. In contrast, the “signal” working point employs more stringent criteria to effectively reject fake leptons, incorporating stricter identification, impact parameter cut, and isolation requirements in addition to the baseline criteria. Search regions in this analysis are defined with exactly three baseline and signal leptons.

Chapter 7

Event Selection

This chapter outlines the selections applied to define signal regions (SRs). SRs are optimized to enhance targeted SUSY signals while reducing the SM backgrounds. Different level of event selection will be discussed from the event cleaning selection (Section 7.1), preselection (Section 7.2), design of the SR binning, and the optimization of background rejection cuts (Section 7.3). The signal composition in each SR is discussed in Section 7.4.

7.1 Event Cleaning

Data utilized for physics analyses must meet specific criteria to ensure the detector's optimal functioning. Events recorded during periods of detector malfunction or those containing unqualified objects, such as cosmic muons and beam-induced backgrounds, should be excluded. The presence of such events can lead to anomalous observables, such as exceptionally high jet p_T or E_T^{miss} . Even a small number of these contaminating events can significantly impact SRs, particularly in analyses targeting high-energy kinematics where only a limited number of background events are anticipated.

Initially, data recorded with more than 10% of sub-detectors in an inappropriate state are

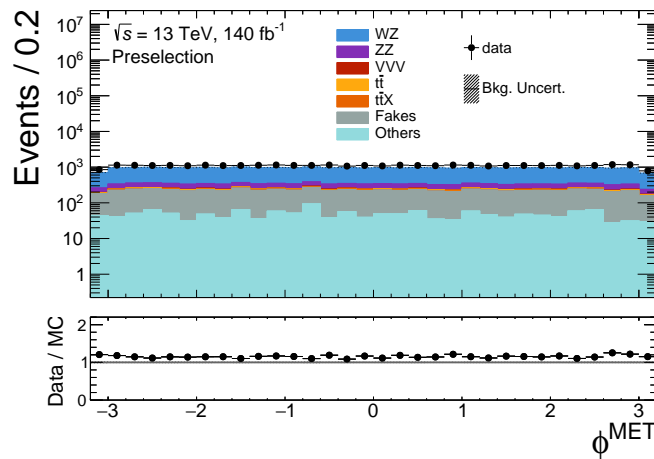


Figure 7.1: Distribution of ϕ direction of E_T^{miss} in preselection region (Table 7.1). The hatched band includes the MC statistical uncertainties. The bottom panel shows the ratio of the observed data and background yield estimated directly from simulation samples. No peak is observed at $|\phi| = 0, \pi$.

excluded from the analysis. Subsequently, events influenced by noise bursts in LAr and SCT, as well as those affected by corrupted data transmission in LAr and the Tile calorimeter, are also vetoed. To eliminate cosmic muons, a requirement is imposed that the muon track must be sufficiently close to the primary vertex, specifically defined by the conditions $|z_0 \sin \theta| < 1$ mm and $|d_0| < 0.2$ mm. Beam-induced backgrounds consist of events featuring muons produced by secondary cascades of protons that travel upstream of the IP. The energy deposits from these muons can be reconstructed as jets, potentially reaching energies comparable to that of the beam. Additionally, high-energy muons with suboptimal momentum measurement can contribute to spurious high E_T^{miss} values, which may extend up to several TeV. Such muons are characterized by the condition $\sigma(q/p)/(q/p) > 0.4$, where q denotes the muon charge, p represents the momentum, and $\sigma(q/p)$ indicates the fitting uncertainty. Any event containing at least one of these poorly measured muons will be vetoed entirely. To reject the jets not originating from the LHC beam collisions, event with jets flagged as “BadLoose” [219] are vetoed. Jets from non-collision backgrounds can be identified by checking the shower shape and direction of the jet relative to the IP. Moreover, jets generated by non-collision backgrounds do not have associated tracks and can be distinguished by considering the ratio of the total p_T of the associated tracks to the total energy of the jet. Fig. 7.1 shows the ϕ distribution of E_T^{miss} (ϕ^{MET}) in the preselection region, which will be defined in Table 7.1. The beam-induced background will cause peaks in ϕ^{MET} distribution at $|\phi^{\text{MET}}| = 0, \pi$ because it is bent in that direction by the recombination dipole. The figure shows that there is no peak around $|\phi^{\text{MET}}| = 0, \pi$ and the data and MC simulations show good agreement.

7.2 Preselection

As mentioned in Section 3.3, the target of this thesis is the $\tilde{\ell}_L^+ \tilde{\ell}_L^-$ and $\tilde{\ell}_L^\pm \tilde{\nu}$ production with the three lepton final state. The preselection is the common selection for all the SRs in this analysis, which is defined in Table 7.1. Fig. 7.2 is a validation plot showing the leading lepton p_T , sub-leading lepton p_T , 3rd leading lepton p_T , $m_{\ell\ell}$, E_T^{miss} , m_T^{min} , and $m_{3\ell}$ distribution of the data and MC simulation after the preselection being applied, which shows a good agreement. The standard definition of transverse mass, m_T , when trying to reconstruct the W boson mass is

$$m_T^2(\ell, \nu) = 2p_T^\ell E_T^{\text{miss}} [1 - \cos(\phi_\ell - \phi^{\text{MET}})], \quad (7.1)$$

which should have a kinematic edge at the W boson mass of 80.4 GeV. m_T^{min} is defined as the minimum m_T of all lepton- E_T^{miss} pairings for which the other two leptons form a same-flavor opposite-sign (SFOS) pair. In three lepton final states, where the major background is WZ , the lepton used in this equation is conventionally the one which is not already assigned to the Z . However, since the Z boson can be off-shell, a selection which minimizes $|m_{\ell\ell} - m_Z|$ may not choose the correct leptons. For this reason m_T^{min} was introduced by an earlier three lepton search [220]. By using m_T^{min} for event selection, sensitivity to signals can be maximized, which will be shown in Fig. 7.4(b)(c).

7.3 Optimization and Definition of SRs

Fig. 7.3(a) shows the lepton charge/flavor combination for the signals and backgrounds. Events with more than one SFOS lepton pair are filled in SFOS bin. Events with zero SFOS pair and more than one different-flavor opposite-sign (DFOS) lepton pair are in DFOS bin and events with same-sign three leptons are filled in SS bin. Nearly 90% of the signal falls into the SFOS bin, and SS lepton combination have a significantly large signal-to-background ratio compared to other

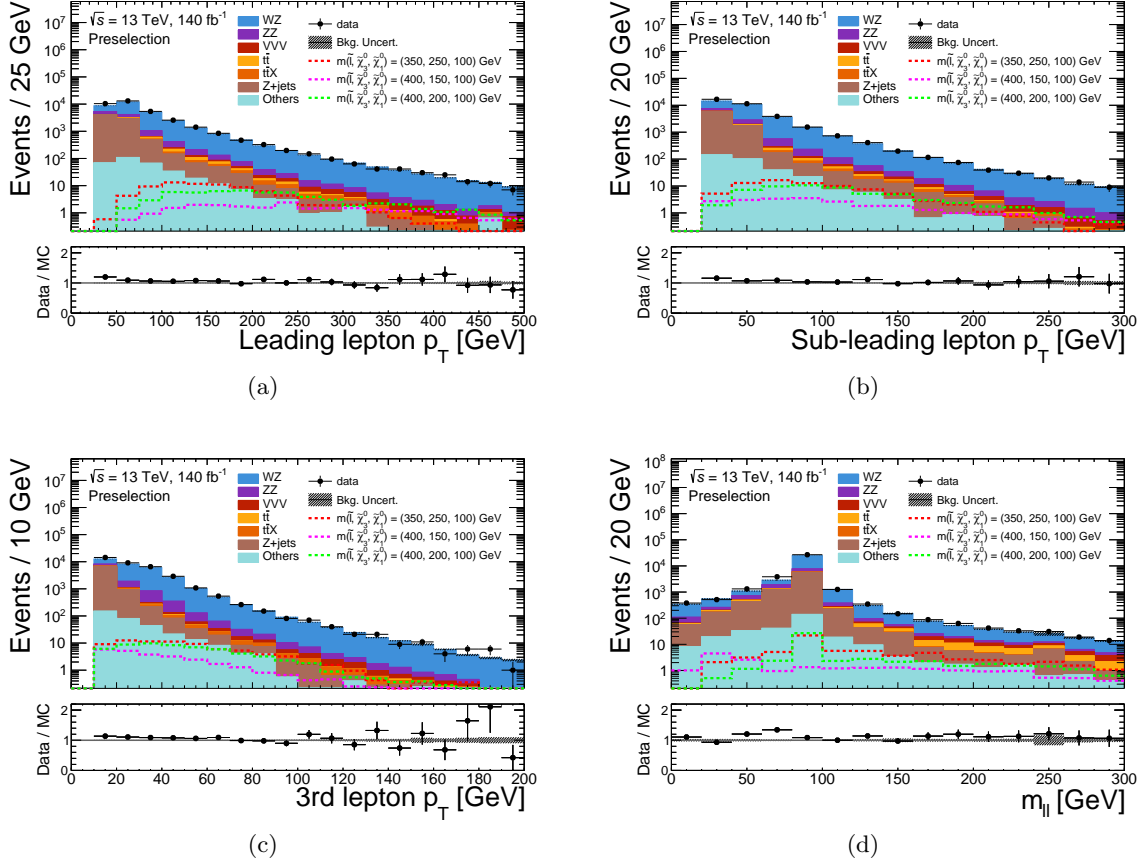


Figure 7.2: Kinematic distribution after the preselection (Table 7.1). The dashed line illustrates signal simulation samples with different masses. The hatched band includes the MC statistical uncertainties. The bottom panel shows the ratio of the observed data and background yield estimated directly from simulation samples.

lepton charge/ flavor combinations. Number of signal events with DFOS pair is similar to that of SS combination, while background level is ~ 100 times larger compared to SS combination. From these observations, we decided to use the SFOS and SS lepton combination as SRs. On the other hand, Fig. 7.3(b) shows the $n_{b\text{-jets}}$ distribution. To reduce the top contribution, $n_{b\text{-jets}} = 0$ selection is imposed to all SRs.

Two types of SRs, SR_{OS} and SR_{SS} are defined. The SRs are designed to optimize the sig-

Table 7.1: Event preselection applied to all events for SRs.

Variables	Preselection
Trigger	single-lepton
$n_{\text{lep}}^{\text{baseline}}, n_{\text{lep}}^{\text{signal}}$	$= 3$
$p_T^{\ell_1}, p_T^{\ell_2}, p_T^{\ell_3}$ [GeV]	$> 28, 20, 10$
$n_{b\text{-jets}}$	$= 0$

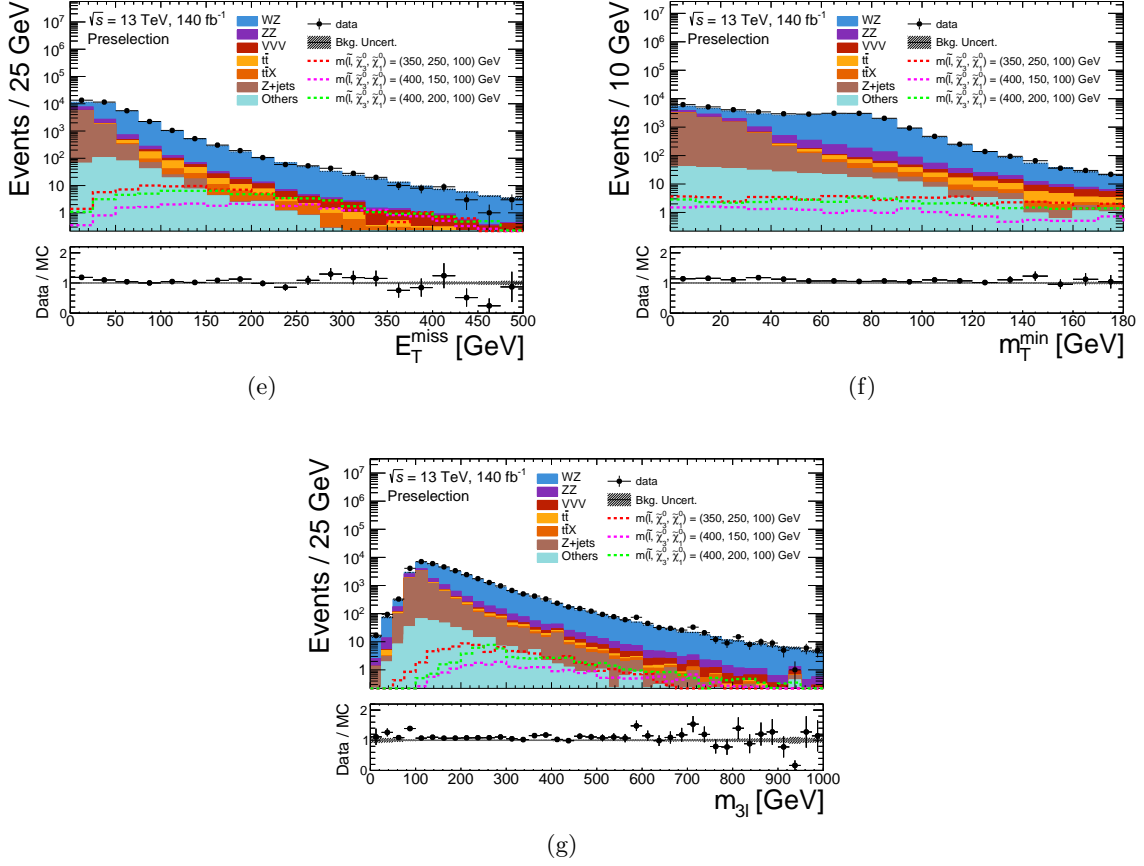


Figure 7.2: Kinematic distribution after the preselection (Table 7.1). The dashed line illustrates signal simulation samples with different masses. The hatched band includes the MC statistical uncertainties. The bottom panel shows the ratio of the observed data and background yield estimated directly from simulation samples. (cont.)

nificance (Z) while assigning a total uncertainty of 30% to the background yields. This level of background uncertainty is reasonable based on the systematic uncertainty estimation which will be outlined in Chapter 9. The significance (Z) is defined as Ref. [221],

$$Z = \sqrt{2 \left(n \ln \left[\frac{n(b + \sigma^2)}{b^2 + n\sigma^2} \right] - \frac{b^2}{\sigma^2} \ln \left[1 + \frac{\sigma^2(n - b)}{b(b + \sigma^2)} \right] \right)}, \quad (7.2)$$

where b is the number of expected background events with uncertainty σ and n is the number of signal events plus the number of background events.

On top of the preselection (Table 7.1), SR0S requires to have at least one SFOS lepton pair. Further cuts are applied to define the regions enriched with signals compared to the SM backgrounds. The E_T^{miss} cut is useful to reduce $Z + \text{jets}$ background, which have no real E_T^{miss} owing to neutrinos, and WZ background which tends to have small E_T^{miss} since both bosons must decay leptonically in a three lepton final state. The E_T^{miss} distribution is shown in Fig. 7.4(a). A lower E_T^{miss} cut of 150 GeV is applied in SR0S. Transverse mass m_T^{min} is also used to reduce WZ background. A comparison between the usual m_T calculated by using the lepton left over from the Z boson and m_T^{min} is shown in Fig. 7.4(b)(c). It can be seen that the m_T has a broader tail compared to m_T^{min} in WZ . Because of the downward shift in background which is not present

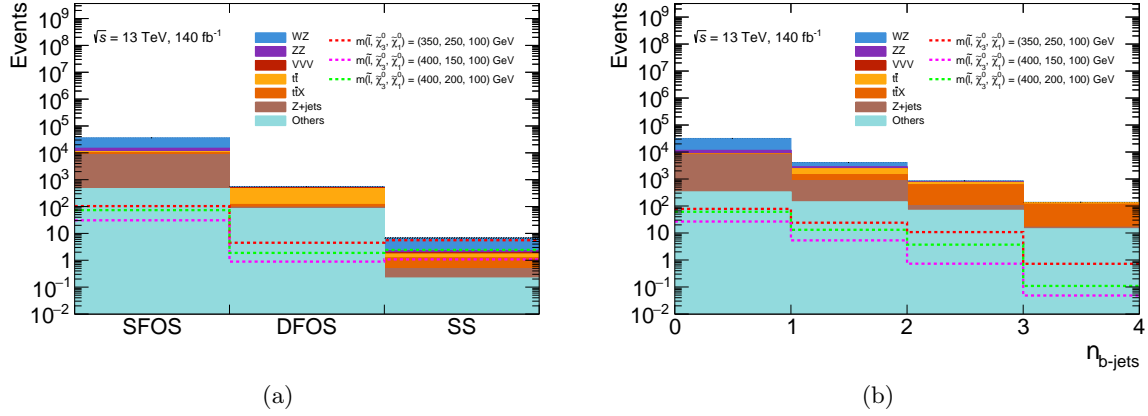


Figure 7.3: (a) Lepton charge/ flavor combination in three lepton final state. Events with more than one same-flavor opposite-sign (SFOS) lepton pair are in SFOS bin. Events with zero SFOS pair and more than one different-flavor opposite-sign (DFOS) lepton pair are in DFOS bin and events with three lepton same-sign are in SS bin. (b) $n_{b\text{-jets}}$ distribution in three lepton final state. The dashed line illustrates signal simulation samples with different masses. The hatched band includes the MC statistical uncertainties. The bottom panel shows the ratio of the observed data and background yield estimated directly from simulation samples.

Table 7.2: Summary of selections for SR definition. The merged cells indicate the common selections being applied across the regions in the same row. “—” indicates the absence of the requirement on the variable specified in the row. The number of same-flavor opposite-charge-sign (SFOS) and different-flavor opposite-charge-sign (DFOS) lepton pairs are represented by n_{SFOS} and n_{DFOS} respectively. If more than one SFOS lepton pairs are present in the event, the invariant mass closest to 91.2 GeV is quoted for $m_{\ell\ell}$.

	SROS-on				SROS-off				SRSS		
Variables	eee	$ee\mu$	$e\mu\mu$	$\mu\mu\mu$	eee	$ee\mu$	$e\mu\mu$	$\mu\mu\mu$	eee	$ee\mu$	2μ ($e\mu\mu + \mu\mu\mu$)
Trigger	single-lepton										
$n_{\text{lep}}^{\text{baseline}}, n_{\text{lep}}^{\text{signal}}$	$= 3$										
$p_{\text{T}}^{\ell_1}, p_{\text{T}}^{\ell_2}, p_{\text{T}}^{\ell_3}$ [GeV]	$> 28, 20, 10$										
$n_{b\text{-jets}}$	$= 0$										
n_{SFOS}	≥ 1				≥ 1				$= 0$		
n_{DFOS}	$-$				$-$				$= 0$		
$m_{\ell\ell}$ [GeV]	$\in [81.2, 101.2]$				$\notin [81.2, 101.2]$				$-$		
$m_{\text{T}}^{\text{min}}$ [GeV]	> 125				> 125				$-$		
$E_{\text{T}}^{\text{miss}}$ [GeV]	> 150				> 150				> 50		
$m_{3\ell}$ binning [GeV] ^a	$\mathbf{a} : \in [30, 200)$ $\mathbf{b} : \in [200, 400)$ $\mathbf{c} : \in [400, +\infty)$								$-$		

^a The $m_{3\ell}$ binning applies separately to each flavor channel of SROS.

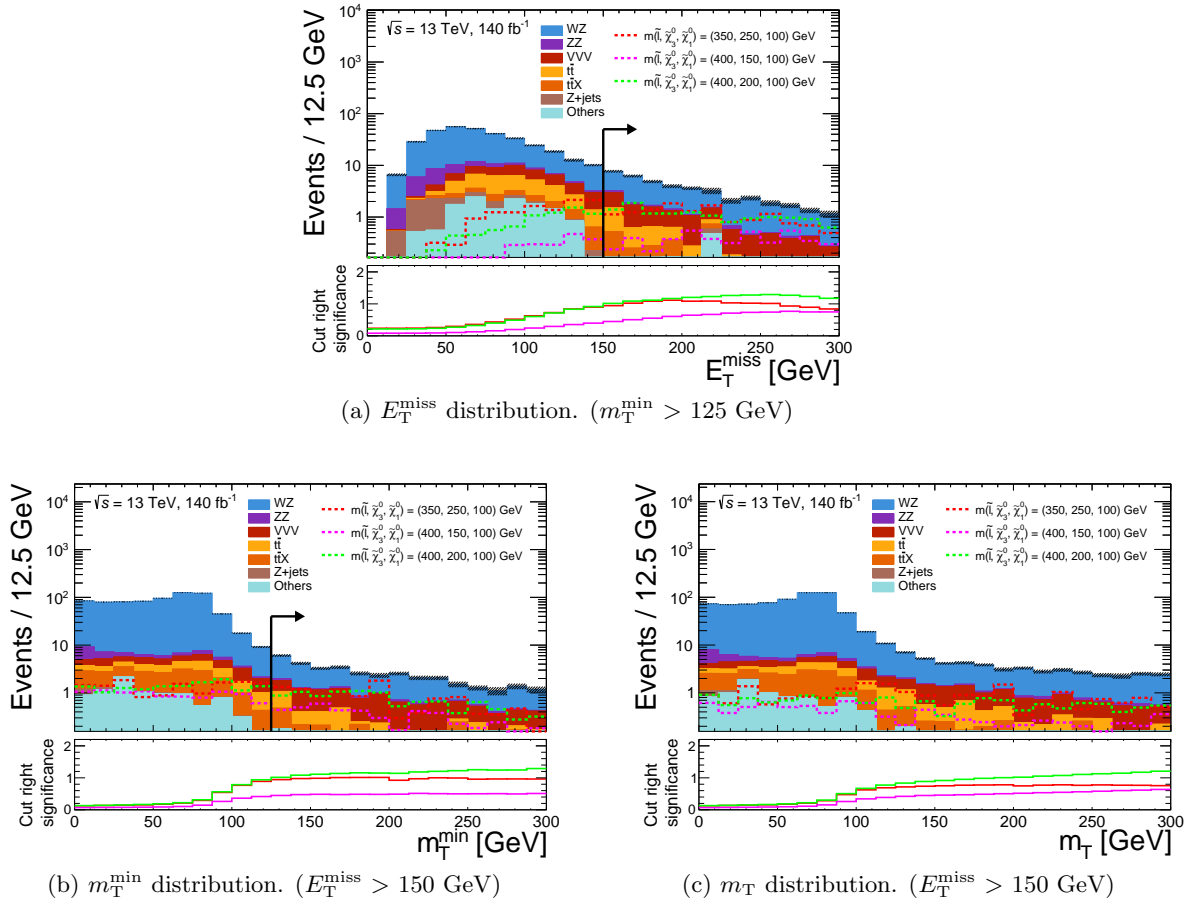


Figure 7.4: E_T^{miss} , m_T^{min} and m_T distributions for SROS. Each plot is drawn without applying selections to the variable illustrated. The dashed line illustrates signal simulation samples with different masses. The hatched band includes the MC statistical uncertainties. The bottom panel shows the significance (Z) calculated by accumulating the yields of the bins on the right side. A total uncertainty of 30% is assumed for background yields.

in signal, m_T^{min} performs better as a discriminating variable than m_T . A lower m_T^{min} cut of 125 GeV is applied in SROS.

SROS is divided into two regions, **SROS-on** and **SROS-off**, based on the invariant mass of the SFOS lepton pair ($m_{\ell\ell}$). In case of more than one SFOS pair, the pair with $m_{\ell\ell}$ closest to the mass of the Z boson is used. **SROS-on** requires $m_{\ell\ell}$ to be consistent with Z boson mass : $\in [81.2, 101.2] \text{ GeV}$ and **SROS-off** to be outside the Z boson mass window : $\notin [81.2, 101.2] \text{ GeV}$.

SROS-on and **SROS-off** are further binned by the triplepton invariant mass ($m_{3\ell}$). As shown in Fig. 7.5, targeted signals exhibit a characteristic peak structure in $m_{3\ell}$ distribution. The position of cut-off in the $m_{3\ell}$ distribution corresponds to the mass splitting of the $\tilde{\ell}_L$ and $\tilde{\chi}_1^0$, reflecting the events with the three leptons originating from the same side of the decay chain. By binning into three regions, $m_{3\ell} \in [30, 200), \in [200, 400), \in [400, \infty) \text{ GeV}$, we achieve a higher sensitivity compared to the inclusive SR, and it also helps us to determine the detailed SUSY mass hierarchy if some deviation from the SM is found. Each $m_{3\ell}$ bin is denoted by the suffix, **a**, **b**, and **c**. Finally, SROS is further divided into four separate flavor channels, eee , $ee\mu$, $e\mu\mu$, $\mu\mu\mu$ ⁸ to maximize the analysis power, resulting in a total of 24 ($= 2 \times 3 \times 4$) SR bins. Table 7.2

⁸This name only describes lepton flavor combination and does not imply p_T order of leptons.

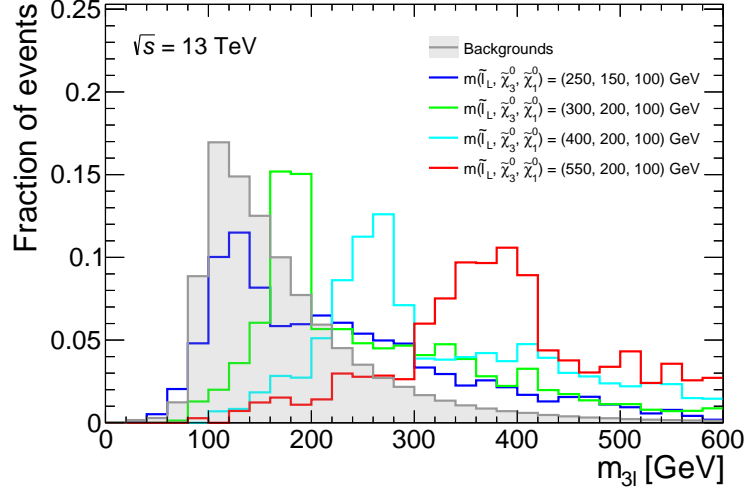


Figure 7.5: Distributions of $m_{3\ell}$ showing the expected SM background as well as signals with various masses, for a selection of exactly three baseline and signal leptons and one or more SFOS lepton pairs. The distributions are normalized to unity. Signals demonstrate a cut-off matching the mass splitting of the $\tilde{\ell}_L$ and $\tilde{\chi}_1^0$, while backgrounds do not. The dominant background in this selection is WZ , with a smooth falling distribution.

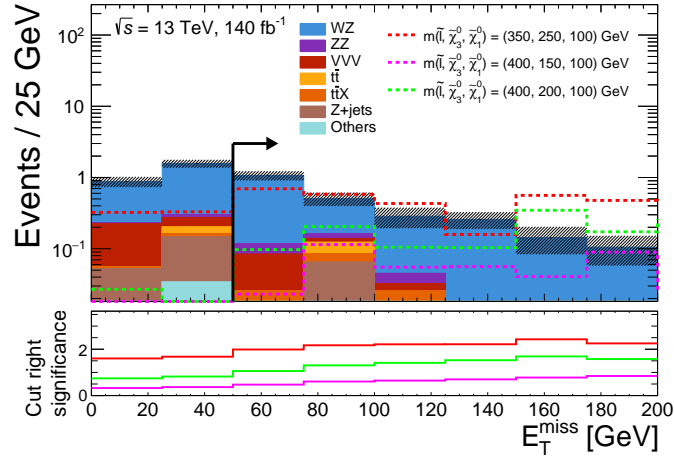


Figure 7.6: E_T^{miss} distribution for SRSS. Plot is drawn without applying the E_T^{miss} selection. The dashed line illustrates signal simulation samples with different masses. The hatched band includes the MC statistical uncertainties. The bottom panel shows the significance (Z) calculated by accumulating the yields of the bins on the right side. A total uncertainty of 30% is assumed for background yields.

summarizes the definition of SROS.

On the other hand, on top of the preselection (Table 7.1), SRSS requires all three leptons to have the same charge. There are very few SM backgrounds which give rise to final states with three same-sign leptons, and only full-leptonically decaying tri-boson (WZZ, ZZZ) remains as an irreducible background. A loose E_T^{miss} cut, $E_T^{\text{miss}} > 50$ GeV, is also applied to reduce the main WZ background while maintaining the number of signals, which E_T^{miss} distribution is

shown in Fig. 7.6. The WZ background contaminates SRSS when the sign of one electron from the Z boson decay is mis-identified. This is called as the *charge-flip* background and the details will be described in Section 8.3. Small E_T^{miss} is expected in WZ since both bosons must decay leptonically in a three lepton final state, while targeted signals have real missing energy from the escaping neutralinos.

In addition, this search is carried out independently in the three separate flavor channels: eee (SRSS- eee), $ee\mu$ (SRSS- $ee\mu$), $e\mu\mu + \mu\mu\mu$ (SRSS- 2μ).⁸ The $e\mu\mu$ and $\mu\mu\mu$ channels are merged due to extremely low background level and difficulty in the background estimation in the $\mu\mu\mu$ channel. This choice has been driven by the different SM background composition which is expected depending of the flavors of the leptons in the final state. Moreover, higher sensitivity is expected for the targeted signal by statistically combining the results in each independent flavor channel. The definition of SRSS is also summarized in Table 7.2.

In this analysis, only the number of events in each SR bin is used to extract the signal, i.e., no shape fit is used. The method for signal extraction will be further discussed in Section 10.1.

7.4 Signal composition in SRs

Signal have several production modes and decay modes. Figures 7.7 and 7.8 show into which SR the signals fall for each production mode and decay mode. Fig. 7.7 is for signal mass $m(\tilde{\ell}_L^\pm, \tilde{\chi}_3^0, \tilde{\chi}_1^0) = (300, 200, 100)$ GeV where the $\tilde{\chi}_3^0 \rightarrow h\tilde{\chi}_1^0$ decay is not allowed, and Fig. 7.8 is for $m(\tilde{\ell}_L^\pm, \tilde{\chi}_3^0, \tilde{\chi}_1^0) = (400, 250, 100)$ GeV where the $\tilde{\chi}_3^0 \rightarrow h\tilde{\chi}_1^0$ decay is allowed. It can be seen that signals in SROS-on are mainly by $\tilde{\ell}_L^\pm \tilde{\nu}$ production with at least one leptonically decaying Z boson which typical feynman diagram is shown in Fig. 7.9(a). SROS-off are dominated by $\tilde{\ell}_L^+ \tilde{\ell}_L^-$ production with at least one leptonically decaying W boson decay as shown in Fig. 7.9(b). Finally, signals in SRSS are mainly by $\tilde{\ell}_L^\pm \tilde{\nu}$ production and decay with same-sign $W^\pm W^\pm$ pair which diagram is shown in Fig. 7.9(c).

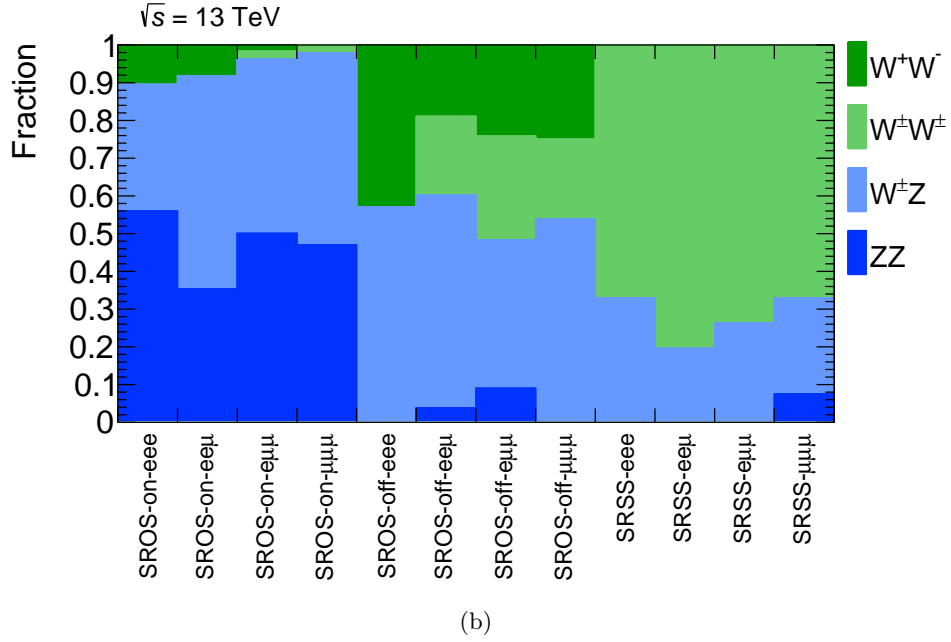
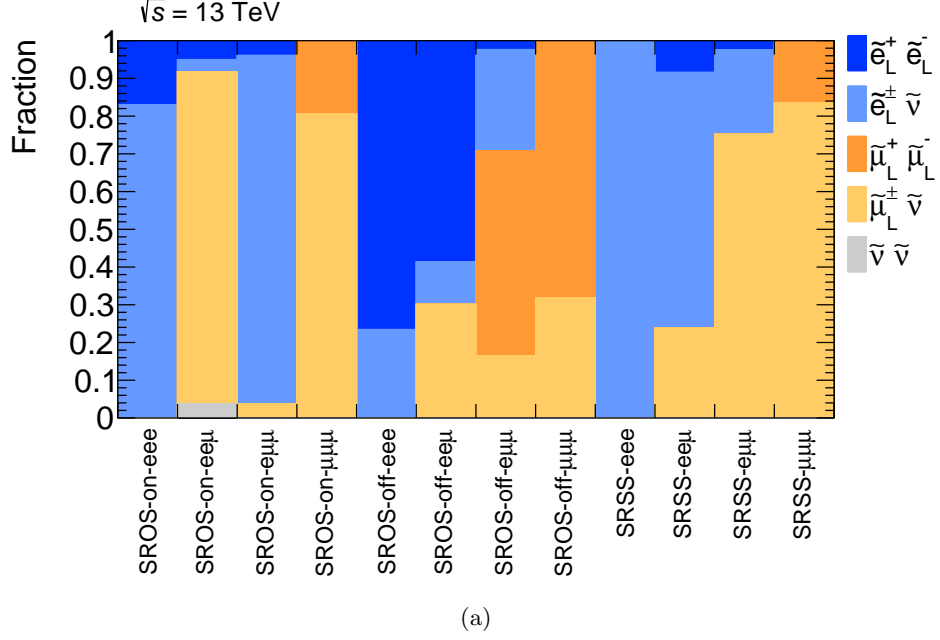


Figure 7.7: Signal composition in terms of (a) production mode and (b) $\tilde{\chi}_3^0$ decay mode in each SR. Signal mass is $m(\tilde{\ell}_L^\pm, \tilde{\chi}_3^0, \tilde{\chi}_1^0) = (300, 200, 100) \text{ GeV}$. The $m_{3\ell}$ bins are merged and **SRSS-2μ** is divided into **SRSS-eμμ** and **SRSS-μμμ** for illustration. $\tilde{\chi}_3^0 \rightarrow h\tilde{\chi}_1^0$ is not allowed in this $\tilde{\chi}_3^0 - \tilde{\chi}_1^0$ mass splitting.

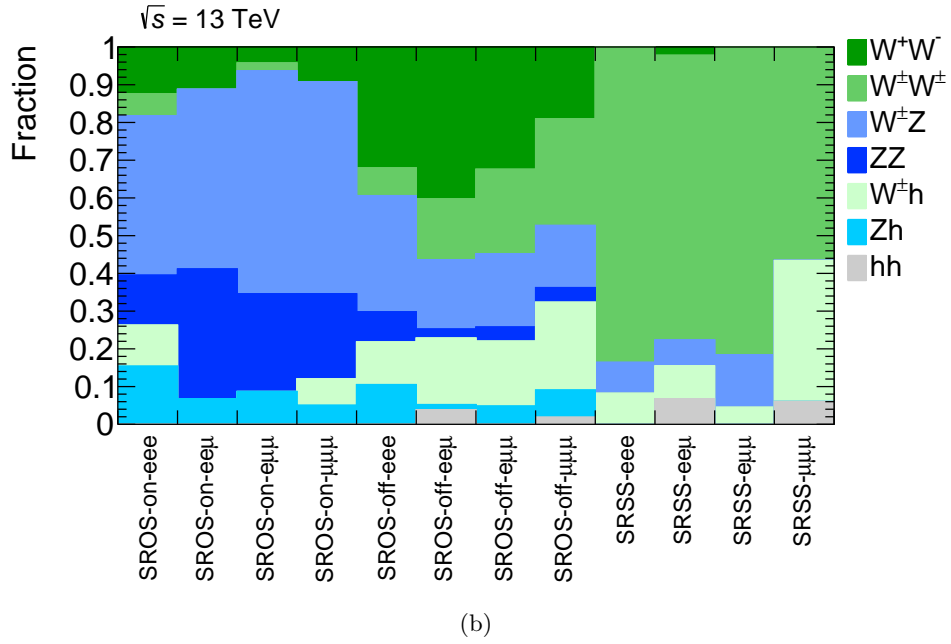
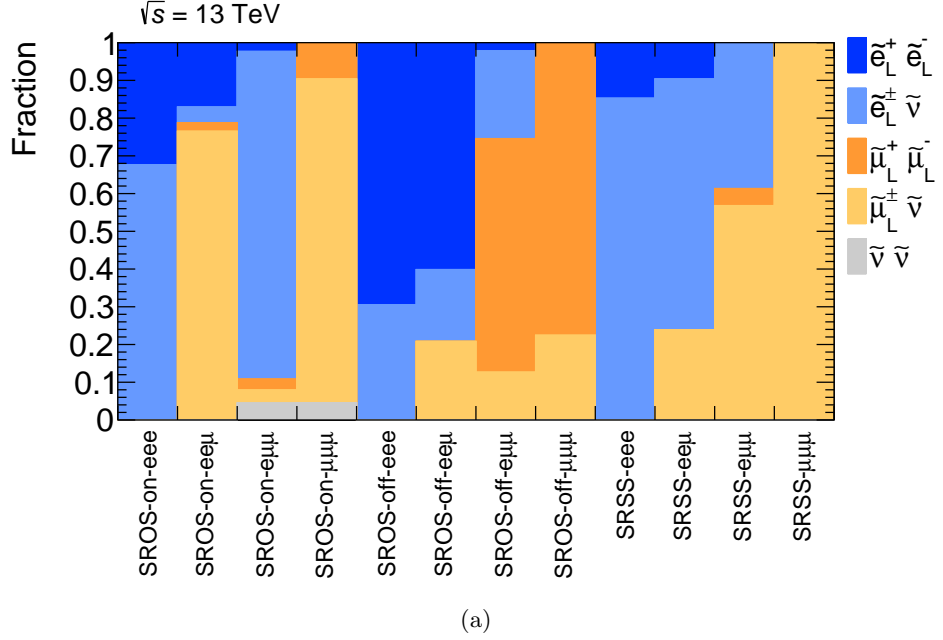


Figure 7.8: Signal composition in terms of (a) production mode and (b) $\tilde{\chi}_3^0$ decay mode in each SR. Signal mass is $m(\tilde{\ell}_L^\pm, \tilde{\chi}_3^0, \tilde{\chi}_1^0) = (400, 250, 100) \text{ GeV}$. The $m_{3\ell}$ bins are merged and **SRSS-2μ** is divided into **SRSS-eμμ** and **SRSS-μμμ** for illustration. $\tilde{\chi}_3^0 \rightarrow h\tilde{\chi}_1^0$ is allowed in this $\tilde{\chi}_3^0 - \tilde{\chi}_1^0$ mass splitting.

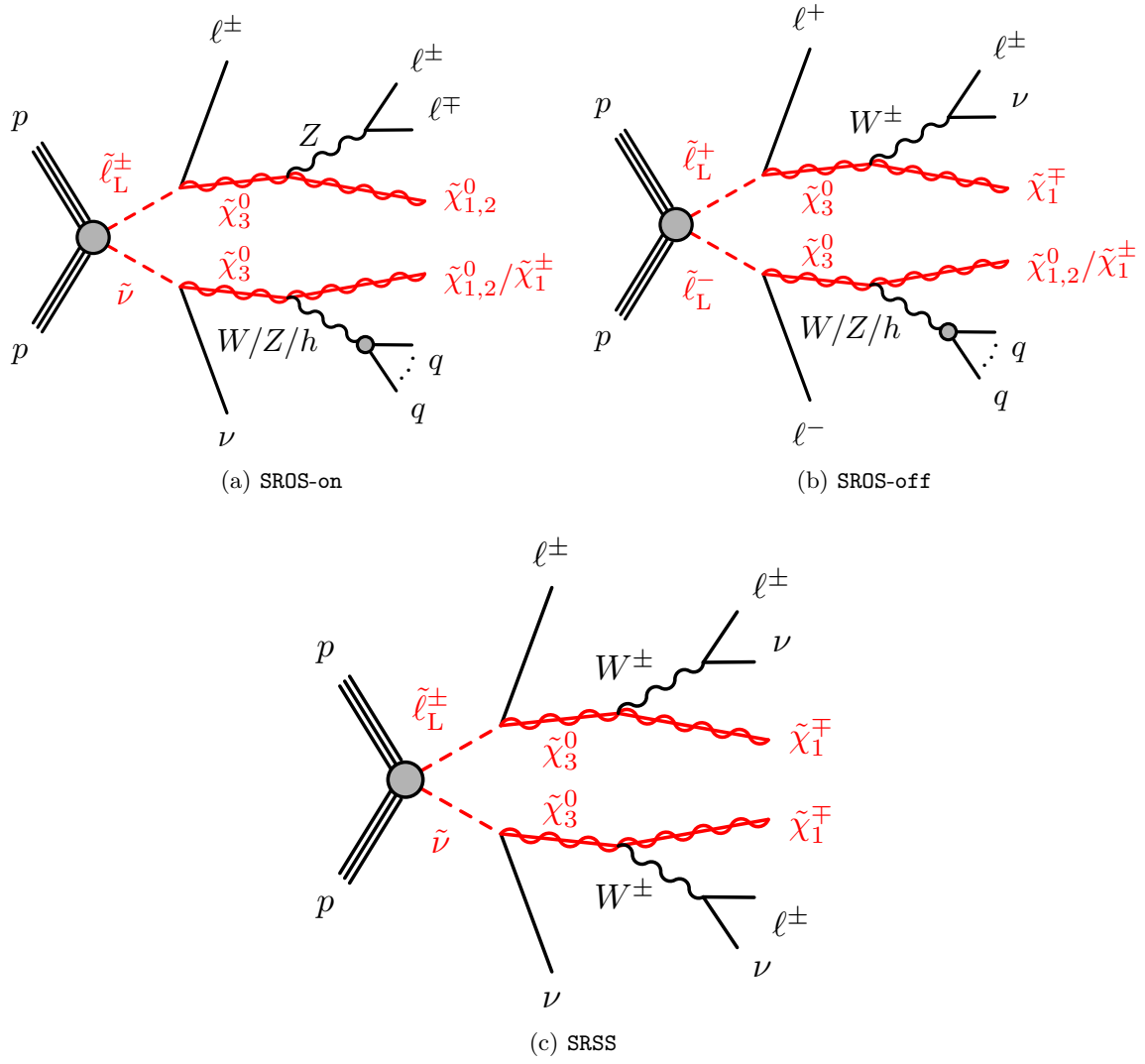


Figure 7.9: Representative feynman diagram in each SR. The decays of $\tilde{\chi}_2^0$ and $\tilde{\chi}_1^\pm$ are ignored as they only result in low-momentum particles that are almost never reconstructed.

Chapter 8

Background Estimation

This chapter outlines the strategy used to estimate the yields of background processes that mainly contribute to the SRs, followed by the strategy to validate this estimation approach. The regions defined to constrain the background yields are called control regions (CRs), while the regions for validation are called validation regions (VRs).

Section 8.1 provides an overview of the main backgrounds and briefly describes the estimation methods. Details of the estimation strategy for each background are described in Sections 8.2, 8.3, and 8.4. Finally, Section 8.5 summarizes the consistency between data and the estimation in VRs defined for each background estimation procedure.

8.1 Background Breakdown in the Signal Regions

The breakdown of physics processes in the SRs, estimated directly from the MC simulation samples, is shown in Fig. 8.1. Backgrounds with one or more fake/non-prompt leptons which do not originate from the hard scattering process are classified as “Fakes”. “Charge-flip” stands for the backgrounds which contain one or more charge-flipped leptons. Top-like backgrounds ($t\bar{t}$ and single-top) is not included in “Fakes” category even if it includes fake/non-prompt leptons in the event, because of the independent estimation method. The “Others” category includes contributions from W +jets, Z +jets, di-boson (excluding full-leptonic $W^\pm Z$ and ZZ), and Higgs processes. The main background consists of $W^\pm Z \rightarrow \ell^\pm \nu \ell^\pm \ell^\mp$, tri-boson and $t\bar{t}$ in SR0S and charge-flip, fake backgrounds in SRSS.

Estimation strategy for each background is briefly summarized below.

WZ background in SR0S: estimated by semi data-driven method

$W^\pm Z \rightarrow \ell^\pm \nu \ell^\pm \ell^\mp$ is a significant background process that contaminate the SR0S. The method used to estimate WZ follows a semi data-driven approach, where expected yields are estimated from MC simulation that is normalized to data in a dedicated CR, which detail will be described in Section 8.2. This approach relies on the fact that WZ is produced via EW processes which can be accurately simulated using MC simulations.

Charge-flip background in SRSS: estimated by semi data-driven method

Charge-flip background is the main background in SRSS- eee and SRSS- $ee\mu$. The charge-flip events are mainly caused by the emission of a bremsstrahlung photon which through interaction with detector material converts into a pair of secondary electron tracks. When one of those tracks happens to better match the position of the calorimeter cluster than the original electron track, which has a charge opposite to that of the prompt electron, it can mimic the signal event. The charge-flip contribution coming from muons is negligible

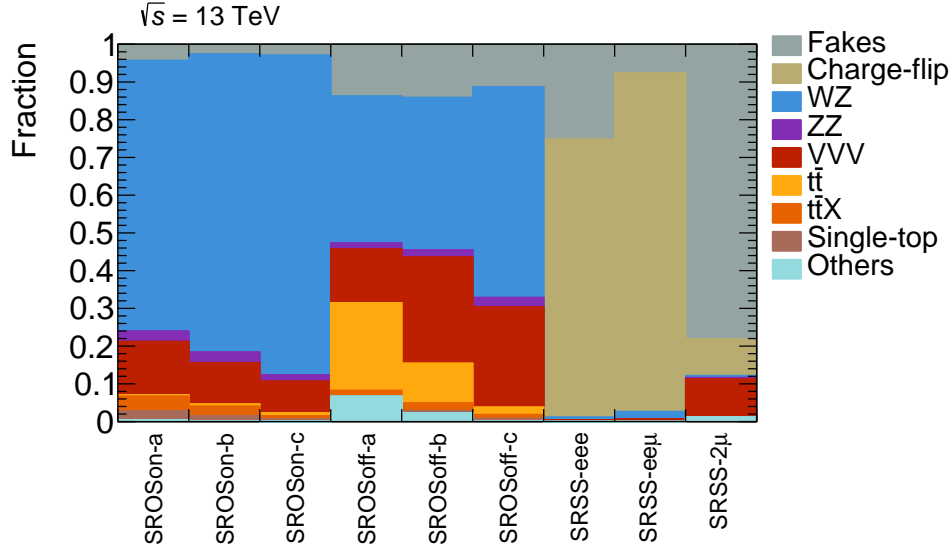


Figure 8.1: Background composition in terms of physics processes in each SR. Backgrounds with one or more fake/non-prompt leptons which do not originate from the hard scattering processes are classified as “Fakes”. “Charge-flip” stands for the backgrounds which contain one or more charge-flipped leptons. Top-like backgrounds ($t\bar{t}$ and single-top) is not included in “Fakes” category in SROS even if it includes fake/non-prompt leptons in the event, because of the independent estimation method. The “Others” category includes contributions from W +jets, Z +jets, di-boson (excluding full-leptonic $W^\pm Z$ and ZZ), and Higgs processes.

due to the overwhelmingly small probability of emitting a bremsstrahlung photon. The contributions of the charge-flip events are evaluated by reweighting the MC simulations using the scale factors obtained from $Z \rightarrow ee$ data. Detail of the methodology will be described in Section 8.3.

Fake background in both SROS and SRSS: estimated by data-driven method

Fake background which contain fake/non-prompt leptons which do not originate from the hard scattering processes contaminates all SRs. Fake and non-prompt leptons arise when a light flavor jet is improperly identified as a lepton, when a heavy flavor hadron decays semi-leptonically, or when a photon converts into a pair of leptons. While heavy flavor decays and photon conversions actually result in a non-prompt but real lepton, we will collectively refer to all of these as “fake” leptons for simplicity. It is normally challenging to accurately model these events as there are many sources of fake lepton processes, each of which is kinematically different and provides a relative contribution to the background estimate that is dependent on the analysis phase-space. A data-driven “Fake Factor” method [222, 223] is used to estimate the fake background, which will be described in Section 8.4.

Top-like backgrounds ($t\bar{t}$, single-top) in SROS: estimated directly by simulation

Top events with three leptons also include fake leptons which come predominantly from b -jets originating from the decay of top quarks, which have a small theory uncertainty. Though events typically involves one fake lepton, the $t\bar{t}$ and single-top backgrounds are exceptionally estimated using the MC simulation since the MC modeling is found to be reasonable, which will be further discussed in Section 8.4.6.

Other backgrounds : estimated directly by simulation

Other backgrounds are directly estimated from MC simulations. Though almost all of them are minor backgrounds, tri-boson backgrounds is the second or third leading background in **SR0S**. Since dedicated CRs or VRs for tri-boson processes is extremely hard to define, tri-boson processes are directly estimated from MC simulations, and instead the cross-section uncertainty is handled carefully (Section 9.1). There is some contribution from WZ and ZZ in **SRSS** as seen in Fig. 8.1. These backgrounds do not yield a final state of same-sign three-lepton at tree-level, but fall into **SRSS** when associated with a final state radiation (FSR) photon which converts into e^+e^- pair. Since these electrons have all the qualities of isolated electrons and the contribution to **SRSS** is minor, these backgrounds are directly estimated by MC simulations.

8.2 Semi Data-driven Background Estimation for WZ

In this analysis, the $W^\pm Z \rightarrow \ell^\pm \nu \ell^\pm \ell^\mp$ process is main background in **SR0S**. Backgrounds originating from WZ are effectively constrained in CR that are kinematically close to **SR0S**. Normalization Factor (NF) for WZ is measured in CR, defined as

$$\text{NF} = \frac{N_{\text{Data}} - N_{\text{non-}WZ \text{ MC}}}{N_{WZ \text{ MC}}}, \quad (8.1)$$

where N_{Data} and $N_{WZ \text{ MC}}$ represent the observed data and the expected yield for WZ in CR, respectively. $N_{\text{non-}WZ \text{ MC}}$ represents the total expected yield from non- WZ backgrounds, including the signal process. The measured NF is applied to the yields of WZ in SRs and VRs estimated from MC simulation in order to obtain the expected yields.

8.2.1 Control Regions and Validation Regions

As discussed in Section 7.3, the **SR0S** is defined in the $m_T^{\min} > 125$ GeV and $E_T^{\text{miss}} > 150$ GeV region. By lowering the m_T^{\min} selection to $40 \leq m_T^{\min} < 80$ GeV, we can obtain a region where WZ dominates while signal contamination is low. This CR is denoted as **CRWZ**. The purity of WZ in **CRWZ** is 94% and the signal contamination in this region does not exceed 3.2%. Extrapolation along m_T^{\min} is motivated by good modeling of m_T^{\min} as shown in Fig. 8.2.

To ensure that the NF obtained in the **CRWZ** can be used in the **SR0S** which is defined in high- m_T^{\min} range, we have defined several VRs which are summarized in Fig. 8.3. These VRs have been defined by relaxing the m_T^{\min} requirement to a medium- m_T^{\min} range ($80 \leq m_T^{\min} < 125$ GeV) or a low- E_T^{miss} range ($80 \leq E_T^{\text{miss}} < 150$ GeV in SFOS on-shell region and $20 \leq E_T^{\text{miss}} < 150$ GeV in SFOS off-shell region). To suppress signal contamination in VRs, the E_T^{miss} range is adjusted in SFOS off-shell region and $n_{\text{jet}} = 0$ cut is additionally imposed in low- E_T^{miss} region VRs. Signal contamination in VRs does not exceed 12% of total background for un-excluded scenarios. The VRs in SFOS on-shell (off-shell) region with medium- m_T^{\min} range and low- E_T^{miss} range are denoted as **VRWZ-on- m_T^{\min}** (**VRWZ-off- m_T^{\min}**) and **VRWZ-on- E_T^{miss}** (**VRWZ-off- E_T^{miss}**) respectively. To summarize, the definition of the CR and VRs for the normalization of WZ is provided in Table 8.1.

8.2.2 Fit Result for WZ normalization

The NF is determined by a background-only fit on the **CRWZ**. During the fit, the NF and all nuisance parameters characterizing statistical and systematic uncertainties are allowed to float. The details of the systematic uncertainties and the statistical procedure will be described in Chapter 9 and Section 10.1. The NF of the WZ is derived to be 1.07 ± 0.06 assuming no signal

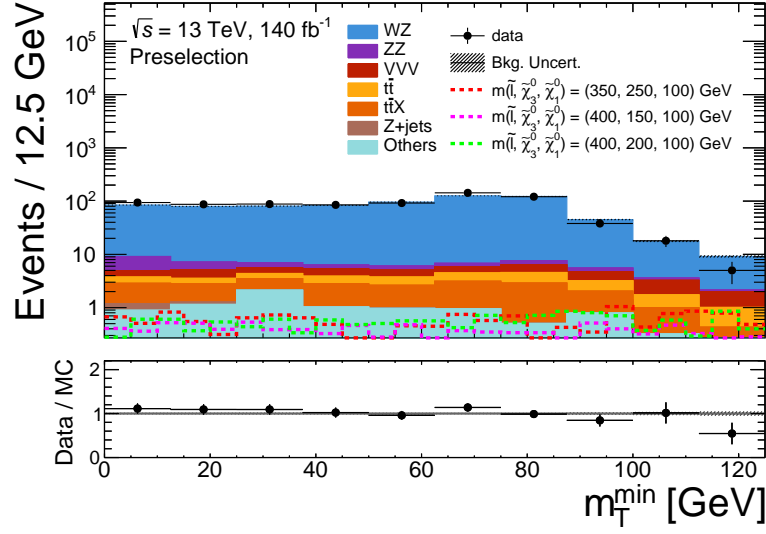


Figure 8.2: Distribution of m_T^{\min} in the SFOS region with $E_T^{\text{miss}} > 150$ GeV cut. Only $m_T^{\min} < 125$ GeV is shown because the SRoS is defined in $m_T^{\min} > 125$ GeV. The dashed line illustrates signal simulation samples with different masses. The hatched band includes the MC statistical uncertainties. The bottom panel shows the ratio of the observed data and background yield estimated directly from simulation samples.

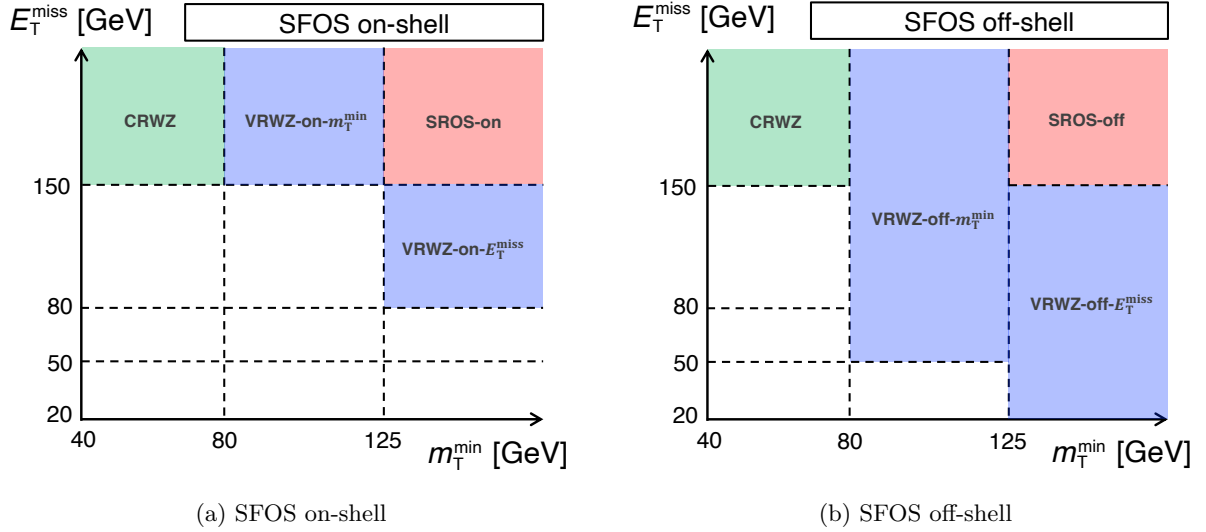


Figure 8.3: Schematic views of region definition for WZ background estimation. The red, green, and blue areas show the SRs, CR, and VRs used for the estimation of WZ . A single NF is constrained by the CR in the low m_T^{\min} range. The NF is extrapolated to the high m_T^{\min} range and multiplied to the WZ yields in the SRs. The VRs to validate the extrapolation of the NF are defined in the medium- m_T^{\min} and low- E_T^{miss} range. (a) “SFOS on-shell” stands for the region with one or more SFOS lepton pairs in the event which have an invariant mass consistent with the Z boson mass. (b) “SFOS off-shell” stands for the region with one or more SFOS lepton pairs in the event with none of them having an invariant mass consistent with the Z boson mass.

Table 8.1: Summary of the selection criteria for the CR and VRs for WZ , for the **SROS-on** and **SROS-off** selection. The merged cells indicate the common selections being applied across the regions in the same row. “–” indicates the absence of the requirement on the variable specified in the row. The number of same-flavor opposite-charge-sign (SFOS) is represented by n_{SFOS} . If more than one SFOS lepton pairs are present in the event, the invariant mass closest to 91.2 GeV is quoted for $m_{\ell\ell}$.

Variables	CRWZ	VRWZ-on- m_T^{\min}	VRWZ-on- E_T^{miss}	VRWZ-off- m_T^{\min}	VRWZ-off- E_T^{miss}
Trigger	single-lepton				
$n_{\text{lep}}^{\text{baseline}}, n_{\text{lep}}^{\text{signal}}$	$= 3$				
$p_T^{\ell_1}, p_T^{\ell_2}, p_T^{\ell_3}$ [GeV]	$> 28, 20, 10$				
$n_{b\text{-jets}}$	$= 0$				
n_{SFOS}	≥ 1				
$m_{\ell\ell}$ [GeV]	–	$\in [81.2, 101.2]$		$\notin [81.2, 101.2]$	
m_T^{\min} [GeV]	$\in [40, 80)$	$\in [80, 125)$	$\in [125, +\infty)$	$\in [80, 125)$	$\in [125, +\infty)$
E_T^{miss} [GeV]	$\in [150, +\infty)$	$\in [150, +\infty)$	$\in [80, 150)$	$\in [50, +\infty)$	$\in [20, 150)$
n_{jets}	–	–	$= 0$	–	$= 0$
$m_{3\ell}$ binning [GeV]	–	$\mathbf{a} : \in [30, 200)$ $\mathbf{b} : \in [200, 400)$ $\mathbf{c} : \in [400, +\infty)$			
WZ purity	94%	93%	80%	87%	54%

Table 8.2: Observed data and estimated yields using results from the background-only fit in the **CRWZ**. The uncertainties include both statistical and systematic uncertainties which will be discussed in Chapter 9.

Region	CRWZ
Observed	356
Fitted SM events	356 ± 19
WZ	335 ± 19
ZZ	2.8 ± 0.6
VVV	4.0 ± 1.5
$t\bar{t}$	4.1 ± 1.4
$t\bar{t}X$	6.6 ± 1.2
Fakes	$0.1 \pm \begin{smallmatrix} 2.6 \\ 0.1 \end{smallmatrix}$
Others	2.8 ± 1.6

contamination. The yields in the VRs are estimated by multiplying the derived NF by the yields of WZ obtained from MC simulation samples. Estimated yield in **CRWZ** is summarized in Table 8.2. The estimated yields and post-fit distributions in each VR are summarized in Tables 8.3-8.4 and Fig. 8.4. The observed data are in good agreement with the estimated numbers and distributions in all VRs.

Table 8.3: Observed data and estimated yields using results from the background-only fit in VRWZ-on- m_T^{\min} and VRWZ-off- m_T^{\min} . The uncertainties include both statistical and systematic uncertainties which will be discussed in Chapter 9.

Region	VRWZ-on- m_T^{\min} -a	VRWZ-on- m_T^{\min} -b	VRWZ-on- m_T^{\min} -c
Observed	51	37	16
Fitted SM events	57 ± 5	42.8 ± 3.1	15.9 ± 1.3
WZ	52 ± 5	40.0 ± 3.0	15.0 ± 1.3
ZZ	0.89 ± 0.21	0.52 ± 0.28	0.12 ± 0.05
VVV	0.9 ± 0.5	0.7 ± 0.4	0.23 ± 0.15
$t\bar{t}$	$0.4 \pm_{0.4}^{0.5}$	0.11 ± 0.11	$0.03 \pm_{0.03}^{0.04}$
$t\bar{t}X$	1.40 ± 0.27	1.18 ± 0.26	0.37 ± 0.11
Fakes	0.9 ± 0.8	$0.00 \pm_{0.00}^{0.25}$	$0.10 \pm_{0.10}^{0.16}$
Others	0.032 ± 0.011	$0.24 \pm_{0.24}^{0.26}$	< 0.004

Region	VRWZ-off- m_T^{\min} -a	VRWZ-off- m_T^{\min} -b	VRWZ-off- m_T^{\min} -c
Observed	263	106	36
Fitted SM events	264 ± 19	132 ± 10	35.0 ± 2.7
WZ	205 ± 16	108 ± 9	29.9 ± 2.5
ZZ	8.1 ± 1.6	2.9 ± 0.6	0.72 ± 0.17
VVV	7.6 ± 3.1	7.3 ± 3.0	2.8 ± 1.2
$t\bar{t}$	22 ± 6	5.5 ± 1.6	0.46 ± 0.31
$t\bar{t}X$	2.9 ± 0.6	2.4 ± 0.5	0.73 ± 0.18
Fakes	4.9 ± 3.1	2.3 ± 1.5	$0.00 \pm_{0.00}^{0.22}$
Others	13 ± 6	3.5 ± 2.0	0.32 ± 0.23

8.3 Charge-flip Background Estimation

The charge-flip background is the main background in $\text{SRSS-}eee$ and $\text{SRSS-}ee\mu$. Charge-flip is predominantly caused by matching of an incorrect track to the electron candidate (Type-1 charge-flip) or the mis-measurement of the curvature of the primary electron track (Type-2 charge-flip). The primary cause for the Type-1 charge-flip is the pair of electrons generated by the bremsstrahlung photon; three tracks are located in close proximity, with two of them having the correct charge assignment, which creates ambiguity in identifying the primary electron track. The schematic of Type-1 charge-flip is shown in Fig. 8.5(a). The main cause for the Type-2 charge-flip is the unconverged bremsstrahlung photon or the almost straight tracks of the high-energy leptons; bremsstrahlung photon can traverse the ID without creating any track and the electron track has usually very few hits or high-energy lepton tracks are approximately straight and it is difficult to determine their curvature. The schematic of Type-2 charge-flip is shown in Fig. 8.5(b). Because muons are much less likely to cause bremsstrahlung due to its heavy mass and also because of the much longer lever arm of the MS compared to the calorimeter, muon charge-flip probability is negligibly small. The fraction of the two charge-flip types depends on the electron p_T and its dependency is shown in Fig. 8.6. It can be seen that Type-1 charge-flip dominates in low p_T region and Type-2 charge-flip starts to account for more than 50% of the total charge-flip for electrons with $p_T > 100$ GeV.

Charge-flip is simulated by GEANT4 in MC samples, but it is not reliable to use it immediately. This is due to the fact that charge-flip mainly occurs as a result of particle interactions

Table 8.4: Observed data and estimated yields using results from the background-only fit in VRWZ-on- E_T^{miss} and VRWZ-off- E_T^{miss} . The uncertainties include both statistical and systematic uncertainties which will be discussed in Chapter 9.

Region	VRWZ-on- E_T^{miss} -a	VRWZ-on- E_T^{miss} -b	VRWZ-on- E_T^{miss} -c
Observed	9	7	3
Fitted SM events	7.9 ± 1.6	8.1 ± 2.0	1.8 ± 0.6
WZ	6.6 ± 1.6	7.4 ± 1.9	1.5 ± 0.5
ZZ	0.49 ± 0.20	0.21 ± 0.10	0.044 ± 0.035
VVV	0.52 ± 0.24	0.56 ± 0.25	0.18 ± 0.09
$t\bar{t}$	< 0.05	< 0.05	< 0.05
$t\bar{t}X$	0.063 ± 0.023	0.026 ± 0.021	$0.010 \pm \begin{smallmatrix} 0.011 \\ 0.010 \end{smallmatrix}$
Fakes	$0.20 \pm \begin{smallmatrix} 0.24 \\ 0.20 \end{smallmatrix}$	$0.00 \pm \begin{smallmatrix} 0.11 \\ 0.00 \end{smallmatrix}$	$0.001 \pm \begin{smallmatrix} 0.013 \\ 0.001 \end{smallmatrix}$
Others	< 0.002	< 0.002	$0.10 \pm \begin{smallmatrix} 0.12 \\ 0.10 \end{smallmatrix}$

Region	VRWZ-off- E_T^{miss} -a	VRWZ-off- E_T^{miss} -b	VRWZ-off- E_T^{miss} -c
Observed	11	10	3
Fitted SM events	12.0 ± 2.9	12.7 ± 3.5	5.1 ± 1.4
WZ	6.1 ± 2.0	7.2 ± 2.3	2.7 ± 1.0
ZZ	0.21 ± 0.08	0.34 ± 0.10	0.15 ± 0.09
VVV	1.5 ± 0.6	1.9 ± 0.8	1.4 ± 0.6
$t\bar{t}$	1.8 ± 0.8	0.74 ± 0.30	$0.04 \pm \begin{smallmatrix} 0.05 \\ 0.04 \end{smallmatrix}$
$t\bar{t}X$	0.08 ± 0.04	0.11 ± 0.05	0.029 ± 0.012
Fakes	$0.00 \pm \begin{smallmatrix} 0.30 \\ 0.00 \end{smallmatrix}$	$0.00 \pm \begin{smallmatrix} 0.20 \\ 0.00 \end{smallmatrix}$	0.31 ± 0.27
Others	2.3 ± 1.5	2.3 ± 2.0	$0.5 \pm \begin{smallmatrix} 0.6 \\ 0.5 \end{smallmatrix}$

with the detector material, necessitating a highly precise modeling of the detector material to reliably predict these events. A data-driven approach is used to tackle this problem; the probability of an electron undergoing charge-flip is measured from the data in $Z \rightarrow ee$ events and compared to the prediction of the MC simulation. $Z \rightarrow ee$ events are used because they are easy to tag and have a sufficient number of statistics for the lepton momentum region of interest. In this analysis, a scale factor is derived for the electron charge-flip probability which is applied to simulated events. The measurement of the charge-flip probability are presented in the following.

8.3.1 Methodology for Charge-flip Scale Factor Estimation

The charge-flip probability is measured performing a likelihood fit on a $Z \rightarrow ee$ data sample in the range of $m_{ee} \in [80, 100]$ GeV. The m_{ee} distribution of same-sign (SS) and opposite-sign (OS) data and MC in $m_{ee} \in [60, 120]$ GeV region is shown in Fig. 8.7(a). The m_{ee} distribution of each charge-flip type is shown in Fig. 8.7(b). SS data and MC have a mass peak around m_Z which is caused by the charge-flip of one electron from $Z \rightarrow ee$. It can be seen that charge-flip occurs with a probability of $\mathcal{O}(10^{-3})$. The mass peak of SS data and MC is shifted to lower $m_{\ell\ell}$ compared to OS data and MC. Fig. 8.7(b) shows that only Type-1 charge flip exhibits this feature. This is because the track and the calorimeter cluster in Type-1 charge-flip mainly arise from the conversion electron which have lower momentum and energy compared to the original electron.

The numbers of SS and OS electron pairs in the sample ($N^{ij} = N_{SS}^{ij} + N_{OS}^{ij}$) are inputs of

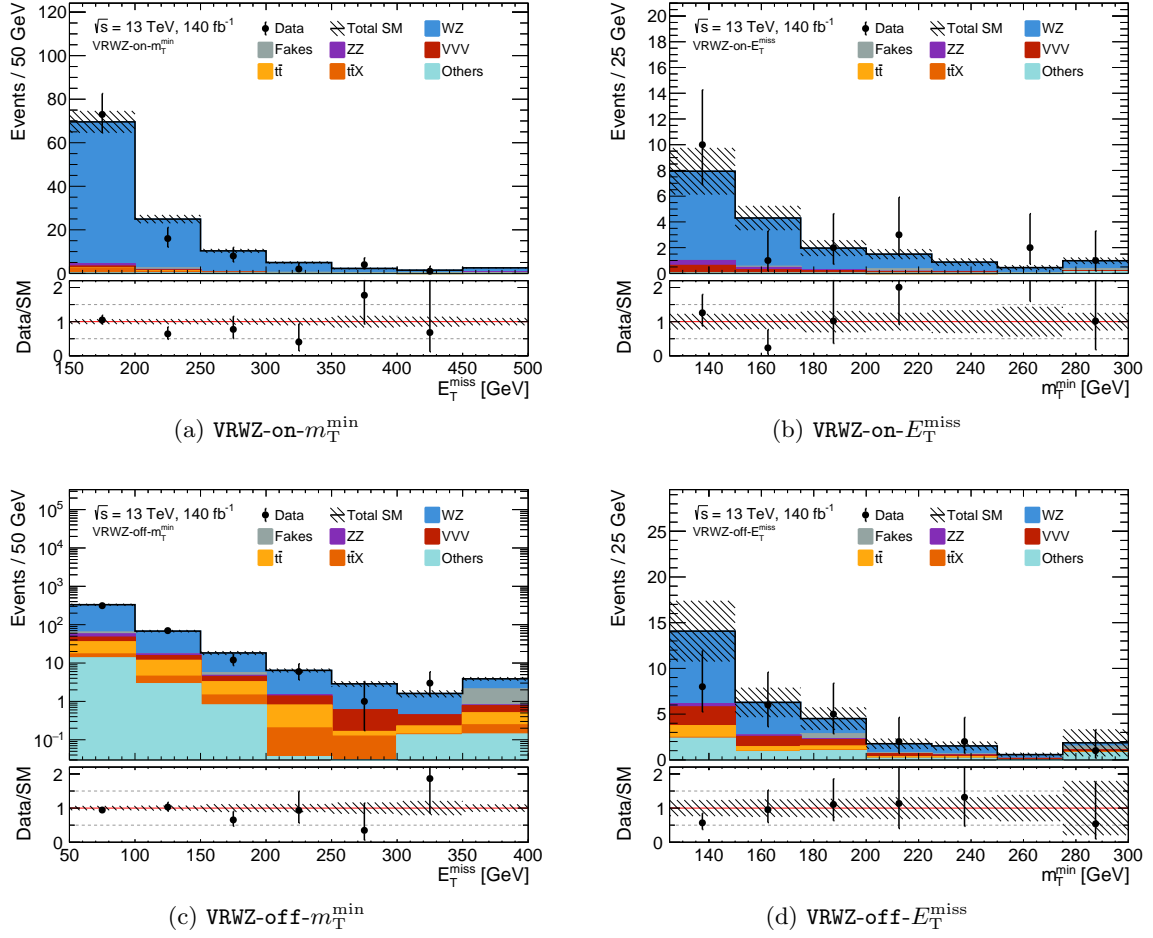


Figure 8.4: Example kinematic distributions after the background-only fit, showing the data and the post-fit expected background. The figure shows the E_T^{miss} and m_T^{\min} distributions in VRs for estimating WZ events. The last bin includes overflow. The “Others” category includes contributions from W +jets, Z +jets, di-boson (excluding full-leptonic $W^\pm Z$ and ZZ), Higgs, and single-top processes. The hatched band includes the combined statistical and systematic uncertainties which will be discussed in Chapter 9. The bottom panel shows the ratio of the observed data to the predicted yields.

the fit. The probability to observe N_{SS}^{ij} SS pairs follows the Poisson probability:

$$f(N_{SS}^{ij}, \lambda) = \frac{\lambda^{N_{SS}^{ij}} e^{-\lambda}}{N_{SS}^{ij}!}, \quad (8.2)$$

with $\lambda = [P_i(1 - P_j) + P_j(1 - P_i)]N^{ij}$ denotes the expected number of SS pairs in bin (i, j) of a given kinematical distribution for the electron, given the charge-flip probabilities P_i and P_j . The log likelihood can be written as

$$-\log \mathcal{L}(\mathbf{P} | \mathbf{N}_{SS}, \mathbf{N}) = \sum_{i,j} \log \{ N^{ij} [P_i(1 - P_j) + P_j(1 - P_i)] \} N_{SS}^{ij} - N^{ij} [P_i(1 - P_j) + P_j(1 - P_i)]. \quad (8.3)$$

The charge-flip probability is parameterized as a function of electron p_T and $|\eta|$. Two type of parametrization is used; full 2D parametrization, $P(p_T, |\eta|)$, which have $N_{\eta\text{-bin}} \times N_{p_T\text{-bin}}$

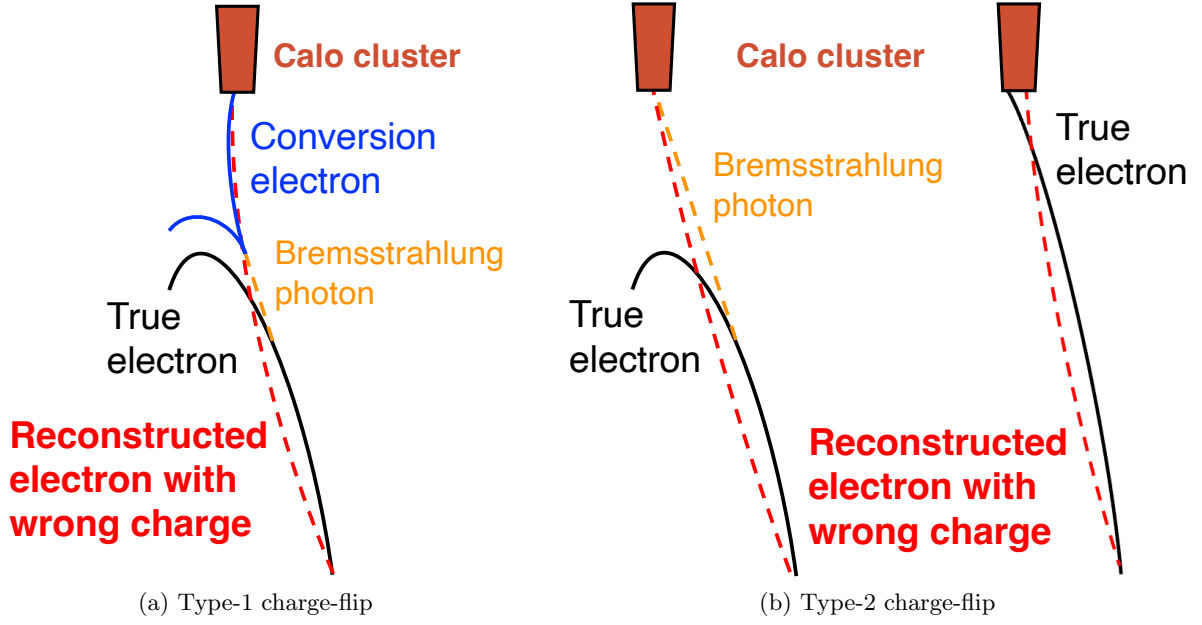


Figure 8.5: Schematic of the charge-flip. (a) Charge-flip caused by the matching of an incorrect track to the electron candidate. The primary cause for the incorrect association of a track with the electron candidate is the pair of electrons generated by the bremsstrahlung photon; three tracks are located in close proximity, with two of them having the correct charge assignment, which creates ambiguity in identifying the primary electron track. (b) Charge-flip caused by the mis-measurement of the curvature of the primary electron track. The main cause for the mis-measurement of the curvature of the primary electron track is the unconverged bremsstrahlung photon or the almost straight tracks of the high-energy leptons; bremsstrahlung photon can traverse the ID without creating any track and the electron track has usually very few hits or high-energy lepton tracks are approximately straight and it is difficult to determine their curvature.

parameters; and $1D \times 1D$ parameterization, $P(p_T, |\eta|) = \sigma(p_T) \times f(|\eta|)$, which decreases the number of parameters to $N_{\eta\text{-bin}} + N_{p_T\text{-bin}} - 1$. In the $1D \times 1D$ parameterization, $\sigma(p_T)$ is set to 0.01 for the first p_T bin to ensure the proper normalization of $P(p_T, |\eta|)$. This $1D \times 1D$ parameterization assumes that bremsstrahlung probability is p_T dependent; it effectively extracts the η dependence of bremsstrahlung probability and scales it with a p_T scale. Fit with $1D \times 1D$ parameterization has a much smaller statistical uncertainty and allows us to measure charge-flip probability of highly energetic electrons ($p_T > 200$ GeV). We use two definitions of p_T and η binning; “fine binning” for the measurement of scale factors with 11 p_T and 15 η bins; and “coarse binning” for the evaluation of parametrization systematic uncertainties with 4 p_T and 7 η bins which will be further discussed later.

A schematic view of the charge-flip scale factor measurement is shown in Fig. 8.8. $m_{ee} \in [80, 100]$ GeV is defined as the main region to measure scale factors and the mass sidebands are defined in $m_{ee} \in [60, 80)$ GeV and $m_{ee} \in (100, 120]$ GeV. MC charge-flip probabilities are measured in the main region using MCs with fake and FSR events removed. FSR is a process where a photon is emitted already in the MC generator as one of final state particles and may convert to a pair of electron-positron in the simulation, which results in the OS or SS electron pair with 50%-50% probability. m_{ee} distribution for FSR events is shown in Fig 8.7(b). Charge-flip is by definition purely a detector effect and should therefore not be a consequence of generator

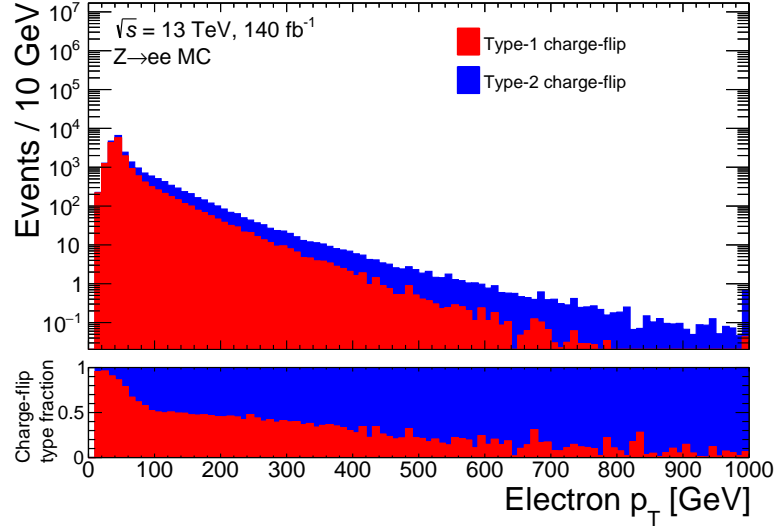


Figure 8.6: Charge-flip type dependency on electron p_T which is measured in $Z \rightarrow ee$ MC. The bottom panel shows the fraction of the two charge-flip types. Type-1 charge-flip is due to the electron candidate being matched to an incorrect track. Type-2 charge-flip is due to the mis-measurement of the curvature of the primary electron track.

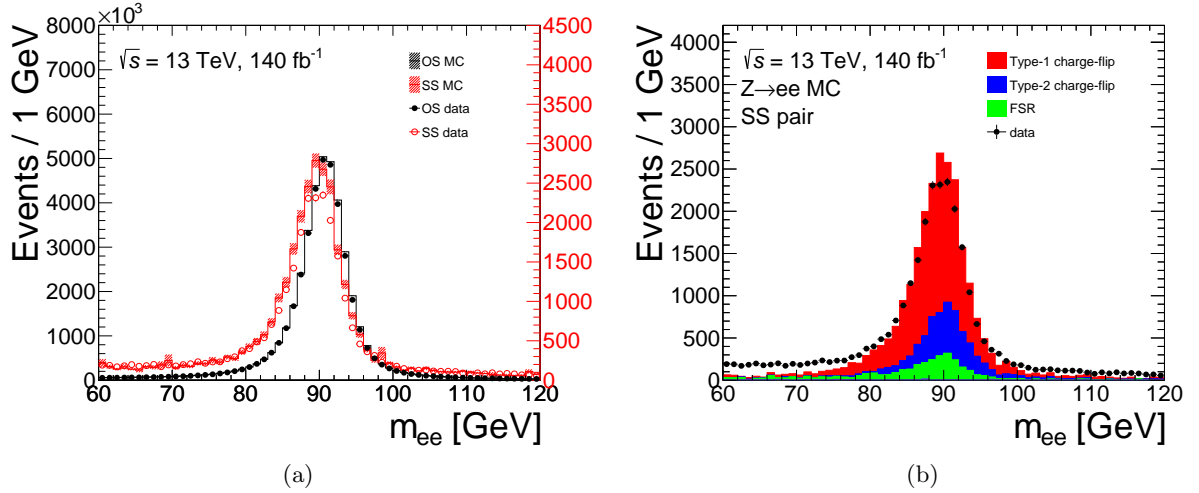


Figure 8.7: $Z \rightarrow ee$ peak used for charge-flip scale factor measurement. (a) The opposite-sign (black) and same-sign (red) $Z \rightarrow ee$ peak. The solid lines correspond to the SM contribution without correction for charge-flip. The hashed band includes the MC statistical uncertainties. Data are represented by the solid dots. (b) Charge-flip type composition in the same-sign $Z \rightarrow ee$ peak. Same-sign electron pair due to final state radiation is denoted as FSR. Type-1 charge-flip is due to the electron candidate being matched to an incorrect track. Type-2 charge-flip is due to the mis-measurement of the curvature of the primary electron track.

level effects, therefore FSR events must be removed from the scale factor measurement. For the data charge-flip probabilities measurement, we need to remove the FSR contribution and processes other than $Z \rightarrow ee$ such as fake lepton events. FSR events in data are subtracted using MC which is denoted as “FSR subtraction” in Fig. 8.8. Since the modeling of fake lepton

events in MC is generally not good, a sideband subtraction method is implemented. Average number of data in two sidebands is used as the background number in the main region and is subtracted from data which is denoted as “Sideband subtraction” in Fig. 8.8.

Charge-flipped electrons in simulated events are corrected with a charge-flip scale factor, w_{CF} . This is defined as $w_{CF} = P(p_T, |\eta|; \text{data})/P(p_T, |\eta|; \text{MC})$. Note that charge-flip probabilities are not used directly in the analysis but rather scale factors are derived as ratio of data to MC charge-flip probabilities. This is because $1D \times 1D$ parametrization introduces a bias in the charge-flip probability originating from the assumption that bremsstrahlung probability is p_T dependent, as shown in Fig. 8.9(a) which compares the measured MC charge-flip probability and the MC truth charge-flip probability with the fine $(p_T, |\eta|)$ binning. As seen in Fig. 8.9, the bias by the $1D \times 1D$ parametrization appears in the low- η high- p_T bins as under-estimation compared to the MC truth charge-flip probability and as over-estimation in the high- η high- p_T bins. With the fine binning, $2D$ parametrization did not converge because of the lack of statistics, however it has a better agreement with the MC truth charge-flip probability which we have confirmed in the coarse $(p_T, |\eta|)$ binning, Fig. 8.9(b). The $1D \times 1D$ parametrization bias in the charge-flip probability will also appear in the measured data charge-flip probability and it is expected to cancel out when we calculate the scale factors, $w_{CF} = P(p_T, |\eta|; \text{data})/P(p_T, |\eta|; \text{MC})$. The potential remaining bias in the scale factors is taken into account by the systematic uncertainty which is evaluated by comparing the $1D \times 1D$ and $2D$ parametrization scale factors in the coarse $(p_T, |\eta|)$ binning.

The data-driven method of determining the charge-flip scale factors is affected by the following systematic uncertainties:

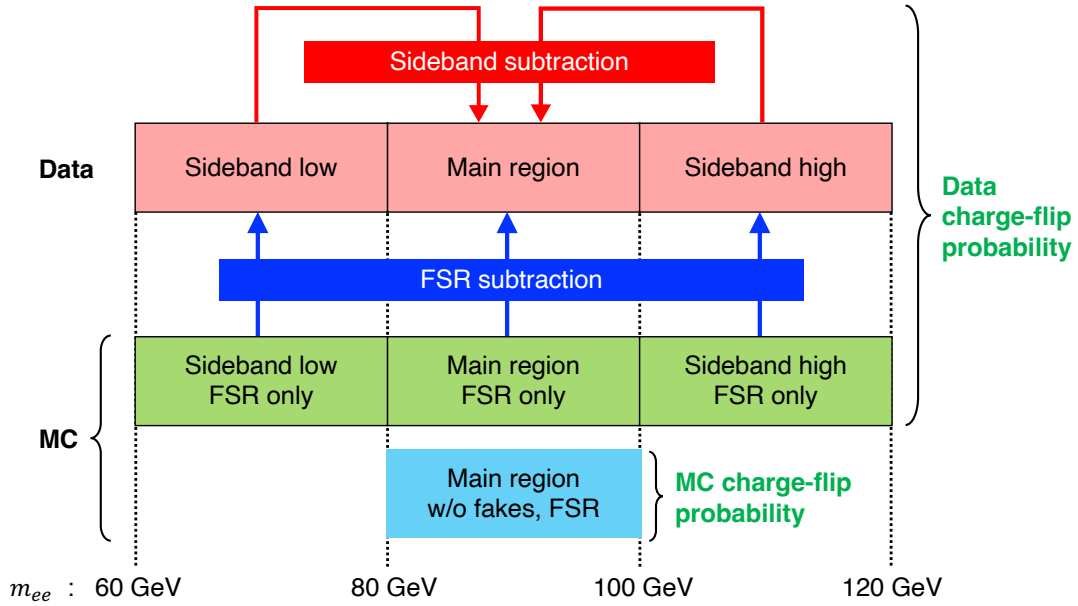


Figure 8.8: Schematic view of the charge-flip scale factor measurement. $m_{ee} \in [80, 100]$ GeV is defined as the main region to measure scale factors. Low and high mass sidebands in $m_{ee} \in [60, 80]$ GeV and $m_{ee} \in (100, 120]$ GeV respectively are defined for the background subtraction in data. MC charge-flip probabilities are measured in the main region using MCs with fake and FSR events removed. Contribution from FSR events in data are subtracted using MC (FSR subtraction). m_{ee} sidebands are used to subtract contribution besides $Z \rightarrow ee$ including fake lepton events. Average number of data in two sidebands is used as the background number in the main region (Sideband subtraction).

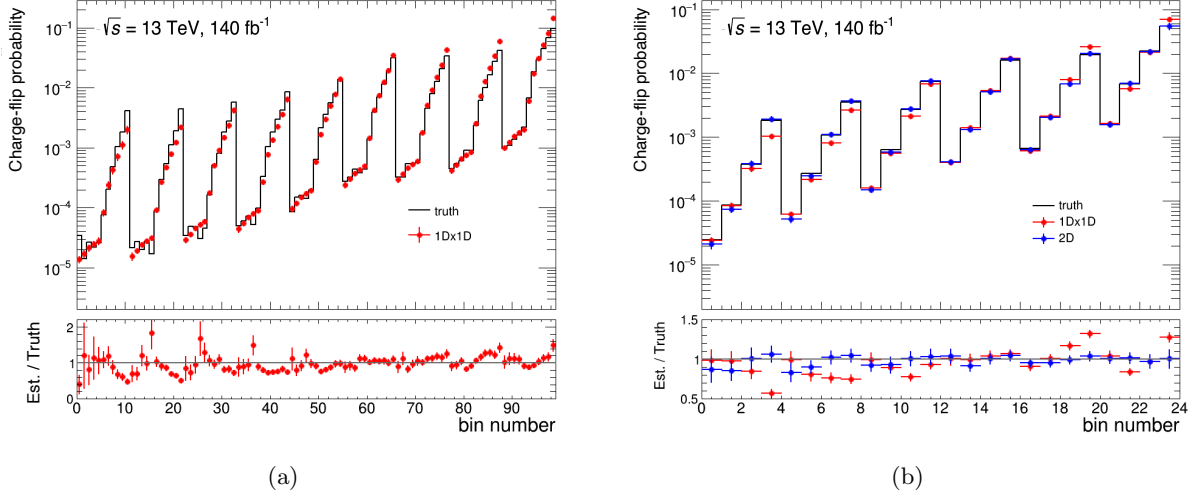


Figure 8.9: Comparison of the measured MC charge-flip probability and the MC truth charge-flip probability. x -axis is $(\eta \text{ bin number}) \times N_{p_T\text{-bin}} + (p_T \text{ bin number})$. Lower panel shows the ratio of estimated and true charge-flip probabilities in MC simulation. (a) $1D \times 1D$ parametrization in fine $(p_T, |\eta|)$ binning. (b) $1D \times 1D$ and $2D$ parametrization in coarse $(p_T, |\eta|)$ binning.

- **Fit uncertainty of the likelihood fit parameters** : Charge-flip scale factors, derived for the SS MC events, have a fit uncertainty assigned through the likelihood fit. They are varied corresponding to the magnitude of the uncertainty to obtain the final statistical uncertainty of the charge-flip background prediction.
- **FSR subtraction variation** : Contribution from FSR photons is subtracted from $Z \rightarrow ee$ peak, since they produce a OS or SS electron pair with 50%-50% probability. FSR subtraction systematic uncertainties are calculated by comparing scale factors with and without FSR subtraction. The difference between the scale factors with FSR subtraction as nominal and without FSR subtraction is assigned as a symmetric uncertainty to scale factors.
- **Sideband subtraction variation** : m_{ee} sideband, $\in [60, 80), (100, 120]$ GeV, is used to subtract contribution besides $Z \rightarrow ee$. Average of the two sidebands is used as the background number in the main region. Sideband subtraction systematic uncertainties are calculated by comparing scale factors with and without sideband subtraction. The difference between the scale factors with sideband subtraction as nominal and without sideband subtraction is assigned as a symmetric uncertainty to scale factors.
- **$1D \times 1D$, $2D$ parametrization non-closure** : Potential difference between $1D \times 1D$ parametrization and $2D$ parametrization is accounted for by applying the symmetric systematic uncertainties obtained by comparing the scale factors between $1D \times 1D$ parametrization and $2D$ parametrization in coarse $(p_T, |\eta|)$ binning. Coarse $(p_T, |\eta|)$ binning is used since $2D$ parametrization fit did not converge for fine $(p_T, |\eta|)$ binning which is used for the $1D \times 1D$ parametrization fit.

8.3.2 Measurement of Charge-flip Scale Factor

Event selection summarized in Table 8.5 is used to extract $Z \rightarrow ee$ events. This region is denoted as CRCF. Charge-flip probabilities vary between 0.001% to 20% depending on p_T and

Table 8.5: Definitions of the CR to measure charge-flip scale factors. n_{SFOS} represents the number of same-flavor opposite-charge-sign (SFOS) lepton pairs.

Variables	CRCF
Trigger	single-electron
$n_{\text{lep}}^{\text{baseline}}, n_{\text{lep}}^{\text{signal}}$	= 2
$p_T^{\ell_1}, p_T^{\ell_2}$ [GeV]	> 28, 10
$n_{b\text{-jets}}$	= 0
n_{SFOS}	= 1
m_{ee} [GeV]	$\in [60, 120]$

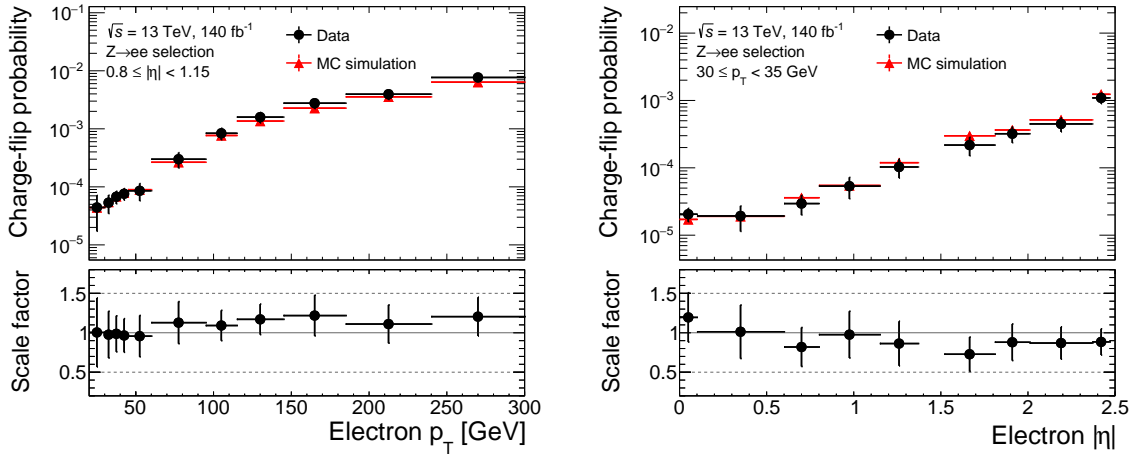


Figure 8.10: Charge-flip probabilities in data and MC (upper panel) and the scale factors (lower panel) as the function of electron p_T at a specific $|\eta|$ slice ($0.8 \leq |\eta| < 1.15$; left) or as the function of electron $|\eta|$ at a specific p_T slice ($30 \leq p_T < 35$ GeV; right). The uncertainties on the data charge-flip probability and the scale factors include both the statistical and systematic components.

$|\eta|$ (examples are in Fig. 8.10, all plots in Appendix B). High p_T electrons tends to have larger charge-flip probability due to the increasing bremsstrahlung probability and the track being straighter. Also high $|\eta|$ electrons tends to have larger charge-flip probability due to more detector materials in the forward region.

Scale factors are calculated based on charge-flip probabilities. Nominal scale factors and relative uncertainties for each systematic variation are shown in Fig. 8.11. These scale factors are derived as the ATLAS-wide official charge-flip scale factor and will also be used by other analyses which are affected by the charge-flip background. The largest MC mismodeling appears at low $|\eta|$ and high p_T region. FSR subtraction and sideband subtraction systematic uncertainties dominates the uncertainty at low p_T region, while the high p_T region uncertainty is mainly from the parametrization non-closure and the fit uncertainty due to small statistics.

A closure test was performed to verify the likelihood fit. SS pairs with the invariant mass $m_{ee} \in [80, 100]$ GeV are selected from data and compared to the charge-flip prediction by applying charge-flip scale factors to SS MC events. The resulting distributions, which is shown in Fig. 8.12, exhibit a good agreement compared to the initial distributions of the SS $Z \rightarrow ee$

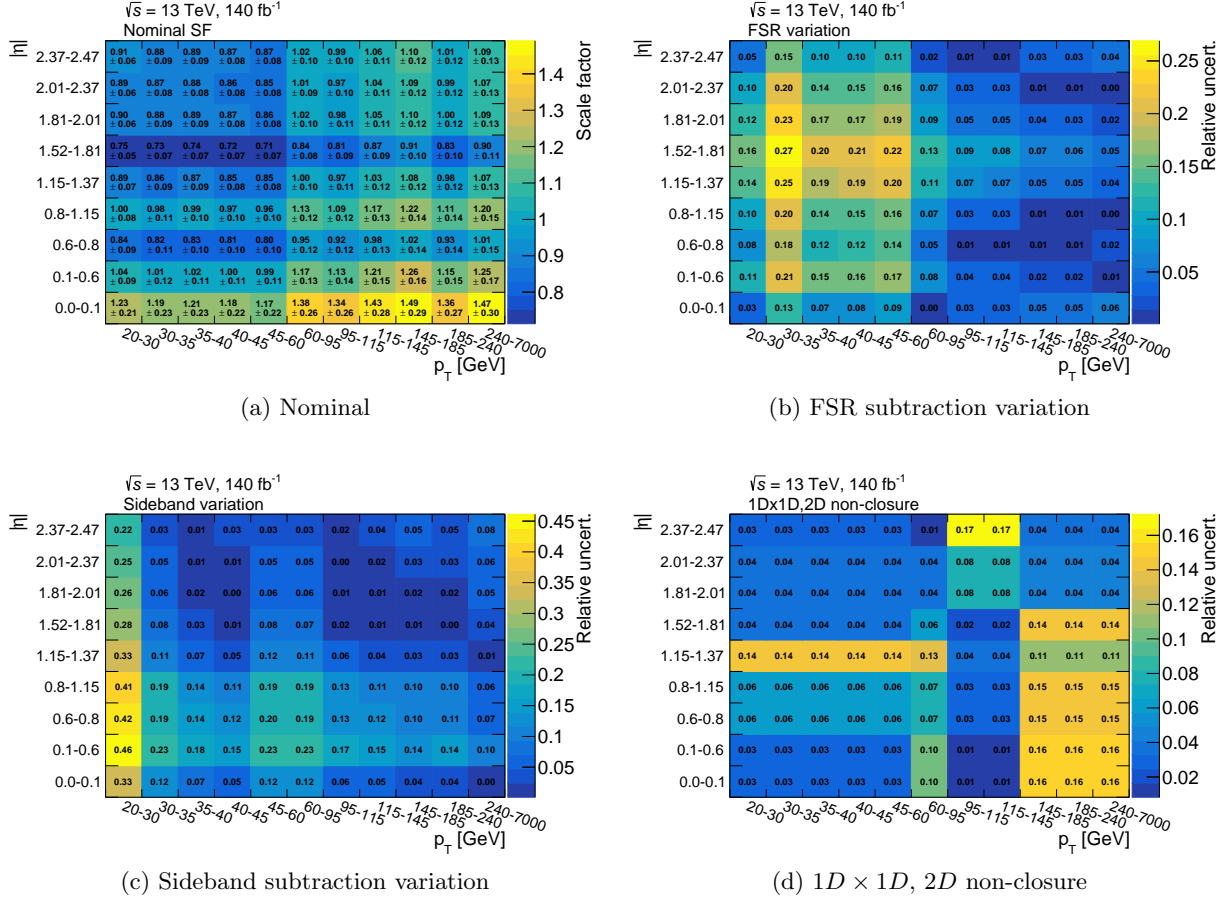


Figure 8.11: The electron charge-flip scale factors and uncertainties. (a) Nominal scale factors. Uncertainties of the likelihood fit are also shown as errors. (b),(c),(d) Relative uncertainties for each systematic uncertainties.

events which are also shown for comparison. These distributions allow to conclude that the reweighting procedure applied to the SS MC events takes into account possible mismodeling of the MC events with respect to the data, and works well.

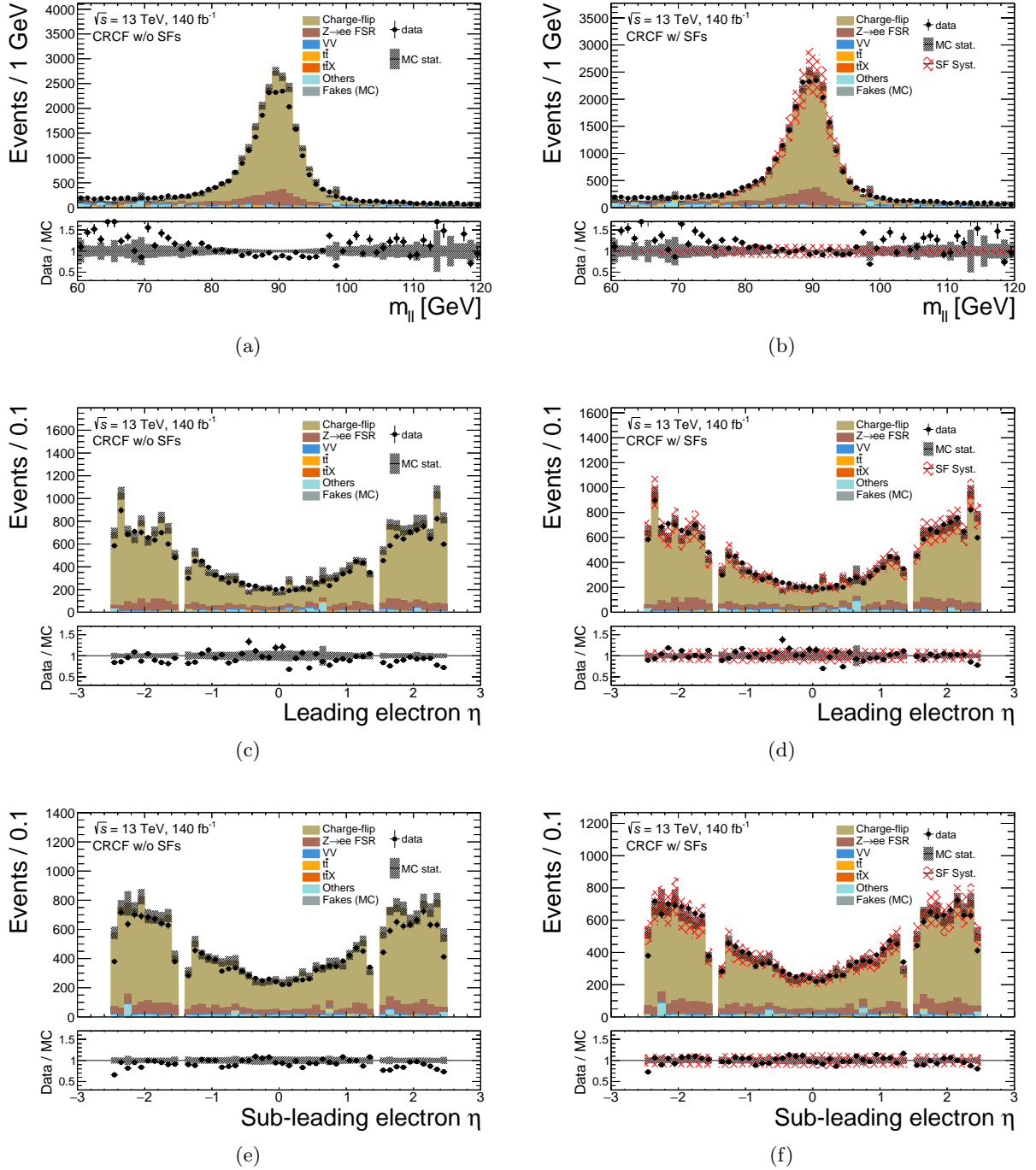


Figure 8.12: Results of the charge-flip closure test. Distributions are shown without (left column) and with (right column) charge-flip scale factors. Distributions besides $m_{\ell\ell}$ use events in the range $m_{\ell\ell} \in [80, 100]$ GeV. The black hatched band includes the MC statistical uncertainties and red hatched band includes the systematic uncertainties on charge-flip scale factors. The bottom panel shows the ratio of the observed data to the predicted yields.

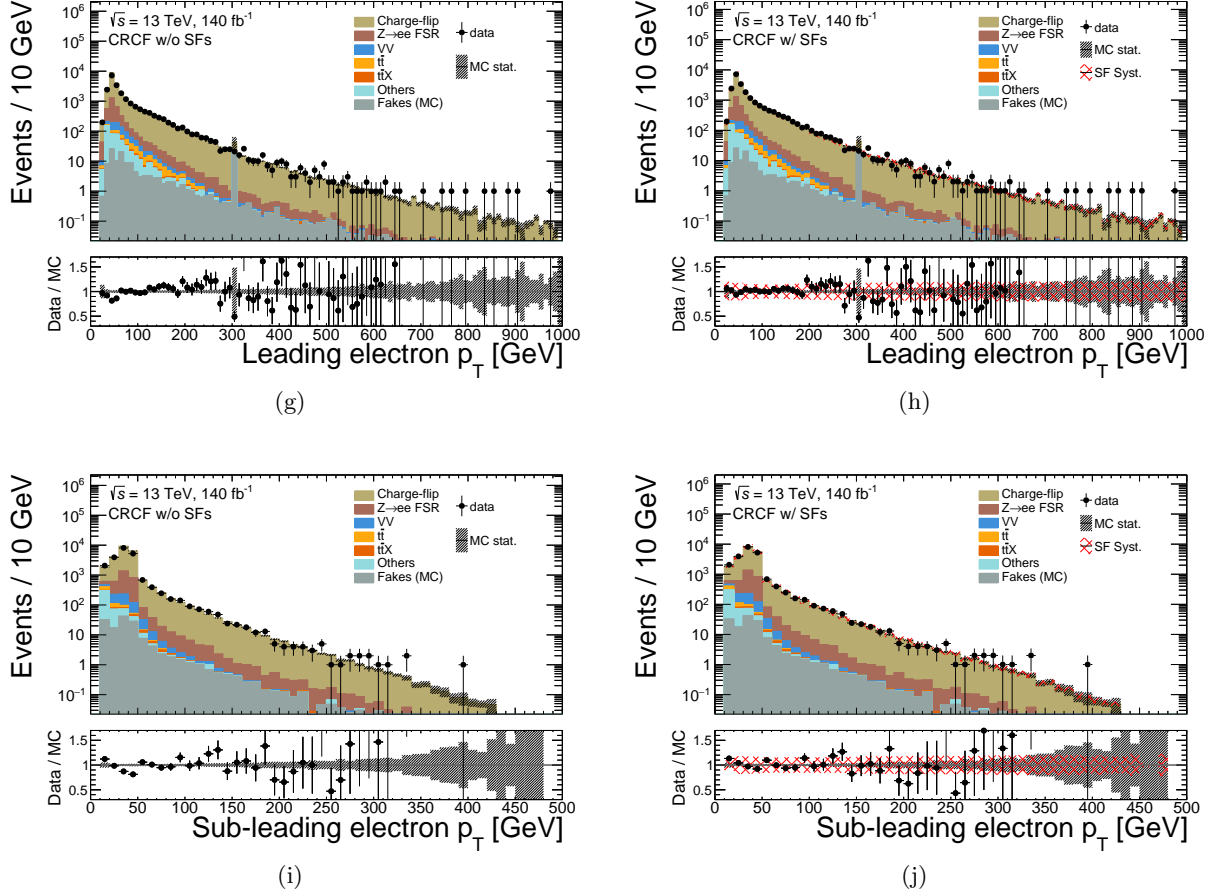


Figure 8.12: Results of the charge-flip closure test. Distributions are shown without (left column) and with (right column) charge-flip scale factors. Distributions besides $m_{\ell\ell} \in [80, 100]$ GeV. The black hatched band includes the MC statistical uncertainties and red hatched band includes the systematic uncertainties on charge-flip scale factors. The bottom panel shows the ratio of the observed data to the predicted yields. (cont.)

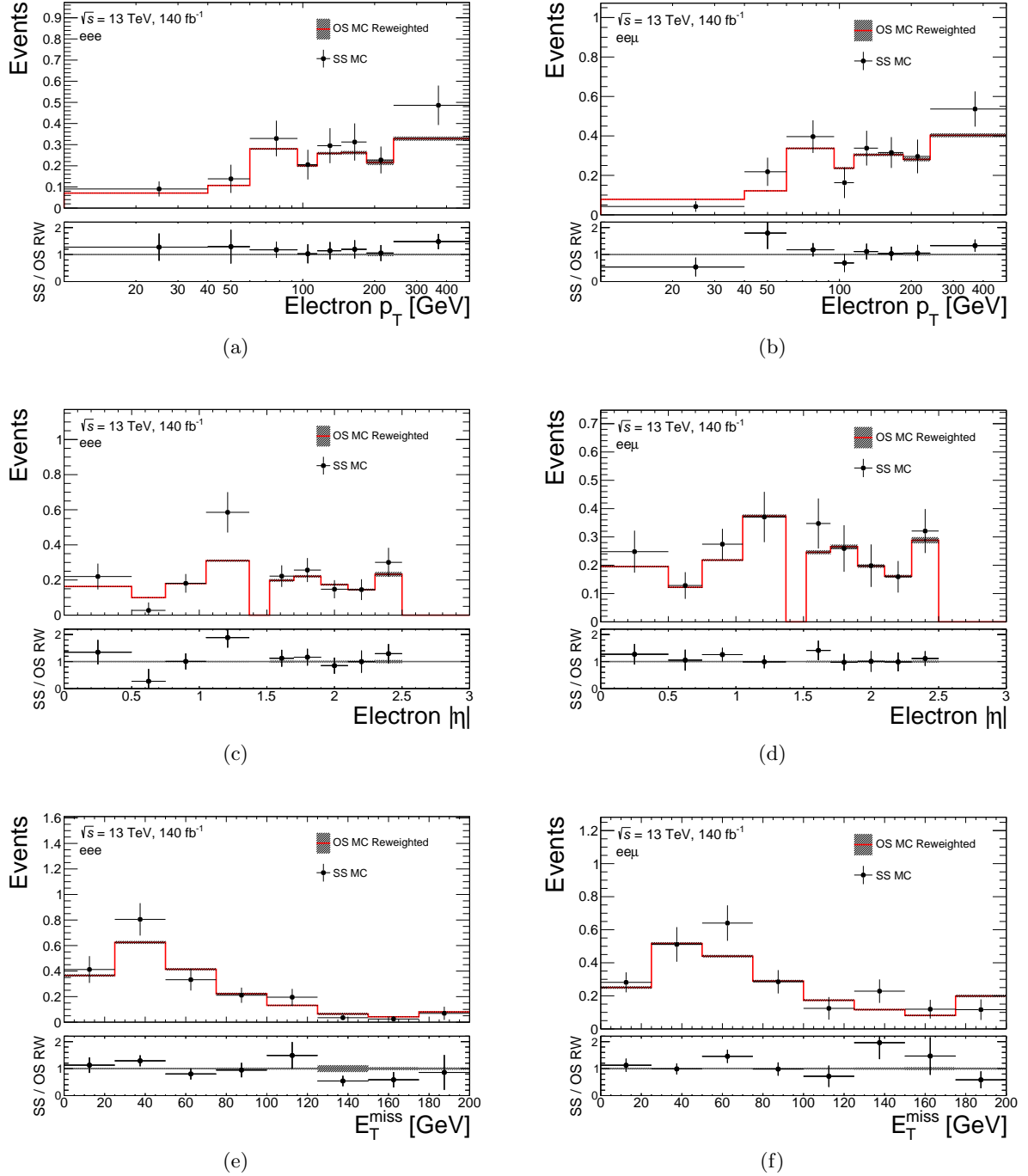


Figure 8.13: WZ OS events reweighting using the $Z \rightarrow ee$ MC charge-flip probability. Left (right) column shows the $p_T, |\eta|$ and E_T^{miss} distribution for eee ($ee\mu$) events. Red line is the reweighted OS distribution with black hatch band showing the MC statistical uncertainties. Black dots show the SS distribution with MC statistical uncertainties. Lower panel shows the ratio of the SS MC and the reweighted OS MC events.

8.3.3 Charge-flip Source Dependency

Charge-flip scale factors are measured using $Z \rightarrow ee$ events, however the main charge-flip source for **SRSS** is WZ . To account for the potential difference between $Z \rightarrow ee$ and WZ , a study on charge-flip source dependency was conducted using $Z \rightarrow ee$ and WZ MCs. WZ OS events are reweighted into SS events using the $Z \rightarrow ee$ MC truth charge-flip probability. The weight used to reweight the OS eee events is

$$w = \frac{\epsilon_1(1 - \epsilon_2)(1 - \epsilon_3) + (1 - \epsilon_1)\epsilon_2\epsilon_3}{1 - (\epsilon_1(1 - \epsilon_2)(1 - \epsilon_3) + (1 - \epsilon_1)\epsilon_2\epsilon_3)}, \quad (8.4)$$

where ϵ_1, ϵ_2 and ϵ_3 are charge-flip probabilities for the three electrons in the OS event and ϵ_1 is the charge-flip probability for the electron that would result in a SS event if this electron charge were mis-identified. On the other hand, the weight used to reweight the OS $ee\mu$ events is

$$w = \frac{\epsilon_1(1 - \epsilon_2)}{1 - (\epsilon_1(1 - \epsilon_2) + (1 - \epsilon_1)\epsilon_2)}, \quad (8.5)$$

where ϵ_1 and ϵ_2 are charge-flip probabilities for the two electrons in the OS event and ϵ_1 is the charge-flip probability for the electron that would result in a SS event if this electron charge were mis-identified. p_T and $|\eta|$ of all electrons and E_T^{miss} distribution in reweighted OS and SS WZ events are presented in Fig. 8.13. Reweighted OS distributions are compatible within statistical uncertainty both in eee and $ee\mu$ events. Conservatively, we decided to apply a 20% flat systematic uncertainty to account for the difference in the charge-flip source.

8.3.4 Validation Regions for Charge-flip Background

To check the charge-flip estimation in **SRSS- eee** and **SRSS- $ee\mu$** , VRs in low E_T^{miss} region is defined as Table 8.6. To increase the statistics, region which does not require ECIDS for the leading lepton, **VRSS-noECIDS**, is also defined. Signal contamination in **VRSS- eee** and **VRSS- $ee\mu$** does not exceed 8% for un-excluded scenarios. Yields are summarized in Table 8.7 and an example kinematic distribution in **VRSS-noECIDS** is shown in Figure 8.14. The observed data are in good agreement with the estimated numbers in all VRs.

Table 8.6: Definitions of the VRs for validating the estimations of the charge-flip events in **SRSS**. In rows where only one value is given it applies to all regions. n_{SFOS} represents the number of same-flavor opposite-charge-sign (SFOS) lepton pairs and n_{DFOS} represents the number of different-flavor opposite-charge-sign (DFOS) lepton pairs in three leptons.

Variables	VRSS (-noECIDS)	
	eee	$ee\mu$
Trigger	single-lepton	
$n_{\text{lep}}^{\text{baseline}}, n_{\text{lep}}^{\text{signal}}$	= 3	
$p_T^{\ell_1}, p_T^{\ell_2}, p_T^{\ell_3}$ [GeV]	> 28, 20, 10	
$n_{b\text{-jets}}$	= 0	
n_{SFOS}	= 0	
n_{DFOS}	= 0	
E_T^{miss} [GeV]	< 50	

Table 8.7: Observed data and estimated yields using results from the background-only fit in VRSS- eee , VRSS- $ee\mu$, VRSS-noECIDS- eee and VRSS-noECIDS- $ee\mu$. The uncertainties include both statistical and systematic uncertainties which will be discussed in Chapter 9.

Region	VRSS- eee	VRSS- $ee\mu$	VRSS-noECIDS- eee	VRSS-noECIDS- $ee\mu$
Observed	2	1	4	4
Total	1.6 ± 0.4	1.2 ± 0.4	4.2 ± 1.2	5.0 ± 1.0
Charge-flip	1.03 ± 0.32	0.97 ± 0.30	2.5 ± 0.7	3.1 ± 0.8
Fakes	0.45 ± 0.21	0.20 ± 0.20	1.6 ± 0.9	1.9 ± 0.6
WZ	0.07 ± 0.07	0.015 ± 0.013	0.09 ± 0.08	0.08 ± 0.07
ZZ	0.013 ± 0.007	< 0.008	$0.019 \pm \begin{smallmatrix} 0.023 \\ 0.019 \end{smallmatrix}$	$0.008 \pm \begin{smallmatrix} 0.010 \\ 0.008 \end{smallmatrix}$
VVV	< 0.005	$0.008 \pm \begin{smallmatrix} 0.011 \\ 0.008 \end{smallmatrix}$	< 0.005	$0.008 \pm \begin{smallmatrix} 0.011 \\ 0.008 \end{smallmatrix}$
$t\bar{t}$	< 0.05	$0.04 \pm \begin{smallmatrix} 0.07 \\ 0.04 \end{smallmatrix}$	< 0.05	$0.04 \pm \begin{smallmatrix} 0.07 \\ 0.04 \end{smallmatrix}$

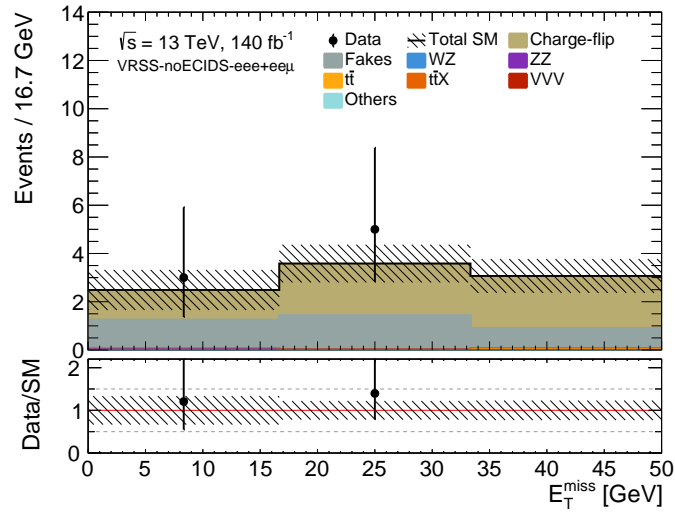


Figure 8.14: Example kinematic distributions for the expected backgrounds and the data, obtained from a background-only fit including systematic uncertainties. The figure shows the E_T^{miss} distribution in the merged region of VRSS-noECIDS- eee and VRSS-noECIDS- $ee\mu$. The “Others” category includes contributions from W +jets, Z +jets, di-boson (excluding full-leptonic $W^\pm Z$ and ZZ), Higgs, and single-top processes. The hatched band includes the combined statistical and systematic uncertainties which will be discussed in Chapter 9. The bottom panel shows the ratio of the observed data to the predicted yields.

8.4 Fake/Non-prompt Lepton Background Estimation

Fake backgrounds which contain fake/non-prompt leptons not originating from the hard scattering processes, arise when a light flavor jet is improperly identified as a lepton, when a heavy flavor hadron decays semi-leptonically, or when a photon converts into a pair of leptons. Fake leptons in the three lepton final state mainly arise from two types of processes:

1. **Di-boson and Z + jets** are backgrounds in this analysis when the bosons decay leptonically and a jet or photon fakes an electron or muon.
2. **$t\bar{t}$ and single-top**, collectively referred to as top-like backgrounds, which all have similar final states and can thus be treated simultaneously. As $t\bar{t}$ has the largest cross-section among the top-like backgrounds and b -jets tend to result in fake leptons more frequently

than light flavor jets or photon conversions, $t\bar{t}$ is typically the dominant process contributing to the top-like backgrounds.

It is normally challenging to accurately model these events. Thus, a data-driven technique is used for estimating these backgrounds excluding the top-like backgrounds. The “Fake Factor method” [222, 223] is used, which relies on inverted lepton identification and isolation criteria to estimate the fake lepton background. The Fake Factor method will be further discussed in Section 8.4.1 and the measurement of Fake Factors will be described in Section 8.4.2. Systematic uncertainties of the fake estimation is listed in Section 8.4.3 and the validation of the Fake Factors is done in Section 8.4.4. Due to the lack of statistics, fake lepton events in SRSS- 2μ are estimated using the “unusual” Fake Factor method. The estimation method and validation is described in Section 8.4.5.

The top-like backgrounds, meanwhile, come predominantly from b -jets originating from the decay of top quark which have small theory uncertainties. MC based approach is used for top-like backgrounds, which will be further discussed in Section 8.4.6.

8.4.1 Fake Factor Method

The Fake Factor method uses two sets of lepton identification criteria. The first is the standard lepton identification used by the analysis (referred to as *signal*, *tight*, or *ID* lepton criteria). The second is an orthogonal criteria (referred to as *loose* or *anti-ID* lepton criteria) which is designed to be enriched in fake leptons by relaxing or inverting various lepton identification criteria. The definitions of the ID and anti-ID lepton criteria for electrons and muons in this analysis are described in Table 8.8.

The Fake Factor F is defined as the ratio of the number of ID leptons to the number of anti-ID leptons, which is measured in a kinematic region primarily consisting of fake leptons. To ensure that only fake leptons are considered in the measurement of F , MC simulation is used to remove contamination of events containing real prompt leptons. Thus, the Fake Factor takes

Table 8.8: ID and anti-ID electron and muon definitions used for the Fake Factor method.

	Electrons	Muons
ID	Pass TightLLH identification $ \eta < 1.37$ or $1.52 < \eta < 2.47$ Tight_VarRad isolation $ d_0/\sigma(d_0) < 5$ $ z_0 \sin \theta < 0.5$ mm Pass overlap removal Pass ECIDS veto Pass Ambiguity cut	Pass Medium identification $ \eta < 2.5$ PfowTight_VarRad isolation $ d_0/\sigma(d_0) < 3$ $ z_0 \sin \theta < 0.5$ mm Pass overlap removal – –
Anti-ID	Pass LooseAndBLayerLLH identification $ \eta < 1.37$ or $1.52 < \eta < 2.47$ $ z_0 \sin \theta < 0.5$ mm Pass overlap removal Pass ECIDS veto Pass Ambiguity cut Not ID	Pass Medium identification $ \eta < 2.5$ $ z_0 \sin \theta < 0.5$ mm Pass overlap removal – – Not ID

the form:

$$F(i) = \frac{N_{\text{ID}}^{\text{data}}(i) - N_{\text{ID}}^{\text{prompt MC}}(i)}{N_{\text{anti-ID}}^{\text{data}}(i) - N_{\text{anti-ID}}^{\text{prompt MC}}(i)}, \quad (8.6)$$

where N is the number of events and i refers to the i^{th} bin (e.g. p_{T} bin). Once the Fake Factors have been measured in this fake-dominated region, it can then be used to obtain the fake background estimate in the SRs. For the Fake Factor method, an “anti-ID CR” is used, which is identical to the SR (or CR/VR) except that one or more of the ID leptons selections are replaced to an anti-ID lepton selection. The estimation for the number of three lepton events containing at least one fake lepton, $N_{\text{Est. Fake}}$, is then:

$$\begin{aligned} N_{\text{Est. Fake}} = & F_1(N_{\text{LTT}}^{\text{data}} - N_{\text{LTT}}^{\text{prompt MC}}) + F_2(N_{\text{TLT}}^{\text{data}} - N_{\text{TLT}}^{\text{prompt MC}}) + F_3(N_{\text{TTL}}^{\text{data}} - N_{\text{TTL}}^{\text{prompt MC}}) \\ & - F_1 F_2(N_{\text{LLT}}^{\text{data}} - N_{\text{LLT}}^{\text{prompt MC}}) - F_1 F_3(N_{\text{LTL}}^{\text{data}} - N_{\text{LTL}}^{\text{prompt MC}}) - F_2 F_3(N_{\text{TLL}}^{\text{data}} - N_{\text{TLL}}^{\text{prompt MC}}) \\ & + F_1 F_2 F_3(N_{\text{LLL}}^{\text{data}} - N_{\text{LLL}}^{\text{prompt MC}}) \end{aligned} \quad (8.7)$$

where the subscript indicates the lepton identification of each lepton (e.g. “LTT” stands for when the leading lepton is *loose* and the sub-leading and third leptons are *tight*) and the F_1, F_2, F_3 correspond to the Fake Factor of each lepton.

8.4.2 Measurement of Fake Factors

The Fake Factors used in the analysis are derived from a region dominated by Z + jets events with fake leptons. This region requires events to have three baseline leptons with at least one SFOS pair of leptons. To suppress WZ and be orthogonal with the analysis SRs, further requirements of $20 \leq E_{\text{T}}^{\text{miss}} < 50$ GeV, $m_{\ell\ell} \in [81.2, 101.2]$ GeV, and $m_{\text{T}}^{\text{min}} < 30$ GeV are imposed, where in cases of ambiguity the $m_{\ell\ell}$ pairing is chosen to be the one which minimizes $|m_{\ell\ell} - m_Z|$. The lower cut to $E_{\text{T}}^{\text{miss}}$ is imposed to make the Fake Factors applicable to SRs, which are defined in the high- $E_{\text{T}}^{\text{miss}}$ region. The ability of the Fake Factors to be applied to SRs will be further discussed in Section 8.4.3. A b -jet veto is imposed to suppress $t\bar{t}$, and events are required to pass the single-lepton trigger, which is being matched to the leptons from the Z boson, such that we don’t obtain a trigger bias for the unpaired lepton. Leptons which trigger the single lepton trigger are required to satisfy the offline p_{T} threshold. Furthermore, the leptons paired to form a Z boson candidate are required to pass the ID lepton criteria, while the remaining, fake-candidate, lepton must satisfy either the ID or the anti-ID criteria. As a substantial number of events were found to have $m_{3\ell}$ consistent with m_Z (due to $Z + \gamma$ events where the photon radiates off of a lepton), a requirement $m_{3\ell} > 105$ GeV is also imposed. The selection criteria used to define this Fake Factor measurement region (CRFF) are summarized in Table 8.9. The lepton p_{T} threshold is reduced to 10 GeV for all leptons to increase statistics and to remove the bias in the lepton p_{T} distribution introduced by p_{T} cuts that depend on the p_{T} order of the leptons. WZ background in CRFF is normalized by using the CR (CRWZ-fakes) which have high WZ purity by changing the $E_{\text{T}}^{\text{miss}}$ and $m_{\text{T}}^{\text{min}}$ requirement ($20 \leq E_{\text{T}}^{\text{miss}} < 50$ GeV, $40 \leq m_{\text{T}}^{\text{min}} < 80$ GeV) compared to CRFF. The WZ NF is found to be 1.13 ± 0.02 .

The distribution of the lepton p_{T} in CRFF is shown in Fig. 8.15. Results of the Fake Factor extraction in CRFF are shown in Fig. 8.16. The Fake Factors shown in Fig. 8.16(a)(b) will be used for the final estimation of the fake background in the SRs. Typical Fake Factor values are 0.04–0.08 (0.08–0.12) for electrons (muons) in a p_{T} range of 4.5–50 (3.0–30) GeV. The data vs. MC Fake Factor agreement is generally worse for electrons than muons, due to the more complicated fake composition. While the fake muons are almost always the result of a heavy flavor decay, the fake electrons are a mixture of heavy and light flavor fakes. The η , ϕ , $E_{\text{T}}^{\text{miss}}$,

and m_T^{\min} dependence of Fake Factors are also shown in Fig. 8.16. Weak dependence on η and ϕ makes further binning of Fake Factors by η or ϕ unnecessary. Also weak dependence on E_T^{miss} and m_T^{\min} makes it possible to extrapolate this Fake Factors to SRs which have large E_T^{miss} and m_T^{\min} (Fake Factor usage to SRs are further studied in Section 8.4.3).

8.4.3 Systematic Uncertainties of the Fake Factor Method

A set of dedicated systematic uncertainties is added to the final fake estimation to reflect the limitation of data-driven method.

- **Statistical uncertainties** : The statistical uncertainties on the Fake Factors are accounted for by error propagation obtaining the variations $F(p_T) \pm 1\sigma$. All the p_T bins are independent measurements with their own $F(p_T)$ and σ , and as a result all the statistical uncertainties have been treated separately. For each event the variation for 1σ up and down is stored to the p_T bin the variation belongs to. Storing the variation for each p_T bin separately allows the fit to pull on each independent measurement of $F(p_T)$. In case of an event with two or more anti-ID leptons where the two leptons fall into the same p_T bin, their F is fully correlated. The uncertainty propagated in that case is $(F(p_T) \pm 1\sigma)^2$.
- **WZ cross-section in MC subtraction** : As shown in Fig. 8.15, there is prompt contamination in the CRFF, mainly in the ID region. The largest background that is subtracted in the measurement region is WZ . The uncertainty on the inclusive cross-section of WZ is 5% [224]. Conservatively, the WZ background subtraction is shifted up and down by 10% to derive Fake Factors, taking into account that Fake Factors are measured per lepton p_T bin. The Fake Factors that account for the uncertainty of the cross-section of WZ is propagated to the uncertainty on the fake estimation. The Fake Factors for this systematic uncertainty are shown in Fig. 8.17.
- **E_T^{miss} cut dependence** : The Fake Factors are measured in the CRFF, limited in $E_T^{\text{miss}} \in [20, 50]$ GeV. To account for possible composition changes in data, an alternative set of

Table 8.9: Definitions of the fake lepton enriched CR used to measure the FFs. In rows where only one value is given it applies to all regions. n_{SFOS} represents the number of same-flavor opposite-charge-sign (SFOS) lepton pairs in three leptons. If more than one SFOS lepton pair is present in the event, the invariant mass of the SFOS lepton pair closest to the Z mass is used as $m_{\ell\ell}$.

Variables	CRFF
Trigger	single-lepton
$n_{\text{lep}}^{\text{baseline}}, n_{\text{lep}}^{\text{signal}}$	= 3
$p_T^{\ell_1}, p_T^{\ell_2}, p_T^{\ell_3}$ [GeV]	> 10, 10, 0
$n_{b\text{-jets}}$	= 0
n_{SFOS}	≥ 1
$m_{\ell\ell}$ [GeV]	$\in [81.2, 101.2]$
m_T^{\min} [GeV]	< 30
E_T^{miss} [GeV]	$\in [20, 50]$
$m_{3\ell}$ [GeV]	> 105

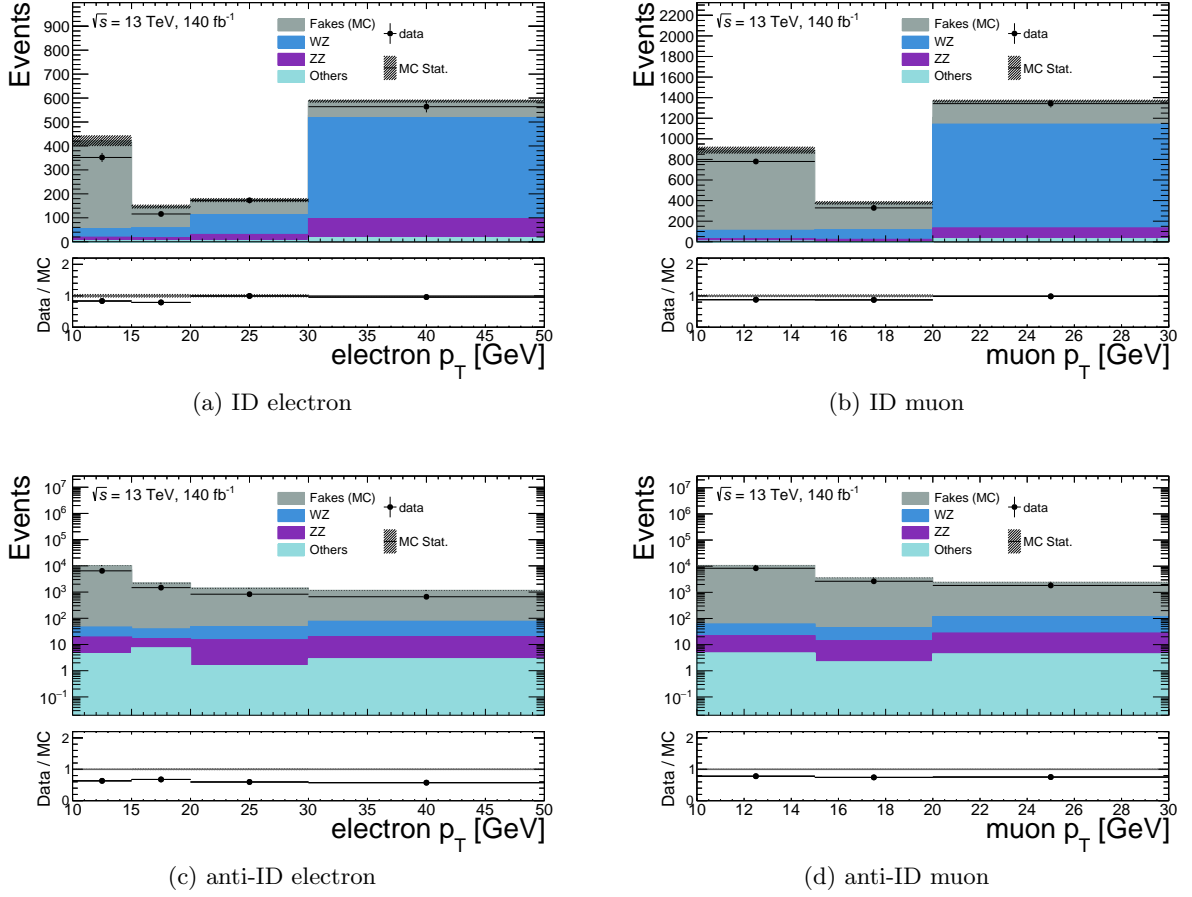


Figure 8.15: Distribution of the lepton p_T in CRFF region detailed in Table 8.9. Top plots are for ID leptons and bottom plots are showing anti-ID lepton distributions. The hatched band includes the MC statistical uncertainties. The bottom panel shows the ratio of the observed data and background yield estimated directly from simulation samples.

Fake Factors has been measured. For the alternative Fake Factors, the CRFF E_T^{miss} cut is changed to $E_T^{\text{miss}} \in [20, 40)$ GeV or to $E_T^{\text{miss}} \in [20, 60)$ GeV. The Fake Factors for this systematic uncertainty are shown in Fig. 8.18.

- **Fake lepton composition** : The composition of the fake leptons in the CRFF and SRs do not match exactly as shown in Fig. 8.19-8.20. “Fake HF” refers to fake leptons originating from heavy-flavor jets, “Fake LF” refers to fake leptons from light-flavor jets, “Fake conv” refers to fake leptons arising from photon conversions, and “Fake other” refers to any other fake leptons, such as those from pile-up. The relative composition of fake muons is similar between the CRFF and SRs, whereas for fake electrons, the heavy-flavor decay and light hadron contribution dominate in CRFF while SRs have sizable contribution from photon conversions. A closure test on MC events (excluding top-like backgrounds) has been performed to verify whether differences in the fake lepton composition hamper the estimation. MC Fake Factors measured in CRFF are used to perform the Fake Factor method in each SR and it is compared to MC fake lepton events in the SR ID region. To increase the statistics, m_T^{min} cut is loosen to $m_T^{\text{min}} > 30$ GeV in SR0S. Fig. 8.21 shows the results. SRSS-2 μ is not included due to different method of fake estimation which is

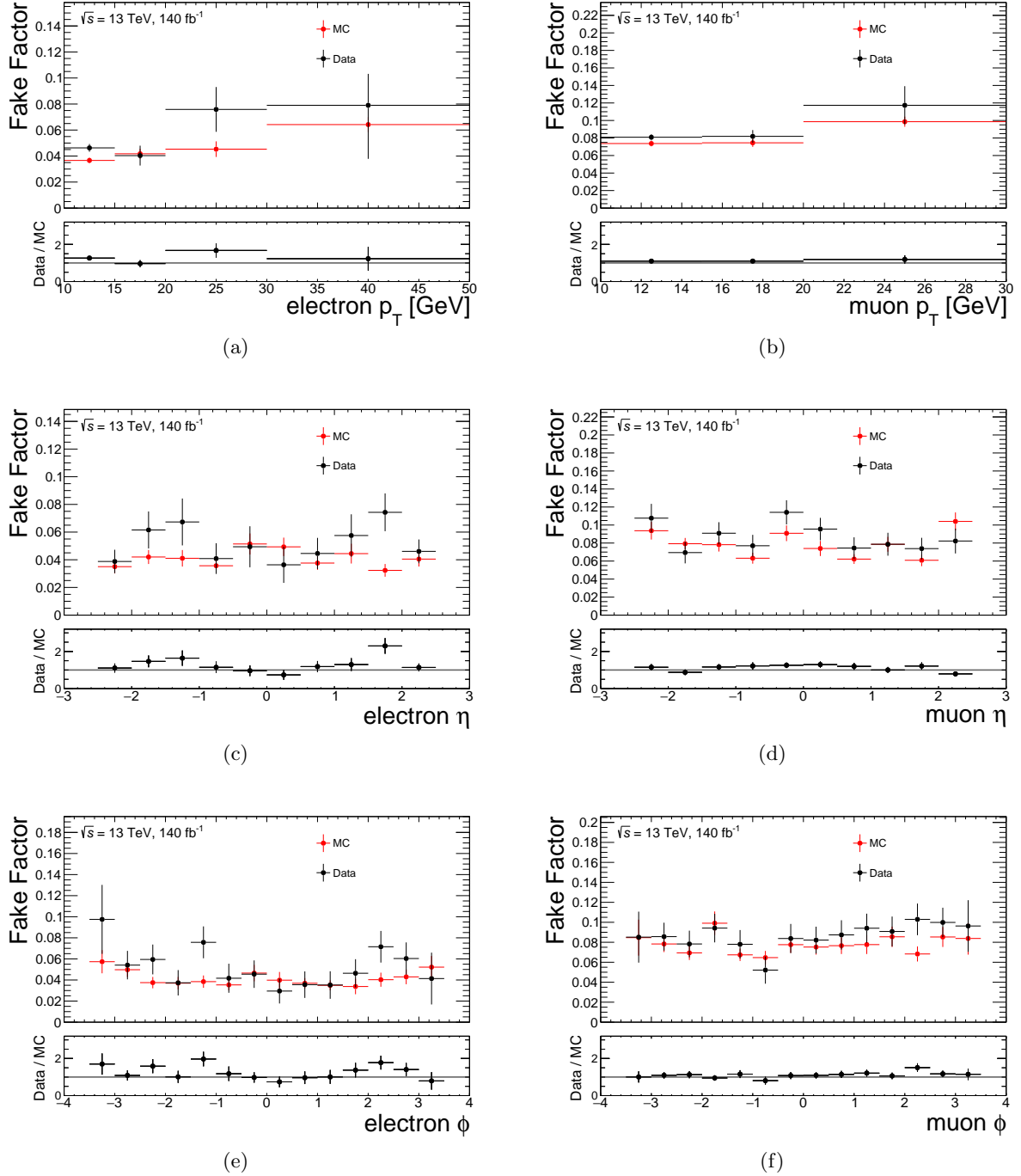


Figure 8.16: Fake Factor extraction results in CRFF detailed in Table 8.9. Extraction is performed for electrons (left column) and muons (right column), separately. All uncertainties shown are only statistical. Lower panel shows the ratio of data and MC Fake Factors.

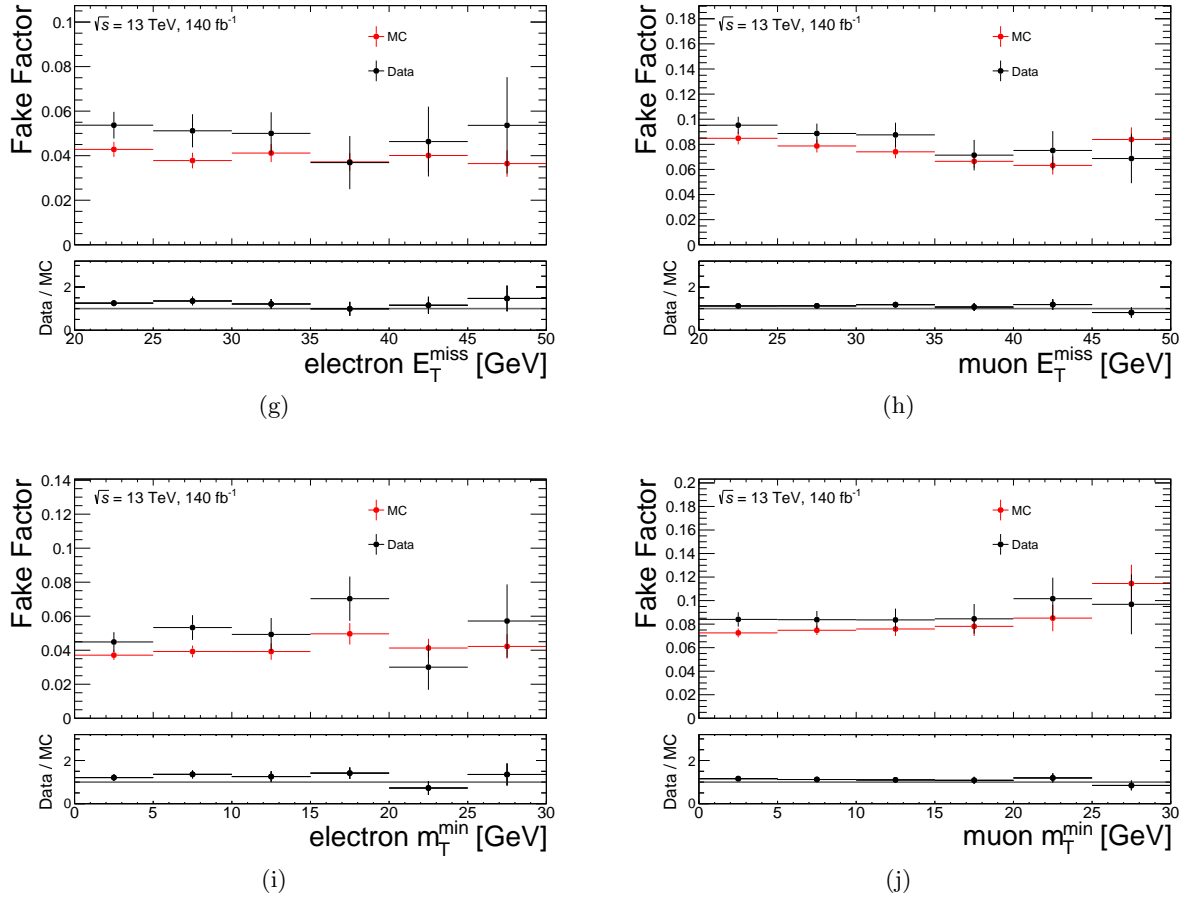


Figure 8.16: Fake Factor extraction results in CRFF detailed in Table 8.9. Extraction is performed for electrons (left column) and muons (right column), separately. All uncertainties shown are only statistical. Lower panel shows the ratio of data and MC Fake Factors. (cont.)

described in Section 8.4.5. Estimated number of fake lepton events are compatible with MC within statistical uncertainties in all region except $\text{SROS-}ee\mu$ $m_{3\ell} \in [200, 400)$ GeV. To cover the non-closure, a flat 28.5% fake composition systematic uncertainty is applied to fake lepton events in $\text{SROS-}ee\mu$ $m_{3\ell} \in [200, 400)$ GeV to realize the agreement in yields between MC fake lepton events and estimated fake lepton events.

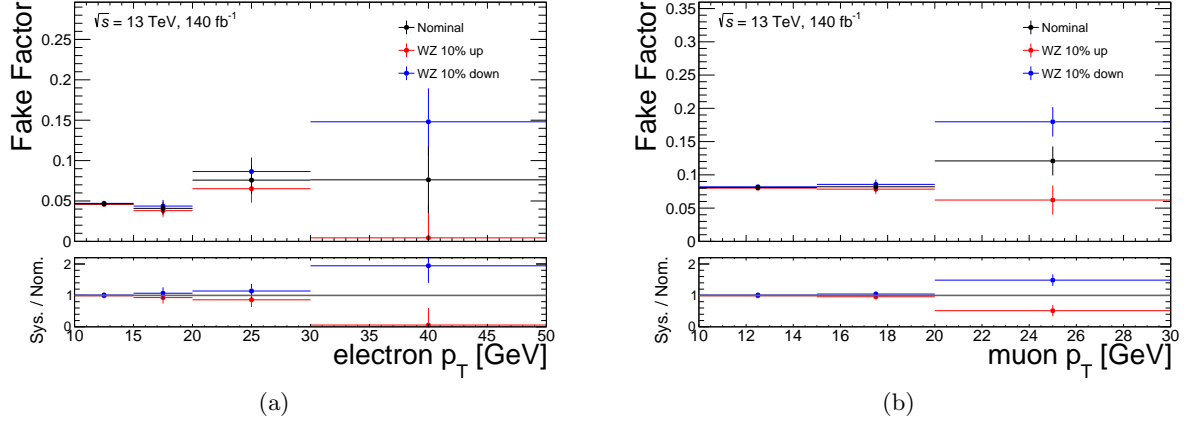


Figure 8.17: WZ cross-section variation systematic uncertainty to Fake Factors. WZ background subtraction is shifted up and down by 10% to derive Fake Factors. All uncertainties shown are only statistical. Lower panel shows the ratio of systematic and nominal Fake Factors.

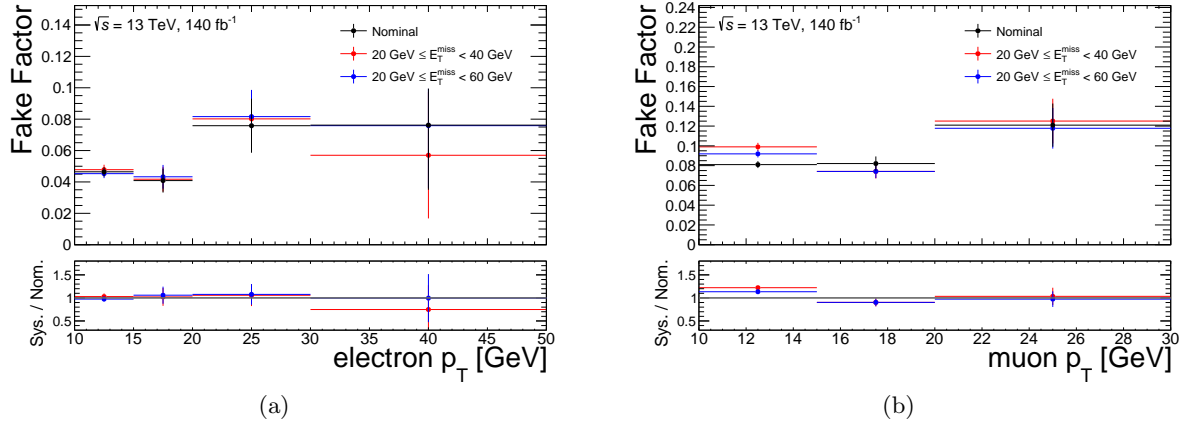


Figure 8.18: CRFF E_T^{miss} cut variation systematic uncertainty to Fake Factors. CRFF E_T^{miss} cut is changed to $E_T^{\text{miss}} \in [20, 40] \text{ GeV}$ or $E_T^{\text{miss}} \in [20, 60] \text{ GeV}$. All uncertainties shown are only statistical. Lower panel shows the ratio of systematic and nominal Fake Factors.

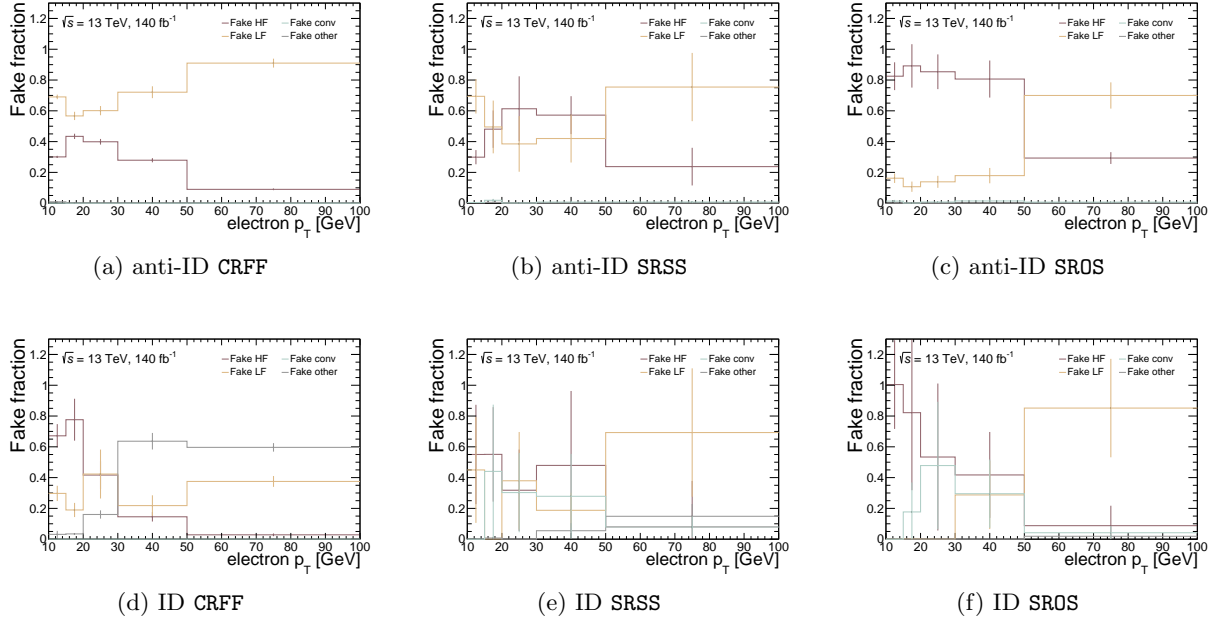


Figure 8.19: Fake composition versus p_T for electrons. “Fake HF” refers to fake leptons originating from heavy-flavor jets, “Fake LF” refers to fake leptons from light-flavor jets, “Fake conv” refers to fake leptons arising from photon conversions, and “Fake other” refers to any other fake leptons, such as those from pile-up.

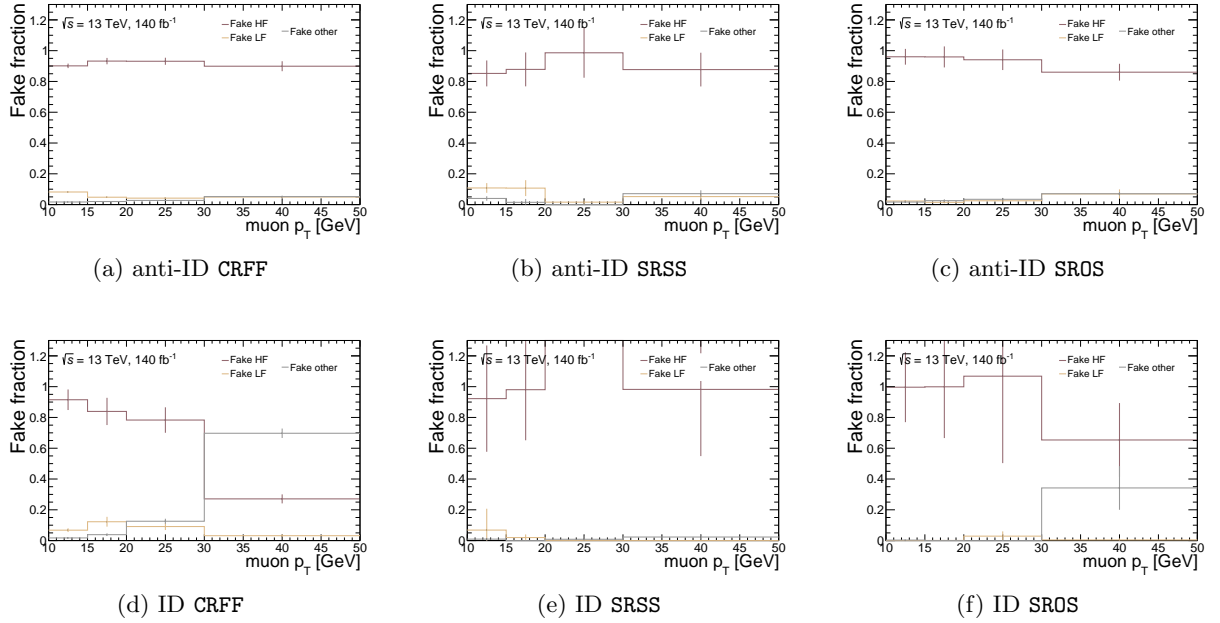


Figure 8.20: Fake composition versus p_T for muons. “Fake HF” refers to fake leptons originating from heavy-flavor jets, “Fake LF” refers to fake leptons from light-flavor jets, and “Fake other” refers to any other fake leptons, such as those from pile-up.

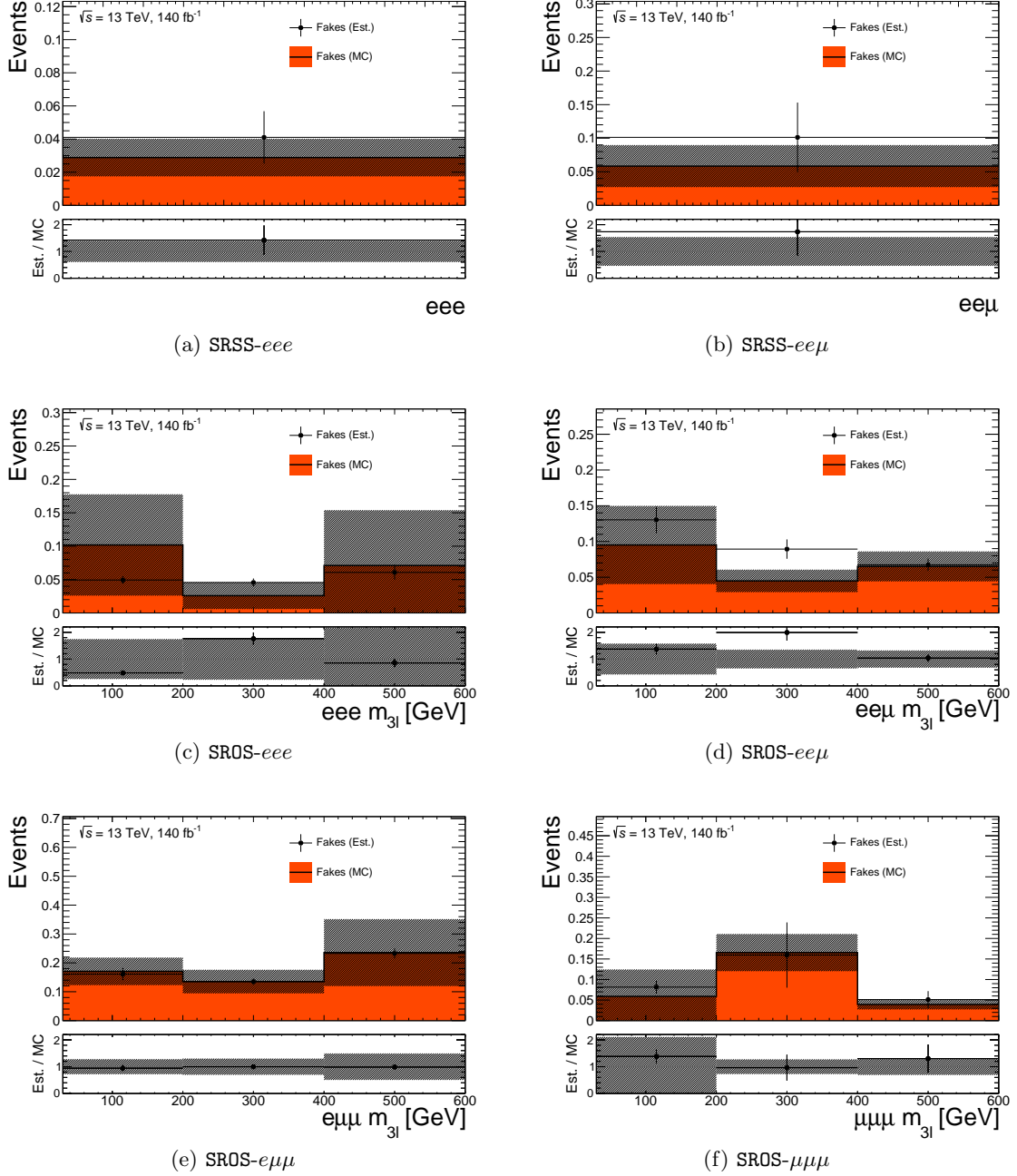


Figure 8.21: Closure test results in SRSS and SROS. The filled histogram shows the number of fake lepton events of MC and dot point indicates the estimation using the Fake Factor method. SRSS- 2μ is not included due to different method of fake estimation (Section 8.4.5). All uncertainties shown are only statistical. Lower panel shows the ratio of estimated and MC fake lepton events.

8.4.4 Validation of Fake Factors

This section validates the fake lepton background prediction. First, Table 8.10 compares data and the background prediction in the **CRFF**, where a good compatibility is expected by construction of the Fake Factor method. The definition of VRs which is denoted as **VRFF** is summarized in Table 8.11. **VRFF** is set to check the availability of Fake Factors to be applied to SFOS off-shell regions which have larger fake contributions in SR. Yields and kinematic distributions in **VRFF** are shown in Table 8.12 and Fig. 8.22. Yields divided according to the lepton flavor are also reported in Table 8.12. All systematic uncertainties, which will be discussed in Chapter 9, are applied and no fit is performed, but the WZ background is scaled by the normalization factors which is obtained in **CRWZ-fakes**.

Table 8.10: Number of observed and expected events in the **CRFF**. The uncertainties include both statistical and systematic uncertainties which will be discussed in Chapter 9.

Region	CRFF
Observed	3840
Total	3860 ± 230
Fakes	1610 ± 240
WZ	1920 ± 40
ZZ	284 ± 32
$t\bar{t}$	7.9 ± 1.1
$t\bar{t}X$	9.8 ± 1.8
VVV	2.39 ± 0.30
Others	22 ± 4

Table 8.11: Definitions of the VRs for validating the estimations of the fake lepton events in **SRFS**. n_{SFOS} represents the number of same-flavor opposite-charge-sign (SFOS) lepton pairs in three leptons. If more than one SFOS lepton pair is present in the event, the invariant mass of the SFOS lepton pair closest to the Z mass is used as $m_{\ell\ell}$.

Variables	VRFF			
	eee	$ee\mu$	$e\mu\mu$	$\mu\mu\mu$
Trigger	single-lepton			
$n_{\text{lep}}^{\text{baseline}}, n_{\text{lep}}^{\text{signal}}$	$= 3$			
$p_T^{\ell_1}, p_T^{\ell_2}, p_T^{\ell_3}$ [GeV]	$> 10, 10, 10$			
$n_{b\text{-jets}}$	$= 0$			
n_{SFOS}	≥ 1			
$m_{\ell\ell}$ [GeV]	$\notin [81.2, 101.2]$			
m_T^{min} [GeV]	< 30			
E_T^{miss} [GeV]	$\in [20, 100)$			
$m_{3\ell}$ [GeV]	> 105			

Table 8.12: Number of observed and expected events in the VRFF. The uncertainties include both statistical and systematic uncertainties which will be discussed in Chapter 9.

Region	VRFF	VRFF- eee	VRFF- $ee\mu$	VRFF- $e\mu\mu$	VRFF- $\mu\mu\mu$
Observed	783	100	129	152	402
Total	790 ± 40	109 ± 16	125 ± 12	152 ± 12	399 ± 24
Fakes	202 ± 34	22 ± 6	51 ± 10	51 ± 10	78 ± 13
WZ	448 ± 15	66 ± 10	50 ± 4	64.4 ± 3.1	268 ± 19
ZZ	59 ± 7	8.8 ± 2.1	8.7 ± 1.3	15.1 ± 2.1	26.7 ± 2.5
$t\bar{t}$	39 ± 6	3.9 ± 0.9	9.6 ± 1.6	9.7 ± 1.7	15.8 ± 2.7
$t\bar{t}X$	4.0 ± 0.7	0.57 ± 0.15	0.71 ± 0.15	1.06 ± 0.24	1.64 ± 0.31
VVV	8.3 ± 0.9	0.79 ± 0.21	2.29 ± 0.34	2.16 ± 0.31	3.04 ± 0.33
Others	25 ± 8	7 ± 6	3.3 ± 0.6	9 ± 4	6.2 ± 1.2

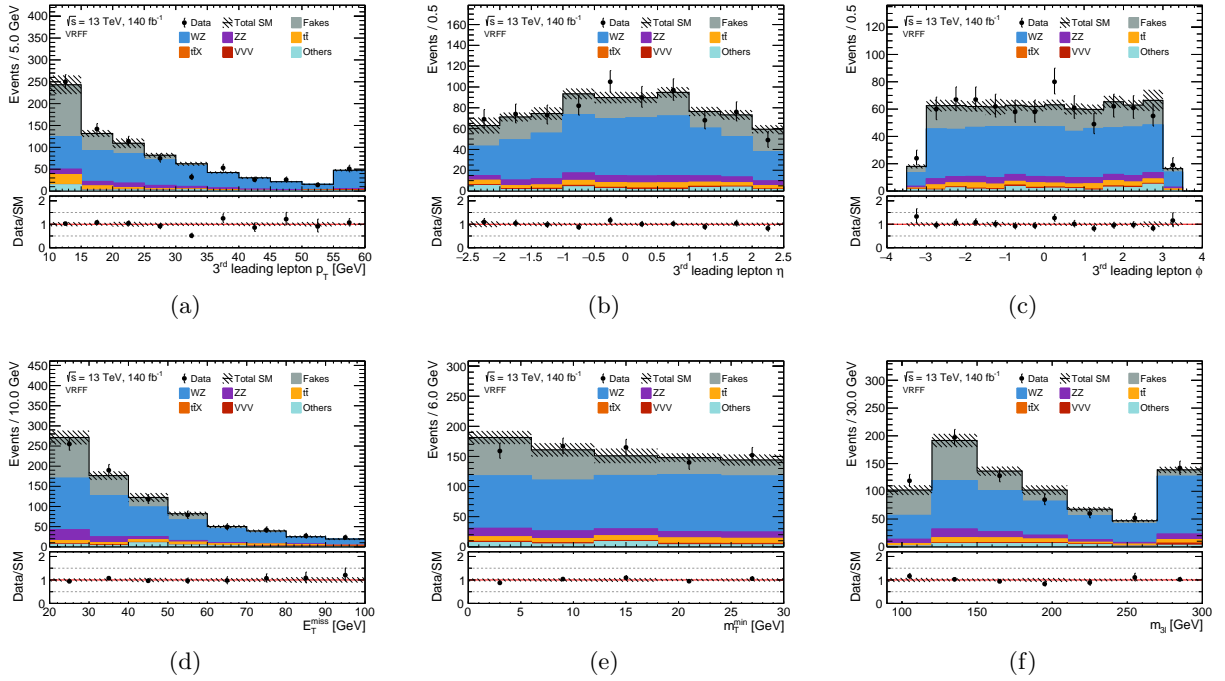


Figure 8.22: Example kinematic distributions, showing the data and the expected background in VRFF. The last bin includes overflow. The “Others” category includes contributions from W +jets, Z +jets, di-boson (excluding full-leptonic $W^\pm Z$ and ZZ), Higgs, and single-top processes. The hatched band includes the combined statistical and systematic uncertainties which will be discussed in Chapter 9. The bottom panel shows the ratio of the observed data to the predicted yields.

8.4.5 Fake Background Estimation for SRSS- 2μ

When the Fake Factor method is naively applied to SRSS- 2μ , we figured out that the total estimation becomes negative and has a large uncertainty (Fig. 8.23). This is due to a very small data statistics in the SRSS- 2μ anti-ID region, resulting in the negative fake estimation, -0.25 ± 0.10 event.

Fig. 8.24 shows the yield in the anti-ID region of SRSS- 2μ loosened by removing the E_T^{miss}

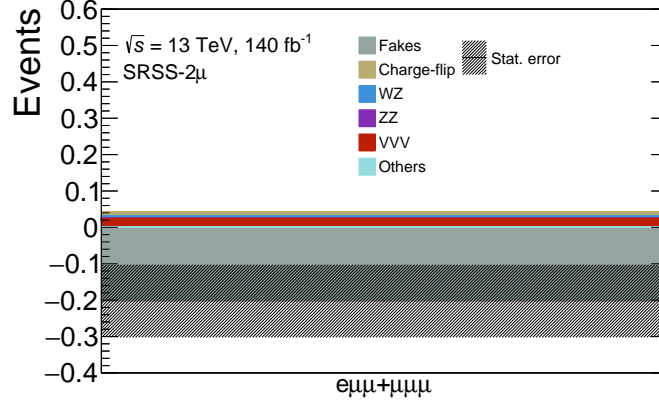


Figure 8.23: Estimation result in SRSS-2 μ when the Fake Factor method is naively applied. All uncertainties shown are only statistical. Central value is negative due to large negative fake estimation.

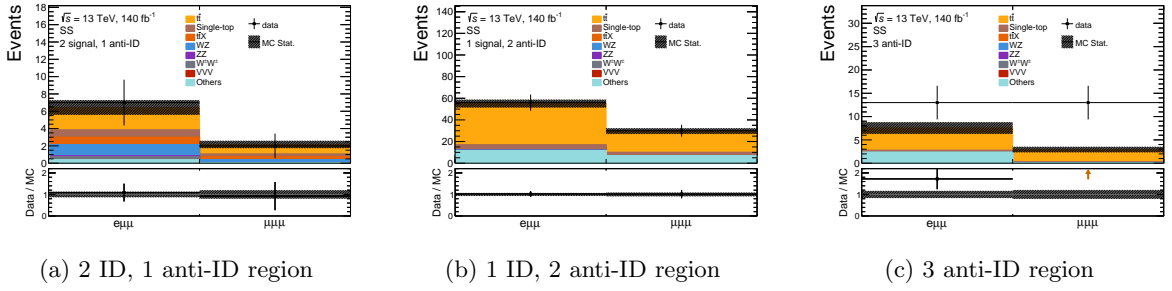


Figure 8.24: Loosen anti-ID region of SRSS-2 μ (no E_T^{miss} cut). MC is not truth matched. The hatched band includes the MC statistical uncertainties. The bottom panel shows the ratio of the observed data to the predicted yields.

cut to increase statistics. MC fake lepton events show a good agreement in the 2 ID, 1 anti-ID and 1 ID, 2 anti-ID regions. Signal contamination in 2 ID, 1 anti-ID region does not exceed 13% for un-excluded scenarios. The discrepancy in 3 anti-ID can be explained by the contributions from multi-jets as the discrepancy disappears when the E_T^{miss} cut is applied. 1 ID, 2 anti-ID and 3 anti-ID regions are dominated by $t\bar{t}$ fakes, while the 2 ID, 1 anti-ID region is composed of $t\bar{t}$, di-boson and $t\bar{t}X$ events. Fake lepton events in SRSS-2 μ are mainly from di-boson and $t\bar{t}X$ events (Fig. 8.25(a)), which have a composition relatively similar to the 2 ID, 1 anti-ID region compared to the 1 ID, 2 anti-ID and 3 anti-ID regions. From MC simulation, it was figured out that fake lepton events in SRSS-2 μ are dominated by “single fake” events which have only one fake lepton out of three leptons as shown in Fig. 8.25(b) and “multi fake” events which have more than two fake leptons can be ignored.

From these observations, we decided to estimate the fake lepton events in SRSS-2 μ by **multiplying the MC fake lepton events in the 2 ID, 1 anti-ID region by the Fake Factors measured in the data** (refer to Fig. 8.16(a)(b)),

$$N_{\text{Est. Fake}} = F_1 N_{\text{LTT}}^{\text{MC Fakes}} + F_2 N_{\text{TLT}}^{\text{MC Fakes}} + F_3 N_{\text{TTL}}^{\text{MC Fakes}}. \quad (8.8)$$

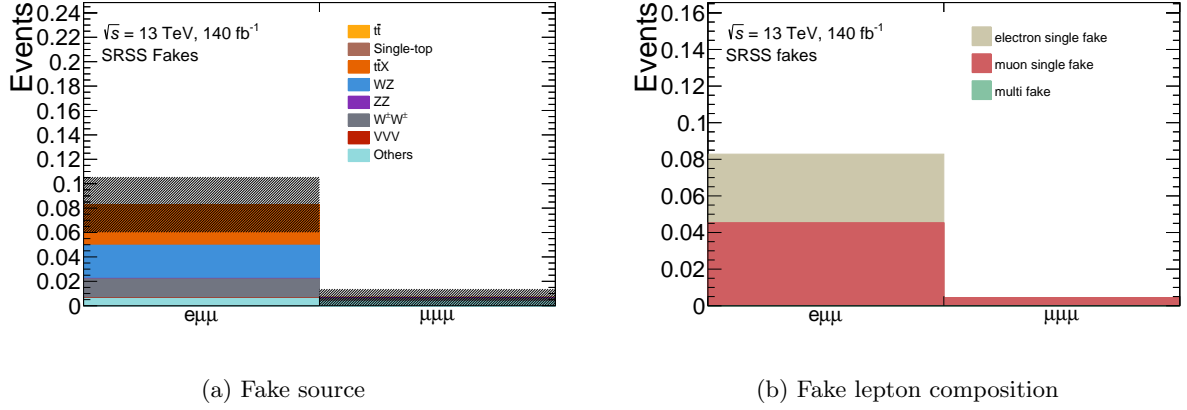


Figure 8.25: (a) : Fake source in SRSS- 2μ by MCs. The hatched band includes the MC statistical uncertainties. (b) : Fake lepton composition in SRSS- 2μ by MCs. “single fake” events contain only one fake lepton, while “multi fake” events contain more than two fake leptons.

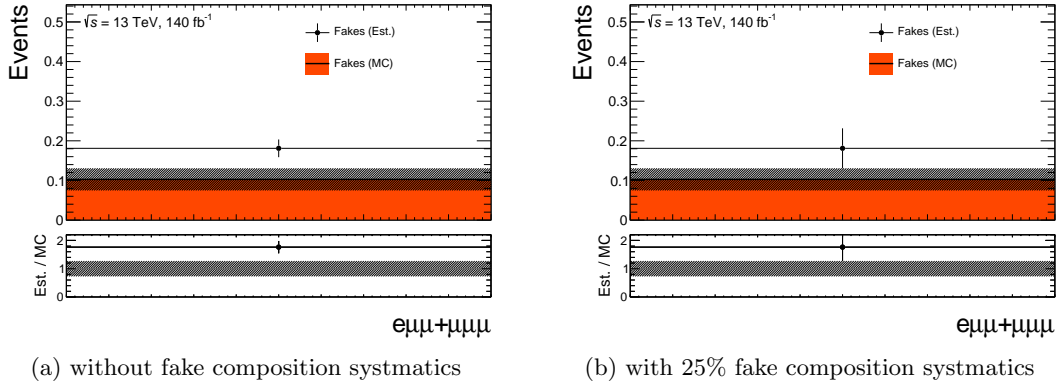


Figure 8.26: Closure test results in SRSS- 2μ . The filled histogram shows the fake expectation from simulation and dot point indicates the estimation using FF method. All uncertainties shown are only statistical. Lower panel shows the ratio of estimated and MC fake lepton events.

As done in Section 8.4.3, a closure test has been performed to check the effect of the different compositions of the fake leptons. MC Fake Factors measured in CRFF are used to perform the Fake Factor method (Eq. 8.8) and it is compared to MC fake lepton events in the SR ID region. The closure test result is demonstrated in Fig. 8.26(a). Some non-closure is observed and a fake composition systematic uncertainty is introduced to take into account this non-closure. Uncertainty of 25% is applied to realize the agreement between MC ID events and estimated fake lepton events, as in Fig. 8.26(b).

VRSS- 2μ is defined to validate the fake estimation method for SRSS- 2μ . To validate the fake lepton events which is dominated in the low p_T region, third lepton p_T cut is reversed against SRSS- 2μ . The cuts are summarized in Table 8.13. Signal contamination in VRSS- 2μ does not exceed 15% for un-excluded scenarios. Table 8.14 shows the yield in VRSS- 2μ and shows a good agreement between data and estimation. An example kinematic distribution in VRSS- 2μ is shown in Figure 8.27. A reasonable agreement is observed.

Table 8.13: Definitions of the VRs for validating the estimations of the fake lepton events in SRSS- 2μ . n_{SFOS} represents the number of same-flavor opposite-charge-sign (SFOS) lepton pairs and n_{DFOS} represents the number of different-flavor opposite-charge-sign (DFOS) lepton pairs in three leptons.

Variables	VRSS
	2μ ($e\mu\mu + \mu\mu\mu$)
Trigger	single-lepton
$n_{\text{lep}}^{\text{baseline}}, n_{\text{lep}}^{\text{signal}}$	= 3
$p_{\text{T}}^{\ell_1}, p_{\text{T}}^{\ell_2}$ [GeV]	> 28, 20
$p_{\text{T}}^{\ell_3}$ [GeV]	< 10
$n_{b\text{-jets}}$	= 0
n_{SFOS}	= 0
n_{DFOS}	= 0
$E_{\text{T}}^{\text{miss}}$ [GeV]	> 50

Table 8.14: Yields for VRSS- 2μ . All uncertainties are included.

Region	VRSS- 2μ
Observed	6
Total	6.9 ± 1.9
Fakes	6.8 ± 1.9
WZ	0.06 ± 0.06
Others	$0.07 \pm \begin{smallmatrix} 0.08 \\ 0.07 \end{smallmatrix}$

8.4.6 Top-like Backgrounds

The top-like backgrounds come predominantly from b -jets originating from the decay of top quark which have small theory uncertainties. This means that a simpler approach based on MC simulation can be used. A CR to normalize the top-like backgrounds in anti-ID regions is constructed using different-flavor opposite-sign three lepton events which is denoted as **CRtt-antiID**. Events must be of the form $e^{\pm}e^{\pm}\mu^{\mp}$ or $e^{\pm}\mu^{\mp}\mu^{\mp}$, where the two same-flavor leptons must have the same-sign and the different flavor lepton must have the opposite-sign. This is advantageous because it guarantees that one of the two same-flavor leptons is the fake lepton, and this criterion allows the CR to be very pure in events with top-like backgrounds. In addition to the different-flavor opposite-sign requirement, a $E_{\text{T}}^{\text{miss}} > 50$ GeV cut is applied for top-like backgrounds purity. The selection criteria is summarized in Table 8.15. Normalization factors are derived separately for fake electron and fake muon events, as well as for events with $n_{b\text{-jets}} = 0$ and $n_{b\text{-jets}} \geq 1$ (to avoid extrapolating over $n_{b\text{-jets}}$). The distributions for this region are shown in Fig. 8.28. The normalization factors for $n_{b\text{-jets}} = 0$ are 1.03 ± 0.06 and 1.07 ± 0.03 for fake electron and fake muon events, respectively. The normalization factors for $n_{b\text{-jets}} \geq 1$ are 0.94 ± 0.03 and 1.03 ± 0.03 for fake electron and fake muon events, respectively.

For validation of top-like backgrounds MC in the ID region, we define a region denoted as **VRtt**. The different-flavor opposite-sign requirement and the number of $n_{b\text{-jets}} \geq 1$ requirement ensures the top-like backgrounds purity as well as the orthogonality to other regions. A $E_{\text{T}}^{\text{miss}}$

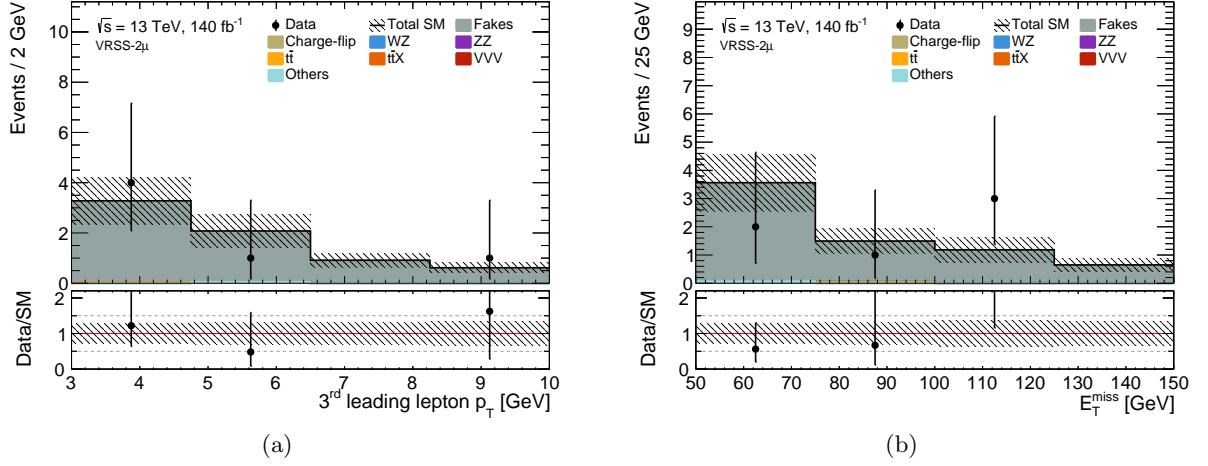


Figure 8.27: Example kinematic distributions for the expected backgrounds and the data, obtained from a background-only fit including systematic uncertainties. The figure shows the (a) $p_T^{\ell_3}$ and (b) E_T^{miss} distribution in VRSS-2 μ . The “Others” category includes contributions from W +jets, Z +jets, di-boson (excluding full-leptonic $W^\pm Z$ and ZZ), Higgs, and single-top processes. The hatched band includes the combined statistical and systematic uncertainties which will be discussed in Chapter 9. The bottom panel shows the ratio of the observed data to the predicted yields.

Table 8.15: Selection criteria used to define CRtt-antiID and VRtt for determining normalization factors for the top-like backgrounds in anti-ID regions and validate top-like backgrounds. “—” indicates no requirement is applied for a given variable/region. n_{SFOS} represents the number of same-flavor opposite-charge-sign (SFOS) lepton pairs and n_{DFOS} represents the number of different-flavor opposite-charge-sign (DFOS) lepton pairs in three leptons.

Variables	CRtt-antiID	VRtt
Trigger	single-lepton	
$n_{\text{lep}}^{\text{baseline}}$	= 3	
$n_{\text{lep}}^{\text{signal}}$	= 2	= 3
$p_T^{\ell_1}, p_T^{\ell_2}, p_T^{\ell_3}$ [GeV]	> 28, 20, 10	
$n_{b\text{-jets}}$	—	≥ 1
n_{SFOS}	= 0	
n_{DFOS}	≥ 1	
E_T^{miss} [GeV]	> 50	

cut is placed in at > 50 GeV to reduce the Z +jets fake background contribution. The cuts are summarized in Table 8.15, while the yields are in Table 8.16. Some kinematic distributions are shown in Fig. 8.29. Good modeling is observed in all of the distributions. To summarize the estimation method, top-like backgrounds in the ID region is estimated directly from MC simulations, while top-like backgrounds in the anti-ID region is treated as prompt events and subtracted from data in the Fake Factor method after applying a NF measured in CRtt-antiID.

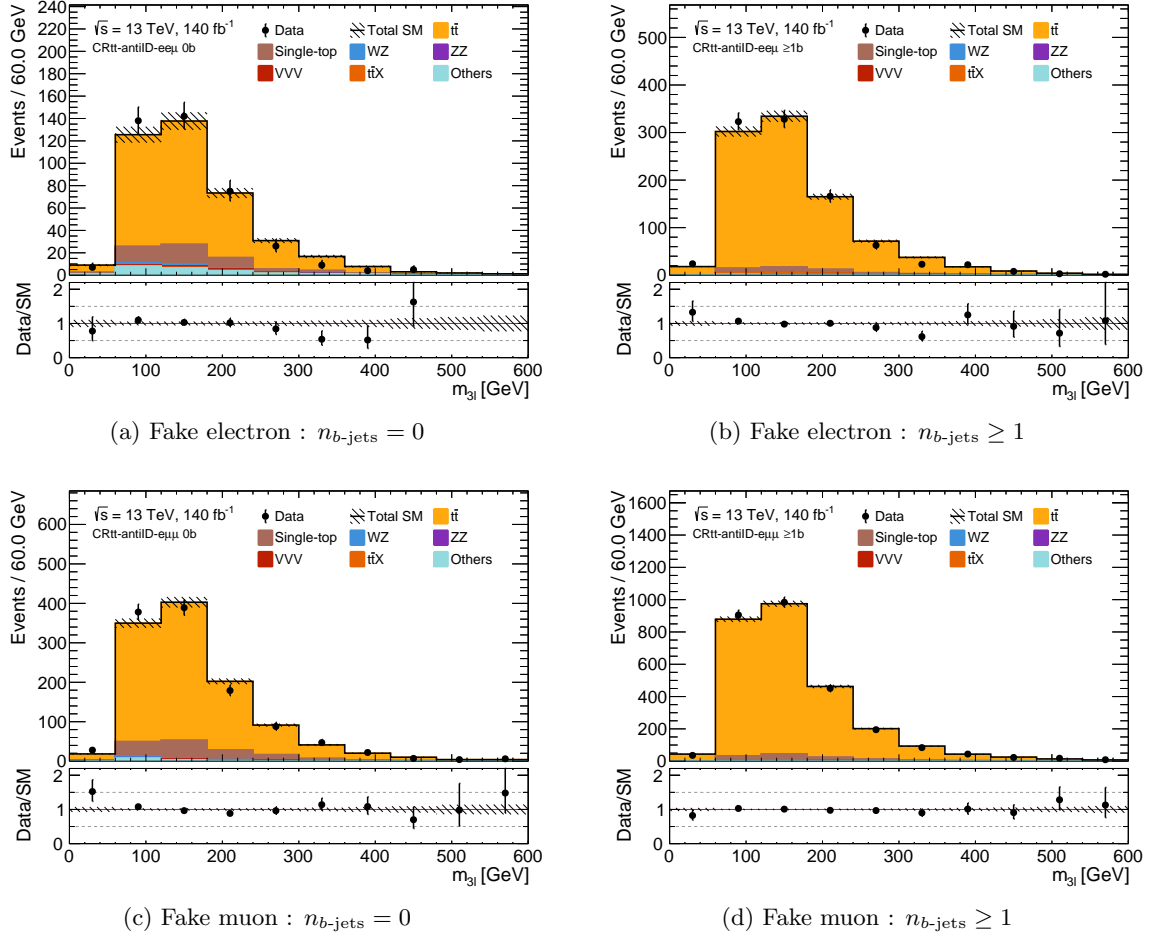
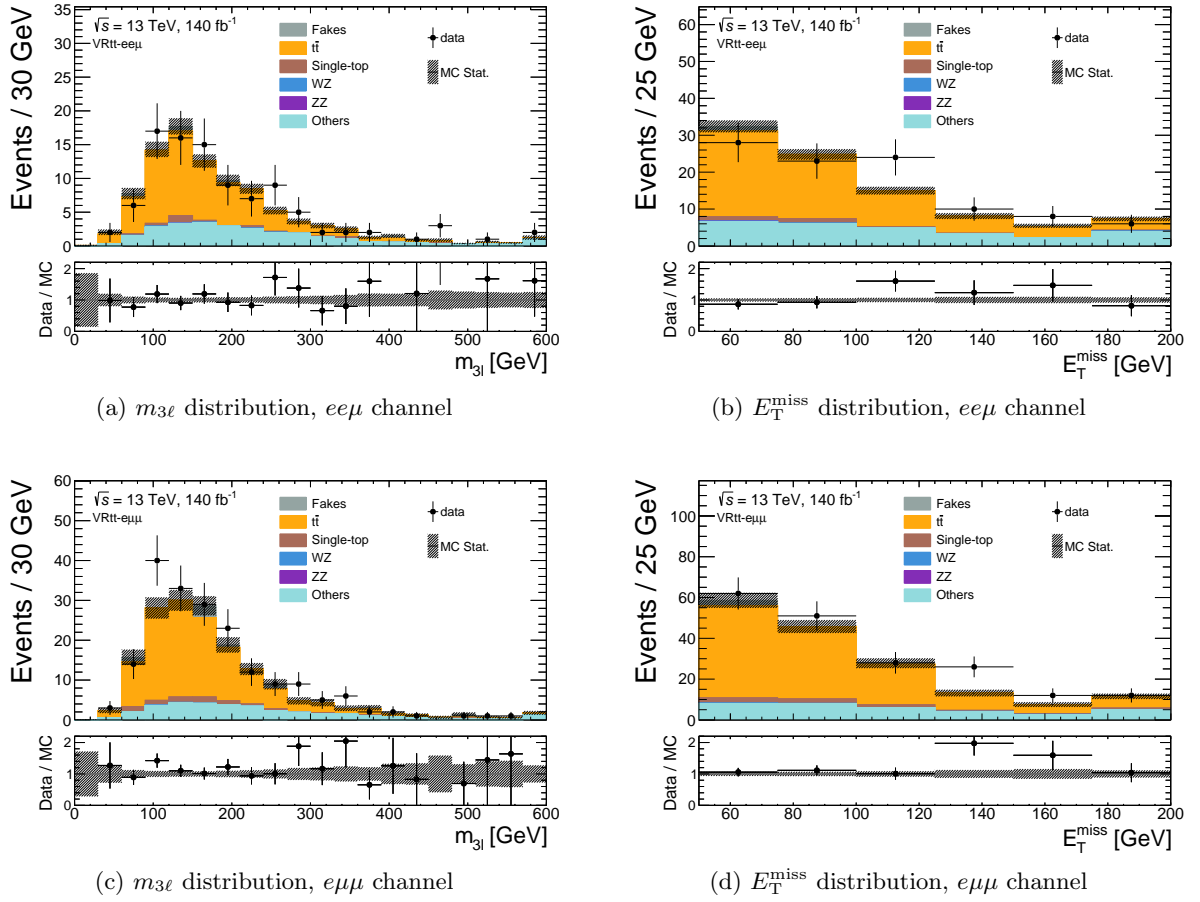


Figure 8.28: Post-fit distributions for events with fake electrons and muons in CRtt-antiID, using only events with two signal leptons and one anti-ID lepton. The hatched band includes the MC statistical uncertainties. The bottom panel shows the ratio of the observed data to the predicted yields.

Table 8.16: Yields for $\text{VRt}\bar{t}$. All uncertainties are included.

Region	$\text{VRt}\bar{t}$
Observed	292
Total	260 ± 60
WZ	0.60 ± 0.20
ZZ	0.036 ± 0.027
VVV	1.9 ± 0.8
$t\bar{t}$	180 ± 50
$t\bar{t}X$	49 ± 9
Fakes	6 ± 6
Others	29 ± 8

Figure 8.29: $m_{3\ell}$ and E_T^{miss} distributions in $\text{VRt}\bar{t}$. The hatched band includes the MC statistical uncertainties. The bottom panel shows the ratio of the observed data to the predicted yields.

8.5 Summary of Background Estimation

A summary of regions is shown in Fig. 8.30. The results of the validation of the background estimation methods described in the previous sections are summarized below. The significance quantifies the difference between the estimated background yields and the data, denoted as χ ,

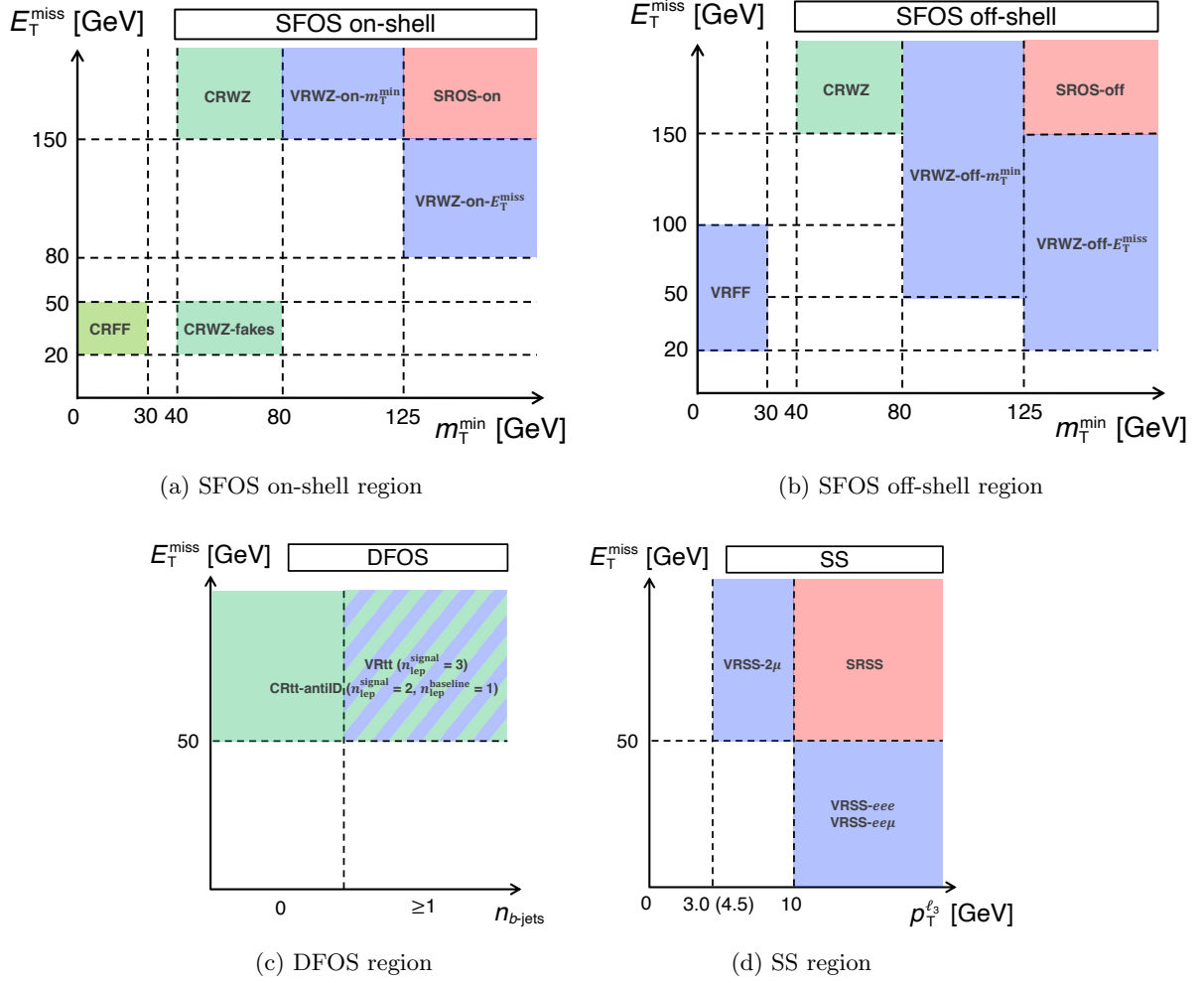


Figure 8.30: Schematics illustrating the selection of the CRs and VRs used to estimate (a)(b) WZ and fake background in SROS, (c) $t\bar{t}$ background in SROS, and (d) charge-flip and fake backgrounds in SRSS, along with the orthogonality with respect to SRs. (a) “SFOS on-shell” stands for the region with one or more SFOS lepton pairs in the event which have the invariant mass consistent with the Z boson mass. (b) “SFOS off-shell” stands for the region with one or more SFOS lepton pairs in the event with none of them having the invariant mass consistent with the Z boson mass. (c) “DFOS” stands for the region with one or more DFOS lepton pairs in the event. (d) “SS” stands for the region with three same-charge-sign leptons in the event.

which is defined as

$$\chi = \frac{n_{\text{obs}} - n_{\text{exp}}}{\sigma_{\text{total}}}, \quad (8.9)$$

$$\sigma_{\text{total}} = \sqrt{\sigma_{\text{exp}}^2 + \sigma_{\text{obs}}^2}, \quad (8.10)$$

where n_{obs} and σ_{obs} are the observed yields and statistical uncertainties, and n_{exp} and σ_{exp} are the expected yield and uncertainties derived from the systematic uncertainties which will be discussed in Chapter 9. The yields and differences for each region are visualized in Fig. 8.31. In all VRs, the expected and observed yields are consistent within the uncertainty.

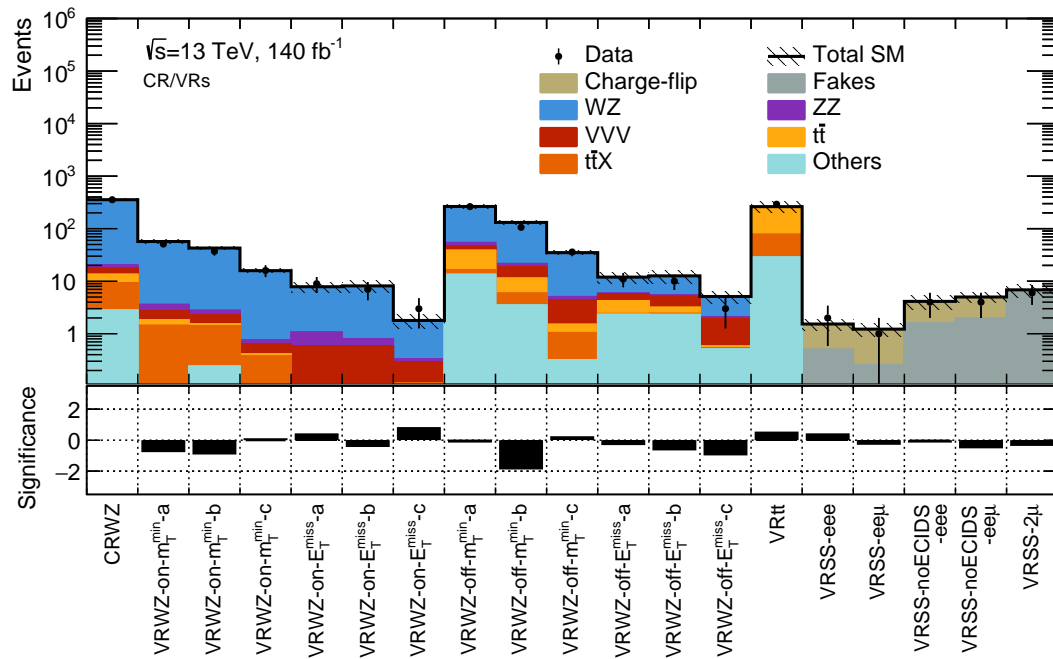


Figure 8.31: Overview of fit results in the CRWZ and VRs. The upper plot summarizes the observed and estimated yields for each region, while the bottom plot illustrates the difference between the observed and estimated yields. The “Other” category includes contributions from W +jets, Z +jets, di-boson (excluding full-leptonic $W^\pm Z$ and ZZ), Higgs, and single-top processes. The hatched band includes the combined statistical and systematic uncertainties which will be discussed in Chapter 9.

Chapter 9

Systematics Uncertainties

The uncertainties of the estimated backgrounds and signal yields are referred to as systematic uncertainties and is discussed in this chapter. This thesis considers three types of systematic uncertainties: theoretical modeling uncertainties, experimental uncertainties, and additional uncertainties arising from the adopted data-driven background estimation strategy discussed in Chapter 8. The contribution to the analysis sensitivity is generally minor, since the total uncertainty in the SRs is dominated by the statistical uncertainty due to the low number of data events in the SRs, as shown in Appendix C.

9.1 Uncertainty for Theoretical Calculation in the Simulation

Theoretical uncertainties arise from the choice of parameters used to generate MC simulation samples, as elaborated in Section 5.2. Varying the parameters has the effect of altering both the cross-section and the shape of the kinematic distribution. This analysis thoroughly evaluates the theoretical uncertainties for all signal and main background processes.

As explained in Section 5.2.1, non-physical variables such as the factorization scale (μ_F) and the renormalization scale (μ_R) are set in the MC simulations. Uncertainties from μ_F and μ_R [225] are evaluated as the variation of the yields obtained by varying these parameters by a factor of 2.0 and 0.5. The PDF [226] and strong coupling constant (α_S) at a specific energy scale are obtained by extrapolating distributions from experiments to higher energy scales using the DGLAP evolution equation and the RGE, respectively. Therefore, experimental uncertainties and missing higher-order calculations in the equations are sources of uncertainties and are evaluated as the variation of the yields obtained using different PDFs and α_S values.

For $W^\pm Z \rightarrow \ell^\pm \nu \ell^\pm \ell^\mp$ and $ZZ \rightarrow \ell^\pm \ell^\mp \ell^\pm \ell^\mp$, we also consider the following theoretical uncertainties. In SHERPA, the energy scale to calculate the overlap between jets from matrix element calculation and parton shower is set to 20 GeV. The uncertainty is evaluated by comparing the yields obtained by varying the energy scale to 30 and 15 GeV. The resummation scale of soft gluon emissions is a potential source of uncertainty and is evaluated by varying the scale by a factor of 0.5 and 2.0. Since $W^\pm Z \rightarrow \ell^\pm \nu \ell^\pm \ell^\mp$ is normalized using the CRWZ, the SRs and the VRs are only affected by the extrapolation of uncertainties from CRWZ.

Single boson and di-boson production are calculated considering NLO QCD corrections, but the contribution of NLO EWK correction becomes more significant, especially in regions where the weak bosons have high transverse momentum. *Additive* scheme of EWK correction is used as nominal as described in Section 5.2.2 and the systematics uncertainty for the EWK correction is evaluated by comparing nominal scheme to *multiplicative* and *exponentiated* scheme.

As mentioned in Section 8.1, the tri-boson background is assigned a special cross-section uncertainty. Tri-boson processes have not yet been precisely measured experimentally, and

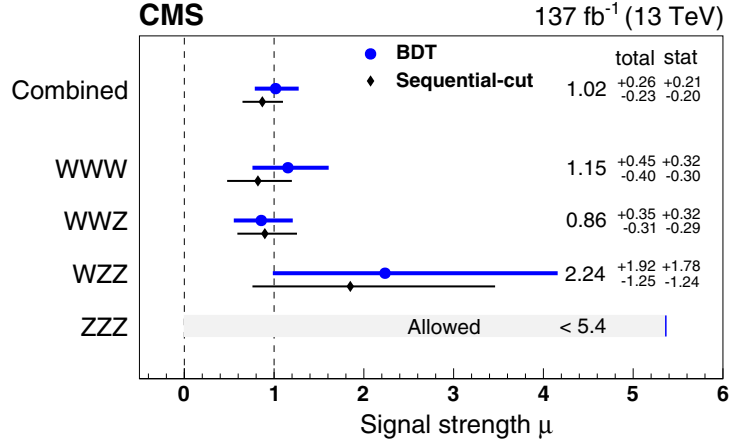


Figure 9.1: Result of the CMS tri-boson measurement [229]. Best fit values of the signal strengths for the BDT-based analyses (blue solid circles) and the sequential-cut analyses (black solid diamonds) are shown. The error bars represent the total uncertainty. For ZZZ production, a 95% confidence level upper limit is shown. The stated numerical values correspond to the BDT-based analysis.

Table 9.1: Cross-section uncertainties for tri-boson processes based on the CMS result [229].

Sample	Cross-section uncertainty (%)
WWW	+45 / -40
WWZ	+35 / -31
WZZ	+192 / -100
ZZZ	+440 / -100

large cross-section uncertainties should be applied. Current best results of tri-boson search at ATLAS [227, 228] and CMS [229] shows the tri-boson cross-section to be consistent with the SM value with large uncertainties. ATLAS has only published the results of WWW and WVZ [227, 228]. As the tri-boson composition in the SRs differs from that based on the cross-section measurement, we want to apply the cross-section uncertainty on each subprocess, thus here we have quoted the tri-boson measurement result of the CMS experiment [229] (Fig. 9.1). The measured signal strength is all consistent with one, therefore the MC normalization is kept as it is⁹ and only the cross-section uncertainties are referred. This is justified by the fact that the CMS measurement is conducted in the three lepton, b -jet veto, Z boson veto, and high m_T region which is not so far from our SRs and the CMS results include the theory uncertainties which was evaluated by CMS. The uncertainties considered are reported in Table 9.1.

For signal samples, in addition to uncertainties from μ_F , μ_R , PDFs, and α_S , theoretical uncertainties for the cross-section are also taken into account.

9.2 Experimental Uncertainty

Experimental uncertainty includes uncertainty in the calibration procedure to match physics objects to data and uncertainty in luminosity measurement and pile-up.

⁹We have checked that WWW cross-section of CMS is consistent to that of the ATLAS WWW MC sample.

Electrons Electrons involve three efficiency uncertainties i.e. reconstruction, identification, and isolation. These are mainly evaluated by the observed differences between the efficiencies measured using the $Z \rightarrow ee$ and $J/\psi \rightarrow ee$ events from data and from the simulation [209]. The uncertainties on the resolution modeling and energy scale are also taken into account. They are evaluated based on the discrepancy between observed and simulated response of the EM calorimeter.

Muons There are four uncertainties related to efficiency and six distinct uncertainties associated with scale concerning muons. These uncertainties arise from the differences observed between the MC predictions and the actual measurements obtained from the $Z \rightarrow \mu\mu$ and $J/\psi \rightarrow \mu\mu$ events [230]. The efficiency uncertainties pertain to aspects such as reconstruction, ineffective muon veto, isolation, and Track-To-Vertex-Association (TTVA). In contrast, the six scale uncertainties consist of two momentum corrections that are independent of charge and four momentum corrections that are dependent on charge.

Jets The residual uncertainty associated with the JES is often the largest source of the instrumental jet uncertainty. This is due to the fact that even a minor adjustment in jet energy can lead to a substantial alteration in the distribution tails. Roughly 100 independent uncertainties are derived from each stage of the calibration process, encompassing both the MC uncertainty and the observed discrepancies between the data and the MC simulations. In this analysis, uncertainties exhibiting similar characteristics are statistically aggregated, resulting in approximately 35 independent uncertainties.

The sub-leading uncertainty associated with the jet pertains to the JER. JER measurement is done by the same dataset used in the in-situ JES calibration, using the well measured objects in di-jet or $Z/\gamma^* + \text{jets}$ events [231]. The measurement of JER is conducted utilizing the same dataset employed for the in-situ JES calibration, which incorporates well-measured objects from di-jet or $Z/\gamma^* + \text{jets}$ events [231]. This uncertainty is derived from the discrepancies observed between data and MC simulations, as well as the extent of the noise term that indicates a limited understanding of its origins. More than 30 independent uncertainties are modeled at each stage of the calibration process, which are subsequently consolidated into approximately 15 independent uncertainties for this analysis.

As most of the analysis' regions involve a b -jet veto, the b -tagging uncertainties are also considered. The uncertainties on the calibration of the efficiencies for b , c , and light-flavor jets are included. The uncertainties arise from the efficiency corrections applied to simulated events, parametrized over the jet p_T and flavor. The b -tagging efficiency uncertainty ranges from 1% to 8% depending on the jet p_T .

Other uncertainties are quoted regarding to the angular position determination (η -calibration uncertainty) or JVT (Jet Vertex Tagger, Section 6.7) modeling.

Missing Transverse Energy In addition to the inherent uncertainties associated with the scales and resolutions of the reconstructed objects, such as electrons, muons, jets, and photons, the E_T^{miss} is further complicated by uncertainties related to the modeling of the soft term, as outlined in Section 6.9. This modeling uncertainty is assessed through the analysis of $Z \rightarrow \mu\mu$ events, where a comparison is made between the observed momentum profile of the soft terms and the anticipated profiles.

Triggers In this analysis, single-electron and single-muon trigger is used as mentioned in Section 5.3. The uncertainty related to the correction of difference between data and simulation is involved.

Luminosity The size of uncertainty on luminosity is obtained by using the LUCID-2 detector [160]. The uncertainty of the combined 2015-2018 integrated luminosity is 0.83% [165].

Pile-up The distribution of the mean number of interactions per crossing in MC simulation samples is reweighted to match the distribution in the data as discussed in Section 5.2.1. The uncertainty of the applied reweighting factor, evaluated with measured inelastic cross-sections [232], is included.

9.3 Uncertainties from Data-driven Background Estimations

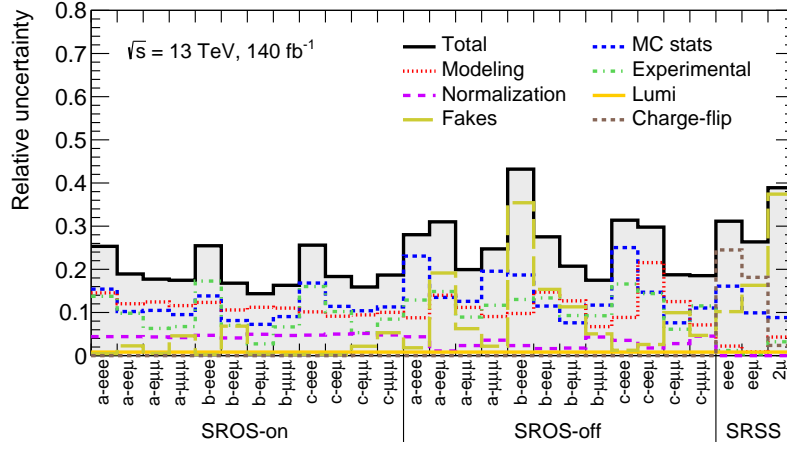
As discussed in Section 8.3 and 8.4, the background estimation methods for the charge-flip and fake lepton backgrounds are associated with several systematic uncertainties. The data-driven method of determining the charge-flip scale factor is affected by the systematic uncertainties related to the fit uncertainty, background subtraction from data, and the charge-flip probability parametrization. Background subtraction systematic uncertainty dominates the uncertainty in low p_T region, while the high p_T region uncertainty is mainly by the parametrization non-closure and the fit uncertainty due to small statistics. In addition to the scale factor uncertainty, 20% flat uncertainty accounting for the difference in charge-flip source in SRs, WZ , and the scale factor measurement region (CRCF), $Z \rightarrow ee$, is also introduced. For the Fake Factor determination, systematic uncertainties regarding the statistical uncertainty, WZ subtraction, and E_T^{miss} cut are considered. A 28.5% (25%) flat uncertainty accounting for the difference in fake lepton composition in $\text{SROS-}ee\mu$ $m_{3\ell} \in [200, 400)$ GeV bin (SRSS- 2μ) and the Fake Factor measurement region (CRFF) is additionally introduced.

9.4 Summary of Systematic Uncertainties

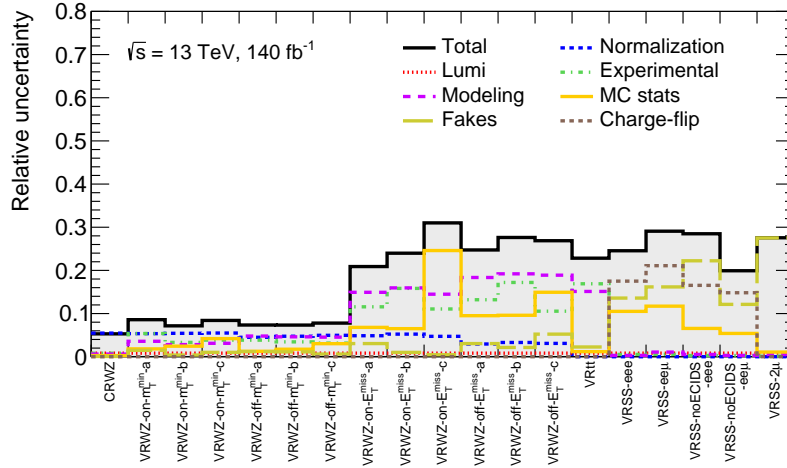
In addition to the uncertainties described above, two additional uncertainties are considered.

- **CR data statistics** : The uncertainty arising from the limited data statistics in CRs. This includes both the CRWZ data statistics for the WZ NF estimation, discussed in Section 8.2 and the anti-ID region data statistics for the fake estimation, discussed in Section 8.4.3.
- **MC statistics** : The uncertainty arising from the limited number of MC simulation samples.

The total systematic uncertainty, along with the breakdown in each SR, CR, and VR is visualized in Fig. 9.2. In SROS-on the leading uncertainty is the MC statistics followed by the theory uncertainty. MC statistics and theory uncertainty are also the important uncertainty in SROS-off . The fake uncertainty is dominant in $\text{SROS-off-b-}ee\mu$ because of the large contribution of fake lepton background compared to WZ . $\text{SRSS-}eee$ and $\text{SRSS-}ee\mu$ are dominated by the charge-flip uncertainty and $\text{SRSS-}2\mu$ is dominated by the fake uncertainty as expected from the background composition.



(a)



(b)

Figure 9.2: Systematic uncertainties on the post-fit background yields in the (a) SRs and (b) CR/VRs for WZ , VR for $t\bar{t}$, charge-flip, and fake leptons. The “MC stats” category represents the uncertainty arising from the limited number of MC simulation samples. The “Modeling” uncertainty category represents the theory uncertainty arising from the choice of parameters for generating MC simulation samples. The “Experimental” category indicates systematic uncertainties originating from the reconstruction, identification, isolation, and calibration of physics objects. The “Normalization” category indicates systematic uncertainties arising from the WZ NF uncertainty involving statistical uncertainty originating from the limited CRWZ statistics. The “Lumi” category represents the integrated luminosity uncertainty. The “Fakes” category involves the uncertainty arising from the fake factor uncertainty, the fake lepton composition difference in CRFF and SRSS- 2μ , and the limited anti-ID CR statistics. The “Charge-flip” category represents the systematic uncertainties originating from the charge-flip scale factor uncertainty and the charge-flip source difference in CRCF and SRs.

Chapter 10

Result

The data in the SRs is compared with the background and signal estimations. To examine the presence of signals, the profile Log Likelihood Ratio (LLR) approach is used. Three types of fit configurations are used to derive the results.

- **Background-only fit** : The purpose is to estimate the backgrounds in SRs and VRs without any signal assumptions. In this configuration the WZ NF and the background nuisance parameters are fit to data in **CRWZ**. No signal is included in the fit. Results can be found in Section 10.2.
- **Model-Dependent Interpretation** : The purpose is to set limits on a specific model of BSM physics. Both **CRWZ** and SRs are used in the fit. The potential signal contribution is also taken into account in all regions. Results can be found in Section 10.3.
- **Model-Independent Search** : The purpose is to set model-independent limits on the number of BSM events in flavor merged inclusive SRs and each SR bin. Both **CRWZ** and a SR are used in the fit. The signal contribution is considered only in the SR. Results can be found in Section 10.4.

10.1 Statistical Analysis and Hypothetical Test

Profile likelihood and treatment of systematic uncertainties Statistical analysis is conducted to assess the alignment between the observed data and the expected SM background, as well as to evaluate scenarios where a specific signal is superimposed. This assessment is carried out using a likelihood function that relies on the probability density distribution [233] concerning the count of observed events within each SR bin. The likelihood is given by

$$\mathcal{L}(\mathbf{n}|\mu_s, \mu_{WZ}, \mathbf{s}, \mathbf{b}, \boldsymbol{\theta}) = \prod_{i \in \{\text{Regions}\}} \mathcal{P}_i \times \prod_{k \in \{\text{Syst. sources}\}} \rho(\theta_k), \quad (10.1)$$

where \mathbf{n} is the vector of numbers of observed events in SRs and **CRWZ**; \mathbf{s} is the vector of expected signal yield in the signal model to be tested; \mathbf{b} is the vector of expected yields of backgrounds; $\boldsymbol{\theta}$ represents the nuisance parameters associated with each systematic uncertainty; μ_{WZ} is the NF for WZ ; and μ_s is the signal strength, serving as a measure of the relative normalization in relation to the signal model under examination. Specifically, a value of $\mu_s = 0$ indicates a hypothesis that considers only the background, while $\mu_s = 1$ corresponds to a hypothesis that aligns with the expected nominal signal level.

The statistical properties of the probability density functions are completely defined by the multiplication of Poisson distributions corresponding to each SR or CR:

$$\mathcal{P}_i = \text{Pois}(n_i|\lambda_i) = \frac{\lambda_i^{n_i}}{n_i!} e^{-\lambda_i}, \quad (10.2)$$

where λ_i is given by:

$$\lambda_i(\mu_s, \mu_{WZ}, \mathbf{s}, \mathbf{b}, \boldsymbol{\theta}) = \mu_s \cdot s_i(\boldsymbol{\theta}) + \mu_{WZ} \cdot b_{i,WZ}(\boldsymbol{\theta}) + \sum_{l \in \{\text{Background w/o NF}\}} b_{i,l}(\boldsymbol{\theta}). \quad (10.3)$$

Systematic uncertainties, indexed by k , are included by adjusting the Poisson mean λ_i using a related nuisance parameter θ_k . A global fit is conducted on the data to find μ_s , μ_{WZ} , and $\boldsymbol{\theta}$ simultaneously by minimizing the likelihood \mathcal{L} (Eq. 10.1). While μ_s and μ_{WZ} can float, the adjustments of the nuisance parameters $\boldsymbol{\theta}$ must be limited to reflect the level of confidence. This is done through “penalty terms” in the likelihood, $\prod_{k \in \text{syst.}} \rho(\theta_k)$, which act as prior constraints. The form of these penalty terms varies based on the statistical characteristics of each systematic uncertainty:

- A Gaussian probability density function is typically used for the most of systematic uncertainties.:

$$\rho(\theta) = \frac{1}{\sqrt{2\pi}\sigma} \exp\left(-\frac{\theta^2}{2}\right). \quad (10.4)$$

- A Gamma probability density function is utilized to characterize uncertainties that adhere to the Poisson distribution, which is commonly associated to the count of data events or selected MC events:

$$\rho(a) = \frac{\lambda^a}{a!} e^{-\lambda}, \quad (10.5)$$

where a is associated with θ through the symmetrized uncertainty σ :

$$\theta = \frac{a - \lambda}{\sigma}. \quad (10.6)$$

A multi-dimensional minimization is conducted across the parameter spaces of all NF, nuisance parameters, and signal strength using the `Minuit2` algorithm [234], which is integrated with a wrapper package; `HistFitter` [235]. Systematic uncertainties that have a negligible effect on the yields in the SR or CR bins, which is assessed by the Kolmogorov-Smirnov test [236], are omitted from the fitting process to streamline the scan by reducing unnecessary dimensions (a process referred to as “pruning”).

Hypothetical testing A hypothetical test of a hypothesis H is conducted by assessing its alignment with observations through the use of the p -value. The p -value associated with testing hypothesis H is the probability to obtain results that show as much or more disagreement with H than the observed results. In order to determine the “test statistic” for the hypothesis test, the profile likelihood ratio is employed as;

$$\lambda(\mu) = \begin{cases} \frac{\mathcal{L}(\mu_s, \hat{\mu}_{WZ}, \hat{\boldsymbol{\theta}})}{\mathcal{L}(\hat{\mu}_s, \hat{\mu}_{WZ}, \hat{\boldsymbol{\theta}})}, & (\hat{\mu}_s > 0), \\ \frac{\mathcal{L}(\mu_s, \hat{\mu}_{WZ}, \hat{\boldsymbol{\theta}})}{\mathcal{L}(0, \hat{\mu}_{WZ}, \hat{\boldsymbol{\theta}}(0))}, & (\hat{\mu}_s < 0). \end{cases} \quad (10.7)$$

where $\hat{\mu}_{WZ}$ and $\hat{\theta}$ denotes the best-fit nuisance parameters with fixed μ_s , while $\hat{\mu}_s$, $\hat{\mu}_{WZ}$ and $\hat{\theta}$ denotes the best-fit parameters with $\hat{\mu}_s$ is allowed to float. Using the profile likelihood ratio as defined, the test statistic is expressed as

$$q_\mu = -2 \ln \lambda(\mu_s). \quad (10.8)$$

The p -value, representing the probability of obtaining the observed data or data that shows greater disagreement with the null hypothesis, can be defined as:

$$p_\mu = \int_{q_{\mu, \text{obs}}}^{\infty} f(q_\mu | \mu_s) dq_\mu, \quad (10.9)$$

where $f(q_\mu | \mu_s)$ represents the probability density function of q_μ with a given μ_s value. Executing the hypothesis test involves obtaining $f(q_\mu | \mu_s)$ for each μ_s value by running pseudo experiments called “toy-experiments”, which requires a substantial amount of computing resources to obtain a distribution with sufficient statistics. Another method is to use the approximation formula such as Wald’s approximation [237],

$$q_\mu = -2 \ln \lambda(\mu_s) = \frac{\mu_s - \hat{\mu}_s}{\sigma^2} + \mathcal{O}(1/\sqrt{N}), \quad (10.10)$$

and the asymptotic formula based on the Asimov dataset [233],

$$f(q_\mu | \mu_s) = \frac{1}{\sqrt{q_\mu}} \frac{1}{\sqrt{2\pi}} \left[\exp \left(-\frac{1}{2} (\sqrt{q_\mu} + \sqrt{R}) \right) + \exp \left(-\frac{1}{2} (\sqrt{q_\mu} - \sqrt{R}) \right) \right], \quad (10.11)$$

$$R := \frac{(\mu_s - \hat{\mu}_s)^2}{\sigma^2},$$

where σ denotes the fitting uncertainty associated with $\hat{\mu}_s$ and N signifies the total number of events observed in SRs. It is important to recognize that the approximation effectively disregards the $\mathcal{O}(1/\sqrt{N})$ terms, approximation that may lack full justification, particularly since the some SRs contain fewer than five events. In the thesis, the result for model-independent search which will be presented in Section 10.4 is obtained using the rigid toy-experiments. On the other hand, for the purpose of limit setting which will be discussed in Section 10.3, Asimov’s formula (Eq. 10.11) is employed to circumvent the impractical computational time associated with the toy-experiments.

To check if the certain signal strength μ_s is excluded, a quantity CL_s is used which is defined as,

$$\text{CL}_s = \frac{\text{CL}_{s+b}}{\text{CL}_b} = \frac{p_{\mu_s}}{p_{\mu=0}}. \quad (10.12)$$

The p -value from the combined signal and background hypothesis is divided by the p -value derived from the background-only hypothesis to avoid setting limits in regions of low experimental sensitivity. The exclusion of a signal hypothesis at the 95% confidence level (CL) is defined to be CL_s less than 0.05.

10.2 Unblinded Signal Regions with Background-only Fit Results

The background expectations for the null signal hypothesis in SRs are determined bin-by-bin through a simultaneous fitting process. This fitting involves the WZ NF, μ_{WZ} , as well as the nuisance parameters related to systematic uncertainties, applied to the data across all pertinent

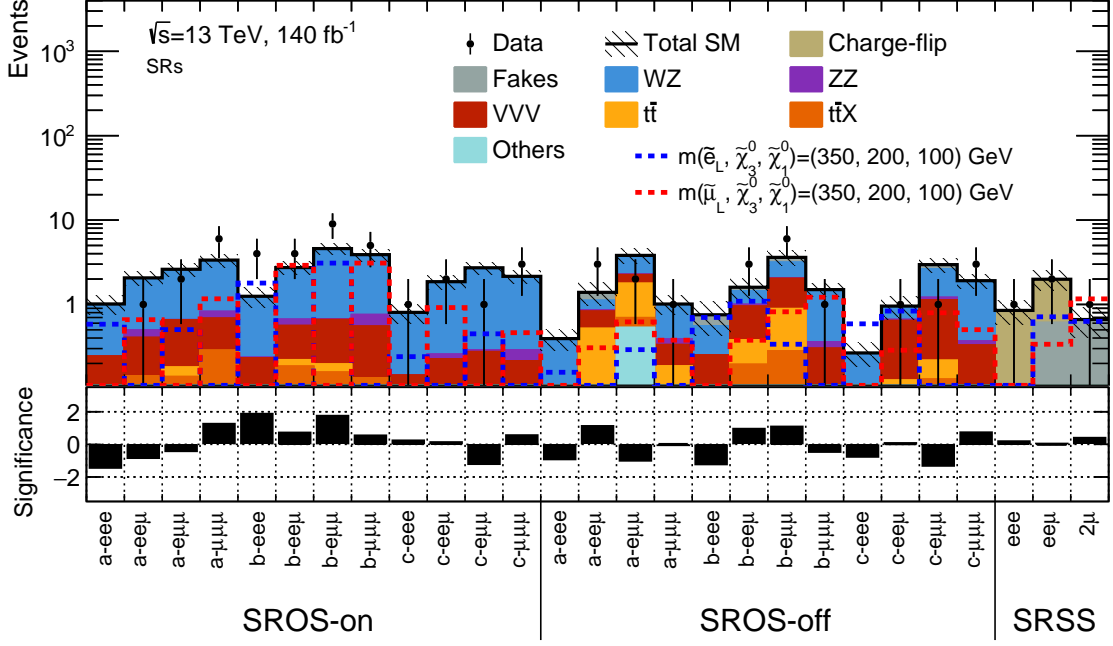


Figure 10.1: (Top) Observed data yields (black dots) and the background expectation (histogram) in the SRs. The hatched band includes the combined statistical and systematic uncertainty on the total estimated backgrounds. The dashed line illustrates signal simulation samples for selectron (blue) and smuon (red) which masses are set to $m(\tilde{\ell}_L, \tilde{\chi}_3^0, \tilde{\chi}_1^0) = (350, 200, 100)$ GeV. (Bottom) Pull between the observed data and the expectation. No significant deviation from expectation exceeding 2σ is observed.

bins of CRWZ and SRs. The unblinded results of the observed data, along with the anticipated backgrounds in the SRs, are presented in Tables 10.1-10.3. The observed data agree with the background-only hypothesis, with no SRs showing deviations exceeding 2σ . The maximum deviation of the data from the background expectation is in **SROS-on-b-eee** with an excess of 1.8σ , followed by a 1.7σ excess in **SROS-on-b-e $\mu\mu$** ; the significances are computed following the prescription in Ref. [238]. The pulls between data and expectation is shown in Fig. 10.1.

Fig. 10.2 and 10.3 show the kinematic distributions of data and prediction in **SROS-on-b-eee** and **SROS-on-b-e $\mu\mu$** where we observed the largest two excesses of data. Kinematic distributions of other regions are shown in Appendix D. It can be seen from Fig. 10.2(a) that the $m_{3\ell}$ distribution of data in **SROS-on-b-eee** is consistent with the signal with $\Delta m(\tilde{\ell}_L, \tilde{\chi}_1^0) \simeq 350$ GeV. As an example, signal mass with $m(\tilde{\ell}_L, \tilde{\chi}_3^0, \tilde{\chi}_1^0) = (450, 200, 100)$ GeV is overlaid. m_T^{min} and E_T^{miss} distribution of **SROS-on-b-eee** are shown in Fig. 10.3(a)(b). The observed data does not seem to contradict the signal distribution, but due to low statistics it is difficult to have a definitive conclusion.

From Fig. 10.2(b), it is seen that data exceeds the prediction at $m_{3\ell} \in [200, 240)$ GeV and $[280, 320)$ GeV bin in **SROS-on-b-e $\mu\mu$** . On the other hand, the E_T^{miss} distribution which is shown in Fig. 10.3(d) looks more unlikely to be explained by the targeted models. Four out of nine events in **SROS-on-b-e $\mu\mu$** fall into $E_T^{\text{miss}} \in [150, 160)$ GeV, while zero events are found in $E_T^{\text{miss}} \in [140, 150)$ GeV. This implies that the excess in **SROS-on-b-e $\mu\mu$** is due to the statistical fluctuations before and after the $E_T^{\text{miss}} > 150$ GeV cut.

Table 10.1: Observed and expected yields after the background-only fit in SR0S-on. The normalization factors of the WZ sample are extracted from CRWZ. The “Others” category includes contributions from W +jets, Z +jets, di-boson (excluding full-leptonic $W^\pm Z$ and ZZ), Higgs, and single-top processes. Combined statistical and systematic uncertainties are presented.

Region	SR0S-on-a-eee	SR0S-on-a-ee μ	SR0S-on-a-e $\mu\mu$	SR0S-on-a- $\mu\mu\mu$
Observed data	0	1	2	6
Fitted SM	1.01 ± 0.26	2.1 ± 0.4	2.6 ± 0.5	3.4 ± 0.6
WZ	0.77 ± 0.20	1.57 ± 0.31	2.0 ± 0.4	2.4 ± 0.5
ZZ	< 0.005	0.090 ± 0.034	< 0.005	0.14 ± 0.05
VVV	0.17 ± 0.13	0.26 ± 0.19	0.47 ± 0.28	0.40 ± 0.31
$t\bar{t}$	< 0.05	< 0.05	$0.04 \pm {}^{0.04}_{0.04}$	< 0.05
$t\bar{t}X$	0.059 ± 0.029	0.14 ± 0.06	0.13 ± 0.05	0.28 ± 0.09
Fakes	< 0.005	$0.00 \pm {}^{0.05}_{0.00}$	$0.000 \pm {}^{0.014}_{0.000}$	$0.11 \pm {}^{0.15}_{0.11}$
Others	$0.019 \pm {}^{0.021}_{0.019}$	< 0.007	0.011 ± 0.005	< 0.006

Region	SR0S-on-b-eee	SR0S-on-b-ee μ	SR0S-on-b-e $\mu\mu$	SR0S-on-b- $\mu\mu\mu$
Observed data	4	4	9	5
Fitted SM	1.25 ± 0.32	2.7 ± 0.5	4.6 ± 0.7	3.9 ± 0.6
WZ	1.01 ± 0.28	1.93 ± 0.33	3.9 ± 0.6	3.1 ± 0.6
ZZ	< 0.005	0.105 ± 0.035	0.012 ± 0.009	0.21 ± 0.06
VVV	0.18 ± 0.13	0.34 ± 0.23	0.46 ± 0.28	0.42 ± 0.30
$t\bar{t}$	< 0.05	$0.04 \pm {}^{0.04}_{0.04}$	$0.04 \pm {}^{0.05}_{0.04}$	< 0.05
$t\bar{t}X$	0.05 ± 0.04	0.18 ± 0.05	0.15 ± 0.07	0.13 ± 0.06
Fakes	< 0.003	$0.14 \pm {}^{0.19}_{0.14}$	$0.000 \pm {}^{0.016}_{0.000}$	< 0.008
Others	< 0.002	< 0.005	< 0.006	< 0.004

Region	SR0S-on-c-eee	SR0S-on-c-ee μ	SR0S-on-c-e $\mu\mu$	SR0S-on-c- $\mu\mu\mu$
Observed data	1	2	1	3
Fitted SM	0.81 ± 0.21	1.86 ± 0.34	2.7 ± 0.4	2.2 ± 0.4
WZ	0.66 ± 0.19	1.60 ± 0.32	2.4 ± 0.4	1.8 ± 0.4
ZZ	< 0.005	0.031 ± 0.028	0.013 ± 0.007	0.073 ± 0.028
VVV	0.09 ± 0.06	0.19 ± 0.10	0.18 ± 0.11	0.20 ± 0.13
$t\bar{t}$	< 0.05	< 0.05	$0.06 \pm {}^{0.08}_{0.06}$	< 0.05
$t\bar{t}X$	0.052 ± 0.026	0.036 ± 0.024	0.031 ± 0.022	$0.011 \pm {}^{0.023}_{0.011}$
Fakes	< 0.002	< 0.004	$0.02 \pm {}^{0.06}_{0.02}$	$0.09 \pm {}^{0.11}_{0.09}$
Others	< 0.002	< 0.002	< 0.001	< 0.001

Table 10.2: Observed and expected yields after the background-only fit in **SR0S-off**. The normalization factors of the WZ sample are extracted from **CRWZ**. The “Others” category includes contributions from W +jets, Z +jets, di-boson (excluding full-leptonic $W^\pm Z$ and ZZ), Higgs, and single-top processes. Combined statistical and systematic uncertainties are presented.

Region	SR0S-off-a-eee	SR0S-off-a-ee μ	SR0S-off-a-e $\mu\mu$	SR0S-off-a- $\mu\mu\mu$
Observed data	0	3	2	1
Fitted SM	0.39 ± 0.11	1.4 ± 0.4	3.8 ± 0.8	1.01 ± 0.25
WZ	0.30 ± 0.10	0.26 ± 0.12	1.54 ± 0.24	0.62 ± 0.21
ZZ	< 0.005	0.027 ± 0.019	0.027 ± 0.016	0.053 ± 0.034
VVV	0.06 ± 0.04	0.31 ± 0.16	0.48 ± 0.20	0.15 ± 0.08
$t\bar{t}$	< 0.05	0.41 ± 0.24	1.1 ± 0.4	0.13 ± 0.10
$t\bar{t}X$	0.028 ± 0.017	0.08 ± 0.04	0.16 ± 0.06	0.046 ± 0.020
Fakes	< 0.007	0.28 ± 0.27	$0.00 \pm \begin{smallmatrix} 0.24 \\ 0.00 \end{smallmatrix}$	$0.000 \pm \begin{smallmatrix} 0.022 \\ 0.000 \end{smallmatrix}$
Others	< 0.01	0.032 ± 0.012	0.5 ± 0.5	0.0101 ± 0.0034

Region	SR0S-off-b-eee	SR0S-off-b-ee μ	SR0S-off-b-e $\mu\mu$	SR0S-off-b- $\mu\mu\mu$
Observed data	0	3	6	1
Fitted SM	0.75 ± 0.33	1.6 ± 0.4	3.6 ± 0.7	1.50 ± 0.26
WZ	0.30 ± 0.10	0.45 ± 0.14	1.10 ± 0.23	1.12 ± 0.22
ZZ	< 0.005	0.049 ± 0.029	0.034 ± 0.023	0.058 ± 0.029
VVV	0.17 ± 0.11	0.57 ± 0.28	1.1 ± 0.5	0.23 ± 0.11
$t\bar{t}$	< 0.05	0.18 ± 0.11	0.61 ± 0.25	< 0.05
$t\bar{t}X$	< 0.01	0.15 ± 0.05	0.24 ± 0.07	0.064 ± 0.031
Fakes	$0.20 \pm \begin{smallmatrix} 0.27 \\ 0.20 \end{smallmatrix}$	$0.15 \pm \begin{smallmatrix} 0.25 \\ 0.15 \end{smallmatrix}$	0.5 ± 0.4	$0.02 \pm \begin{smallmatrix} 0.08 \\ 0.02 \end{smallmatrix}$
Others	$0.07 \pm \begin{smallmatrix} 0.11 \\ 0.07 \end{smallmatrix}$	0.040 ± 0.016	0.039 ± 0.011	< 0.01

Region	SR0S-off-c-eee	SR0S-off-c-ee μ	SR0S-off-c-e $\mu\mu$	SR0S-off-c- $\mu\mu\mu$
Observed data	0	1	1	3
Fitted SM	0.27 ± 0.08	0.96 ± 0.28	3.0 ± 0.6	1.91 ± 0.35
WZ	0.16 ± 0.07	0.29 ± 0.09	1.43 ± 0.22	1.49 ± 0.30
ZZ	< 0.005	0.020 ± 0.013	0.09 ± 0.04	0.04 ± 0.04
VVV	0.063 ± 0.026	0.52 ± 0.25	0.9 ± 0.4	0.31 ± 0.15
$t\bar{t}$	< 0.05	$0.04 \pm \begin{smallmatrix} 0.05 \\ 0.04 \end{smallmatrix}$	0.09 ± 0.07	< 0.05
$t\bar{t}X$	0.039 ± 0.029	0.08 ± 0.04	0.12 ± 0.05	$0.02 \pm \begin{smallmatrix} 0.05 \\ 0.02 \end{smallmatrix}$
Fakes	< 0.003	$0.000 \pm \begin{smallmatrix} 0.025 \\ 0.000 \end{smallmatrix}$	0.33 ± 0.30	$0.05 \pm \begin{smallmatrix} 0.09 \\ 0.05 \end{smallmatrix}$
Others	< 0.002	< 0.005	< 0.01	< 0.004

Table 10.3: Observed and expected yields after the background-only fit in SRSS. Combined statistical and systematic uncertainties are presented.

Region	SRSS- eee	SRSS- $e\mu\mu$	SRSS- 2μ
Observed data	1	2	1
Fitted SM	0.85 ± 0.26	2.0 ± 0.5	0.66 ± 0.26
Charge-flip	0.74 ± 0.25	1.4 ± 0.4	0.015 ± 0.006
Fakes	$0.06 \pm^{0.09}_{0.06}$	0.57 ± 0.33	0.55 ± 0.25
WZ	< 0.01	0.032 ± 0.027	< 0.005
VVV	< 0.01	$0.012 \pm^{0.018}_{0.012}$	$0.016 \pm^{0.022}_{0.016}$
$t\bar{t}$	$0.04 \pm^{0.04}_{0.04}$	< 0.05	0.08 ± 0.06

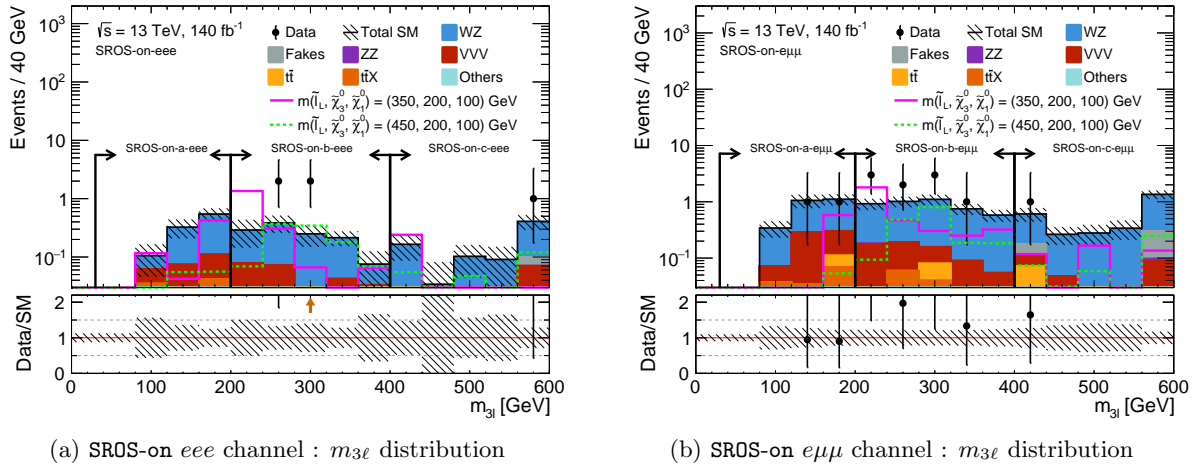


Figure 10.2: Post-fit distributions of $m_{3\ell}$ in (a) SRSS-on- eee channel and (b) SRSS-on- $e\mu\mu$ channel. The bins enclosed by arrows indicate the respective regions. The hatched band includes the combined statistical and systematic uncertainty on the total estimated backgrounds. The overflow is included in the highest bin. Pink and green lines represent the expected distributions of the typical signal targeted in the SR bin. The bottom panels show the ratio of the observed data to the predicted total background yields.

10.3 Model-dependent Interpretation – Constraints on the Benchmark Models

Exclusion limits for specific models are determined by performing a hypothesis test that incorporates signal yields estimated from simulation samples in SRs and CRWZ into the likelihood. To derive the NF of WZ , signal contamination in CRWZ is considered. In the background-only fit, μ_{WZ} is found to be 1.07 ± 0.06 , while with the signal hypothesis of $m(\tilde{\ell}_L, \tilde{\chi}_3^0, \tilde{\chi}_1^0) = (300, 200, 100)$ GeV, μ_{WZ} is derived to be 1.05 ± 0.06 . The results are consistent within the NF uncertainty. All SRs are incorporated into the fitting procedure to calculate the CL_s value. The CL_s value is calculated for the $\mu_s = 1$ hypothesis for each signal grid point. The CL_s values between each signal grid point are smoothly interpolated, and the points with $CL_s = 0.05$ are connected to form the exclusion limit. Given the large number of signal points tested, an asymptotic approximation [233] is employed in the CL_s calculation instead of the full calculation using toy-experiments. The difference between the CL_s obtained from the two methods is at most 40%, which can be

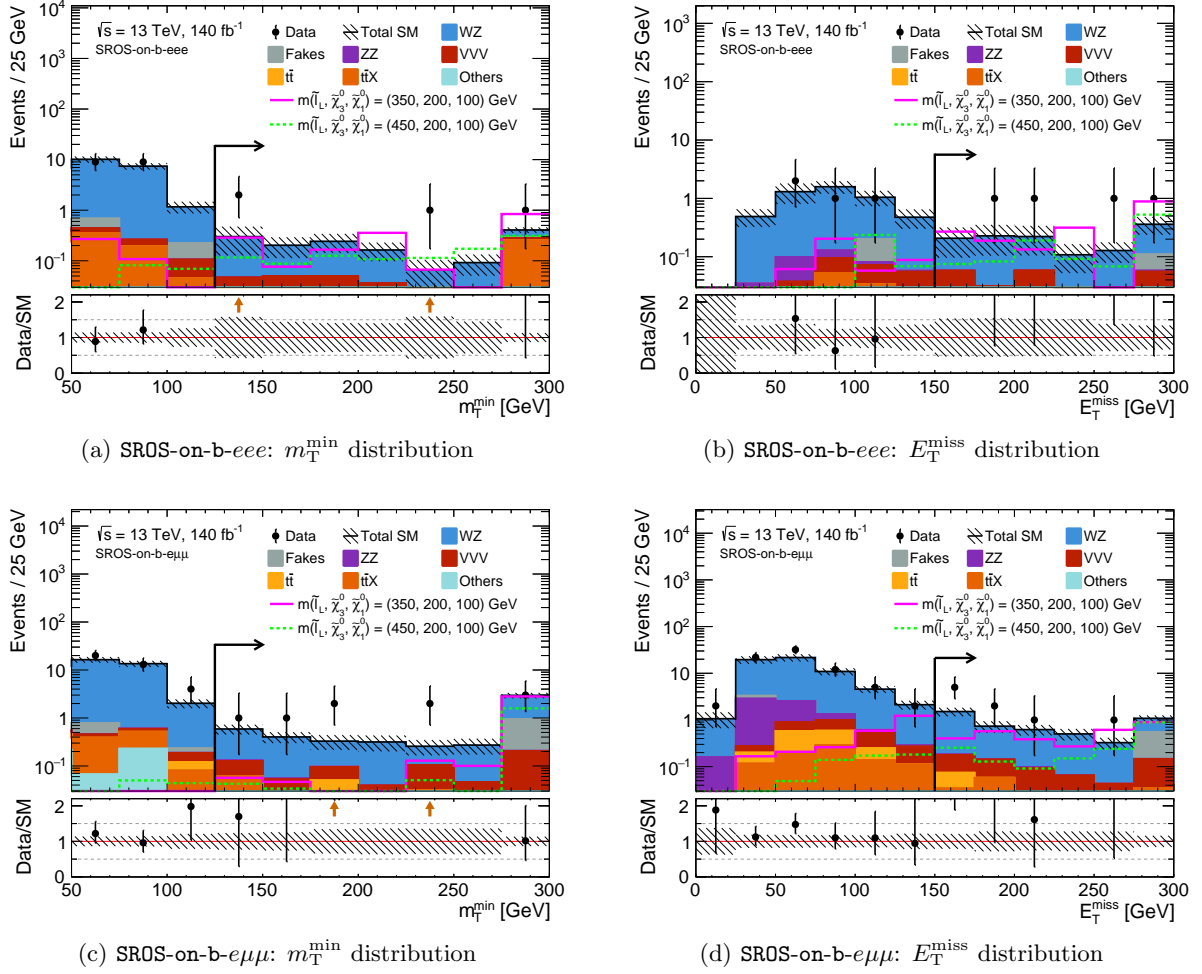


Figure 10.3: Post-fit distributions in (a)(b) SR0S-on-b-eee and (c)(d) SR0S-on-b-e $\mu\mu$. Each plot is drawn without applying selections to the variable illustrated. Arrows indicate the selection which are applied in SRs. The hatched band includes the combined statistical and systematic uncertainty on the total estimated backgrounds. The overflow is included in the highest bin. Pink and green lines represent the expected distributions of the typical signal targeted in the SR bin. The bottom panels show the ratio of the observed data to the predicted total background yields.

translated into a difference of up to 10% in the cross-section upper limit and negligible in the mass reach.

The expected and observed exclusion limit for the slepton-bino-higgsino model with LSP mass of 100 GeV or 150 GeV is shown in Fig. 10.4. Here selectron and smuon are assumed to be at the same mass. By this study, slepton mass up to 450 (420) GeV is excluded with the lightest SUSY particle mass being 100 (150) GeV. Exclusion limits obtained by only including SR0S or SRSS in the exclusion fit are shown in Fig. 10.5 which are overlaid to the combined exclusion limits. We can also think about the case where only the selectron or the smuon is light. Fig. 10.6 (Fig. 10.7) shows the exclusion contours assuming only the selectron (smuon) is light. As slight data excess in the SR0S-on region is observed, the exclusion counter has shrunk especially in the $\Delta m(\tilde{\chi}_3^0, \tilde{\chi}_1^0) > m_Z$ region. From Fig. 10.5, SR0S is mainly sensitive to the region with sufficiently large $\Delta m(\tilde{\ell}_L, \tilde{\chi}_3^0)$ and $\Delta m(\tilde{\chi}_3^0, \tilde{\chi}_1^0)$. This is due to the E_T^{miss} and m_T^{\min} cut imposed to SR0S which

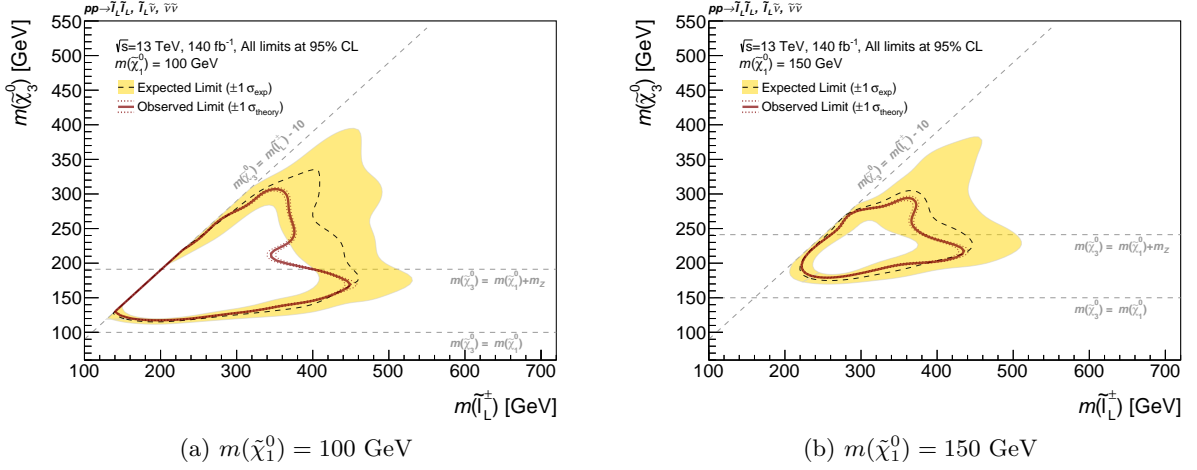


Figure 10.4: Exclusion contours on the $m(\tilde{\chi}_3^0)$ vs. $m(\tilde{\ell}_L^\pm)$ plane obtained including all SRs and assuming $m(\tilde{e}_L) = m(\tilde{\mu}_L)$. The expected 95% CL exclusion limits are shown in the dashed black lines, with the yellow bands indicating $\pm 1\sigma_{\text{exp}}$ including all uncertainties except for the signal cross-section uncertainty. The observed 95% CL exclusion limits are shown in the red solid lines, with the dotted red bands indicating $\pm 1\sigma_{\text{theory}}$ due to signal cross-section uncertainty.

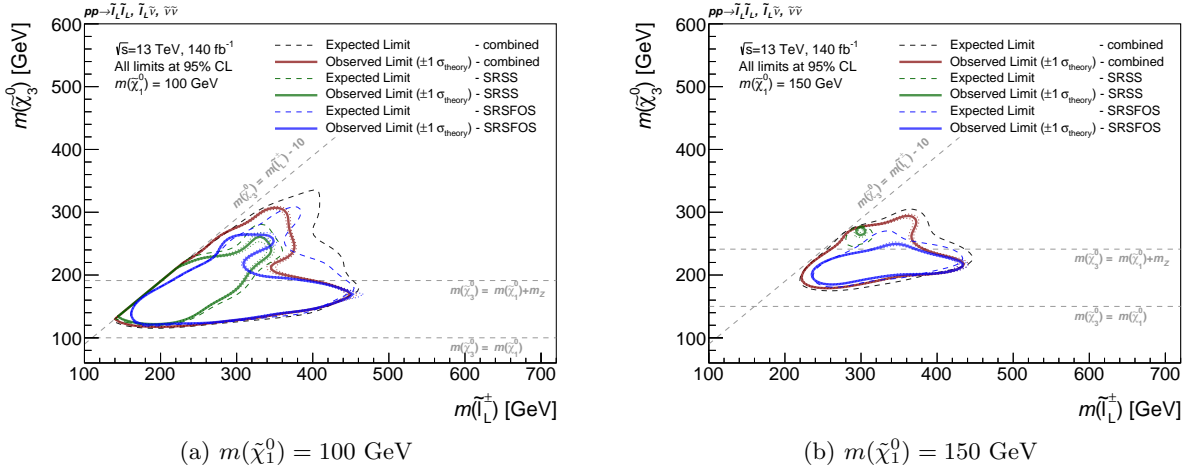


Figure 10.5: Exclusion contours on the $m(\tilde{\chi}_3^0)$ vs. $m(\tilde{\ell}_L^\pm)$ plane obtained assuming $m(\tilde{e}_L) = m(\tilde{\mu}_L)$. Exclusion contours obtained by including only SRSS or SRSFOS are overlaid. The expected 95% CL exclusion limits are shown in the colored dashed lines. The observed 95% CL exclusion limits are shown in the solid lines.

is introduced to reduce the WZ background but also loses the sensitivity to compressed signals. On the other hand, SRSS reaches its sensitivity to small $\Delta m(\tilde{\ell}_L, \tilde{\chi}_3^0)$ region. However, due to the need for both leptons from two W bosons to be reconstructed in order for the signals to fall into SRSS (cf. Fig 7.7, 7.8), SRSS rapidly loses sensitivity in the small $\Delta m(\tilde{\chi}_3^0, \tilde{\chi}_1^0)$ region.

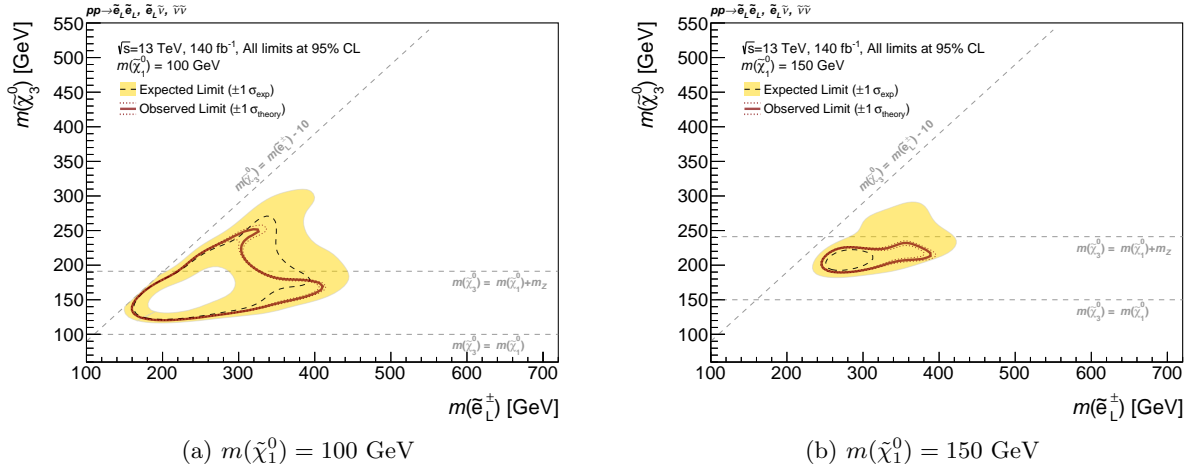


Figure 10.6: Exclusion contours on the $m(\tilde{\chi}_3^0)$ vs. $m(\tilde{e}_L^\pm)$ plane obtained including all SRs and only the selectron signals. The expected 95% CL exclusion limits are shown in the dashed black lines, with the yellow bands indicating $\pm 1\sigma_{\text{exp}}$ including all uncertainties except for the signal cross-section uncertainty. The observed 95% CL exclusion limits are shown in the red solid lines, with the dotted red bands indicating $\pm 1\sigma_{\text{theory}}$ due to signal cross-section uncertainty.

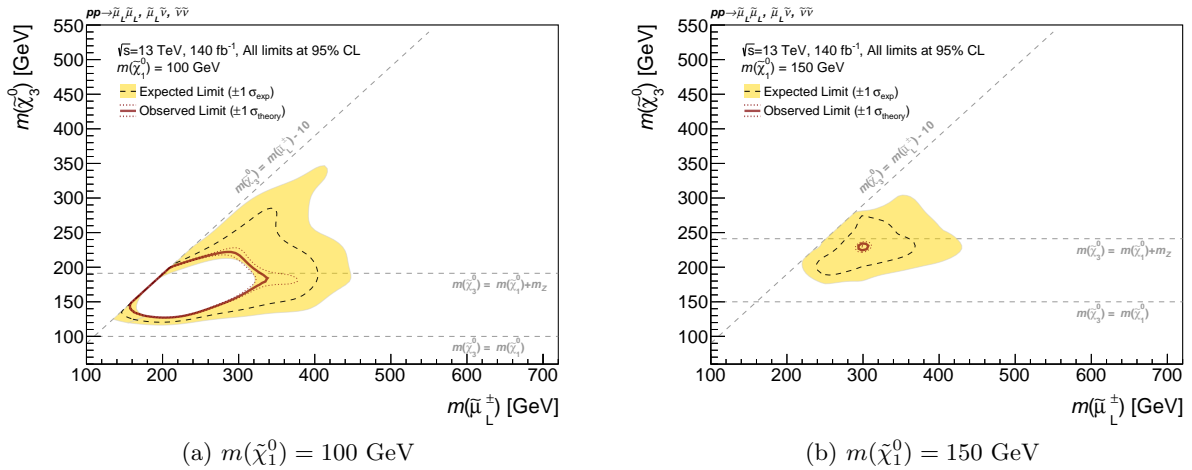


Figure 10.7: Exclusion contours on the $m(\tilde{\chi}_3^0)$ vs. $m(\tilde{\mu}_L^\pm)$ plane obtained including all SRs and only the smuon signals. The expected 95% CL exclusion limits are shown in the dashed black lines, with the yellow bands indicating $\pm 1\sigma_{\text{exp}}$ including all uncertainties except for the signal cross-section uncertainty. The observed 95% CL exclusion limits are shown in the red solid lines, with the dotted red bands indicating $\pm 1\sigma_{\text{theory}}$ due to signal cross-section uncertainty.

10.4 Model-independent Search – Upper Limits on BSM Events

Upper limits on the number of model-independent BSM signal yields are established by performing a hypothesis test with the null hypothesis describing a background-only scenario, which is called the “discovery fit”. The discovery fit is performed for the flavor merged inclusive SRs and each SR bins to derive the expected and the observed 95% CL upper limits on the number of the generic BSM signal events (S_{exp}^{95} and S_{obs}^{95}) as well as the one-sided p -value ($p(s = 0)$) of the background-only hypothesis. Toy-experiments are used for the calculation. As no specific

models are being considered for the signals, the signal yields are included exclusively in the SR bins and not in the CRWZ. The upper limits derived using the flavor merged inclusive SRs and each SR bins are summarized in Table 10.4. An upper limit is placed on the visible cross-section, which is defined as the product of the cross-section and the acceptance. The equation describing this limit is

$$\langle\epsilon\sigma\rangle_{\text{obs}}^{95} = S_{\text{obs}}^{95}/(\text{Integrated luminosity} = 140 \text{ fb}^{-1}), \quad (10.13)$$

where S_{obs}^{95} is the upper limit placed on the number of BSM events. Given the data excess in **SR0S-on-b-eee** and **SR0S-on-b-e $\mu\mu$** , the upper limits placed on S_{obs}^{95} are larger than S_{exp}^{95} in these SRs. S_{obs}^{95} is consistent to S_{exp}^{95} in other regions where the observed number of events is consistent with the expectation.

Table 10.4: Observed (N_{obs}) yields after the discovery fit and the expected (N_{exp}) after the background-only fit for flavor merged inclusive SRs and each SR bin. The third and fourth columns list the 95% CL upper limits on the visible cross-section (σ_{vis}^{95}) and on the number of signal events (S_{obs}^{95}). The fifth column (S_{exp}^{95}) shows the 95% CL upper limit on the number of signal events, given the expected number (and $\pm 1\sigma$ excursions of the expectation) of background events. The last two columns indicate the CL_b value, i.e. the confidence level observed for the background-only hypothesis, and the discovery p -value ($p(s=0)$). If the observed yield is below the expected yield, the p -value is capped at 0.5.

Region	N_{obs}	N_{exp}	$\langle \epsilon \sigma \rangle_{\text{obs}}^{95} [\text{fb}]$	S_{obs}^{95}	S_{exp}^{95}	CL_b	$p(s=0) (Z)$
SR0S-on-a	9	8.94 ± 1.33	0.06	8.1	$7.6^{+3.1}_{-2.1}$	0.58	0.49 (0.01)
SR0S-on-b	22	12.33 ± 1.67	0.14	19.2	$9.9^{+3.9}_{-2.3}$	0.98	0.01 (2.24)
SR0S-on-c	7	7.49 ± 0.99	0.05	6.8	$7.0^{+2.9}_{-2.1}$	0.46	0.50 (0.00)
SR0S-off-a	6	6.33 ± 1.08	0.04	6.1	$6.6^{+2.9}_{-1.9}$	0.39	0.50 (0.00)
SR0S-off-b	10	7.47 ± 1.25	0.07	9.3	$7.4^{+2.8}_{-2.0}$	0.78	0.24 (0.71)
SR0S-off-c	5	5.72 ± 0.91	0.04	5.7	$6.2^{+2.8}_{-1.6}$	0.41	0.50 (0.00)
SRSS	4	3.50 ± 0.78	0.04	6.1	$5.4^{+2.0}_{-1.4}$	0.65	0.33 (0.43)
SR0S-on-a-eee	0	1.01 ± 0.26	0.02	3.0	$3.7^{+1.3}_{-0.6}$	0.20	0.50 (0.00)
SR0S-on-a-ee μ	1	2.06 ± 0.40	0.03	3.8	$4.4^{+1.6}_{-1.0}$	0.26	0.50 (0.00)
SR0S-on-a-e $\mu\mu$	2	2.61 ± 0.50	0.03	4.5	$4.7^{+2.0}_{-1.0}$	0.41	0.50 (0.00)
SR0S-on-a- $\mu\mu\mu$	6	3.36 ± 0.60	0.06	8.4	$5.4^{+2.1}_{-1.3}$	0.91	0.07 (1.46)
SR0S-on-b-eee	4	1.25 ± 0.42	0.05	7.1	$4.3^{+1.4}_{-0.8}$	0.96	0.03 (1.82)
SR0S-on-b-ee μ	4	2.74 ± 0.46	0.04	6.2	$4.9^{+1.9}_{-1.1}$	0.78	0.21 (0.79)
SR0S-on-b-e $\mu\mu$	9	4.59 ± 0.66	0.08	11.0	$6.1^{+2.3}_{-1.5}$	0.97	0.04 (1.79)
SR0S-on-b- $\mu\mu\mu$	5	3.89 ± 0.66	0.05	6.8	$5.3^{+2.4}_{-1.4}$	0.72	0.25 (0.69)
SR0S-on-c-eee	1	0.81 ± 0.24	0.03	3.8	$3.3^{+1.4}_{-0.3}$	0.64	0.35 (0.38)
SR0S-on-c-ee μ	2	1.86 ± 0.36	0.03	4.6	$4.2^{+1.7}_{-1.1}$	0.57	0.41 (0.23)
SR0S-on-c-e $\mu\mu$	1	2.72 ± 0.47	0.02	3.5	$4.7^{+2.0}_{-1.2}$	0.15	0.50 (0.00)
SR0S-on-c- $\mu\mu\mu$	3	2.15 ± 0.41	0.04	5.5	$4.6^{+1.7}_{-1.1}$	0.73	0.26 (0.65)
SR0S-off-a-eee	0	0.39 ± 0.11	0.02	3.0	$3.1^{+1.0}_{-0.0}$	0.34	0.50 (0.00)
SR0S-off-a-ee μ	3	1.39 ± 0.43	0.04	5.6	$4.1^{+1.4}_{-0.8}$	0.85	0.17 (0.96)
SR0S-off-a-e $\mu\mu$	2	3.81 ± 0.76	0.03	4.1	$5.3^{+2.2}_{-1.2}$	0.17	0.50 (0.00)
SR0S-off-a- $\mu\mu\mu$	1	1.01 ± 0.28	0.03	3.5	$3.6^{+1.5}_{-0.6}$	0.48	0.50 (0.00)
SR0S-off-b-eee	0	0.75 ± 0.33	0.02	2.9	$3.1^{+1.3}_{-0.1}$	0.26	0.50 (0.00)
SR0S-off-b-ee μ	3	1.60 ± 0.44	0.04	5.7	$4.2^{+1.8}_{-1.0}$	0.81	0.19 (0.89)
SR0S-off-b-e $\mu\mu$	6	3.61 ± 0.76	0.06	7.7	$5.4^{+2.2}_{-1.4}$	0.85	0.17 (0.95)
SR0S-off-b- $\mu\mu\mu$	1	1.50 ± 0.28	0.03	3.7	$3.9^{+1.7}_{-0.9}$	0.40	0.50 (0.00)
SR0S-off-c-eee	0	0.27 ± 0.08	0.02	3.0	$3.1^{+0.8}_{-0.0}$	0.38	0.50 (0.00)
SR0S-off-c-ee μ	1	0.96 ± 0.28	0.03	3.6	$3.6^{+1.2}_{-0.5}$	0.50	0.50 (0.00)
SR0S-off-c-e $\mu\mu$	1	2.96 ± 0.56	0.02	3.4	$4.7^{+2.0}_{-1.1}$	0.13	0.50 (0.00)
SR0S-off-c- $\mu\mu\mu$	3	1.91 ± 0.35	0.04	5.4	$4.3^{+1.8}_{-1.1}$	0.76	0.23 (0.73)
SRSS-eee	1	0.85 ± 0.26	0.03	4.0	$3.4^{+1.4}_{-0.3}$	0.66	0.34 (0.41)
SRSS-ee μ	2	1.99 ± 0.52	0.03	4.5	$4.3^{+1.8}_{-1.1}$	0.55	0.42 (0.19)
SRSS-2 μ	1	0.66 ± 0.26	0.03	4.0	$3.1^{+1.2}_{-0.1}$	0.73	0.27 (0.62)

Chapter 11

Discussion

11.1 What is Unique/Important in This Study?

This work is the first dedicated search for the (left-handed) slepton-bino-higgsino model which is motivated by the muon $g - 2$ anomaly and dark matter. We have systematically analyzed all of the mass hierarchy sub-scenarios which can explain the muon $g - 2$ anomaly and summarized which sub-scenarios are viable in terms of the dark matter and studied the constraints from the LHC (Chapter 3). The slepton-bino-higgsino model was elucidated to be the only mass hierarchy which has not been optimally explored (Section 3.2). For the search of the slepton-bino-higgsino model, we have defined several optimal SRs which include the three lepton same-sign region with b -jet veto which have never been explored at LHC (Section 7.3). One important work in this thesis is the derivation of the electron charge-flip scale factors (Section 8.3.2). These scale factors are derived as the ATLAS-wide official charge-flip scale factors and will be used by other ATLAS analyses which are affected by the charge-flip background. Another important achievement of this study is the establishment of the background estimation method for $\text{SRSS-}2\mu$ (Section 8.4.5). It is extremely hard to estimate the background in this unusual phase space which is dominated by fake lepton events and has very low background level. By checking the MC-data agreement in the anti-ID region, fake process composition and the number of fake leptons, we have established and validated the fake background estimation method which is described as Eq. 8.8.

I carried out all parts of the analysis, including target definition, analysis strategy development, estimation of background events, evaluation of systematic uncertainties, and statistical interpretation.

11.2 Implication to Muon $g - 2$ Anomaly

This analysis gives a new constraint to the slepton-bino-higgsino model, consistent with the muon $g - 2$ anomaly and the dark matter direct detection. Figure 11.1 shows the overlay of the expected and observed exclusion limits of this analysis and the mass points consistent with the muon $g - 2$ anomaly with $m(\tilde{\chi}_1^0) = 150$ GeV. Green mass points explain the muon $g - 2$ [36] anomaly within 2σ , W boson mass [144] within 2σ , and satisfy the dark matter relic density constraint [26], the dark matter direct detection constraint by the LZ experiment [27], and the ATLAS higgsino search constraints [101, 104, 105]. As discussed in Section 3.2.2, mass points distribute in the region where $\Delta m(\tilde{\chi}_3^0, \tilde{\chi}_1^0) > 90$ GeV by the DM direct detection constraint. Though this analysis excludes some of these phenomenologically motivated mass points, left-handed sleptons which can explain the muon $g - 2$ anomaly can be heavy up to ~ 800 GeV in the case of $m(\tilde{\chi}_1^0) = 150$ GeV with large $\tan\beta$. More statistics of collision data are needed to

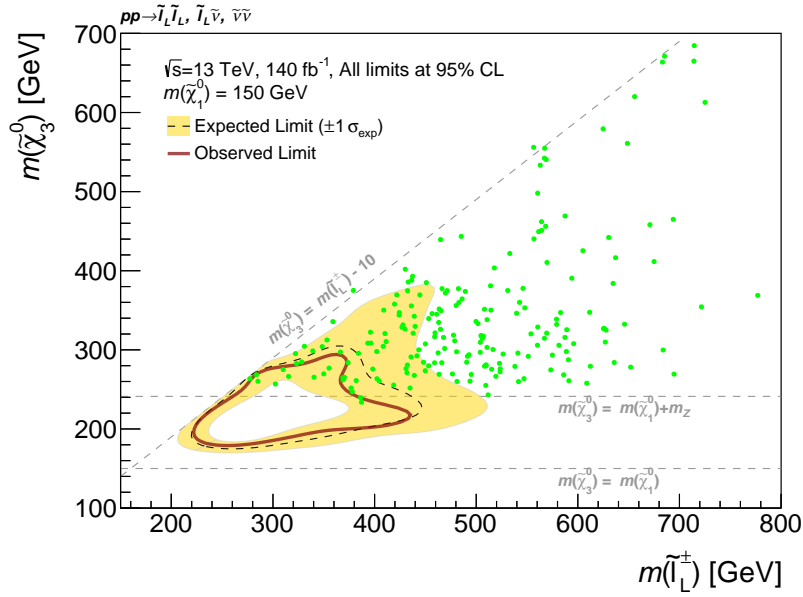


Figure 11.1: Overlay of the expected and observed exclusion limit of this analysis and the mass points consistent with the muon $g - 2$ anomaly with $m(\tilde{\chi}_1^0) = 150$ GeV. Green mass points explain the muon $g - 2$ anomaly [36] within 2σ , W boson mass [144] within 2σ , and satisfy the dark matter relic density constraint [26], the dark matter direct detection constraint by the LZ experiment [27] and the ATLAS higgsino search constraints [101, 104, 105]. This analysis excludes some of these phenomenologically motivated mass points.

test the entire region which can explain the muon $g - 2$ anomaly. The sensitivity projection in the future LHC experiment will be discussed in Section 11.4.

11.3 Limit on the Higgsino Mass

At the LHC, higgsinos are searched individually using the disappearing track signature [103, 239], displaced track signature [101], and multi-lepton signatures [104, 105, 120]. Fig. 11.2 illustrates exclusion limits set by analyses targeting the compressed higgsino states in the ATLAS and LEP experiments. Due to the small production cross-section of higgsinos and difficulty in the reconstruction of low p_T objects, higgsinos are only excluded up to 190 GeV where $\Delta m(\tilde{\chi}_1^\pm, \tilde{\chi}_1^0) > 0.3$ GeV and there are even mass splittings where LEP is still the strongest limit around $\Delta m(\tilde{\chi}_1^\pm, \tilde{\chi}_1^0) = 1$ GeV.

We have calculated the maximum exclusion of the LSP mass, $m(\tilde{\chi}_1^0)$, by interpolating the CL_s between different LSP masses. Fig. 11.3 shows the expected and observed maximum exclusion of $m(\tilde{\chi}_1^0)$ in the $\Delta m(\tilde{\ell}_L, \tilde{\chi}_3^0)$ vs. $\Delta m(\tilde{\chi}_3^0, \tilde{\chi}_1^0)$ plane. This analysis is most sensitive to mass differences around $\Delta m(\tilde{\ell}_L, \tilde{\chi}_3^0) = \Delta m(\tilde{\chi}_3^0, \tilde{\chi}_1^0) = 50$ -100 GeV because of the sufficient mass splitting and relatively low mass sleptons. The observed (expected) exclusion on $m(\tilde{\chi}_1^0)$ extends up to 205 (215) GeV. Be careful that we are assuming higgsinos to be mass degenerate (Section 3.3), thus Fig. 11.2 and 11.3 cannot be naively compared. However, the statement that we are able to set a strong constraint to the higgsino mass in a certain mass hierarchy is still valid.

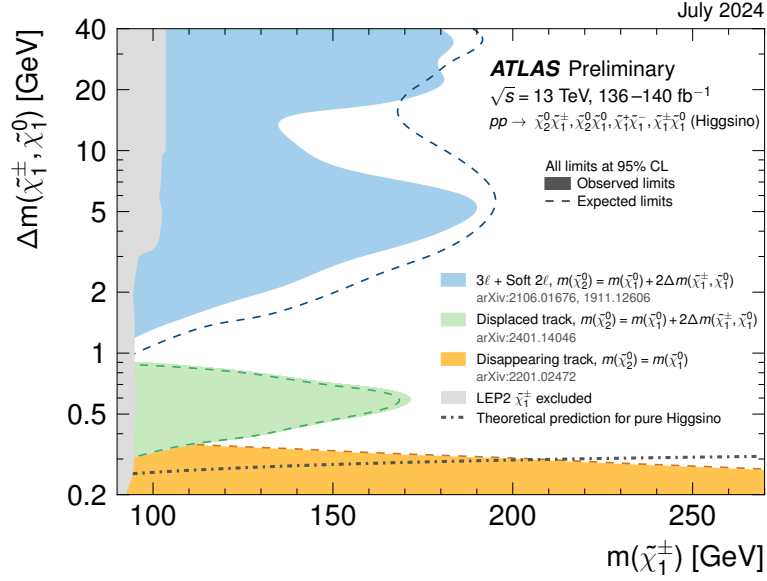


Figure 11.2: Exclusion limits at 95% CL for higgsino pair production ($\tilde{\chi}_1^+ \tilde{\chi}_1^-$, $\tilde{\chi}_1^\pm \tilde{\chi}_1^0$, $\tilde{\chi}_1^\pm \tilde{\chi}_2^0$, and $\tilde{\chi}_1^0 \tilde{\chi}_2^0$) with off-shell SM-boson-mediated decays into the nearly-degenerate lightest neutral higgsino ($\tilde{\chi}_1^0$) and soft leptons or pions [240]. The limits are calculated based on the pure higgsinos production cross-section and shown as a function of mass splitting $\Delta m(\tilde{\chi}_1^\pm, \tilde{\chi}_1^0)$ and mass $m(\tilde{\chi}_1^\pm)$. Assumptions for the mass of the charged higgsino ($\tilde{\chi}_1^\pm$) in relation to the masses of the two neutral higgsinos ($\tilde{\chi}_1^0, \tilde{\chi}_2^0$) are indicated per analysis in the legend.

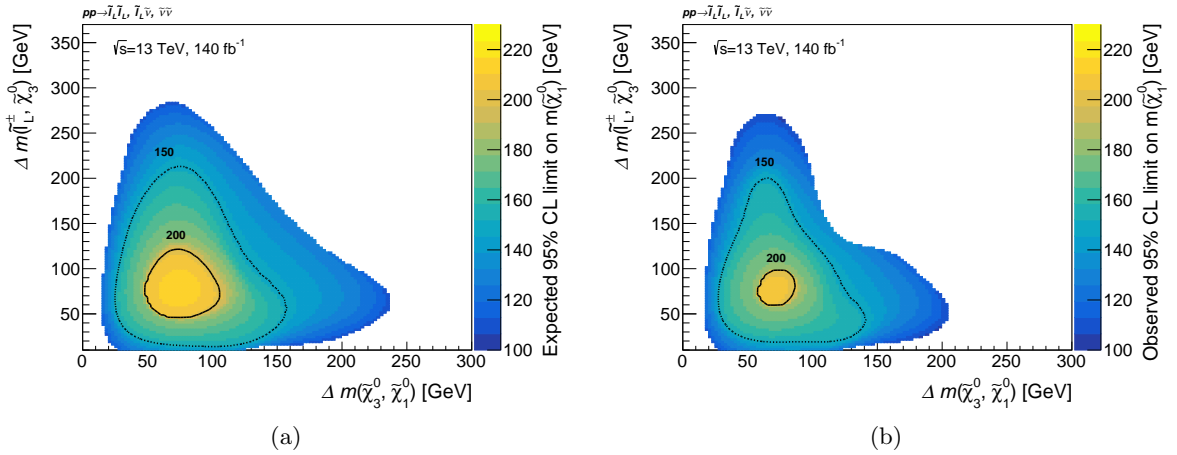


Figure 11.3: (a) Expected and (b) observed maximum exclusion of $m(\tilde{\chi}_1^0)$ in the $\Delta m(\tilde{\ell}_L, \tilde{\chi}_3^0)$ vs. $\Delta m(\tilde{\chi}_3^0, \tilde{\chi}_1^0)$ plane. The dotted (solid) contour line indicate 150 (200) GeV limit of $\tilde{\chi}_1^0$ mass. In the white region, the lower limit on the $\tilde{\chi}_1^0$ mass is below 100 GeV.

11.4 Future Prospect

The LHC Run 3 period has started in 2022, increasing the center-of-mass energy to 13.6 TeV and is expected to obtain about 500 fb^{-1} data, including the data acquired in previous runs, by mid 2026. After a four-year shutdown period, the center-of-mass energy will be increased to 14 TeV and is expected to obtain about $3000\text{--}4000 \text{ fb}^{-1}$ of data in about ten years. This period is called the High-Luminosity LHC (HL-LHC), and the high statistics will be utilized

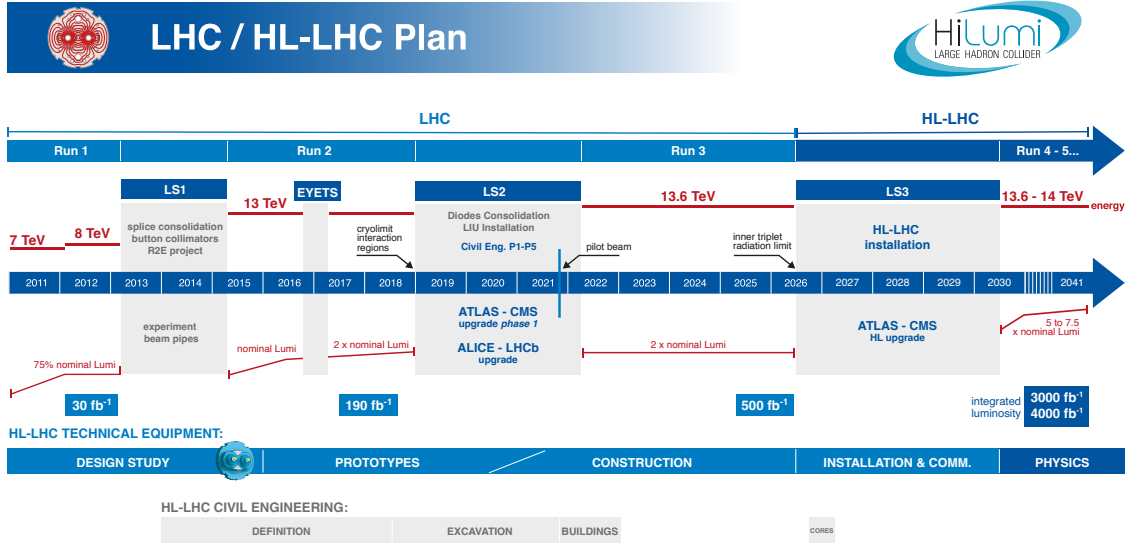


Figure 11.4: LHC accelerator operations and upgrade plan [241]. The LHC Run 3 period has started from 2022 and HL-LHC is planned to start from 2030.

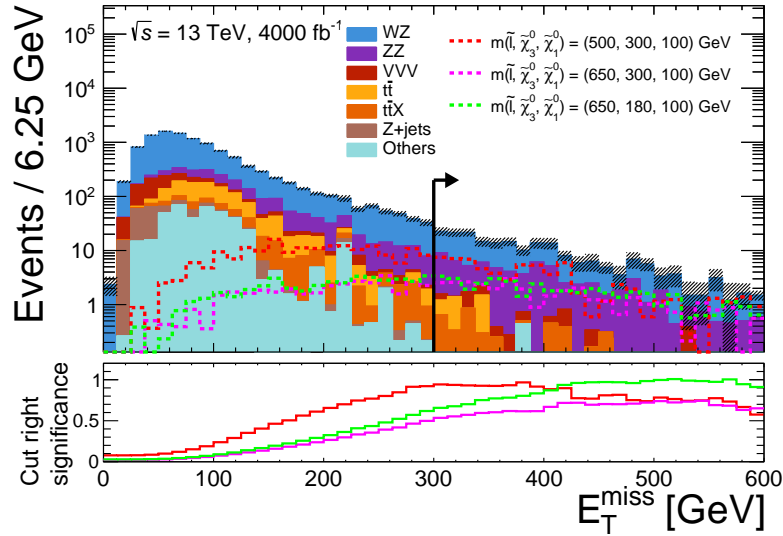


Figure 11.5: E_T^{miss} distribution for SROS scaled to 4000 fb⁻¹. $m_T^{\text{min}} > 125$ GeV cut is imposed. The dashed lines illustrate signal simulation with different masses. The bottom panel shows the significance (Z) calculated by accumulating the yields of the bins on the right side. A total uncertainty of 30% is assumed for background yields.

to detect new particles with small production cross-sections and to make precise measurements of the Higgs boson. The LHC and HL-LHC plan is summarized in Fig. 11.4. We will discuss the extended sensitivity of this analysis targeting the slepton-bino-higgsino scenario using data obtained during Run 3 and HL-LHC. The HL-LHC increases the instantaneous luminosity by a factor of 5 to 7.5 relative to the nominal value to achieve high statistics. However, this increase in luminosity will also result in a significant rise in radiation levels due to an increase in the mean

number of interactions per crossing. The trigger rate will increase significantly, necessitating upgrades to the trigger system, the data acquisition system, and the electronics. Specifically, the end-cap muon trigger system will be substantially upgraded which will be further discussed in Appendix A.

The sensitivity of the slepton-bino-higgsino analysis is evaluated with the expected data statistics recorded during Run 3 and HL-LHC. Since a large increase in statistics is expected for HL-LHC, the E_T^{miss} selection is tightened from 150 GeV to 300 GeV in SRSS to increase the signal-to-background ratio. Fig. 11.5 shows the E_T^{miss} distribution for SRSS scaled to 4000 fb⁻¹. $E_T^{\text{miss}} > 300$ GeV is chosen to maximize the sensitivity to sleptons heavier than them targeted in this Run 2 analysis. With sufficient data statistics, SRSS-2 μ will be able to be divided in to SRSS- $e\mu\mu$ and SRSS- $\mu\mu\mu$ which will enhance the sensitivity especially to smuons. Fig. 11.6 shows the expected exclusion limits and 5 σ discovery contour for data statistics which will be obtained by Run 3 (400 fb⁻¹) and HL-LHC (4000 fb⁻¹) under the assumption that systematic uncertainties are equivalent to those of the Run 2 analysis. Using the large statistics of 4000 fb⁻¹ expected in

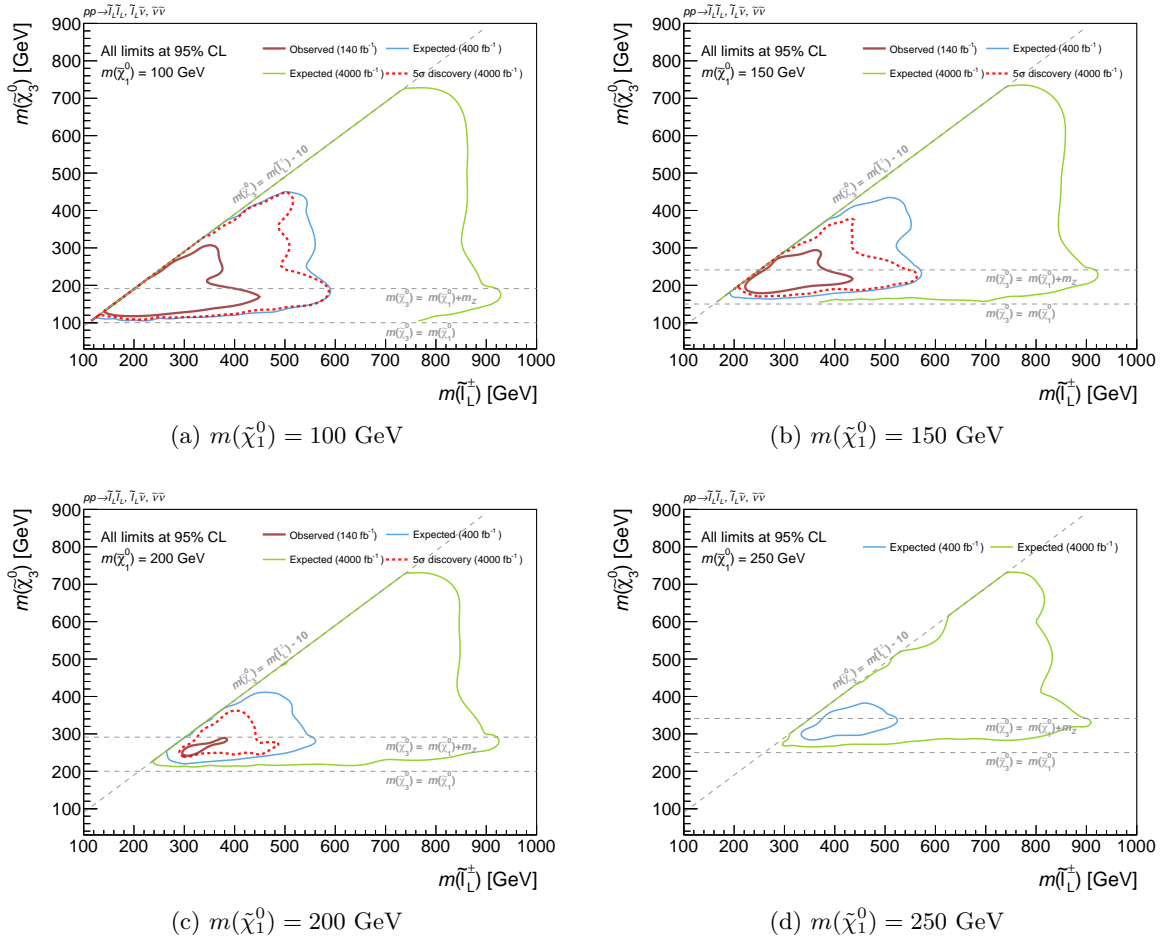


Figure 11.6: Future projection of the expected exclusion limits and 5 σ discovery contour by the slepton-bino-higgsino analysis using the data collected during the Run 3 and HL-LHC. The red solid line illustrates the observed exclusion limits at the 95% CL in the displaced track analysis using the Run 2 data. The green and blue lines illustrate the expected exclusion limit at the 95% CL with integrated luminosity of 400 fb⁻¹ and 4000 fb⁻¹. The red dashed lines illustrate the expected 5 σ discovery contour with integrated luminosity of 4000 fb⁻¹.

the HL-LHC, the sensitivity can be extended up to 800-900 GeV sleptons and sleptons lighter than 400-600 GeV can be discovered. From Fig. 3.7 and Fig. 11.6, it can be seen that after HL-LHC, almost all mass region consistent with the muon $g - 2$ anomaly can be excluded.

Chapter 12

Conclusion

This thesis presents a search for the cascade decay of left-handed sleptons and sneutrinos using 140 fb^{-1} of proton-proton collision data at $\sqrt{s} = 13 \text{ TeV}$, collected by the ATLAS detector at the Large Hadron Collider (LHC). The search focuses on final states with exactly three leptons. In the targeted model, sleptons are assumed to decay into a Higgsino-dominated lightest supersymmetric particle (LSP) via a bino-dominated neutralino, whose mass lies between that of the slepton and the LSP. This model is motivated by the muon $g - 2$ anomaly and the presence of dark matter.

The search employs two complementary analysis strategies. The first strategy targets events with a same-flavor opposite-sign lepton pair exhibiting a large transverse mass and significant missing transverse energy (SR0S). The second strategy focuses on events with three leptons of the same electric charge (SRSS). This latter region is novel, as it has not been previously explored at the LHC, and is primarily dominated by reducible backgrounds, such as electron charge-flip and fake lepton events. Background estimation methods for the prompt WZ process, charge-flip, and fake lepton backgrounds are developed and validated using dedicated control and validation regions. In the unblinded signal regions, no significant excess over the Standard Model predictions is observed, allowing exclusion limits to be set on the targeted model at the 95% confidence level. Slepton masses up to 450 (420) GeV are excluded for an LSP mass of 100 (150) GeV. However, a slight data excess was observed in the SR0S on-shell region, leading to a reduction in the observed exclusion reach compared to the expected exclusion limits, particularly in the phase space where $\Delta m(\tilde{\chi}_3^0, \tilde{\chi}_1^0) > m_Z$.

Looking ahead to the High-Luminosity LHC (HL-LHC) with an integrated luminosity of $\mathcal{L} = 4000 \text{ fb}^{-1}$, the sensitivity to slepton masses is projected to extend to the 800-900 GeV range, with discovery potential for sleptons lighter than 400-600 GeV. Following the HL-LHC program, nearly the entire mass region consistent with the muon $g - 2$ anomaly is expected to be explored.

Acknowledgement

I would like to thank the many people who helped me in the course of this research. First of all, I would like to thank my advisor, Prof. Masaya Ishino, who gave me a lot of advice on the content of my research and presentation materials. Dr. Yasuyuki Okumura helped me in various aspects. In particular, detailed comments on technical aspects helped me to proceed smoothly with this research. I would like to express my sincere gratitude to Dr. Tomoyuki Saito, Dr. Tatsuya Masubuchi, Dr. Takuya Nobe, Dr. Yuji Enari, Dr. Ryu Sawada, Dr. Masahiko Saito, and Dr. Masahiro Morinaga not only provided important comments and suggestions at the analysis meetings, but also helped me by correcting my slides and practicing my presentation for the conference. I am grateful to Prof. Shoji Asai for giving me a variety of research themes.

I am also deeply grateful to the members of the thesis defense committee, Prof. Yutaka Ushiroda, Prof. Masashi Yokoyama, Prof. Tsutomu Mibe, Prof. Shigeki Matsumoto, and Dr. Taikan Suehara, for their constructive feedback and diverse perspectives, which greatly enhanced the quality of this work.

A special thanks goes to Dr. Shion Chen for his invaluable support in the analysis, dedicated role as the analysis contact, effective coordination within the group, and insightful comments on the paper. Without him, I would not have been able to push forward the analysis and overcome various difficulties. I am very appreciate for all the very useful advices, comments and discussions.

Dr. Sara Alderweireldt, Dr. Reina Camacho Toro, Dr. Daniela Kock, and Dr. Sonia Carra led the analysis in ATLAS and provided many comments at group and sub-group meetings.

During my life at CERN, Mr. Yuichiro Hayashi and Mr. Wonho Jang were my roommates, sharing the tough feeling of Ph.D. I am specially grateful to Dr. Yuya Mino and Dr. Kaito Sugizaki for supporting and having discussions about my analysis. I would also like to extend my gratitude to my ATLAS Japan colleagues at CERN: Ms. Haruka Asada, Dr. Minori Fujimoto, Dr. Moe Wakida, Dr. Reiyo Oishi, Dr. Yunjian He, Mr. Aoto Tanaka, Mr. Hiroki Ito, Dr. Tingyu Zhang, Ms. Tsuru Kimu, Dr. Wickremasinghe Lakmin, Mr. Yoshiaki Tsujikawa, Mr. Daiya Akiyama, Mr. Jiaqi Zang, Mr. Takane Sano, Dr. Yuki Mitsumori, Mr. Chihiro Kawamoto, Ms. Erika Yamashita, Ms. Marin Furukawa, Ms. Sayuka Kita, Mr. Yuya Ohsumi, Ms. Arisa Wada, Mr. Daisuke Hashimoto, Mr. Ren Nagasaka, and Mr. Yoshifumi Narukawa.

Throughout my master's and doctoral programs, I am deeply grateful to everyone in the ATLAS Japan TGC group for their significant support in the muon trigger upgrade for HL-LHC and the commissioning towards Run 3.

I would also like to thank the ICEPP secretaries for all the administrative work they did for me, including travel arrangements to CERN, which allowed me to concentrate on my research. Finally, I would like to thank my family for their constant support.

Appendices

Appendix A

End-cap Muon Trigger Upgrade for the HL-LHC

To cope with the higher trigger rate in HL-LHC, the end-cap muon trigger system in ATLAS will be substantially upgraded. All trigger logic and readout boards will be replaced, except for the ASD boards on the TGC chamber which converts analog signals to digital signals. Below is first an overview of the TGC electronics system at HL-LHC, followed by a description of my personal contribution.

Three TGC stations, called M1, M2, and M3 from the inside, are located outside the magnetic field. Each wire and strip layer is slightly shifted in the η and ϕ direction, which provides improved position resolution by taking the coincidence between each layer. M1, M2, and M3 have disk-like structures, and the three stations are called the TGC Big Wheel (TGC BW). Muons produced from the IP pass the toroidal magnetic field applied in the ϕ direction and

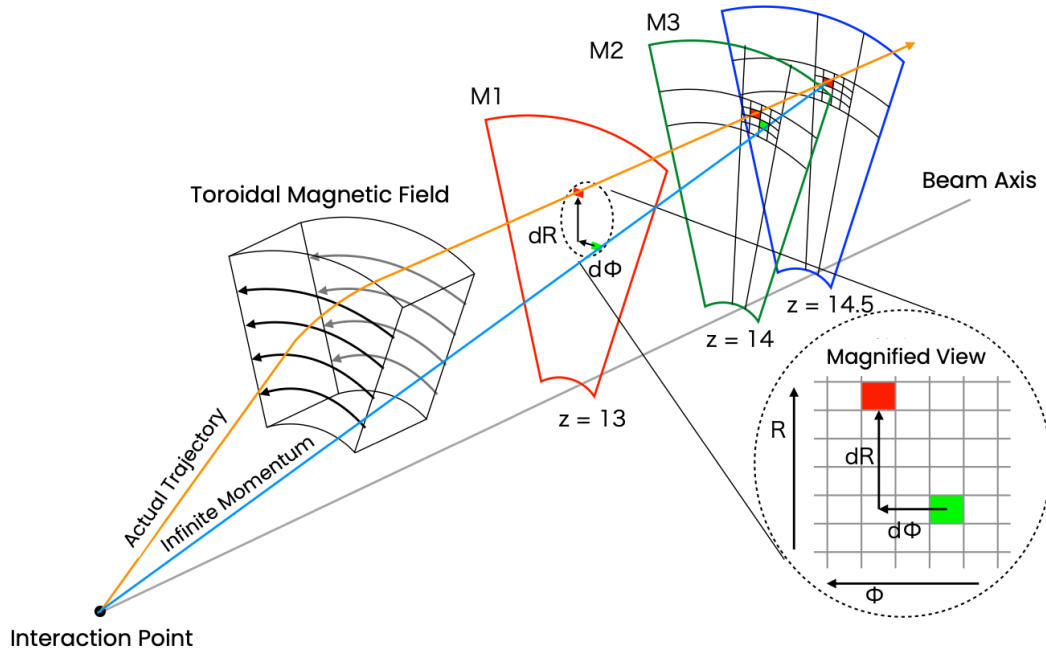


Figure A.1: Overview of the end-cap muon trigger logic. The p_T is measured by calculating the difference in r -position and ϕ -position at M1 relative to M3 between the hit positions at M1, M2 and M3 and the trajectory of a muon that passes through with infinite momentum.

bent in the η direction. The curvature of the muon tracks depends on the p_T . Therefore, it is possible to calculate the p_T of a muon by measuring its change in position in the r and ϕ directions compared to when it passes through with infinite momentum. Fig. A.1 shows a schematic of the trigger logic.

To realize this trigger logic, several types of electronics are combinedly used as shown in Fig. A.2 which is the overview of the TGC electronics system in the HL-LHC. The upgraded system consists of the Primary Processor boards (PS board) and JTAG Assistance Hub (JATHub) in the frontend and Sector Logic boards (SL) in the backend. Besides the digital components, the analogue Amplifier-Shaper-Discriminator (ASD) cards are mounted on the TGC detectors. When muon passes through TGC, the detector generates an analog signal and the ASD sends digitized hit signals to PS board. Then, the PS board aligns signal timing, and performs hit bunch crossing identification (BCID). Next, the PS board sends a fixed-length binary hit-map to SL at every 40 MHz bunch crossing. After that, the SL reconstructs muon track candidates and calculates p_T for each muon. Finally, the SL sends muon candidates to the down-stream trigger system and on acceptance of trigger send readout data from the L0 buffer to the data acquisition system. The trigger and clock signal is distributed from the Central Trigger Processor (CTP) to each SL, and then to each PS board through the optical fibers. JATHub is an independent control module and takes responsibility for FPGA configuration, error recovery and clock phase monitoring of PS boards.

The PS board is equipped with eight Patch Panel (PP) ASICs and one Xilinx Kintex-7 FPGA. The PP ASICs align the signal arrival timing before the BCID, exploiting variable delays available at the input stage. These PP ASIC signal delay parameters have variations due to different muon time of flight and ASD signal cable length. The BCID is performed by PP ASICs with a configurable gate-width. The PS board FPGAs receive 40 MHz LHC clock distributed from the SL via optical links and recover the clock with a fixed latency in the individual FPGAs. A FPGA aligns the clock phase with the other PS boards within $\mathcal{O}(100)$ ps precision, using variable delay owing to the built-in phase-locked loop of the FPGA clocking resource, for optimal performance of BCID. Alignment of the LHC clock phase, provided to the PP ASICs in all 1,434 PS boards, enables the BCID gate-timing to be matched between PP ASICs, and the BCID gate-width to be kept as the minimum necessary length. Precisely aligned gate timing and small gate width ensure high probability of correct BCID while minimizing the chance of contributions from background that are out of sync with the proton bunch crossing timing, such as those originated from low-energy neutrons and photons. Clock phase delay parameters have variations to compensate difference of fiber length between SL and PS boards. The PS board also provides the threshold voltage to the discriminator on ASD cards, driven and monitored by DACs and ADCs on the PS boards. Threshold voltage values also have variations due to different optimized threshold value for each chamber. Each PS board is configured with dedicated parameters including the signal delay, BCID gate width, signal mask for PP ASIC, 40 MHz clock delay, and ASD threshold voltage value for the PS board FPGA, for a total of $\sim 2,200$ bits.

Using the hit signals from PS boards, SL performs muon track reconstruction and p_T estimation. SL reads out hit data for each triggered event. SL also receives and distributes 40 MHz clock to front-end PS boards with a fixed latency. Each SL is configured with dedicated parameters including the signal delay (25 ns step) and L0 buffer depth, for a total of ~ 800 bits. Among these parameters, there are static parameters, that are constant during the detector operations, and dynamic parameters, which could change. For example, since the muon time-of-flight and ASD cable length do not change, the PP ASIC signal delay is a static parameter. On the other hand, the ASD threshold voltage value is a dynamic parameter, because the detector conditions can change during the operation.

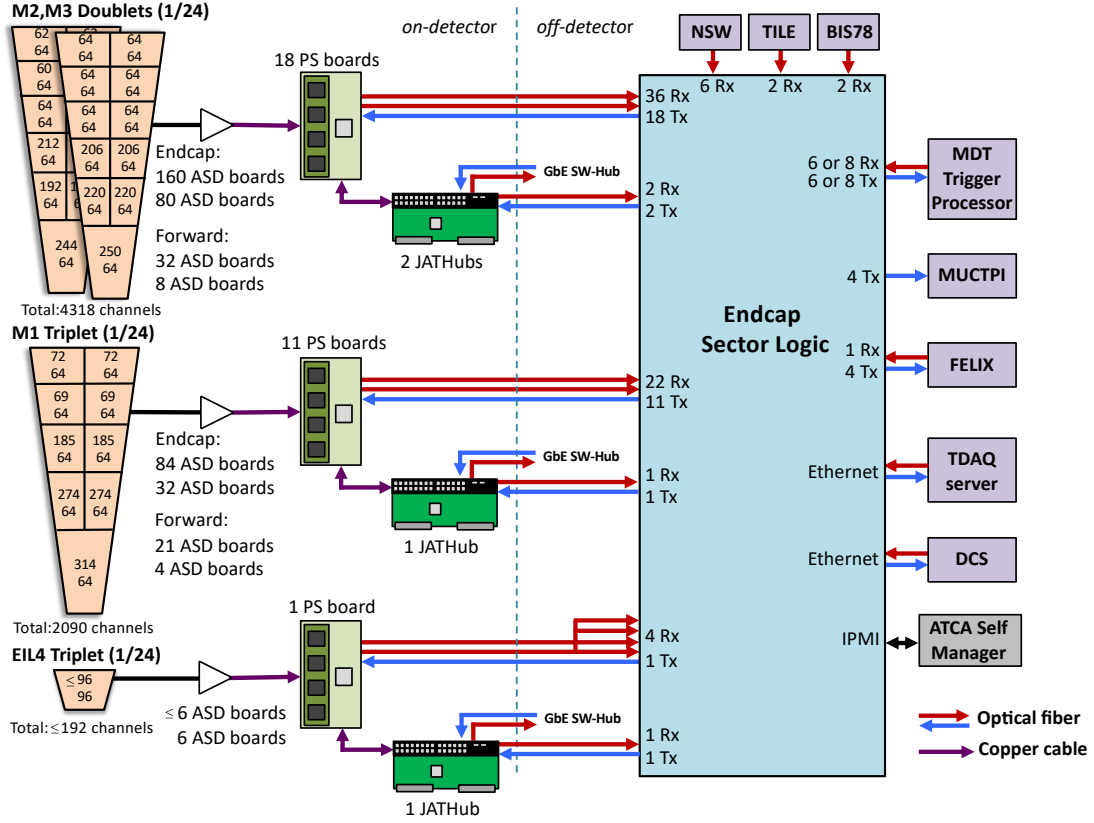


Figure A.2: Overview of the TGC electronics system in the HL-LHC ATLAS experiment [242]. In this figure, the 1/24 area of one side of the end-cap is shown. Signals from the TGC detector are converted to digital signals by ASD, and after BCID is performed by the PS board installed in the ATLAS cavern, all signals are transferred to the SL. One SL is in charge of 1/24 of one side of the end-cap and estimates the p_T of the muon by pattern matching using the information from several detectors mainly by TGC. The trigger and clock signal is distributed from the CTP to each SL, and then to each PS board. JATHub is independent from the data path and is responsible for configuring the FPGA on the PS board, handling unrecoverable SEU errors, and monitoring the phase of the LHC bunch crossing clocks on the PS board.

JATHub is a control hub module for the FPGAs on PS boards, equipped with the Xilinx Zynq-7000 System-on-a-Chip (SoC) device. The Zynq SoC integrates a Processor System including ARM-based processor with a Programmable Logic (PL) part equivalent to Xilinx 7-series FPGA and acts as the main driver of the front-end control system. One JATHub module is connectable to maximum 11 PS boards through category 6 cables, and 148 JATHub modules will control all 1,434 PS boards. JATHub has an Ethernet interface via optical fibers (1000BASE-X), exploiting built-in transceivers in the PL part of the Zynq. The PS part of the Zynq controls the JTAG signals for the configuration and debugging of FPGA on the PS board. JATHub is responsible for triggering the reconfiguration of PS board FPGAs in case that unrecoverable Single Event Upset (SEU) errors happen in the configuration memory by radiation effects. PS board FPGAs run the Xilinx Soft Error Mitigation (SEM) controllers to detect and recover SEU errors automatically. When the SEM controller observes an unrecoverable SEU error, the PS board FPGA asserts a recovery request signal to JATHub. Then, the JATHub initiates the entire recovery process based on the flash memory on PS board.

All of the basic functions of the PS board, SL and JATHub have been implemented (e.g. the

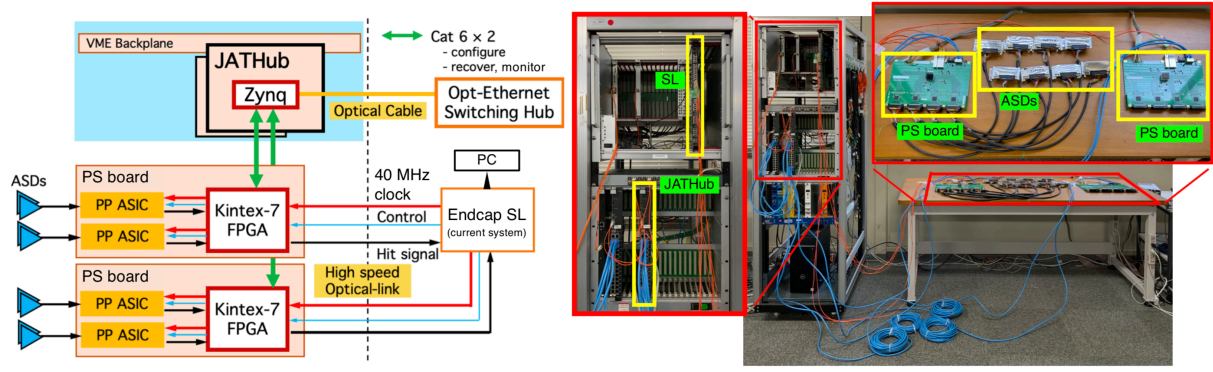


Figure A.3: The schematic (left) and photo (right) of the testbed for system-level commissioning of the TGC front-end electronics at HL-LHC. The testbed consists of the PS board and JATHub and the SL. SL and PS boards are connected by optical fibers, while JATHub and PS board are connected by category 6 cables.

fixed latency clock distribution, clock phase alignment, PP ASIC and DAC configuration, data readout from PS board to SL, register control and SEU recovery) and tested in the system level testbed which schematic and photo is shown in Fig. A.3.

We have designed and implemented a new scheme called Autonomous Control Mechanism (ACM) to handle the parameters which have large variation, and to realize the advancement and automation of the electronics control system. ACM on each electronics recognizes the situation by itself (e.g. FPGA power-up or reconfiguration, serial link lost and transceiver reset signal) and takes the necessary actions automatically (e.g. initialize serial link, re-establish clock with a fixed latency manner and configure registers) without communication with the central control system. Parameters for configuring the electronics are typically written from the back-end system, as in the current Run 3 TGC system. However, by this method, parameters must be written each time the electronics are powered on or reconfigured, and it is usually time-consuming because the electronics are accessed sequentially from the back-end where the current TGC system takes four minutes to set parameters for all electronics every time data-taking starts. Reconfiguration of electronics is required in case of electronics errors such as single event upsets or serial link lost. In the ACM, parameters are stored in non-volatile flash memory on each board. Electronics with FPGA are often equipped with the flash memory to store firmware for the FPGA. Extended use of the external non-volatile flash memory allows us to store dedicated parameters in addition to the firmware. This way the frontend electronics can restore the fully tuned and dedicated parameters without real-time communication with the backend system in configuration, such as after the power cycle and reconfigurations.

ACM has two main functions: parameter configuration and serial link (re-)establishment with the fixed latency clock recovery.

Parameter configuration by ACM ACM recognizes that the FPGA power is turned on or reconfigured then the “Flash controller” reads the parameters from the external non-volatile flash memory and store it to the “Parameter register” in the FPGA. Parameter register stores parameters in triplicate to build a robust mechanism for single event upsets. Based on the stored parameters, ACM configures the FPGA registers, PP ASIC parameters, and adjusts the phase of the 40 MHz clock. By introducing ACM, the time required to configure electronics can be drastically reduced compared to current system.

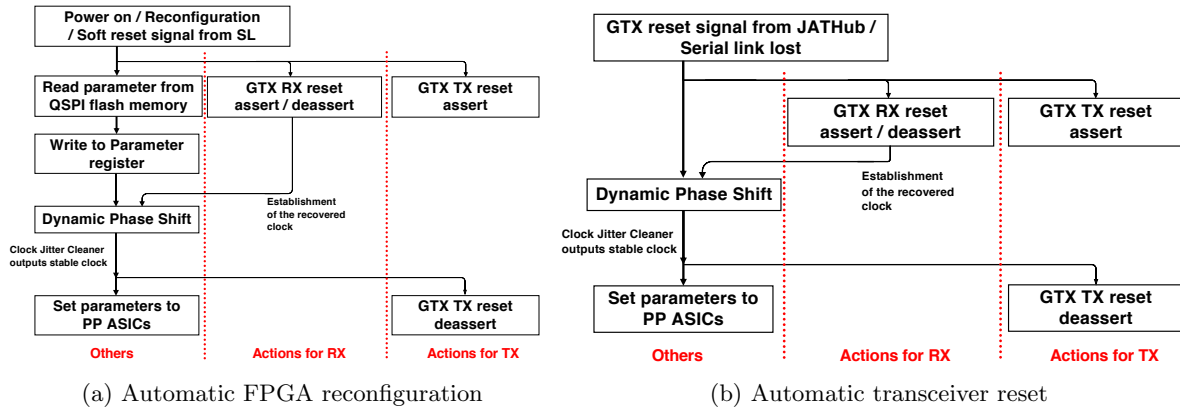


Figure A.4: Overall procedure for ACM.

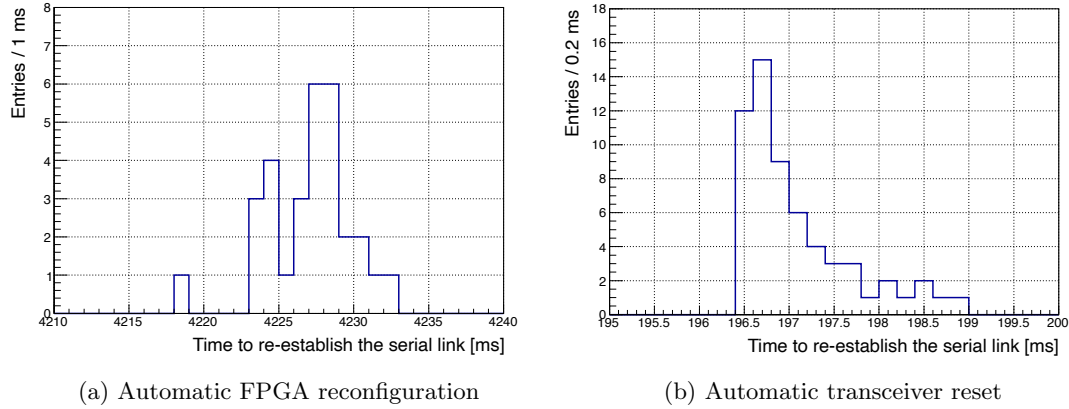


Figure A.5: Performance evaluation of ACM on PS board.

Serial link (re-)establishment by ACM Multiple steps are required to recover the clock in the fixed latency and (re-)establish the serial link with link protocol of 8b10b. The detection of the comma character (especially K28.5) is performed in the receiver, and the phase of recovered clock is controlled from FPGA logic. There is 1 Unit Interval randomness in the phase of the recovered clock depending on the evenness of the number of clock shifts required to detect comma, and the receiver is reset repeatedly until the correct phase is achieved. All of these steps are incorporated into the ACM framework, and ACM performs automatically the multiple steps in the correct sequence.

Overall procedure for ACM Procedures for parameter configuration and serial link establishment have to be performed in the correct sequence. For example, the clock phase adjustment to align the clock phases between PS boards (Dynamic phase shift) have to be performed only after the clock recovery is completed in the receiver. And also the transmitter reset must be deasserted only after the clock jitter cleaner outputs stable clock, because transmitter uses this clock as the reference clock.

Fig. A.4 shows the overall procedure for ACM. Fig. A.4(a) refers to the procedure for automatic FPGA reconfiguration, which works when the FPGA is powered on or reconfigured. Fig. A.4(b) is the procedure for automatic transceiver reset, which works when the FPGA receives the transceiver reset signal or the serial link is lost. It can be seen from Fig. A.4(a)(b)

that the above requirements are satisfied and that the parameter setting procedure, which is unnecessary for automatic transceiver reset, is omitted from Fig. A.4(b). Fig. A.5(a) shows the time distribution after the transceiver receives reset signal until the PS board ACM re-establishes the serial link with SL. It takes 196.5 – 199 ms, and 99% of the time is spent waiting for the jitter cleaner to output a stable clock. The time varies depending on how many times the receiver needs to be reset before the correct phase clock is obtained. Fig. A.5(b) shows the time distribution after the FPGA receives reconfiguration signal until the PS board ACM re-establishes the serial link with SL. It takes 4218 – 4233 ms, and 95% of the time is spent for programming the FPGA with the firmware. It was shown that, by introducing ACM, the time required for electronics to be configured can be significantly reduced, which minimizes the possible downtime in case of errors during the data taking. This significant time reduction was achieved by first storing parameters on each board, eliminating the need for writing parameters from the back-end sequentially, and then enabling each electronics to recognize the situation and take necessary actions automatically by introducing ACM, eliminating the need to communicate with the central control system.

The installation of these TGC electronics into the ATLAS cavern and counting room will start from 2026 and HL-LHC is planned to start from 2030.

Appendix B

Charge-flip probabilities and scale factors

A full set of charge-flip probabilities and scale factors mentioned in Section 8.3.2 is presented.

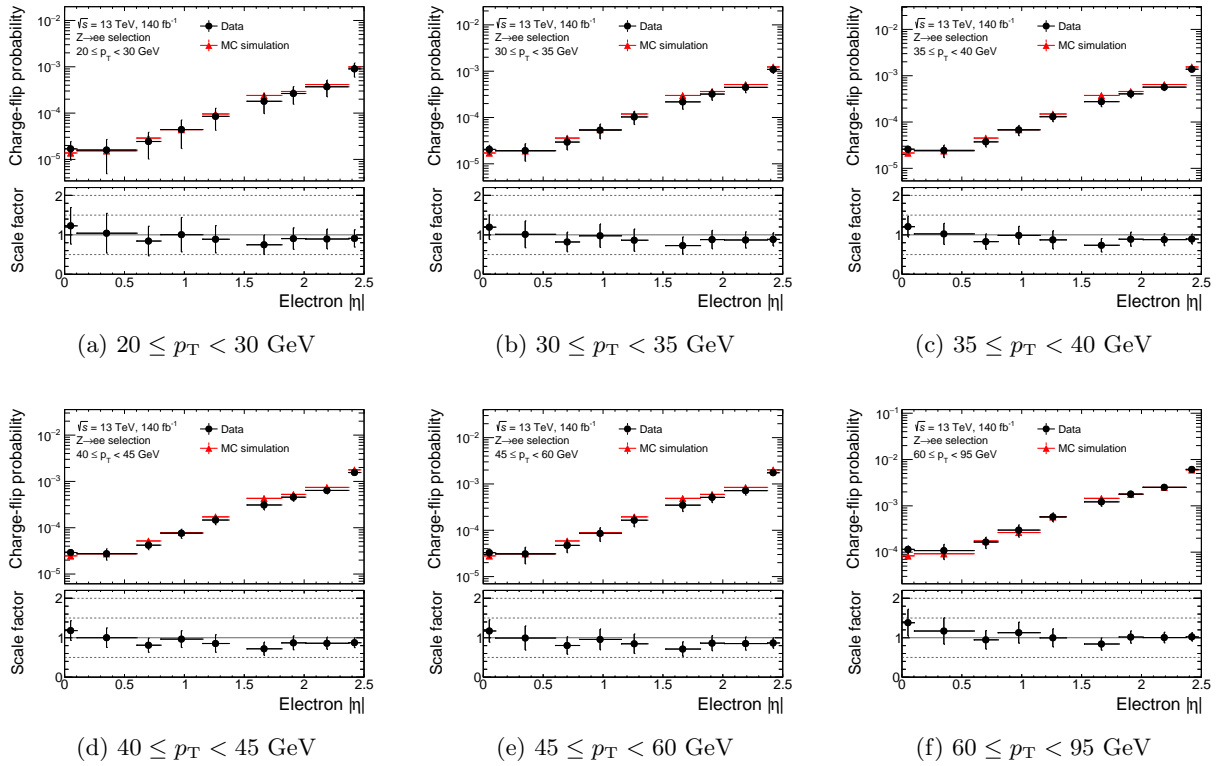


Figure B.1: Charge-flip probabilities in data and MC (upper panel) and the scale factors (lower panel) as the function of electron $|\eta|$. The uncertainties on the data charge-flip probability and the scale factors include both the statistical and systematic components.

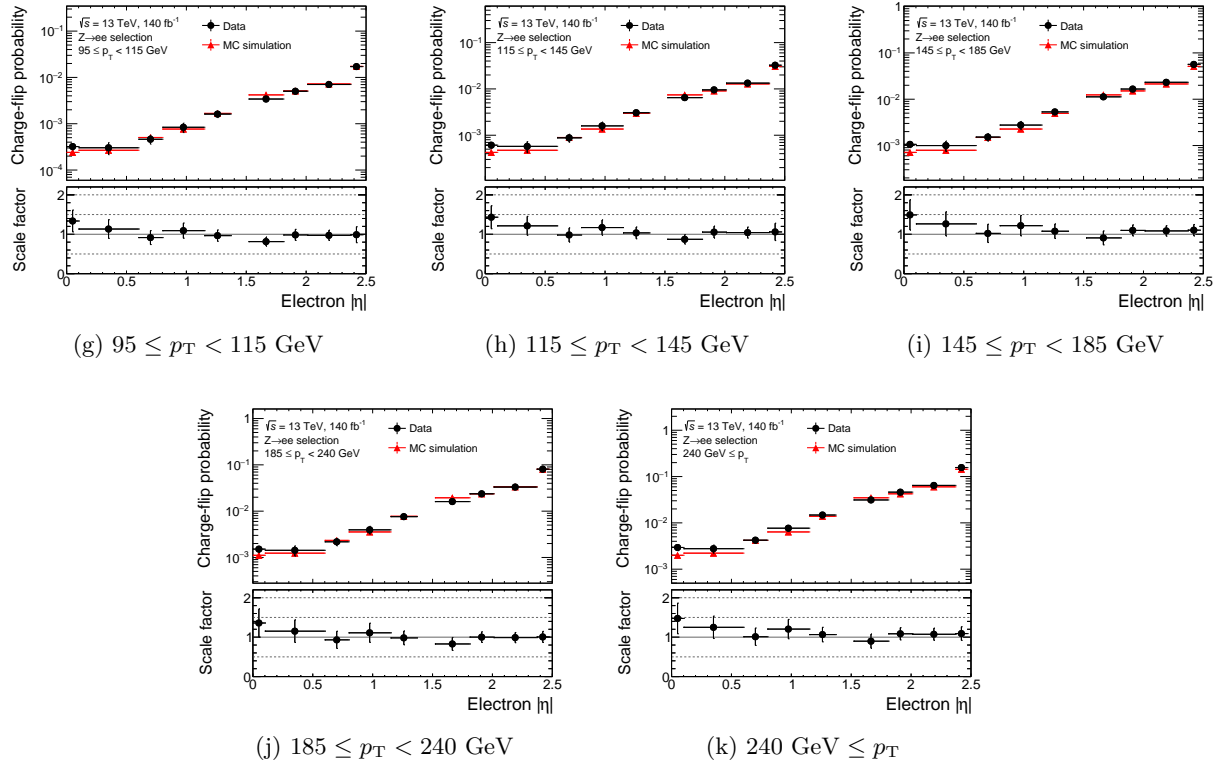


Figure B.1: Charge-flip probabilities in data and MC (upper panel) and the scale factors (lower panel) as the function of electron $|\eta|$. The uncertainties on the data charge-flip probability and the scale factors include both the statistical and systematic components. (cont.)

Appendix C

Comparison of the magnitude of systematic and statistical uncertainties

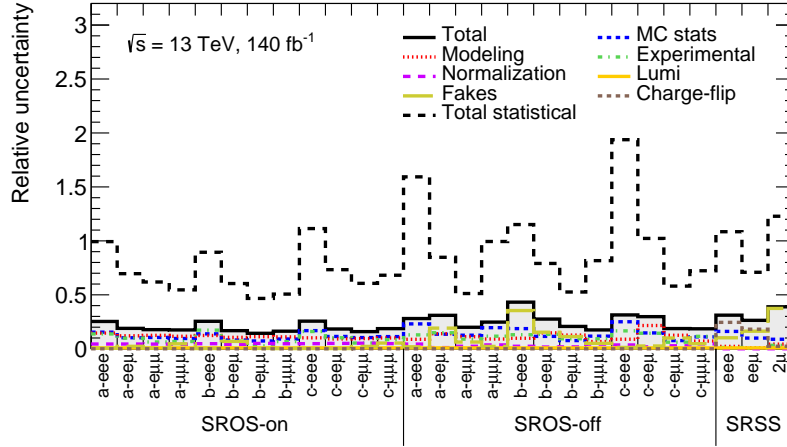


Figure C.1: Systematic uncertainties on the post-fit background yields in the SRs. The “MC stats” category represents the uncertainty arising from the limited number of MC simulation samples. The “Modeling” uncertainty category represents the theory uncertainty arising from the choice of parameters for generating MC simulation samples. The “Experimental” category indicates systematic uncertainties originating from the reconstruction, identification, isolation, and calibration of physics objects. The “Normalization” category indicates systematic uncertainties arising from the WZ NF uncertainty involving statistical uncertainty originating from the limited CRWZ statistics. The “Lumi” category represents the integrated luminosity uncertainty. The “Fakes” category involves the uncertainty arising from the fake factor uncertainty, the fake lepton composition difference in CRFF and SRSS- 2μ and the limited anti-ID CR statistics. The “Charge-flip” category represents the systematic uncertainties originating from the charge-flip scale factor uncertainty and the charge-flip source difference in CRCF and SRs. Relative total statistical uncertainty, $\sqrt{N_{\text{exp}}}/N_{\text{exp}}$, is shown as “Total statistical”.

Appendix D

Kinematic Distributions in Signal Regions

Kinematic distributions of the unblinded SRs are listed.

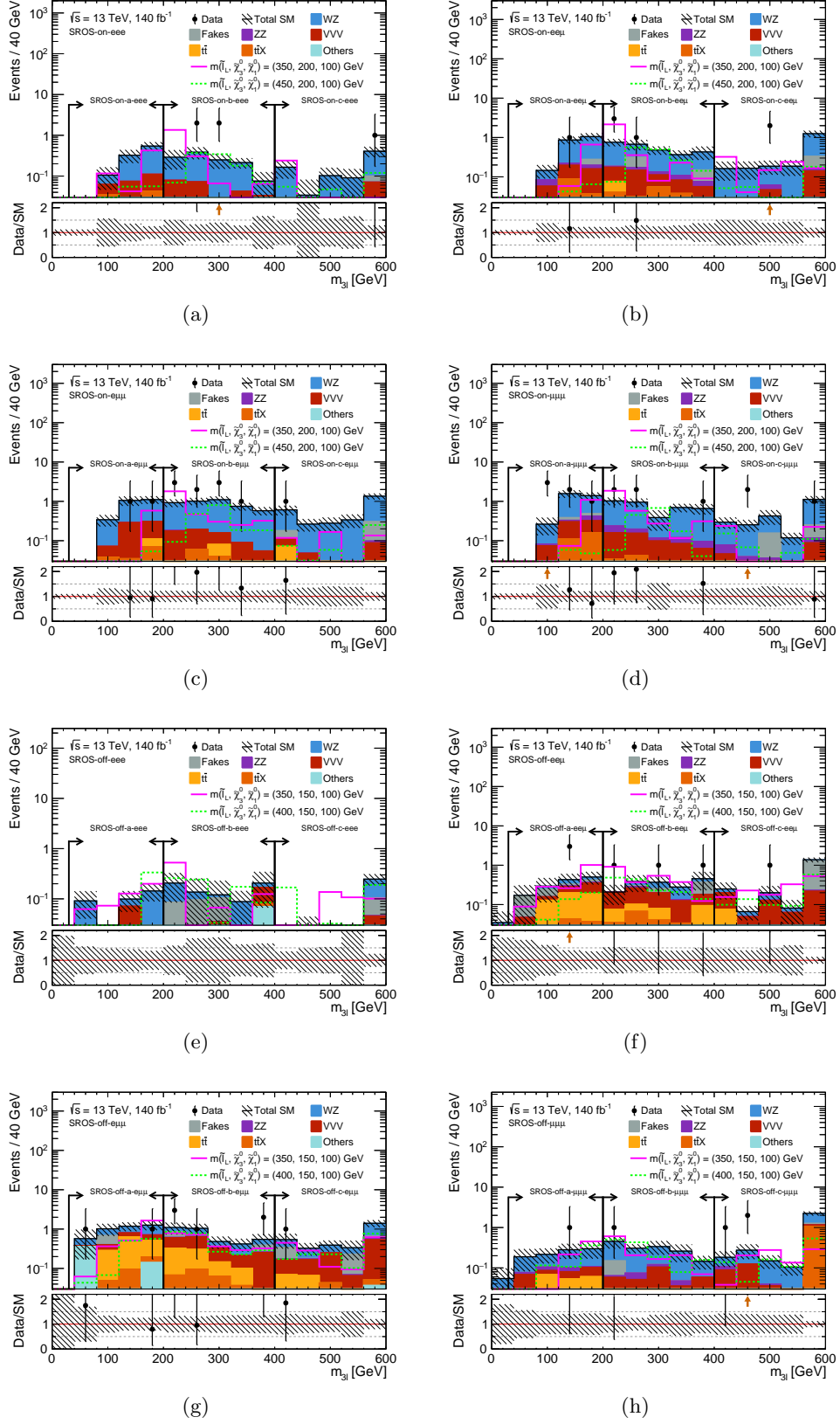


Figure D.1: Post-fit distributions of $m_{3\ell}$ in SROS. The bins enclosed by arrows indicate the respective regions. The hatched band includes the combined statistical and systematic uncertainty on the total estimated backgrounds. The overflow is included in the highest bin. Pink and green lines represent the expected distributions of the typical signal targeted in the SR bin. The bottom panels show the ratio of the observed data to the predicted total background yields.

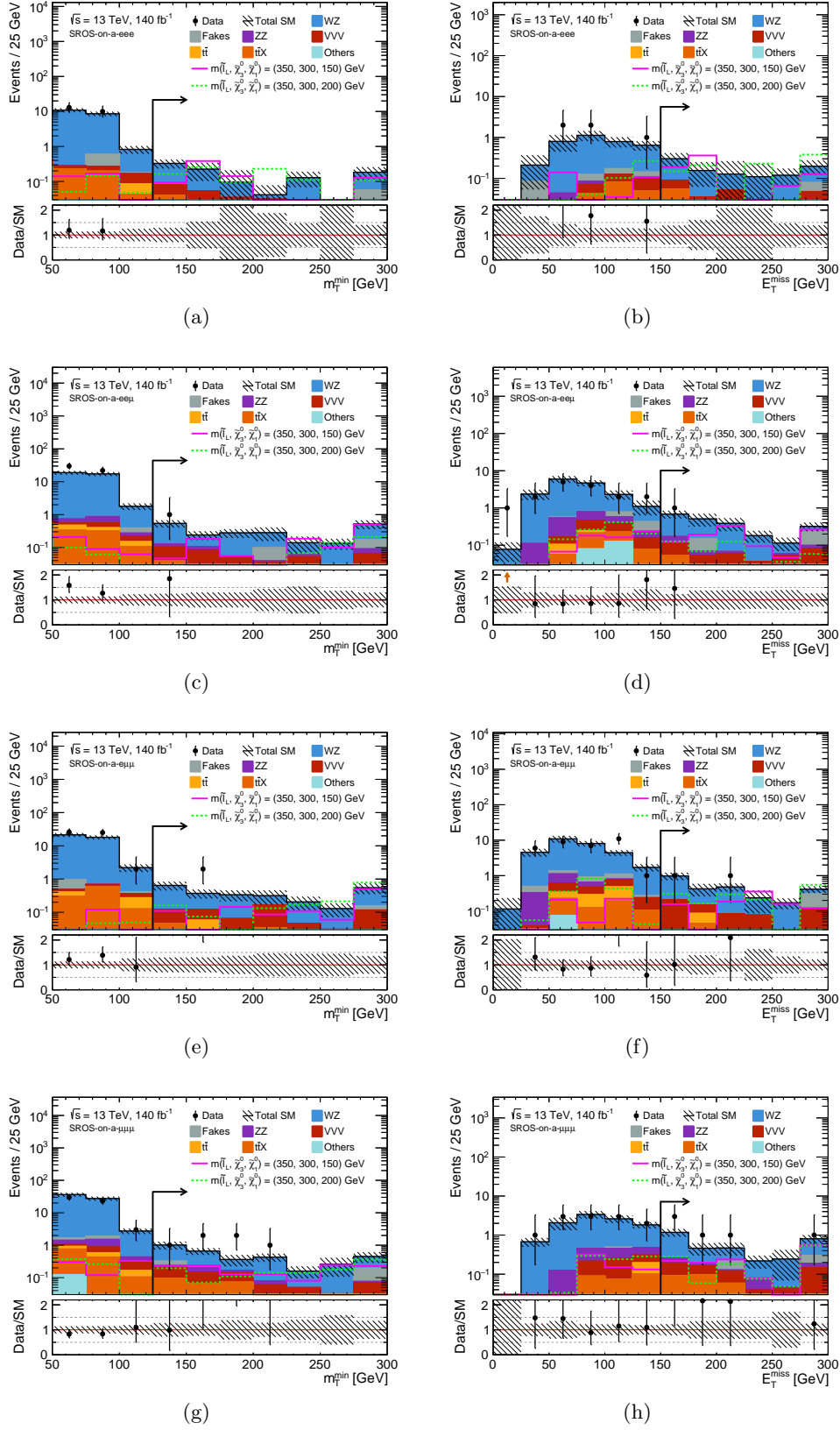


Figure D.2: Post-fit distributions in SROS-on-a. Each plot is drawn without applying selections to the variable illustrated. Arrows indicate the selection which are applied in SRs. The hatched band includes the combined statistical and systematic uncertainty on the total estimated backgrounds. The overflow is included in the highest bin. Pink and green lines represent the expected distributions of the typical signal targeted in the SR bin. The bottom panels show the ratio of the observed data to the predicted total background yields.

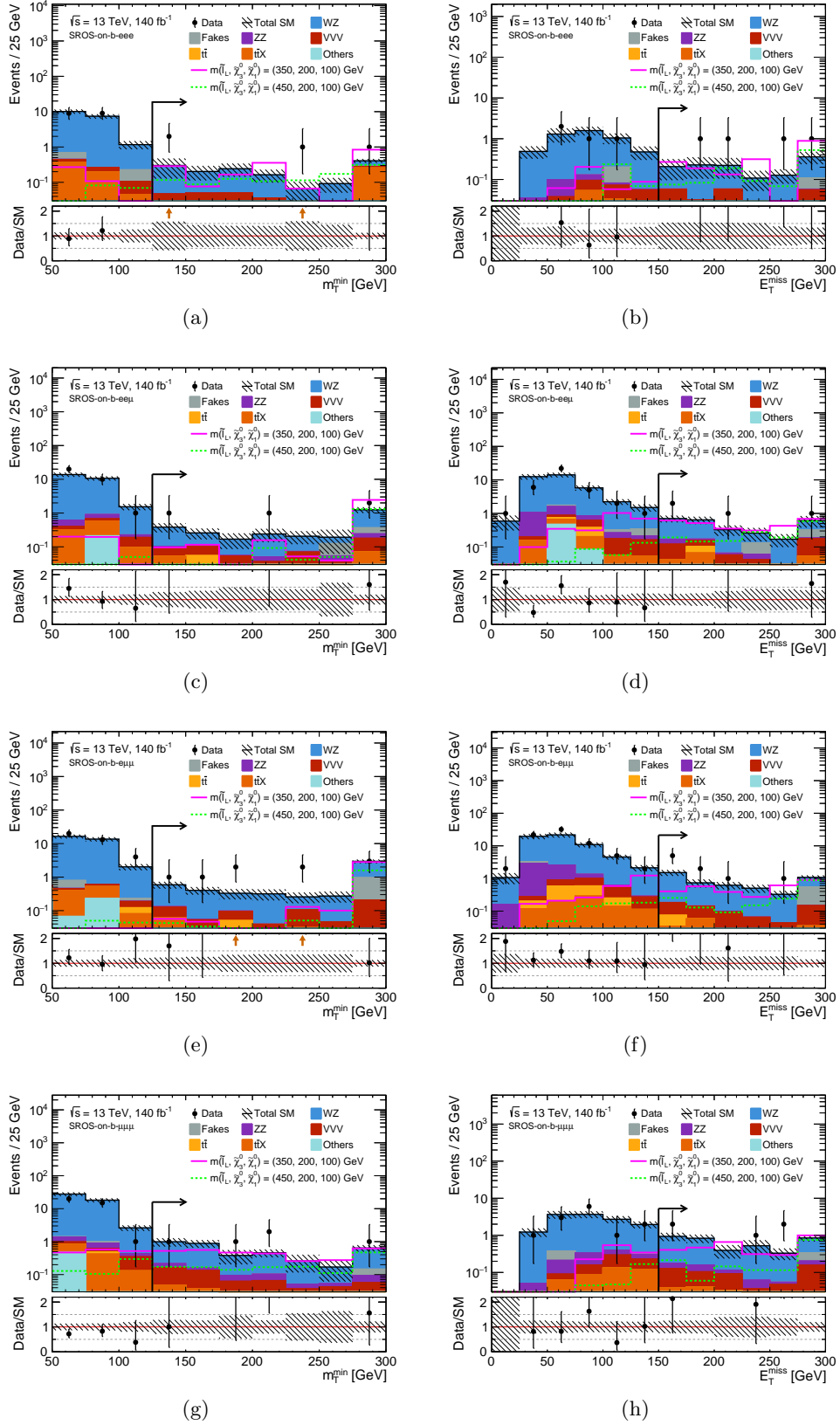


Figure D.3: Post-fit distributions in SROS-on-b. Each plot is drawn without applying selections to the variable illustrated. Arrows indicate the selection which are applied in SRs. The hatched band includes the combined statistical and systematic uncertainty on the total estimated backgrounds. The overflow is included in the highest bin. Pink and green lines represent the expected distributions of the typical signal targeted in the SR bin. The bottom panels show the ratio of the observed data to the predicted total background yields.

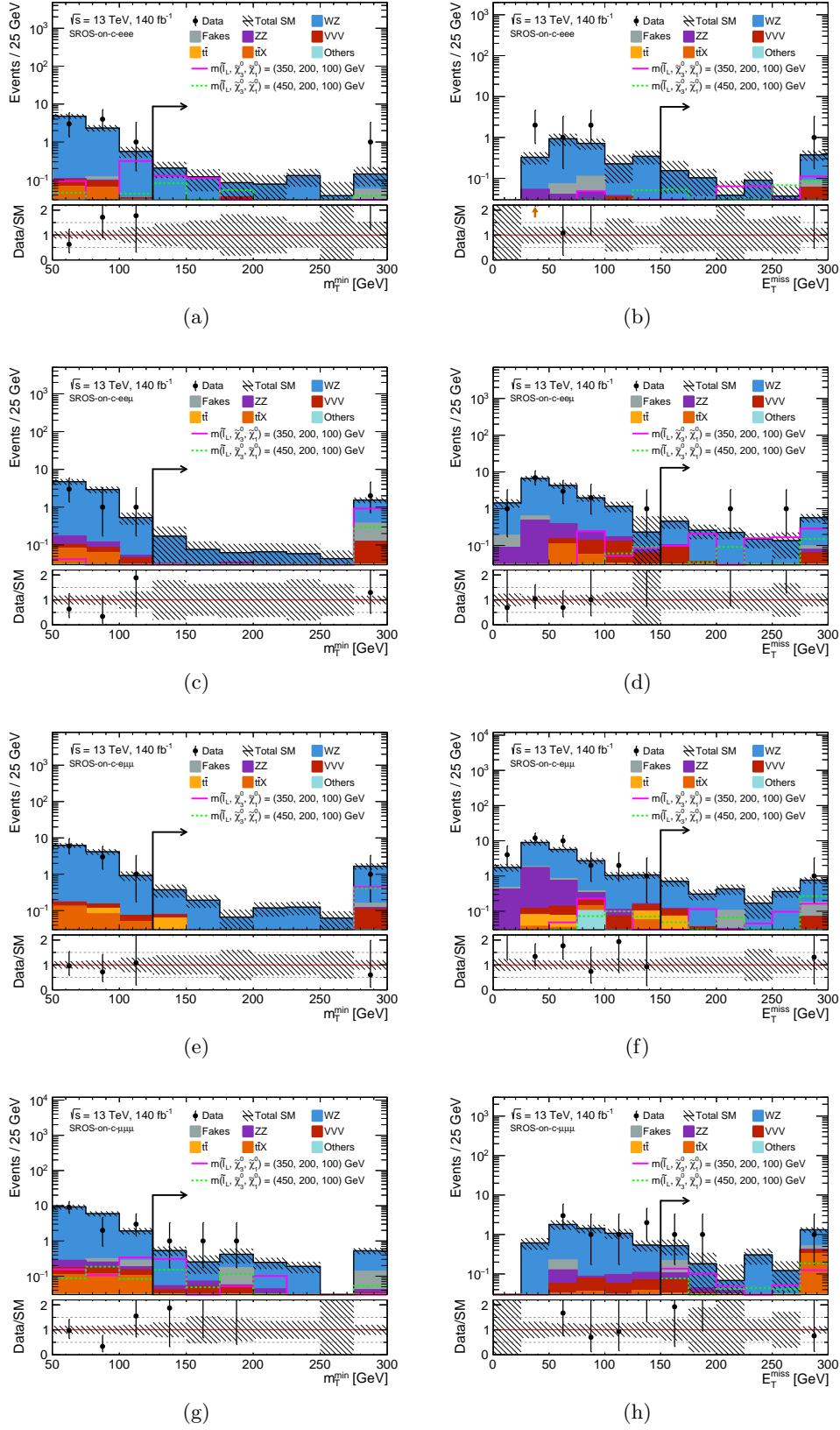


Figure D.4: Post-fit distributions in SROS-on-c. Each plot is drawn without applying selections to the variable illustrated. Arrows indicate the selection which are applied in SRs. The hatched band includes the combined statistical and systematic uncertainty on the total estimated backgrounds. The overflow is included in the highest bin. Pink and green lines represent the expected distributions of the typical signal targeted in the SR bin. The bottom panels show the ratio of the observed data to the predicted total background yields.

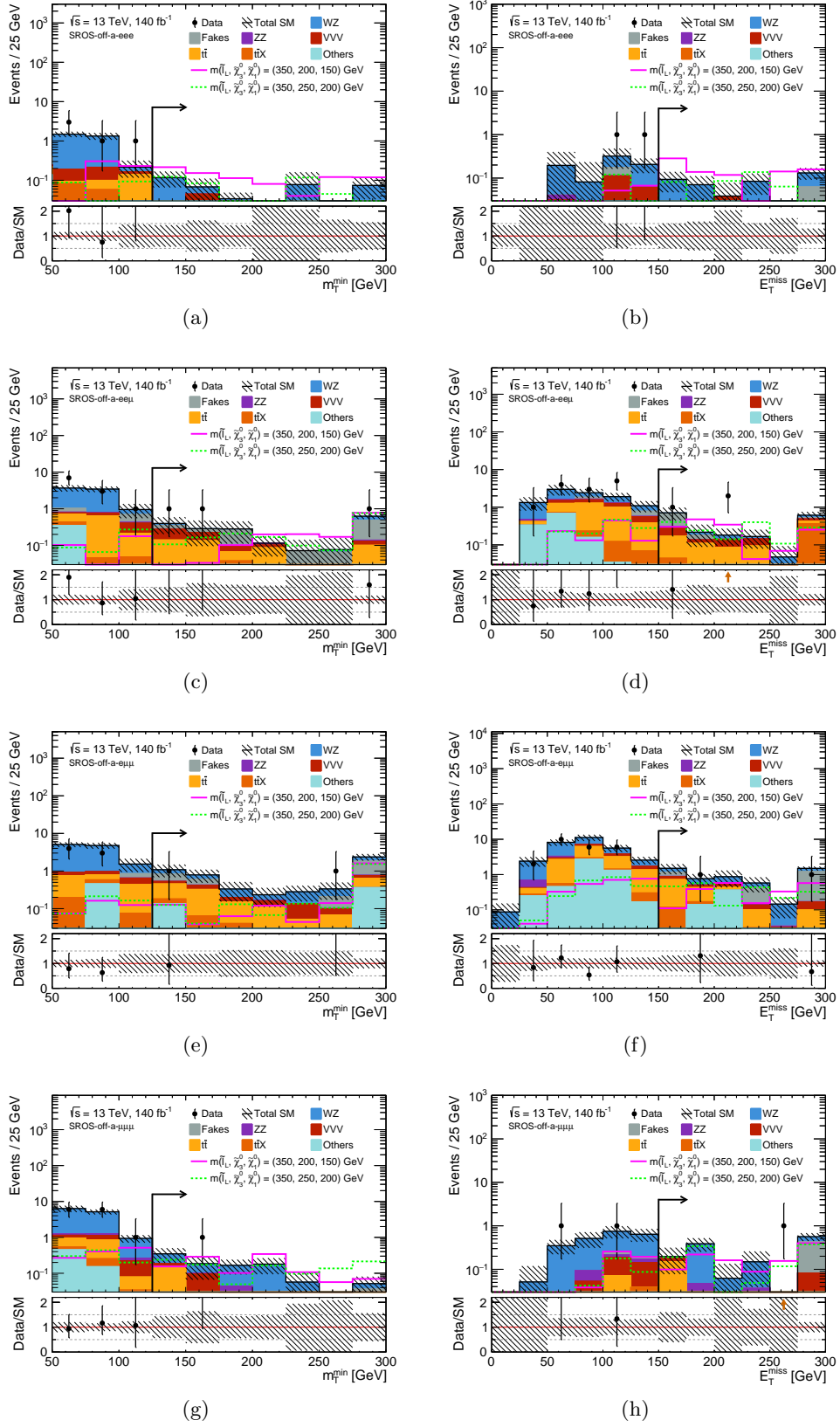


Figure D.5: Post-fit distributions in SROS-off-a. Each plot is drawn without applying selections to the variable illustrated. Arrows indicate the selection which are applied in SRs. The hatched band includes the combined statistical and systematic uncertainty on the total estimated backgrounds. The overflow is included in the highest bin. Pink and green lines represent the expected distributions of the typical signal targeted in the SR bin. The bottom panels show the ratio of the observed data to the predicted total background yields.

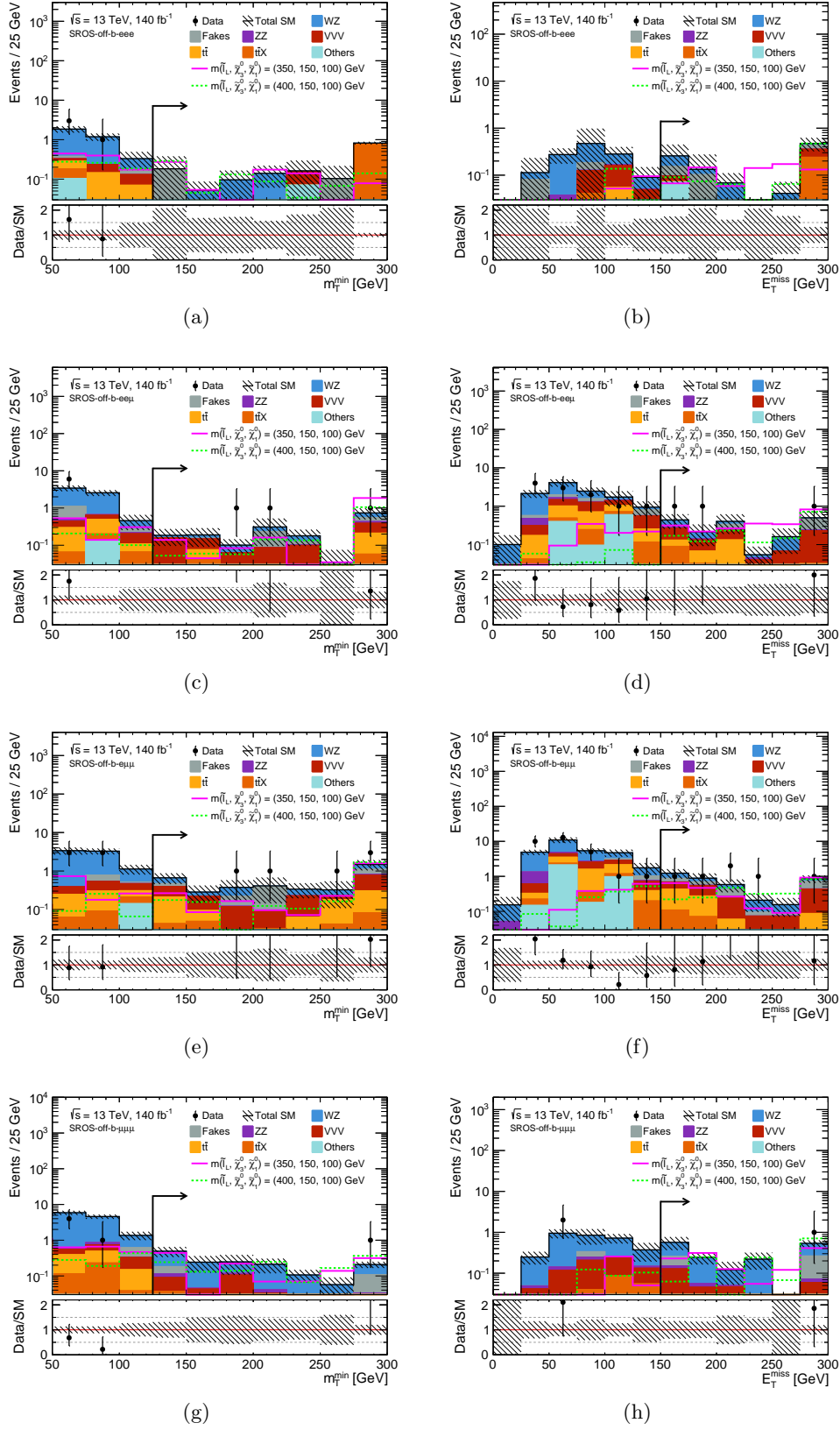


Figure D.6: Post-fit distributions in SROS-off-b. Each plot is drawn without applying selections to the variable illustrated. Arrows indicate the selection which are applied in SRs. The hatched band includes the combined statistical and systematic uncertainty on the total estimated backgrounds. The overflow is included in the highest bin. Pink and green lines represent the expected distributions of the typical signal targeted in the SR bin. The bottom panels show the ratio of the observed data to the predicted total background yields.

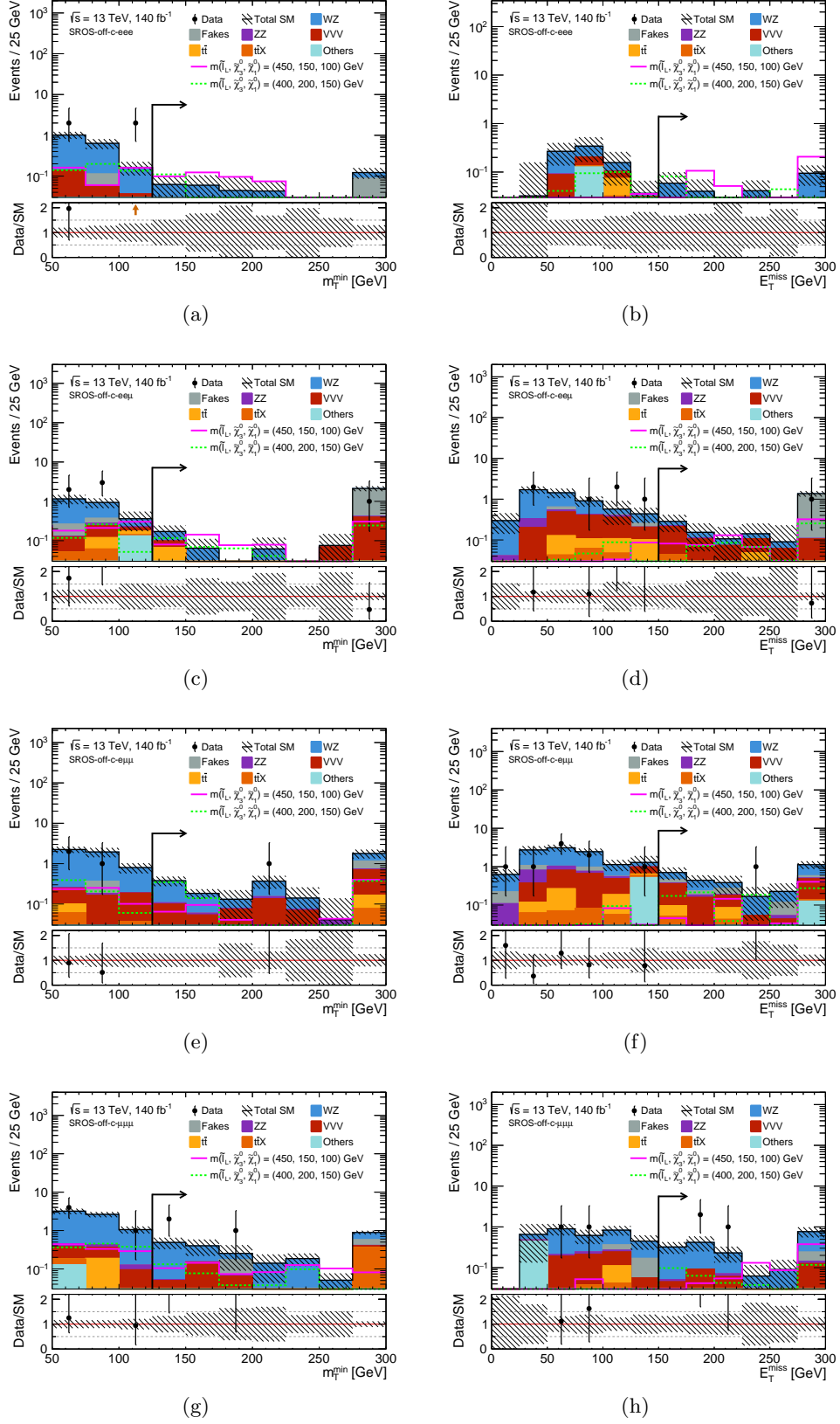


Figure D.7: Post-fit distributions in SROS-off-c. Each plot is drawn without applying selections to the variable illustrated. Arrows indicate the selection which are applied in SRs. The hatched band includes the combined statistical and systematic uncertainty on the total estimated backgrounds. The overflow is included in the highest bin. Pink and green lines represent the expected distributions of the typical signal targeted in the SR bin. The bottom panels show the ratio of the observed data to the predicted total background yields.

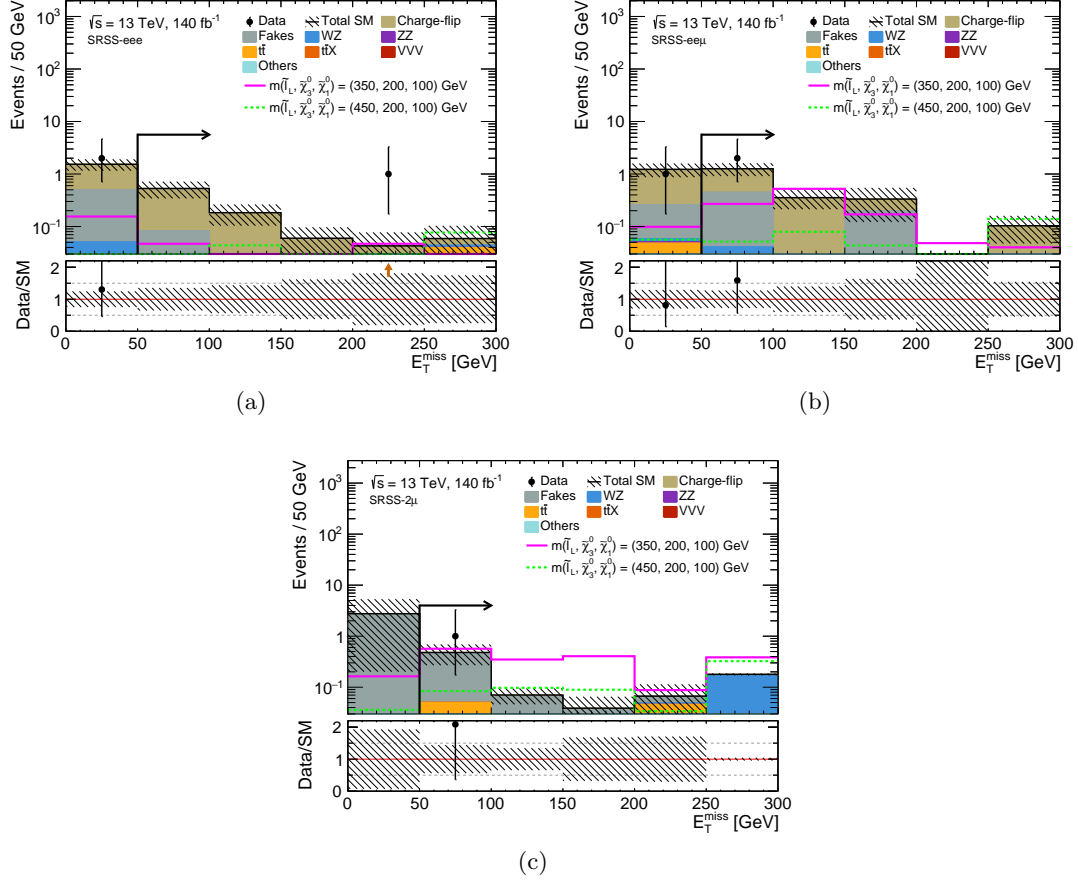


Figure D.8: Post-fit distributions of E_T^{miss} in SRSS. Each plot is drawn without applying selections to the variable illustrated. Arrows indicate the selection which are applied in SRs. The hatched band includes the combined statistical and systematic uncertainty on the total estimated backgrounds. The overflow is included in the highest bin. Pink and green lines represent the expected distributions of the typical signal targeted in the SR bin. The bottom panels show the ratio of the observed data to the predicted total background yields.

Appendix E

Auxiliary Materials

E.1 Acceptance and Efficiency

Signal acceptance is given by the ratio of weighted selected events by the SR to the weighted total generated events. The selection is based on generator-level particle information. The efficiency of lepton reconstruction/identification and b -tagging are treated as 100%. The signal acceptance is summarized in Figure [E.1](#).

Signal efficiency is defined by the number of events of reconstructed-level signal simulation divided by the number of events obtained at generator level. The signal efficiency is summarized in Figure [E.2](#).

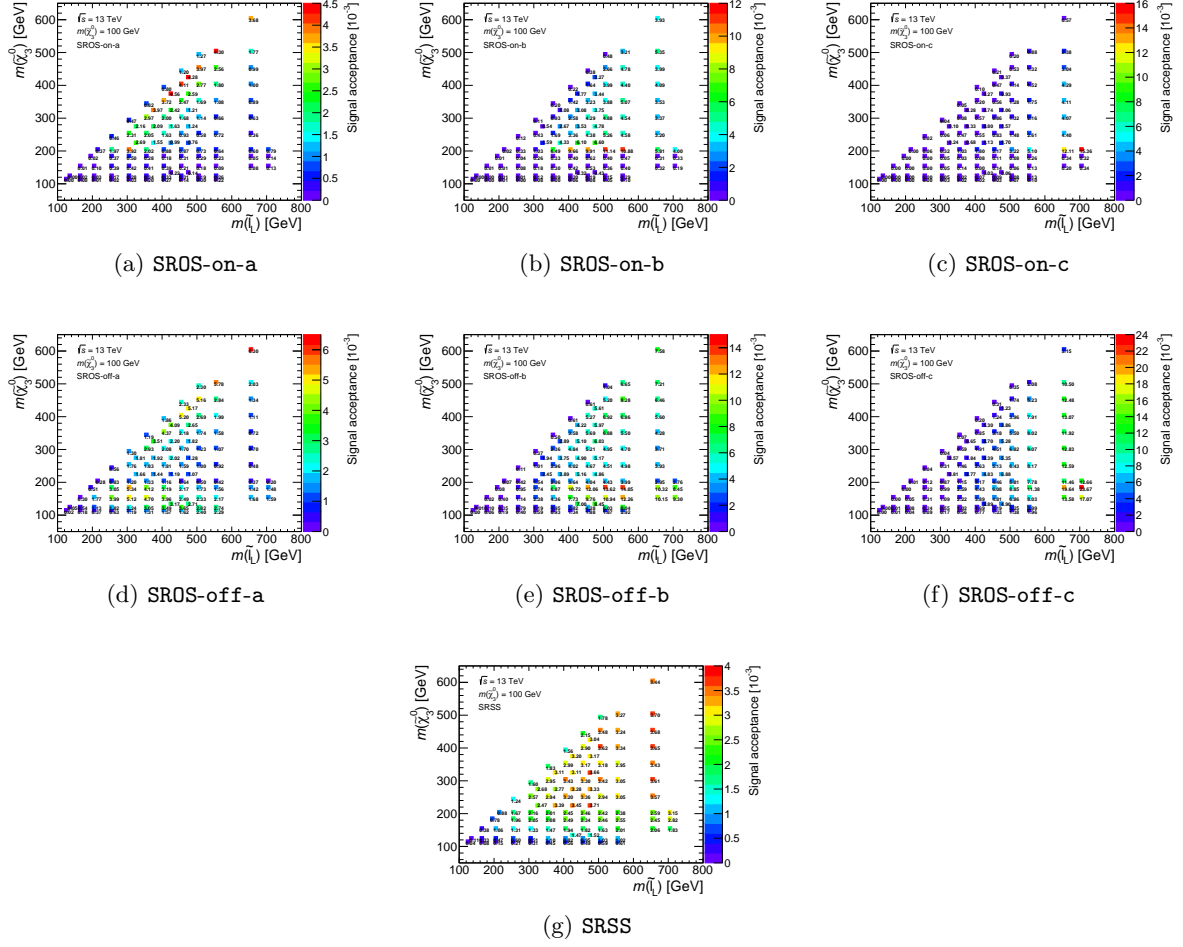


Figure E.1: Signal acceptance of signals with $m(\tilde{\chi}_1^0) = 100$ GeV by the flavor merged SRs, evaluated using MC simulation. The acceptance is given by the ratio of weighted selected events by the SR to the weighted total generated events. The selection is based on generator-level particle information. The efficiency of lepton reconstruction/identification and b -tagging are treated as 100%.

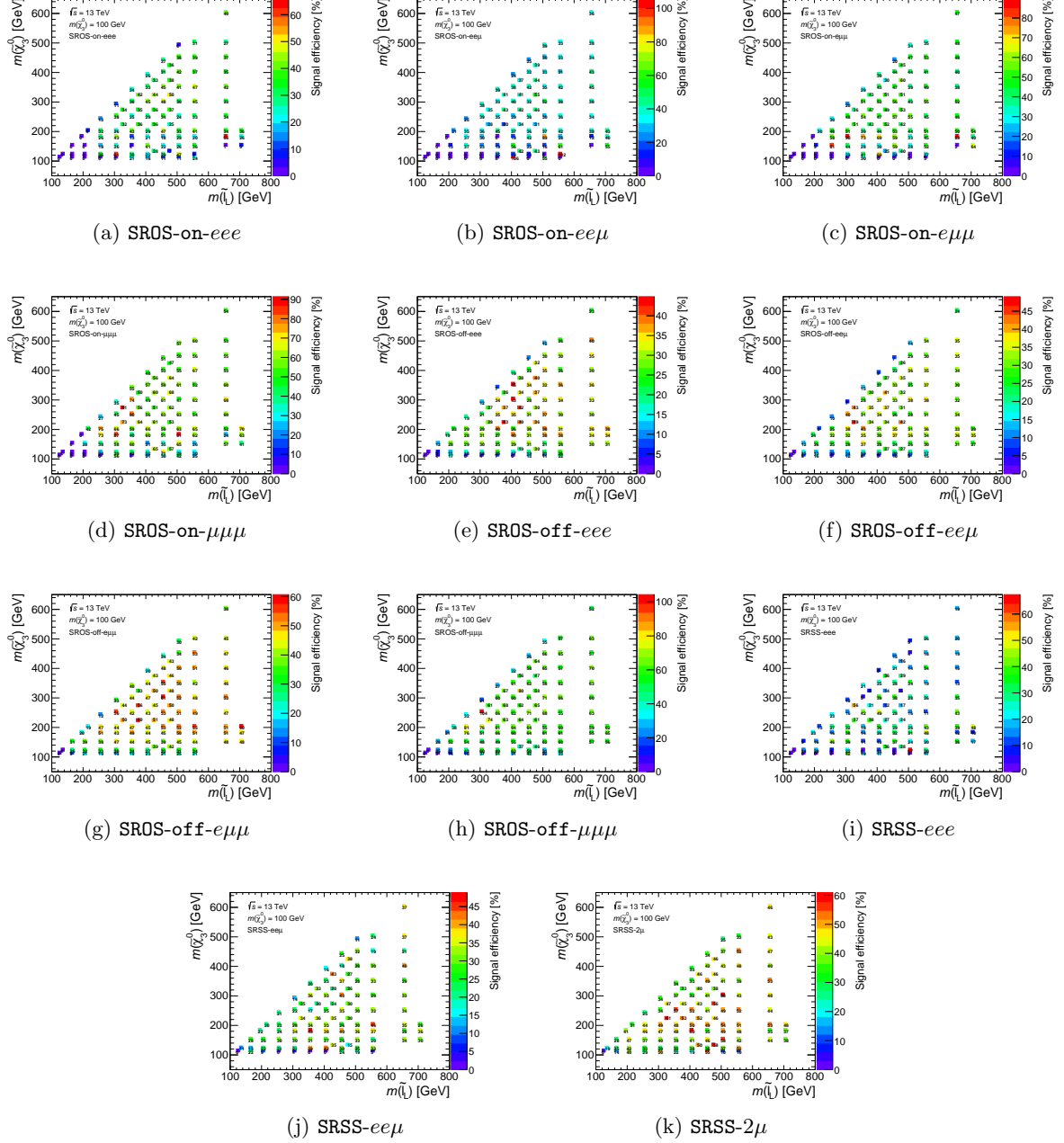


Figure E.2: Signal efficiencies of signals with $m(\tilde{\chi}_1^0) = 100$ GeV by the $m_{3\ell}$ merged SROS and SRSS, evaluated using MC simulation. The efficiency is defined by the number of events of reconstructed-level signal simulation divided by the number of events obtained at generator level. Efficiency below 0.002% is rounded to be 0.00 in the entry. The spiky efficiency values are because of the difference between the truth and reconstructed samples amplified by a statistical fluctuation due to the limited statistics.

E.2 Cross-section Upper Limits

The expected and observed upper limits on the cross-section are given in Fig. E.3 and E.4, respectively.

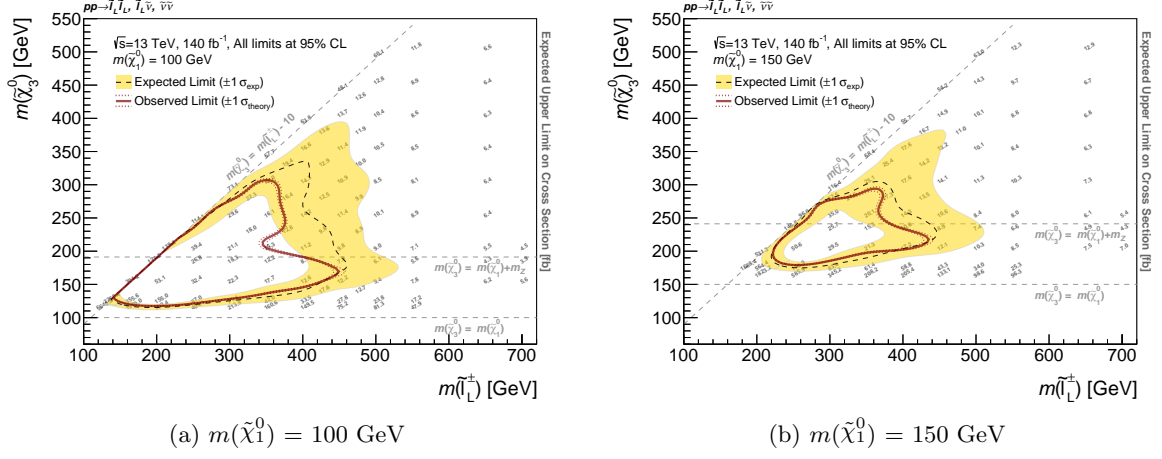


Figure E.3: The expected upper limits on the cross-section for each signal grid point. The gray numbers represent the values. The expected (dashed) and observed (solid) 95% CL exclusion limits are overlaid.

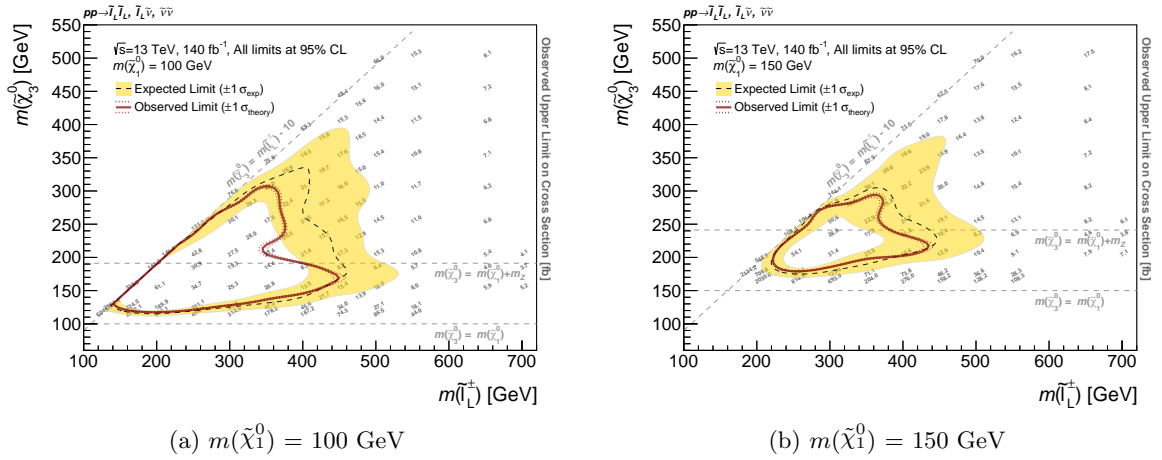


Figure E.4: The observed upper limits on the cross-section for each signal grid point. The gray numbers represent the values. The expected (dashed) and observed (solid) 95% CL exclusion limits are overlaid.

Bibliography

- [1] M. Peskin and D. V. Schröder, *An introduction to Quantum Field Theory*. Westview, 1995, <https://catalogue.library.cern/literature/sjq69-f2x52>.
- [2] F. Halzen and A. D. Martin, *Quarks & Leptons: An Introductory Course in Modern Particle Physics*, Wiley, 1984, <https://catalogue.library.cern/literature/dlep3-z9988>.
- [3] F. Englert and R. Brout, “Broken symmetry and the mass of gauge vector mesons,” *Phys. Rev. Lett.*, vol. 13, p. 321, 1964. DOI: [10.1103/PhysRevLett.13.321](https://doi.org/10.1103/PhysRevLett.13.321).
- [4] P. W. Higgs, “Broken symmetries, massless particles and gauge fields,” *Phys. Lett.*, vol. 12, p. 132, 1964. DOI: [10.1016/0031-9163\(64\)91136-9](https://doi.org/10.1016/0031-9163(64)91136-9).
- [5] S. L. Glashow, “Partial-symmetries of weak interactions,” *Nucl. Phys.*, vol. 22, p. 579, 1961. DOI: [10.1016/0029-5582\(61\)90469-2](https://doi.org/10.1016/0029-5582(61)90469-2).
- [6] S. Weinberg, “A model of leptons,” *Phys. Rev. Lett.*, vol. 19, p. 1264, 1967. DOI: [10.1103/PhysRevLett.19.1264](https://doi.org/10.1103/PhysRevLett.19.1264).
- [7] A. Salam and J. C. Ward, “Electromagnetic and weak interactions,” *Phys. Lett.*, vol. 13, p. 168, 1964. DOI: [10.1016/0031-9163\(64\)90711-5](https://doi.org/10.1016/0031-9163(64)90711-5).
- [8] M. Kobayashi and T. Masukawa, “CP-Violation in the Renormalizable Theory of Weak Interaction,” *Prog. of Theo. Phys.*, vol. 49, p. 652, 1973. DOI: [10.1143/PTP.49.652](https://doi.org/10.1143/PTP.49.652).
- [9] Y. Golfand and E. Likhtman, “Extension of the Algebra of Poincare Group Generators and Violation of P Invariance,” *JETP Lett.*, vol. 13, p. 323, 1971, [*Pisma Zh. Eksp. Teor. Fiz.* **13** (1971) 452].
- [10] D. Volkov and V. Akulov, “Is the neutrino a goldstone particle?” *Phys. Lett. B*, vol. 46, p. 109, 1973. DOI: [10.1016/0370-2693\(73\)90490-5](https://doi.org/10.1016/0370-2693(73)90490-5).
- [11] J. Wess and B. Zumino, “Supergauge transformations in four dimensions,” *Nucl. Phys. B*, vol. 70, p. 39, 1974. DOI: [10.1016/0550-3213\(74\)90355-1](https://doi.org/10.1016/0550-3213(74)90355-1).
- [12] J. Wess and B. Zumino, “Supergauge invariant extension of quantum electrodynamics,” *Nucl. Phys. B*, vol. 78, p. 1, 1974. DOI: [10.1016/0550-3213\(74\)90112-6](https://doi.org/10.1016/0550-3213(74)90112-6).
- [13] S. Ferrara and B. Zumino, “Supergauge invariant Yang-Mills theories,” *Nucl. Phys. B*, vol. 79, p. 413, 1974. DOI: [10.1016/0550-3213\(74\)90559-8](https://doi.org/10.1016/0550-3213(74)90559-8).
- [14] A. Salam and J. Strathdee, “Super-symmetry and non-Abelian gauges,” *Phys. Lett. B*, vol. 51, p. 353, 1974. DOI: [10.1016/0370-2693\(74\)90226-3](https://doi.org/10.1016/0370-2693(74)90226-3).
- [15] S. Weinberg, “Implications of dynamical symmetry breaking,” *Phys. Rev. D*, vol. 13, p. 974, 1976. DOI: [10.1103/PhysRevD.13.974](https://doi.org/10.1103/PhysRevD.13.974).
- [16] S. Weinberg, “Implications of dynamical symmetry breaking: an addendum,” *Phys. Rev. D*, vol. 19, p. 1277, 1979. DOI: [10.1103/PhysRevD.19.1277](https://doi.org/10.1103/PhysRevD.19.1277).

- [17] E. Gildener, “Gauge-symmetry hierarchies,” *Phys. Rev. D*, vol. 14, p. 1667, 1976. DOI: [10.1103/PhysRevD.14.1667](https://doi.org/10.1103/PhysRevD.14.1667).
- [18] E. Gildener, “Dynamics of spontaneous symmetry breaking in the Weinberg-Salam theory,” *Phys. Rev. D*, vol. 20, p. 2619, 1979. DOI: [10.1103/PhysRevD.20.2619](https://doi.org/10.1103/PhysRevD.20.2619).
- [19] S. P. Martin, “A Supersymmetry Primer,” *Adv. Ser. Direct. High Energy Phys.*, vol. 18, p. 1, 1998. DOI: [10.1142/9789812839657_0001](https://doi.org/10.1142/9789812839657_0001). arXiv: [hep-ph/9709356](https://arxiv.org/abs/hep-ph/9709356).
- [20] V. C. Rubin and W. K. Ford Jr, “Rotation of the andromeda nebula from a spectroscopic survey of emission regions,” *The Astro. Journal*, vol. 159, p. 379, 1970. DOI: [10.1086/150317](https://doi.org/10.1086/150317).
- [21] V. C. Rubin, W. K. Ford Jr, and N. Thonnard, “Rotational properties of 21 SC galaxies with a large range of luminosities and radii, from NGC 4605/R= 4kpc/to UGC 2885/R= 122 kpc,” *The Astro. Journal*, vol. 238, p. 471, 1980. DOI: [10.1086/150317](https://doi.org/10.1086/150317).
- [22] G. Steigman and M. S. Turner, “Cosmological constraints on the properties of weakly interacting massive particles,” *Nuclear Physics B*, vol. 253, pp. 375–386, 1985.
- [23] G. Bertone, D. Hooper, and J. Silk, “Particle dark matter: Evidence, candidates and constraints,” *Physics Reports*, vol. 405, no. 5, pp. 279–390, 2005.
- [24] G. Arcadi *et al.*, “The waning of the wimp? a review of models, searches, and constraints,” *The European Physical Journal C*, vol. 78, no. 3, p. 203, 2018.
- [25] L. Roszkowski, E. M. Sessolo, and S. Trojanowski, “Wimp dark matter candidates and searches—current status and future prospects,” *Reports on Progress in Physics*, vol. 81, no. 6, p. 066 201, 2018.
- [26] Planck Collaboration, “Planck 2018 results,” *Astron. Astrophys.*, vol. 641, A6, 2020. DOI: [10.1051/0004-6361/201833910](https://doi.org/10.1051/0004-6361/201833910).
- [27] LUX-ZEPLIN Collaboration, “First Dark Matter Search Results from the LUX-ZEPLIN (LZ) Experiment,” *Phys. Rev. Lett.*, vol. 131, p. 041 002, 2023. DOI: [10.1103/PhysRevLett.131.041002](https://doi.org/10.1103/PhysRevLett.131.041002).
- [28] Yue Meng *et al.* (PandaX-4T Collaboration), “Dark Matter Search Results from the PandaX-4T Commissioning Run,” *Phys. Rev. Lett.*, vol. 127, p. 261 802, 2021. DOI: [10.1103/PhysRevLett.127.261802](https://doi.org/10.1103/PhysRevLett.127.261802).
- [29] E. Aprile *et al.* (XENON Collaboration), “Dark Matter Search Results from a One Ton-Year Exposure of XENON1T,” *Phys. Rev. Lett.*, vol. 121, p. 111 302, 2018. DOI: [10.1103/PhysRevLett.121.111302](https://doi.org/10.1103/PhysRevLett.121.111302).
- [30] D. S. Akerib *et al.* (LUX Collaboration), “Results from a Search for Dark Matter in the Complete LUX Exposure,” *Phys. Rev. Lett.*, vol. 118, p. 021 303, 2017. DOI: [10.1103/PhysRevLett.118.021303](https://doi.org/10.1103/PhysRevLett.118.021303).
- [31] R. Ajaj *et al.* (DEAP Collaboration), “Search for dark matter with a 231-day exposure of liquid argon using DEAP-3600 at SNOLAB,” *Phys. Rev. D*, vol. 100, p. 022 004, 2019. DOI: [10.1103/PhysRevD.100.022004](https://doi.org/10.1103/PhysRevD.100.022004).
- [32] J. Hisano, S. Matsumot, M. Nagai, O. Saito, and M. Senami, “Non-perturbative effect on thermal relic abundance of dark matter,” *Physics Letters B*, vol. 646, no. 1, pp. 34–38, 2007.
- [33] P. A. M. Dirac, “The quantum theory of electron. 2,” *Proc. R. Soc. Lond. A*, vol. 118, p. 351, 1928. DOI: [10.1098/rspa.1928.0056](https://doi.org/10.1098/rspa.1928.0056).

- [34] J. S. Schwinger, “On quantum electrodynamics and the magnetic moment of the electron,” *Phys. Rev.*, vol. 73, p. 416, 1948. DOI: [10.1103/PhysRev.73.416](https://doi.org/10.1103/PhysRev.73.416).
- [35] E989 Collaboration, “Muon ($g-2$) Technical Design Report,” arXiv: [1501.06858 \[hep-ex\]](https://arxiv.org/abs/1501.06858).
- [36] Muon $g-2$ Collaboration, “Measurement of the Positive Muon Anomalous Magnetic Moment to 0.20 ppm,” *Phys. Rev. Lett.*, vol. 131, p. 161802, 2023. DOI: [10.1103/PhysRevLett.131.161802](https://doi.org/10.1103/PhysRevLett.131.161802).
- [37] Muon $g-2$ Collaboration, “Measurement of the Positive Muon Anomalous Magnetic Moment to 0.46 ppm,” *Phys. Rev. Lett.*, vol. 126, p. 141801, 2021. DOI: [10.1103/PhysRevLett.126.141801](https://doi.org/10.1103/PhysRevLett.126.141801).
- [38] Muon $g-2$ Collaboration, “Final report of the E821 muon anomalous magnetic moment measurement at BNL,” *Phys. Rev. D*, vol. 73, p. 072003, 2016. DOI: [10.1103/PhysRevD.73.072003](https://doi.org/10.1103/PhysRevD.73.072003).
- [39] S. Laporta, “High-precision calculation of the 4-loop contribution to the electron $g-2$ in QED,” *Phys. Lett. B*, vol. 772, p. 232, 2017. DOI: [10.1016/j.physletb.2017.06.056](https://doi.org/10.1016/j.physletb.2017.06.056).
- [40] T. Aoyama, M. Hayakawa, T. Kinoshita, M. Nio, “Tenth-order electron anomalous magnetic moment — contribution of diagrams without closed lepton loops,” *Phys. Rev. D*, vol. 91, p. 033006, 2015. DOI: [10.1103/PhysRevD.91.033006](https://doi.org/10.1103/PhysRevD.91.033006).
- [41] T. Aoyama, M. Hayakawa, T. Kinoshita, M. Nio, “Complete tenth-order QED contribution to the muon $g-2$,” *Phys. Rev. Lett.*, vol. 109, p. 111808, 2012. DOI: [10.1103/PhysRevLett.109.111808](https://doi.org/10.1103/PhysRevLett.109.111808).
- [42] T. Aoyama, T. Kinoshita and M. Nio, “Theory of the Anomalous Magnetic Moment of the Electron,” *Atoms*, vol. 7, p. 28, 2019. DOI: [10.3390/atoms7010028](https://doi.org/10.3390/atoms7010028).
- [43] S. Volkov, “Calculating the five-loop QED contribution to the electron anomalous magnetic moment: graphs without lepton loops,” *Phys. Rev. D*, vol. 100, p. 096004, 2019. DOI: [10.1103/PhysRevD.100.096004](https://doi.org/10.1103/PhysRevD.100.096004).
- [44] A.L. Kataev, “Renormalization group and the five loop QED asymptotic contributions to the muon anomaly,” *Phys. Lett. B*, vol. 284, p. 401, 1992. DOI: [10.1016/0370-2693\(92\)90452-A](https://doi.org/10.1016/0370-2693(92)90452-A).
- [45] S. Laporta, “Analytical and numerical contributions of some tenth order graphs containing vacuum polarization insertions to the muon ($g-2$) in QED,” *Phys. Lett. B*, vol. 328, p. 522, 1994. DOI: [10.1016/0370-2693\(94\)91513-X](https://doi.org/10.1016/0370-2693(94)91513-X).
- [46] P. A. Baikov, A. Maier, P. Marquard, “The QED vacuum polarization function at four loops and the anomalous magnetic moment at five loops,” *Nucl. Phys. B*, vol. 877, p. 647, 2013. DOI: [10.1016/j.nuclphysb.2013.10.020](https://doi.org/10.1016/j.nuclphysb.2013.10.020).
- [47] A. Czarnecki, W. J. Marciano and A. Vainshtein, “Refinements in electroweak contributions to the muon anomalous magnetic moment,” *Phys. Rev. D*, vol. 67, p. 073006, 2003. DOI: [10.1103/PhysRevD.67.073006](https://doi.org/10.1103/PhysRevD.67.073006).
- [48] C. Gnendiger, D. Stöckinger and H. Stöckinger-Kim, “The electroweak contributions to $(g-2)_\mu$ after the Higgs-boson mass measurement,” *Phys. Rev. D*, vol. 88, p. 053005, 2013. DOI: [10.1103/PhysRevD.88.053005](https://doi.org/10.1103/PhysRevD.88.053005).
- [49] T. Aoyama et al., “The anomalous magnetic moment of the muon in the Standard Model,” *Phys. Rep.*, vol. 887, p. 1, 2020. DOI: [10.1016/j.physrep.2020.07.006](https://doi.org/10.1016/j.physrep.2020.07.006).
- [50] S. J. Brodsky, E. De Rafael, “Suggested boson - lepton pair couplings and the anomalous magnetic moment of the muon,” *Phys. Rev.*, vol. 168, p. 1620, 1968. DOI: [10.1103/PhysRev.168.1620](https://doi.org/10.1103/PhysRev.168.1620).

- [51] B. E. Lautrup, E. De Rafael, “Calculation of the sixth-order contribution from the fourth-order vacuum polarization to the difference of the anomalous magnetic moments of muon and electron,” *Phys. Rev.*, vol. 174, p. 1835, 1968. DOI: [10.1103/PhysRev.174.1835](https://doi.org/10.1103/PhysRev.174.1835).
- [52] P. Masjuan and P. Sanchez-Puertas, “Pseudoscalar-pole contribution to the $(g_\mu - 2)$: A rational approach,” *Phys. Rev. D*, vol. 95, p. 054026, 2017. DOI: [10.1103/PhysRevD.95.054026](https://doi.org/10.1103/PhysRevD.95.054026).
- [53] G. Colangelo, M. Hoferichter, M. Procura and P. Stoffer, “Dispersion relation for hadronic light-by-light scattering: two-pion contributions,” *JHEP*, vol. 04, p. 161, 2017. DOI: [10.1007/JHEP04\(2017\)161](https://doi.org/10.1007/JHEP04(2017)161).
- [54] M. Hoferichter, B. L. Hoid, B. Kubis, S. Leupold and S. P. Schneider, “Dispersion relation for hadronic light-by-light scattering: pion pole,” *JHEP*, vol. 10, p. 141, 2018. DOI: [10.1007/JHEP10\(2018\)141](https://doi.org/10.1007/JHEP10(2018)141).
- [55] A. Gérardin, H. B. Meyer and A. Nyffeler, “Lattice calculation of the pion transition form factor with $N_f = 2 + 1$ Wilson quarks,” *JHEP*, vol. 100, p. 034520, 2019. DOI: [10.1103/PhysRevD.100.034520](https://doi.org/10.1103/PhysRevD.100.034520).
- [56] J. Bijnens, N. Hermansson-Truedsson and A. Rodríguez-Sánchez, “Short-distance constraints for the HLbL contribution to the muon anomalous magnetic moment,” *Phys. Lett. B*, vol. 798, p. 134994, 2019. DOI: [10.1016/j.physletb.2019.134994](https://doi.org/10.1016/j.physletb.2019.134994).
- [57] G. Colangelo, F. Hagelstein, M. Hoferichter, L. Laub and P. Stoffer, “Longitudinal short-distance constraints for the hadronic light-by-light contribution to $(g - 2)_\mu$ with large- N_c Regge models,” *JHEP*, vol. 03, p. 101, 2020. DOI: [10.1007/JHEP03\(2020\)101](https://doi.org/10.1007/JHEP03(2020)101).
- [58] V. Pauk, M. Vanderhaeghen, “Single meson contributions to the muon’s anomalous magnetic moment,” *Eur. Phys. J. C*, vol. 74, p. 3008, 2014. DOI: [10.1140/epjc/s10052-014-3008-y](https://doi.org/10.1140/epjc/s10052-014-3008-y).
- [59] I. Danilkin, M. Vanderhaeghen, “Light-by-light scattering sum rules in light of new data,” *Phys. Rev. D*, vol. 95, p. 014019, 2017. DOI: [10.1103/PhysRevD.95.014019](https://doi.org/10.1103/PhysRevD.95.014019).
- [60] M. Knecht, S. Narison, A. Rabemananjara, D. Rabetiarivony, “Scalar meson contributions to a_μ from hadronic light-by-light scattering,” *Phys. Lett. B*, vol. 787, p. 111, 2018. DOI: [10.1016/j.physletb.2018.10.048](https://doi.org/10.1016/j.physletb.2018.10.048).
- [61] G. Eichmann, C.S. Fischer, R. Williams, “Kaon-box contribution to the anomalous magnetic moment of the muon,” *Phys. Rev. D*, vol. 101, p. 054015, 2020. DOI: [10.1103/PhysRevD.101.054015](https://doi.org/10.1103/PhysRevD.101.054015).
- [62] P. Roig, P. Sánchez-Puertas, “Axial-vector exchange contribution to the hadronic light-by-light piece of the muon anomalous magnetic moment,” *Phys. Rev. D*, vol. 101, p. 074019, 2020. DOI: [10.1103/PhysRevD.101.074019](https://doi.org/10.1103/PhysRevD.101.074019).
- [63] T. Blum, N. Christ, M. Hayakawa, T. Izubuchi, L. Jin, C. Jung, C. Lehner, “The hadronic light-by-light scattering contribution to the muon anomalous magnetic moment from lattice QCD,” *Phys. Rev. Lett.*, vol. 124, p. 132002, 2020. DOI: [10.1103/PhysRevLett.124.132002](https://doi.org/10.1103/PhysRevLett.124.132002).
- [64] E. H. Chao, R.J. Hudspith, A. Gérardin, J.R. Green, H.B. Meyer, K. Ottnad, “Hadronic light-by-light contribution to $(g - 2)_\mu$ from lattice QCD: a complete calculation,” *Eur. Phys. J. C*, vol. 81, p. 651, 2021. DOI: [10.1140/epjc/s10052-021-09455-4](https://doi.org/10.1140/epjc/s10052-021-09455-4).
- [65] D. Giusti, F. Sanfilippo, S. Simula, “Light-quark contribution to the leading hadronic vacuum polarization term of the muon $g - 2$ from twisted-mass fermions,” *Phys. Rev. D*, vol. 98, p. 114504, 2018. DOI: [10.1103/PhysRevD.98.114504](https://doi.org/10.1103/PhysRevD.98.114504).

- [66] D. Giusti, V. Lubicz, G. Martinelli, F. Sanfilippo, S. Simula, “Electromagnetic and strong isospin-breaking corrections to the muon $g - 2$ from lattice QCD+QED,” *Phys. Rev. D*, vol. 99, p. 114502, 2019. DOI: [10.1103/PhysRevD.99.114502](https://doi.org/10.1103/PhysRevD.99.114502).
- [67] A. Gérardin, M. Cè, G. von Hippel, B. Hörz, H.B. Meyer, D. Mohler, K. Ottnad, J. Wilhelm, H. Wittig, “The leading hadronic contribution to $(g - 2)_\mu$ from lattice QCD with $N_f = 2 + 1$ flavours of $O(a)$ improved Wilson quarks,” *Phys. Rev. D*, vol. 100, p. 014510, 2019. DOI: [10.1103/PhysRevD.100.014510](https://doi.org/10.1103/PhysRevD.100.014510).
- [68] C. T. H. Davies, et al., “Hadronic-vacuum-polarization contribution to the muon’s anomalous magnetic moment from four-flavor lattice QCD,” *Phys. Rev. D*, vol. 101, p. 034512, 2020. DOI: [10.1103/PhysRevD.101.034512](https://doi.org/10.1103/PhysRevD.101.034512).
- [69] B. Chakraborty, et al., “Strong-isospin-breaking correction to the muon anomalous magnetic moment from lattice QCD at the physical point,” *Phys. Rev. Lett.*, vol. 120, p. 152001, 2018. DOI: [10.1103/PhysRevLett.120.152001](https://doi.org/10.1103/PhysRevLett.120.152001).
- [70] E. Shintani, Y. Kuramashi, “Study of systematic uncertainties in hadronic vacuum polarization contribution to muon $g - 2$ with $2 + 1$ flavor lattice QCD,” *Phys. Rev. D*, vol. 100, p. 034517, 2019. DOI: [10.1103/PhysRevD.100.034517](https://doi.org/10.1103/PhysRevD.100.034517).
- [71] T. Blum, P. A. Boyle, V. Gülpers, T. Izubuchi, L. Jin, C. Jung, A. Jüttner, C. Lehner, A. Portelli, J. T. Tsang, “Calculation of the hadronic vacuum polarization contribution to the muon anomalous magnetic moment,” *Phys. Rev. Lett.*, vol. 121, p. 022003, 2018. DOI: [10.1103/PhysRevLett.121.022003](https://doi.org/10.1103/PhysRevLett.121.022003).
- [72] S. Borsanyi, et al., “Hadronic vacuum polarization contribution to the anomalous magnetic moments of leptons from first principles,” *Phys. Rev. Lett.*, vol. 121, p. 022002, 2018. DOI: [10.1103/PhysRevLett.121.022002](https://doi.org/10.1103/PhysRevLett.121.022002).
- [73] C. Lehner, A. S. Meyer, “Consistency of hadronic vacuum polarization between lattice QCD and the R-ratio,” *Phys. Rev. D*, vol. 101, p. 074515, 2020. DOI: [10.1103/PhysRevD.101.074515](https://doi.org/10.1103/PhysRevD.101.074515).
- [74] S. Borsanyi, et al., “Leading hadronic contribution to the muon magnetic moment from lattice QCD,” *Nature*, vol. 593, p. 51, 2021. DOI: [10.1038/s41586-021-03418-1](https://doi.org/10.1038/s41586-021-03418-1).
- [75] M. Della Morte, A. Francis, V. Gülpers, G. Herdoíza, G. von Hippel, H. Horch, B. Jäger, H.B. Meyer, A. Nyffeler, H. Wittig, “The hadronic vacuum polarization contribution to the muon $g - 2$ from lattice QCD,” *J. High Energy Phys.*, vol. 10, p. 020, 2017. DOI: [10.1007/JHEP10\(2017\)020](https://doi.org/10.1007/JHEP10(2017)020).
- [76] B. Chakraborty, C.T.H. Davies, P.G. de Oliveira, J. Koponen, G.P. Lepage, R.S. Van de Water, “The hadronic vacuum polarization contribution to a_μ from full lattice QCD,” *Phys. Rev. D*, vol. 96, p. 034516, 2017. DOI: [10.1103/PhysRevD.96.034516](https://doi.org/10.1103/PhysRevD.96.034516).
- [77] C. Aubin, T. Blum, C. Tu, M. Golterman, C. Jung, S. Peris, “Light quark vacuum polarization at the physical point and contribution to the muon $g - 2$,” *Phys. Rev. D*, vol. 101, p. 014503, 2020. DOI: [10.1103/PhysRevD.101.014503](https://doi.org/10.1103/PhysRevD.101.014503).
- [78] A. Keshavarzi, D. Nomura and T. Teubner, “ $g - 2$ Of charged leptons, $\alpha(M_Z^2)$, and the hyperfine splitting of muonium,” *Phys. Rev. D*, vol. 101, p. 014029, 2020. DOI: [10.1103/PhysRevD.101.014029](https://doi.org/10.1103/PhysRevD.101.014029).
- [79] M. Davier, A. Hoecker, B. Malaescu and Z. Zhang, “A new evaluation of the hadronic vacuum polarisation contributions to the muon anomalous magnetic moment and to $\alpha(m_Z^2)$,” *Eur. Phys. J. C*, vol. 80, p. 241, 2020. DOI: [10.1140/epjc/s10052-020-7792-2](https://doi.org/10.1140/epjc/s10052-020-7792-2).

- [80] F. Jegerlehner, *The Anomalous Magnetic Moment of the Muon*. Springer, 2017, <https://link.springer.com/book/10.1007/978-3-319-63577-4>.
- [81] M. Benayoun, L. Delbuono, F. Jegerlehner, “BHLS₂, a new breaking of the hls model and its phenomenology,” *Eur. Phys. J. C*, vol. 80, p. 81, 2020. DOI: [10.1140/epjc/s10052-020-7611-9](https://doi.org/10.1140/epjc/s10052-020-7611-9).
- [82] F. Burger, X. Feng, G. Hotzel, K. Jansen, M. Petschlies, D.B. Renner, “Four-flavour leading-order hadronic contribution to the muon anomalous magnetic moment,” *J. High Energy Phys.*, vol. 02, p. 099, 2014. DOI: [10.1007/JHEP02\(2014\)099](https://doi.org/10.1007/JHEP02(2014)099).
- [83] A. El-Khadra, *Theory Overview: First Results from the Muon g-2 Experiment at Fermilab*. 2021.
- [84] A. Boccaletti *et al.*, *High precision calculation of the hadronic vacuum polarisation contribution to the muon anomaly*, 2024. arXiv: [2407.10913 \[hep-lat\]](https://arxiv.org/abs/2407.10913). [Online]. Available: <https://arxiv.org/abs/2407.10913>.
- [85] G. F. Giudice and R. Rattazzi, “Theories with gauge-mediated supersymmetry breaking,” *Phys. Reports*, vol. 322, p. 419, 1999. DOI: [10.1016/S0370-1573\(99\)00042-3](https://doi.org/10.1016/S0370-1573(99)00042-3).
- [86] G. F. Giudice *et al.*, “Gaugino mass without singlets,” *JHEP*, vol. 12, p. 027, 1998. DOI: [10.1088/1126-6708/1998/12/027](https://doi.org/10.1088/1126-6708/1998/12/027).
- [87] L. Randall and R. Sundrum, “Out of this world supersymmetry breaking,” *Nucl. Phys. B*, vol. 557, p. 79, 1999. DOI: [10.1016/S0550-3213\(99\)00359-4](https://doi.org/10.1016/S0550-3213(99)00359-4).
- [88] J. Wess and J. Bagger, *Supersymmetry and supergravity*. Princeton university press, 1992.
- [89] Super-Kamiokande Collaboration, “Search for proton decay via $p \rightarrow e^+ \pi^0$ and $p \rightarrow \mu^+ \pi^0$ with an enlarged fiducial volume in Super-Kamiokande I-IV,” *Phys. Rev. D*, vol. 102, p. 112 011, 2020. DOI: [10.1016/S0550-3213\(99\)00359-4](https://doi.org/10.1016/S0550-3213(99)00359-4).
- [90] N. Nagata and S. Shirai, “Higgsino dark matter in high-scale supersymmetry,” *JHEP*, vol. 2015, p. 29, 2015. DOI: [10.1007/JHEP01\(2015\)029](https://doi.org/10.1007/JHEP01(2015)029).
- [91] J. Hisano, S. Matsumoto, M. M. Nojiri, O. Saito, “Direct detection of the Wino and Higgsino-like neutralino dark matter at one-loop level,” *Phys. Rev. D*, vol. 71, p. 015 007, 2005. DOI: [10.1103/PhysRevD.71.015007](https://doi.org/10.1103/PhysRevD.71.015007).
- [92] N. Nagata and S. Shirai, “Higgsino dark matter in high-scale supersymmetry,” *Journal of High Energy Physics*, vol. 2015, no. 1, p. 29, 2015.
- [93] N. Nagata and S. Shirai, “Electroweakly interacting dirac dark matter,” *Phys. Rev. D*, vol. 91, p. 055 035, 5 2015. DOI: [10.1103/PhysRevD.91.055035](https://doi.org/10.1103/PhysRevD.91.055035). [Online]. Available: <https://link.aps.org/doi/10.1103/PhysRevD.91.055035>.
- [94] T. Moroi, “Muon anomalous magnetic dipole moment in the minimal supersymmetric standard model,” *Phys. Rev. D*, vol. 53, p. 6565, 1996. DOI: [10.1103/PhysRevD.53.6565](https://doi.org/10.1103/PhysRevD.53.6565).
- [95] T. Falk, K. A. Olive, and M. Srednicki, “Heavy sneutrinos as dark matter,” *Phys. Lett. B*, vol. 339, p. 248, 1994. DOI: [10.1016/0370-2693\(94\)90639-4](https://doi.org/10.1016/0370-2693(94)90639-4).
- [96] K. Griest and D. Seckel, “Three exceptions in the calculation of relic abundances,” *Phys. Rev. D*, vol. 43, p. 3191, 1991. DOI: [10.1103/PhysRevD.43.3191](https://doi.org/10.1103/PhysRevD.43.3191).
- [97] C. Cheung, L. J. Hall, D. Pinner, and J. T. Ruderman, “Prospects and blind spots for neutralino dark matter,” *JHEP*, vol. 05, p. 100, 2013. DOI: [10.1007/JHEP05\(2013\)100](https://doi.org/10.1007/JHEP05(2013)100).
- [98] M. Farina, M. Kadastik, D. Pappadopulo, J. Pata, M. Raidal, and A. Strumia, “Implications of XENON100 and LHC results for Dark Matter models,” *Nucl. Phys.*, vol. 853, p. 607, 2011. DOI: [10.1016/j.nuclphysb.2011.08.003](https://doi.org/10.1016/j.nuclphysb.2011.08.003).

- [99] M. Ibe, S. Matsumoto and R. Saito, “Mass splitting between charged and neutral winos at two-loop level,” *Phys. Lett. B*, vol. 721, p. 252, 2013. DOI: [10.1016/j.physletb.2013.03.015](#).
- [100] G. F. Giudice, T. Han, K. Wang, and L. Wang, “Nearly degenerate gauginos and dark matter at the LHC,” *Phys. Rev. D*, vol. 81, p. 115011, 2010. DOI: [10.1103/PhysRevD.81.115011](#).
- [101] ATLAS Collaboration, “Search for Nearly Mass-Degenerate Higgsinos Using Low-Momentum Mildly Displaced Tracks in pp Collisions at $\sqrt{s} = 13$ TeV with the ATLAS Detector,” *Phys. Rev. Lett.*, vol. 132, p. 221801, 2024. DOI: [10.1103/PhysRevLett.132.221801](#). arXiv: [2401.14046 \[hep-ex\]](#).
- [102] ATLAS Collaboration, “Search for long-lived charginos based on a disappearing-track signature using 136 fb^{-1} of pp collisions at $\sqrt{s} = 13$ TeV with the ATLAS detector,” *Eur. Phys. J. C*, vol. 82, p. 606, 2022. DOI: [10.1140/epjc/s10052-022-10489-5](#). arXiv: [2201.02472 \[hep-ex\]](#).
- [103] ATLAS Collaboration, “Search for long-lived charginos based on a disappearing-track signature in pp collisions at $\sqrt{s} = 13$ TeV with the ATLAS detector,” *JHEP*, vol. 06, p. 022, 2018. DOI: [10.1007/JHEP06\(2018\)022](#). arXiv: [1712.02118 \[hep-ex\]](#).
- [104] ATLAS Collaboration, “Searches for electroweak production of supersymmetric particles with compressed mass spectra in $\sqrt{s} = 13$ TeV pp collisions with the ATLAS detector,” *Phys. Rev. D*, vol. 101, p. 052005, 2020. DOI: [10.1103/PhysRevD.101.052005](#). arXiv: [1911.12606 \[hep-ex\]](#).
- [105] ATLAS Collaboration, “Search for chargino–neutralino pair production in final states with three leptons and missing transverse momentum in $\sqrt{s} = 13$ TeV pp collisions with the ATLAS detector,” *Eur. Phys. J. C*, vol. 81, p. 1118, 2021. DOI: [10.1140/epjc/s10052-021-09749-7](#). arXiv: [2106.01676 \[hep-ex\]](#).
- [106] ATLAS Collaboration, “Search for electroweak production of supersymmetric states in scenarios with compressed mass spectra at $\sqrt{s} = 13$ TeV with the ATLAS detector,” *Phys. Rev. D*, vol. 97, p. 052010, 2018. DOI: [10.1103/PhysRevD.97.052010](#). arXiv: [1712.08119 \[hep-ex\]](#).
- [107] CMS Collaboration, “Search for disappearing tracks in proton–proton collisions at $\sqrt{s} = 13$ TeV,” *Phys. Lett. B*, vol. 806, p. 135502, 2020. DOI: [10.1016/j.physletb.2020.135502](#). arXiv: [2004.05153 \[hep-ex\]](#).
- [108] CMS Collaboration, “Search for disappearing tracks as a signature of new long-lived particles in proton–proton collisions at $\sqrt{s} = 13$ TeV,” *JHEP*, vol. 08, p. 016, 2018. DOI: [10.1007/JHEP08\(2018\)016](#). arXiv: [1804.07321 \[hep-ex\]](#).
- [109] CMS Collaboration, “Search for supersymmetry in final states with two or three soft leptons and missing transverse momentum in proton–proton collisions at $\sqrt{s} = 13$ TeV,” *JHEP*, vol. 04, p. 091, 2021. DOI: [10.1007/JHEP04\(2022\)091](#). arXiv: [2111.06296 \[hep-ex\]](#).
- [110] CMS Collaboration, “Search for new physics in events with two soft oppositely charged leptons and missing transverse momentum in proton–proton collisions at $\sqrt{s} = 13$ TeV,” *Phys. Lett. B*, vol. 782, p. 440, 2018. DOI: [10.1016/j.physletb.2018.05.062](#). arXiv: [1801.01846 \[hep-ex\]](#).

- [111] ATLAS Collaboration, “Search for electroweak production of charginos and sleptons decaying into final states with two leptons and missing transverse momentum in $\sqrt{s} = 13$ TeV pp collisions using the ATLAS detector,” *Eur. Phys. J. C*, vol. 80, p. 123, 2020. DOI: [10.1140/epjc/s10052-019-7594-6](https://doi.org/10.1140/epjc/s10052-019-7594-6). arXiv: [1908.08215](https://arxiv.org/abs/1908.08215) [hep-ex].
- [112] ATLAS Collaboration, “Search for direct pair production of sleptons and charginos decaying to two leptons and neutralinos with mass splittings near the W -boson mass in $\sqrt{s} = 13$ TeV pp collisions with the ATLAS detector,” 2022. arXiv: [2209.13935](https://arxiv.org/abs/2209.13935) [hep-ex].
- [113] ATLAS Collaboration, “Search for charginos and neutralinos in final states with two boosted hadronically decaying bosons and missing transverse momentum in pp collisions at $\sqrt{s} = 13$ TeV with the ATLAS detector,” *Phys. Rev. D*, vol. 104, p. 112 010, 2021. DOI: [10.1103/PhysRevD.104.112010](https://doi.org/10.1103/PhysRevD.104.112010). arXiv: [2108.07586](https://arxiv.org/abs/2108.07586) [hep-ex].
- [114] ATLAS Collaboration, “Search for direct production of electroweakinos in final states with missing transverse momentum and a Higgs boson decaying into photons in pp collisions at $\sqrt{s} = 13$ TeV with the ATLAS detector,” *JHEP*, vol. 10, p. 005, 2020. DOI: [10.1007/JHEP10\(2020\)005](https://doi.org/10.1007/JHEP10(2020)005). arXiv: [2004.10894](https://arxiv.org/abs/2004.10894) [hep-ex].
- [115] ATLAS Collaboration, “Search for chargino–neutralino production with mass splittings near the electroweak scale in three-lepton final states in $\sqrt{s} = 13$ TeV pp collisions with the ATLAS detector,” *Phys. Rev. D*, vol. 101, p. 072 001, 2020. DOI: [10.1103/PhysRevD.101.072001](https://doi.org/10.1103/PhysRevD.101.072001). arXiv: [1912.08479](https://arxiv.org/abs/1912.08479) [hep-ex].
- [116] ATLAS Collaboration, “Search for direct production of electroweakinos in final states with one lepton, missing transverse momentum and a Higgs boson decaying into two b -jets in pp collisions at $\sqrt{s} = 13$ TeV with the ATLAS detector,” *Eur. Phys. J. C*, vol. 80, p. 691, 2020. DOI: [10.1140/epjc/s10052-020-8050-3](https://doi.org/10.1140/epjc/s10052-020-8050-3). arXiv: [1909.09226](https://arxiv.org/abs/1909.09226) [hep-ex].
- [117] CMS Collaboration, “Search for higgsinos decaying to two Higgs bosons and missing transverse momentum in proton–proton collisions at $\sqrt{s} = 13$ TeV,” *JHEP*, vol. 05, p. 014, 2022. DOI: [10.1007/JHEP05\(2022\)014](https://doi.org/10.1007/JHEP05(2022)014). arXiv: [2201.04206](https://arxiv.org/abs/2201.04206) [hep-ex].
- [118] CMS Collaboration, “Search for electroweak production of charginos and neutralinos at $\sqrt{s} = 13$ TeV in final states containing hadronic decays of WW , WZ , or WH and missing transverse momentum,” 2022. arXiv: [2205.09597](https://arxiv.org/abs/2205.09597) [hep-ex].
- [119] CMS Collaboration, “Search for supersymmetry in final states with two oppositely charged same-flavor leptons and missing transverse momentum in proton–proton collisions at $\sqrt{s} = 13$ TeV,” *JHEP*, vol. 04, p. 123, 2020. DOI: [10.1007/JHEP04\(2021\)123](https://doi.org/10.1007/JHEP04(2021)123). arXiv: [2012.08600](https://arxiv.org/abs/2012.08600) [hep-ex].
- [120] CMS Collaboration, “Search for electroweak production of charginos and neutralinos in proton–proton collisions at $\sqrt{s} = 13$ TeV,” *JHEP*, vol. 04, p. 147, 2021. DOI: [10.1007/JHEP04\(2022\)147](https://doi.org/10.1007/JHEP04(2022)147). arXiv: [2106.14246](https://arxiv.org/abs/2106.14246) [hep-ex].
- [121] CMS Collaboration, “Search for chargino–neutralino production in events with Higgs and W bosons using 137 fb^{-1} of proton–proton collisions at $\sqrt{s} = 13$ TeV,” *JHEP*, vol. 10, p. 045, 2021. DOI: [10.1007/JHEP10\(2021\)045](https://doi.org/10.1007/JHEP10(2021)045). arXiv: [2107.12553](https://arxiv.org/abs/2107.12553) [hep-ex].
- [122] M. Endo, K. Hamaguchi, T. Kitahara, T. Yoshinaga, “Probing Bino contribution to muon $g - 2$,” *JHEP*, vol. 2013, p. 13, 2013. DOI: [10.1007/JHEP11\(2013\)013](https://doi.org/10.1007/JHEP11(2013)013).
- [123] P. Athron et al., “GM2Calc: precise MSSM prediction for $g - 2$ of the muon,” *Eur. Phys. J. C*, vol. 76, p. 62, 2016. DOI: [10.1140/epjc/s10052-015-3870-2](https://doi.org/10.1140/epjc/s10052-015-3870-2).
- [124] P. von Weitershausen, M. Schafer, H. Stockinger-Kim and D. Stockinger, “Photonic supersymmetric two-loop corrections to the muon magnetic moment,” *Phys. Rev. D*, vol. 81, p. 093 004, 2010. DOI: [10.1140/epjc/s10052-015-3870-2](https://doi.org/10.1140/epjc/s10052-015-3870-2).

- [125] H. Fargnoli, C. Gnendiger, S. Paßehr, D. Stöckinger and H. Stöckinger-Kim, “Two-loop corrections to the muon magnetic moment from fermion/sfermion loops in the MSSM: detailed results,” *JHEP*, vol. 2014, p. 70, 2014. DOI: [10.1007/JHEP02\(2014\)070](https://doi.org/10.1007/JHEP02(2014)070).
- [126] M. Bach, J. h. Park, D. Stöckinger and H. Stöckinger-Kim, “Large muon $g - 2$ with TeV-scale SUSY masses for $\tan \beta \rightarrow \text{inf}$,” *JHEP*, vol. 2015, p. 26, 2015. DOI: [10.1007/JHEP10\(2015\)026](https://doi.org/10.1007/JHEP10(2015)026).
- [127] S. Heinemeyer, W. Hollik, D. Stöckinger, A. M. Weber and G. Weiglein, “Precise prediction for M_W in the MSSM,” *JHEP*, vol. 08, p. 052, 2006. DOI: [10.1088/1126-6708/2006/08/052](https://doi.org/10.1088/1126-6708/2006/08/052).
- [128] S. Heinemeyer, W. Hollik, A. M. Weber and G. Weiglein, “Z Pole observables in the mssm,” *JHEP*, vol. 04, p. 039, 2008. DOI: [10.1088/1126-6708/2008/04/039](https://doi.org/10.1088/1126-6708/2008/04/039).
- [129] S. Heinemeyer, W. Hollik, G. Weiglein and L. Zeune, “Implications of LHC search results on the W boson mass prediction in the MSSM,” *JHEP*, vol. 2013, p. 084, 2013. DOI: [10.1088/1126-6708/2008/04/039](https://doi.org/10.1088/1126-6708/2008/04/039).
- [130] CDF Collaboration, “High-precision measurement of the W boson mass with the CDF II detector,” *Science*, vol. 376, p. 170, 2022. DOI: [10.1126/science.abk1781](https://doi.org/10.1126/science.abk1781).
- [131] G. Belanger, F. Boudjema, A. Pukhov and A. Semenov, “micrOMEGAs: A program for calculating the relic density in the MSSM,” *Comput. Phys. Commun.*, vol. 149, p. 103, 2002. DOI: [10.1016/S0010-4655\(02\)00596-9](https://doi.org/10.1016/S0010-4655(02)00596-9).
- [132] G. Belanger, F. Boudjema, A. Pukhov and A. Semenov, “micrOMEGAs 2.0: A program to calculate the relic density of dark matter in a generic model,” *Comput. Phys. Commun.*, vol. 176, p. 367, 2007. DOI: [10.1016/j.cpc.2006.11.008](https://doi.org/10.1016/j.cpc.2006.11.008).
- [133] G. Belanger, F. Boudjema, A. Pukhov and A. Semenov, “micrOMEGAs 2.0.7: a program to calculate the relic density of dark matter in a generic model,” *Comput. Phys. Commun.*, vol. 177, p. 894, 2007. DOI: [10.1016/j.cpc.2007.08.002](https://doi.org/10.1016/j.cpc.2007.08.002).
- [134] F. Feroz, M. P. Hobson, “Multimodal nested sampling: an efficient and robust alternative to Markov Chain Monte Carlo methods for astronomical data analyses,” *Mon. Not. Roy. Astron. Soc.*, vol. 384, p. 449, 2008. DOI: [10.1111/j.1365-2966.2007.12353.x](https://doi.org/10.1111/j.1365-2966.2007.12353.x).
- [135] F. Feroz, M. P. Hobson, M. Bridges, “MultiNest: an efficient and robust Bayesian inference tool for cosmology and particle physics,” *Mon. Not. Roy. Astron. Soc.*, vol. 398, p. 1601, 2009. DOI: [10.1111/j.1365-2966.2009.14548.x](https://doi.org/10.1111/j.1365-2966.2009.14548.x).
- [136] F. Feroz, M. P. Hobson, E. Cameron, A. N. Pettitt, “Importance Nested Sampling and the MultiNest Algorithm,” *The Open Journal of Astrophys.*, vol. 2, 2019. DOI: [10.21105/astro.1306.2144](https://doi.org/10.21105/astro.1306.2144).
- [137] W. Porod, “SPHeno, a program for calculating supersymmetric spectra, SUSY particle decays and SUSY particle production at e^+e^- colliders,” *Comput. Phys. Commun.*, vol. 153, p. 275, 2003. DOI: [10.1016/S0010-4655\(03\)00222-4](https://doi.org/10.1016/S0010-4655(03)00222-4).
- [138] W. Porod, “SPHeno 3.1: extensions including flavour, CP-phases and models beyond the MSSM,” *Comput. Phys. Commun.*, vol. 183, p. 2458, 2012. DOI: [10.1016/j.cpc.2012.05.021](https://doi.org/10.1016/j.cpc.2012.05.021).
- [139] ALEPH, DELPHI, L3, OPAL Experiments, LEPSUSYWG/02-04.1, “Combined LEP Chargino Results, up to 208 GeV for low DM,” [Online]. Available: [7Bhttps://lepsusy.web.cern.ch/lepsusy/www/inoslowdmsummer02/charginolowdm_pub.html%7D](https://lepsusy.web.cern.ch/lepsusy/www/inoslowdmsummer02/charginolowdm_pub.html%7D).

- [140] S. Thomas, J. D. Wells, “Phenomenology of Massive Vectorlike Doublet Leptons,” *JHEP*, vol. 81, p. 34, 1998. DOI: [10.1103/PhysRevLett.81.34](https://doi.org/10.1103/PhysRevLett.81.34).
- [141] ATLAS Collaboration, “Search for supersymmetry in events with four or more charged leptons in 139 fb^{-1} of $\sqrt{s} = 13\text{ TeV}$ pp collisions with the ATLAS detector,” *JHEP*, vol. 07, p. 167, 2021. DOI: [10.1007/JHEP07\(2021\)167](https://doi.org/10.1007/JHEP07(2021)167). arXiv: [2103.11684](https://arxiv.org/abs/2103.11684) [hep-ex].
- [142] ATLAS Collaboration, *SimpleAnalysis: Truth-level Analysis Framework*, ATL-PHYS-PUB-2022-017, 2022. [Online]. Available: <https://cds.cern.ch/record/2805991>.
- [143] ATLAS Collaboration, “Search for trilepton resonances from chargino and neutralino pair production in $\sqrt{s} = 13\text{ TeV}$ pp collisions with the ATLAS detector,” *Phys. Rev. D*, vol. 103, p. 112 003, 2020. DOI: [10.1103/PhysRevD.103.112003](https://doi.org/10.1103/PhysRevD.103.112003). arXiv: [2011.10543](https://arxiv.org/abs/2011.10543) [hep-ex].
- [144] Particle Data Group, P. Zyla, *et al.*, “Review of Particle Physics,” *PTEP*, vol. 2020, no. 8, p. 083C01, 2020. DOI: [10.1093/ptep/ptaa104](https://doi.org/10.1093/ptep/ptaa104).
- [145] T. Aoyama, T. Kinoshita, and M. Nio, “Theory of the anomalous magnetic moment of the electron,” *Atoms*, vol. 7, no. 1, 2019, ISSN: 2218-2004. DOI: [10.3390/atoms7010028](https://doi.org/10.3390/atoms7010028). [Online]. Available: <https://www.mdpi.com/2218-2004/7/1/28>.
- [146] T. Aoyama, T. Kinoshita, and M. Nio, “Revised and improved value of the qed tenth-order electron anomalous magnetic moment,” *Phys. Rev. D*, vol. 97, p. 036 001, 3 2018. DOI: [10.1103/PhysRevD.97.036001](https://doi.org/10.1103/PhysRevD.97.036001). [Online]. Available: <https://link.aps.org/doi/10.1103/PhysRevD.97.036001>.
- [147] L. Morel, Z. Yao, P. Cladé, and S. Guellati-Khélifa, “Determination of the fine-structure constant with an accuracy of 81 parts per trillion,” *Nature*, vol. 588, no. 7836, pp. 61–65, 2020. DOI: [10.1038/s41586-020-2964-7](https://doi.org/10.1038/s41586-020-2964-7). [Online]. Available: <https://doi.org/10.1038/s41586-020-2964-7>.
- [148] R. H. Parker, C. Yu, W. Zhong, B. Estey, and H. Müller, “Measurement of the fine-structure constant as a test of the standard model,” *Science*, vol. 360, no. 6385, pp. 191–195, Apr. 2018, ISSN: 1095-9203. DOI: [10.1126/science.aap7706](https://doi.org/10.1126/science.aap7706). [Online]. Available: <http://dx.doi.org/10.1126/science.aap7706>.
- [149] X. Fan, T. G. Myers, B. A. D. Sukra, and G. Gabrielse, “Measurement of the electron magnetic moment,” *Phys. Rev. Lett.*, vol. 130, p. 071 801, 7 2023. DOI: [10.1103/PhysRevLett.130.071801](https://doi.org/10.1103/PhysRevLett.130.071801). [Online]. Available: <https://link.aps.org/doi/10.1103/PhysRevLett.130.071801>.
- [150] D. Hanneke, S. Fogwell, and G. Gabrielse, “New measurement of the electron magnetic moment and the fine structure constant,” *Phys. Rev. Lett.*, vol. 100, p. 120 801, 12 2008. DOI: [10.1103/PhysRevLett.100.120801](https://doi.org/10.1103/PhysRevLett.100.120801). [Online]. Available: <https://link.aps.org/doi/10.1103/PhysRevLett.100.120801>.
- [151] J. Alwall, P. Schuster, and N. Toro, “Simplified models for a first characterization of new physics at the LHC,” *Phys. Rev. D*, vol. 79, p. 075 020, 2009. DOI: [10.1103/PhysRevD.79.075020](https://doi.org/10.1103/PhysRevD.79.075020). arXiv: [0810.3921](https://arxiv.org/abs/0810.3921) [hep-ph].
- [152] H. Baer, V. Barger, X. Tata, and K. Zhang, “Winos from natural susy at the high luminosity lhc,” *Phys. Rev. D*, vol. 109, p. 015 027, 1 2024. DOI: [10.1103/PhysRevD.109.015027](https://doi.org/10.1103/PhysRevD.109.015027). [Online]. Available: <https://link.aps.org/doi/10.1103/PhysRevD.109.015027>.
- [153] L. Evans and P. Bryant, “LHC Machine,” *JINST*, vol. 3, S08001, 2008. DOI: [10.1088/1748-0221/3/08/S08001](https://doi.org/10.1088/1748-0221/3/08/S08001).

- [154] ATLAS Collaboration, “The ATLAS Experiment at the CERN Large Hadron Collider,” *JINST*, vol. 3, S08003, 2008. DOI: [10.1088/1748-0221/3/08/S08003](https://doi.org/10.1088/1748-0221/3/08/S08003).
- [155] CMS Collaboration, “The CMS Experiment at the CERN LHC,” *JINST*, vol. 3, S08004, 2008. DOI: [10.1088/1748-0221/3/08/S08004](https://doi.org/10.1088/1748-0221/3/08/S08004).
- [156] The ALICE Collaboration, “The ALICE experiment at the CERN LHC,” *JINST*, vol. 3, S080012, 2008. DOI: [10.1088/1748-0221/3/08/S08002](https://doi.org/10.1088/1748-0221/3/08/S08002).
- [157] The LHCb Collaboration, “The LHCb Detector at the LHC,” *JINST*, vol. 3, S08005, 2008. DOI: [10.1088/1748-0221/3/08/S08005](https://doi.org/10.1088/1748-0221/3/08/S08005).
- [158] E. Mobs, *The CERN accelerator complex - August 2018. Complexe des accélérateurs du CERN - Août 2018*, 2018. [Online]. Available: <https://cds.cern.ch/record/2636343>.
- [159] H. Wiedemann, *Particle Accelerator Physics I. Basic Principles and Linear Beam Dynamics*. Berlin, Germany: Springer, 1999. DOI: [10.1007/978-3-662-03827-7](https://doi.org/10.1007/978-3-662-03827-7).
- [160] G. Avoni et. al., “The new LUCID-2 detector for luminosity measurement and monitoring in ATLAS,” *JINST*, vol. 13, P07017, 2018. DOI: [10.1088/1748-0221/13/07/P07017](https://doi.org/10.1088/1748-0221/13/07/P07017).
- [161] ATLAS Collaboration, “ATLAS Detector and Physics Performance: Technical Design Report, Volume 1,” ATLAS-TDR-14; CERN-LHCC-99-014, 1999. [Online]. Available: <https://cds.cern.ch/record/391176>.
- [162] ATLAS Collaboration, “Alignment of the ATLAS Inner Detector in Run-2,” *Eur. Phys. J. C*, vol. 80, p. 1194, 2020. DOI: [10.1140/epjc/s10052-020-08700-6](https://doi.org/10.1140/epjc/s10052-020-08700-6). arXiv: [2007.07624](https://arxiv.org/abs/2007.07624) [hep-ex].
- [163] ATLAS Collaboration, “Operation of the ATLAS trigger system in Run 2,” *JINST*, vol. 15, P10004, 2020. DOI: [10.1088/1748-0221/15/10/P10004](https://doi.org/10.1088/1748-0221/15/10/P10004). arXiv: [2007.12539](https://arxiv.org/abs/2007.12539) [hep-ex].
- [164] ATLAS Collaboration, “ATLAS data quality operations and performance for 2015–2018 data-taking,” *JINST*, vol. 15, P04003, 2020. DOI: [10.1088/1748-0221/15/04/P04003](https://doi.org/10.1088/1748-0221/15/04/P04003). arXiv: [1911.04632](https://arxiv.org/abs/1911.04632) [physics.ins-det].
- [165] ATLAS Collaboration, “Luminosity determination in pp collisions at $\sqrt{s} = 13$ TeV using the ATLAS detector at the LHC,” 2022. arXiv: [2212.09379](https://arxiv.org/abs/2212.09379) [hep-ex].
- [166] P. Skands, “QCD for Collider Physics,” arXiv: [1104.2863](https://arxiv.org/abs/1104.2863) [hep-ph].
- [167] G. Altarelli and G. Parisi, “Asymptotic freedom in parton language,” *Nucl. Phys. B*, vol. 126, p. 298, 1977. DOI: [10.1016/0550-3213\(77\)90384-4](https://doi.org/10.1016/0550-3213(77)90384-4).
- [168] V. Gribov and L. Lipatov, “Deep inelastic electron scattering in perturbation theory,” *Phys. Lett. B*, vol. 37, p. 78, 1971. DOI: [10.1016/0550-3213\(77\)90384-4](https://doi.org/10.1016/0550-3213(77)90384-4).
- [169] Y. L. Dokshitzer, “Calculation of the Structure Functions for Deep Inelastic Scattering and e^+e^- Annihilation by Perturbation Theory in Quantum Chromodynamics,” *Sov. Phys. JETP*, vol. 46, p. 641, 1977.
- [170] B. Andersson, G. Gustafson, G. Ingelman, and T. Sjöstrand, “Parton fragmentation and string dynamics,” *Phys. Rept.*, vol. 97, pp. 31–145, 1983. DOI: [10.1016/0370-1573\(83\)90080-7](https://doi.org/10.1016/0370-1573(83)90080-7).
- [171] ATLAS Collaboration, *Summary of ATLAS Pythia 8 tunes*, ATL-PHYS-PUB-2012-003, 2012. [Online]. Available: <https://cds.cern.ch/record/1474107>.
- [172] A. D. Martin, W. J. Stirling, R. S. Thorne, and G. Watt, “Heavy-quark mass dependence in global PDF analyses and 3- and 4-flavour parton distributions,” *Eur. Phys. J. C*, vol. 70, p. 51, 2010. DOI: [10.1140/epjc/s10052-010-1462-8](https://doi.org/10.1140/epjc/s10052-010-1462-8). arXiv: [1007.2624](https://arxiv.org/abs/1007.2624) [hep-ph].

- [173] ATLAS Collaboration, “The ATLAS Simulation Infrastructure,” *Eur. Phys. J. C*, vol. 70, p. 823, 2010. DOI: [10.1140/epjc/s10052-010-1429-9](https://doi.org/10.1140/epjc/s10052-010-1429-9). arXiv: [1005.4568](https://arxiv.org/abs/1005.4568) [[physics.ins-det](#)].
- [174] GEANT4 Collaboration, S. Agostinelli, *et al.*, “GEANT4 – a simulation toolkit,” *Nucl. Instrum. Meth. A*, vol. 506, p. 250, 2003. DOI: [10.1016/S0168-9002\(03\)01368-8](https://doi.org/10.1016/S0168-9002(03)01368-8).
- [175] ATLAS Collaboration, “AtlFast3: The Next Generation Of Fast Simulation in ATLAS,” *Comput. Softw. Big Sci.*, vol. 6, p. 7, 2021. DOI: [10.1007/s41781-021-00079-7](https://doi.org/10.1007/s41781-021-00079-7). arXiv: [2109.02551](https://arxiv.org/abs/2109.02551) [[hep-ex](#)].
- [176] E. Bothmann *et al.*, “Event generation with Sherpa 2.2,” *SciPost Phys.*, vol. 7, no. 3, p. 034, 2019. DOI: [10.21468/SciPostPhys.7.3.034](https://doi.org/10.21468/SciPostPhys.7.3.034). arXiv: [1905.09127](https://arxiv.org/abs/1905.09127) [[hep-ph](#)].
- [177] R. D. Ball *et al.*, “Parton distributions for the LHC run II,” *JHEP*, vol. 04, p. 040, 2015. DOI: [10.1007/JHEP04\(2015\)040](https://doi.org/10.1007/JHEP04(2015)040). arXiv: [1410.8849](https://arxiv.org/abs/1410.8849) [[hep-ph](#)].
- [178] S. Schumann and F. Krauss, “A parton shower algorithm based on Catani–Seymour dipole factorisation,” *JHEP*, vol. 03, p. 038, 2008. DOI: [10.1088/1126-6708/2008/03/038](https://doi.org/10.1088/1126-6708/2008/03/038). arXiv: [0709.1027](https://arxiv.org/abs/0709.1027) [[hep-ph](#)].
- [179] ATLAS Collaboration, “Modelling and computational improvements to the simulation of single vector-boson plus jet processes for the ATLAS experiment,” *JHEP*, vol. 08, p. 089, 2021. DOI: [10.1007/JHEP08\(2022\)089](https://doi.org/10.1007/JHEP08(2022)089). arXiv: [2112.09588](https://arxiv.org/abs/2112.09588) [[hep-ex](#)].
- [180] F. Buccioni *et al.*, “OpenLoops 2,” *Eur. Phys. J. C*, vol. 79, no. 10, p. 866, 2019. DOI: [10.1140/epjc/s10052-019-7306-2](https://doi.org/10.1140/epjc/s10052-019-7306-2). arXiv: [1907.13071](https://arxiv.org/abs/1907.13071) [[hep-ph](#)].
- [181] F. Cascioli, P. Maierhöfer, and S. Pozzorini, “Scattering Amplitudes with Open Loops,” *Phys. Rev. Lett.*, vol. 108, p. 111601, 2012. DOI: [10.1103/PhysRevLett.108.111601](https://doi.org/10.1103/PhysRevLett.108.111601). arXiv: [1111.5206](https://arxiv.org/abs/1111.5206) [[hep-ph](#)].
- [182] F. Buccioni, S. Pozzorini, and M. Zoller, “On-the-fly reduction of open loops,” *Eur. Phys. J. C*, vol. 78, no. 1, p. 70, 2018. DOI: [10.1140/epjc/s10052-018-5562-1](https://doi.org/10.1140/epjc/s10052-018-5562-1). arXiv: [1710.11452](https://arxiv.org/abs/1710.11452) [[hep-ph](#)].
- [183] A. Denner, S. Dittmaier, and L. Hofer, “COLLIER: a fortran-based complex one-loop library in extended regularizations,” *Comput. Phys. Commun.*, vol. 212, pp. 220–238, 2017. DOI: [10.1016/j.cpc.2016.10.013](https://doi.org/10.1016/j.cpc.2016.10.013). arXiv: [1604.06792](https://arxiv.org/abs/1604.06792) [[hep-ph](#)].
- [184] S. Frixione, G. Ridolfi, and P. Nason, “A positive-weight next-to-leading-order Monte Carlo for heavy flavour hadroproduction,” *JHEP*, vol. 09, p. 126, 2007. DOI: [10.1088/1126-6708/2007/09/126](https://doi.org/10.1088/1126-6708/2007/09/126). arXiv: [0707.3088](https://arxiv.org/abs/0707.3088) [[hep-ph](#)].
- [185] P. Nason, “A new method for combining NLO QCD with shower Monte Carlo algorithms,” *JHEP*, vol. 11, p. 040, 2004. DOI: [10.1088/1126-6708/2004/11/040](https://doi.org/10.1088/1126-6708/2004/11/040). arXiv: [hep-ph/0409146](https://arxiv.org/abs/hep-ph/0409146).
- [186] S. Frixione, P. Nason, and C. Oleari, “Matching NLO QCD computations with parton shower simulations: the POWHEG method,” *JHEP*, vol. 11, p. 070, 2007. DOI: [10.1088/1126-6708/2007/11/070](https://doi.org/10.1088/1126-6708/2007/11/070). arXiv: [0709.2092](https://arxiv.org/abs/0709.2092) [[hep-ph](#)].
- [187] S. Alioli, P. Nason, C. Oleari, and E. Re, “A general framework for implementing NLO calculations in shower Monte Carlo programs: the POWHEG BOX,” *JHEP*, vol. 06, p. 043, 2010. DOI: [10.1007/JHEP06\(2010\)043](https://doi.org/10.1007/JHEP06(2010)043). arXiv: [1002.2581](https://arxiv.org/abs/1002.2581) [[hep-ph](#)].
- [188] T. Sjöstrand *et al.*, “An introduction to PYTHIA 8.2,” *Comput. Phys. Commun.*, vol. 191, p. 159, 2015. DOI: [10.1016/j.cpc.2015.01.024](https://doi.org/10.1016/j.cpc.2015.01.024). arXiv: [1410.3012](https://arxiv.org/abs/1410.3012) [[hep-ph](#)].
- [189] ATLAS Collaboration, *ATLAS Pythia 8 tunes to 7 TeV data*, ATL-PHYS-PUB-2014-021, 2014. [Online]. Available: <https://cds.cern.ch/record/1966419>.

- [190] D. J. Lange, “The EvtGen particle decay simulation package,” *Nucl. Instrum. Meth. A*, vol. 462, p. 152, 2001. DOI: [10.1016/S0168-9002\(01\)00089-4](https://doi.org/10.1016/S0168-9002(01)00089-4).
- [191] J. Alwall *et al.*, “The automated computation of tree-level and next-to-leading order differential cross sections, and their matching to parton shower simulations,” *JHEP*, vol. 07, p. 079, 2014. DOI: [10.1007/JHEP07\(2014\)079](https://doi.org/10.1007/JHEP07(2014)079). arXiv: [1405.0301](https://arxiv.org/abs/1405.0301) [[hep-ph](#)].
- [192] L. Lönnblad, “Correcting the Colour-Dipole Cascade Model with Fixed Order Matrix Elements,” *JHEP*, vol. 05, p. 046, 2002. DOI: [10.1088/1126-6708/2002/05/046](https://doi.org/10.1088/1126-6708/2002/05/046). arXiv: [hep-ph/0112284](https://arxiv.org/abs/hep-ph/0112284).
- [193] L. Lönnblad and S. Prestel, “Matching tree-level matrix elements with interleaved showers,” *JHEP*, vol. 03, p. 019, 2012. DOI: [10.1007/JHEP03\(2012\)019](https://doi.org/10.1007/JHEP03(2012)019). arXiv: [1109.4829](https://arxiv.org/abs/1109.4829) [[hep-ph](#)].
- [194] B. Fuks, M. Klasen, D. R. Lamprea, and M. Rothering, “Precision predictions for electroweak superpartner production at hadron colliders with RESUMINO,” *Eur. Phys. J. C*, vol. 73, p. 2480, 2013. DOI: [10.1140/epjc/s10052-013-2480-0](https://doi.org/10.1140/epjc/s10052-013-2480-0). arXiv: [1304.0790](https://arxiv.org/abs/1304.0790) [[hep-ph](#)].
- [195] P. Artoisenet, R. Frederix, O. Mattelaer, and R. Rietkerk, “Automatic spin-entangled decays of heavy resonances in Monte Carlo simulations,” *JHEP*, vol. 03, p. 015, 2013. DOI: [10.1007/JHEP03\(2013\)015](https://doi.org/10.1007/JHEP03(2013)015). arXiv: [1212.3460](https://arxiv.org/abs/1212.3460) [[hep-ph](#)].
- [196] S. Frixione, E. Laenen, P. Motylinski, and B. R. Webber, “Angular correlations of lepton pairs from vector boson and top quark decays in Monte Carlo simulations,” *JHEP*, vol. 04, p. 081, 2007. DOI: [10.1088/1126-6708/2007/04/081](https://doi.org/10.1088/1126-6708/2007/04/081). arXiv: [hep-ph/0702198](https://arxiv.org/abs/hep-ph/0702198).
- [197] ATLAS Collaboration, “Performance of electron and photon triggers in ATLAS during LHC Run 2,” *Eur. Phys. J. C*, vol. 80, p. 47, 2020. DOI: [10.1140/epjc/s10052-019-7500-2](https://doi.org/10.1140/epjc/s10052-019-7500-2). arXiv: [1909.00761](https://arxiv.org/abs/1909.00761) [[hep-ex](#)].
- [198] ATLAS Collaboration, “Performance of the ATLAS muon triggers in Run 2,” *JINST*, vol. 15, P09015, 2020. DOI: [10.1088/1748-0221/15/09/p09015](https://doi.org/10.1088/1748-0221/15/09/p09015). arXiv: [2004.13447](https://arxiv.org/abs/2004.13447) [[hep-ex](#)].
- [199] Y. Mino, “Search for higgsinos with compressed mass spectra using low-momentum mildly-displaced tracks with the ATLAS detector,”
- [200] ATLAS Collaboration, *The Optimization of ATLAS Track Reconstruction in Dense Environments*, ATL-PHYS-PUB-2015-006, 2015. [Online]. Available: <https://cds.cern.ch/record/2002609>.
- [201] R. Frühwirth, “Application of Kalman filtering to track and vertex fitting,” *Nucl. Instr. and Methods in Phys. Research Sec. A*, vol. 262, p. 444, 1987.
- [202] ATLAS Collaboration, *ATLAS Track Reconstruction – General Overview*, 2023. [Online]. Available: <https://atlassoftwaredocs.web.cern.ch/trackingTutorial/idooverview/>.
- [203] ATLAS Collaboration, “Reconstruction of primary vertices at the ATLAS experiment in Run 1 proton–proton collisions at the LHC,” *Eur. Phys. J. C*, vol. 77, p. 332, 2017. DOI: [10.1140/epjc/s10052-017-4887-5](https://doi.org/10.1140/epjc/s10052-017-4887-5). arXiv: [1611.10235](https://arxiv.org/abs/1611.10235) [[hep-ex](#)].
- [204] W. Wolfgang, *Adaptive Vertex Reconstruction*, 2008. [Online]. Available: <https://cds.cern.ch/record/1166320>.
- [205] ATLAS Collaboration, “Electron and photon performance measurements with the ATLAS detector using the 2015–2017 LHC proton–proton collision data,” *JINST*, vol. 14, P12006, 2019. DOI: [10.1088/1748-0221/14/12/P12006](https://doi.org/10.1088/1748-0221/14/12/P12006). arXiv: [1908.00005](https://arxiv.org/abs/1908.00005) [[hep-ex](#)].

- [206] W. Lampl *et al.*, *Calorimeter Clustering Algorithms: Description and Performance*, ATL-LARG-PUB-2008-002, 2008. [Online]. Available: <https://cds.cern.ch/record/1099735>.
- [207] ATLAS Collaboration, *Improved electron reconstruction in ATLAS using the Gaussian Sum Filter-based model for bremsstrahlung*, ATLAS-CONF-2012-047, 2012. [Online]. Available: <https://cds.cern.ch/record/1449796>.
- [208] ATLAS Collaboration, “Electron and photon energy calibration with the ATLAS detector using LHC Run 1 data,” *Eur. Phys. J. C*, vol. 74, p. 3071, 2014. DOI: [10.1140/epjc/s10052-014-3071-4](https://doi.org/10.1140/epjc/s10052-014-3071-4). arXiv: [1407.5063](https://arxiv.org/abs/1407.5063) [hep-ex].
- [209] ATLAS Collaboration, “Electron reconstruction and identification in the ATLAS experiment using the 2015 and 2016 LHC proton–proton collision data at $\sqrt{s} = 13$ TeV,” *Eur. Phys. J. C*, vol. 79, p. 639, 2019. DOI: [10.1140/epjc/s10052-019-7140-6](https://doi.org/10.1140/epjc/s10052-019-7140-6). arXiv: [1902.04655](https://arxiv.org/abs/1902.04655) [hep-ex].
- [210] ATLAS Collaboration, “Muon reconstruction and identification efficiency in ATLAS using the full Run 2 pp collision data set at $\sqrt{s} = 13$ TeV,” *Eur. Phys. J. C*, vol. 81, p. 578, 2021. DOI: [10.1140/epjc/s10052-021-09233-2](https://doi.org/10.1140/epjc/s10052-021-09233-2). arXiv: [2012.00578](https://arxiv.org/abs/2012.00578) [hep-ex].
- [211] ATLAS Collaboration, “Jet reconstruction and performance using particle flow with the ATLAS Detector,” *Eur. Phys. J. C*, vol. 77, p. 466, 2017. DOI: [10.1140/epjc/s10052-017-5031-2](https://doi.org/10.1140/epjc/s10052-017-5031-2). arXiv: [1703.10485](https://arxiv.org/abs/1703.10485) [hep-ex].
- [212] M. Cacciari, G. P. Salam, and G. Soyez, “The anti- k_t jet clustering algorithm,” *JHEP*, vol. 04, p. 063, 2008. DOI: [10.1088/1126-6708/2008/04/063](https://doi.org/10.1088/1126-6708/2008/04/063). arXiv: [0802.1189](https://arxiv.org/abs/0802.1189) [hep-ph].
- [213] ATLAS Collaboration, “Performance of pile-up mitigation techniques for jets in pp collisions at $\sqrt{s} = 8$ TeV using the ATLAS detector,” *Eur. Phys. J. C*, vol. 76, p. 581, 2016. DOI: [10.1140/epjc/s10052-016-4395-z](https://doi.org/10.1140/epjc/s10052-016-4395-z). arXiv: [1510.03823](https://arxiv.org/abs/1510.03823) [hep-ex].
- [214] ATLAS Collaboration, “ATLAS b -jet identification performance and efficiency measurement with $t\bar{t}$ events in pp collisions at $\sqrt{s} = 13$ TeV,” *Eur. Phys. J. C*, vol. 79, p. 970, 2019. DOI: [10.1140/epjc/s10052-019-7450-8](https://doi.org/10.1140/epjc/s10052-019-7450-8). arXiv: [1907.05120](https://arxiv.org/abs/1907.05120) [hep-ex].
- [215] S. D. Ellis and D. E. Soper, “Successive combination jet algorithm for hadron collisions,” *Phys. Rev. D*, vol. 48, pp. 3160–3166, 7 1993. DOI: [10.1103/PhysRevD.48.3160](https://doi.org/10.1103/PhysRevD.48.3160). [Online]. Available: <https://link.aps.org/doi/10.1103/PhysRevD.48.3160>.
- [216] S. Catani, Y. Dokshitzer, M. Seymour, and B. Webber, “Longitudinally-invariant k_\perp -clustering algorithms for hadron-hadron collisions,” *Nuclear Physics B*, vol. 406, no. 1, pp. 187–224, 1993.
- [217] M. Cacciari and G. P. Salam, “Pileup subtraction using jet areas,” *Physics Letters B*, vol. 659, no. 1, pp. 119–126, 2008.
- [218] ATLAS Collaboration, “Performance of missing transverse momentum reconstruction with the ATLAS detector using proton–proton collisions at $\sqrt{s} = 13$ TeV,” *Eur. Phys. J. C*, vol. 78, p. 903, 2018. DOI: [10.1140/epjc/s10052-018-6288-9](https://doi.org/10.1140/epjc/s10052-018-6288-9). arXiv: [1802.08168](https://arxiv.org/abs/1802.08168) [hep-ex].
- [219] ATLAS Collaboration, *Selection of jets produced in 13 TeV proton–proton collisions with the ATLAS detector*, ATLAS-CONF-2015-029, 2015. [Online]. Available: <https://cds.cern.ch/record/2037702>.

- [220] ATLAS Collaboration, “Search for electroweak production of supersymmetric particles in final states with two or three leptons at $\sqrt{s} = 13$ TeV with the ATLAS detector,” *Eur. Phys. J. C*, vol. 78, p. 995, 2018. DOI: [10.1140/epjc/s10052-018-6423-7](https://doi.org/10.1140/epjc/s10052-018-6423-7). arXiv: [1803.02762](https://arxiv.org/abs/1803.02762) [hep-ex].
- [221] ATLAS Collaboration, *Formulae for Estimating Significance*, ATL-PHYS-PUB-2020-025, 2020. [Online]. Available: <https://cds.cern.ch/record/2736148>.
- [222] ATLAS Collaboration, “Measurement of the WW cross section in $\sqrt{s} = 7$ TeV pp collisions with the ATLAS detector and limits on anomalous gauge couplings,” *Phys. Lett. B*, vol. 712, p. 289, 2012. DOI: [10.1016/j.physletb.2012.05.003](https://doi.org/10.1016/j.physletb.2012.05.003). arXiv: [1203.6232](https://arxiv.org/abs/1203.6232) [hep-ex].
- [223] ATLAS Collaboration, *Prospects for Higgs boson searches using the $H \rightarrow WW^{(*)} \rightarrow \ell\nu\ell\nu$ decay mode with the ATLAS detector at 10 TeV*, ATL-PHYS-PUB-2010-005, 2010. [Online]. Available: <https://cds.cern.ch/record/1270568>.
- [224] ATLAS Collaboration, *Measurement of $W^{\pm}Z$ production cross sections and gauge boson polarisation in pp collisions at $\sqrt{s} = 13$ TeV with the ATLAS detector*, ATLAS-CONF-2018-034, 2018. [Online]. Available: <https://cds.cern.ch/record/2630187>.
- [225] ATLAS Collaboration, *Multi-boson simulation for 13 TeV ATLAS analyses*, ATL-PHYS-PUB-2016-002, 2016. [Online]. Available: <https://cds.cern.ch/record/2119986>.
- [226] J. Butterworth *et al.*, “PDF4LHC recommendations for LHC Run II,” *J. Phys. G*, vol. 43, p. 023 001, 2016. DOI: [10.1088/0954-3899/43/2/023001](https://doi.org/10.1088/0954-3899/43/2/023001). arXiv: [1510.03865](https://arxiv.org/abs/1510.03865) [hep-ph].
- [227] ATLAS Collaboration, “Evidence for the production of three massive vector bosons with the ATLAS detector,” *Phys. Lett. B*, vol. 798, p. 134 913, 2019. DOI: [10.1016/j.physletb.2019.134913](https://doi.org/10.1016/j.physletb.2019.134913). arXiv: [1903.10415](https://arxiv.org/abs/1903.10415) [hep-ex].
- [228] ATLAS Collaboration, “Observation of WWW Production in pp Collisions at $\sqrt{s} = 13$ TeV with the ATLAS Detector,” *Phys. Rev. Lett.*, vol. 129, p. 061 803, 2022. DOI: [10.1103/PhysRevLett.129.061803](https://doi.org/10.1103/PhysRevLett.129.061803). arXiv: [2201.13045](https://arxiv.org/abs/2201.13045) [hep-ex].
- [229] CMS Collaboration, “Observation of the production of three massive gauge bosons at $\sqrt{s} = 13$ TeV,” *Phys. Rev. Lett.*, vol. 125, p. 151 802, 2020. DOI: [10.1103/PhysRevLett.125.151802](https://doi.org/10.1103/PhysRevLett.125.151802). arXiv: [2006.11191](https://arxiv.org/abs/2006.11191) [hep-ex].
- [230] ATLAS Collaboration, “Muon reconstruction performance of the ATLAS detector in proton–proton collision data at $\sqrt{s} = 13$ TeV,” *Eur. Phys. J. C*, vol. 76, p. 292, 2016. DOI: [10.1140/epjc/s10052-016-4120-y](https://doi.org/10.1140/epjc/s10052-016-4120-y). arXiv: [1603.05598](https://arxiv.org/abs/1603.05598) [hep-ex].
- [231] ATLAS Collaboration, “Jet energy scale measurements and their systematic uncertainties in proton–proton collisions at $\sqrt{s} = 13$ TeV with the ATLAS detector,” *Phys. Rev. D*, vol. 96, p. 072 002, 2017. DOI: [10.1103/PhysRevD.96.072002](https://doi.org/10.1103/PhysRevD.96.072002). arXiv: [1703.09665](https://arxiv.org/abs/1703.09665) [hep-ex].
- [232] ATLAS Collaboration, “Measurement of the Inelastic Proton–Proton Cross Section at $\sqrt{s} = 13$ TeV with the ATLAS Detector at the LHC,” *Phys. Rev. Lett.*, vol. 117, p. 182 002, 2016. DOI: [10.1103/PhysRevLett.117.182002](https://doi.org/10.1103/PhysRevLett.117.182002). arXiv: [1606.02625](https://arxiv.org/abs/1606.02625) [hep-ex].
- [233] G. Cowan, K. Cranmer, E. Gross, and O. Vitells, “Asymptotic formulae for likelihood-based tests of new physics,” *Eur. Phys. J. C*, vol. 71, p. 1554, 2011. DOI: [10.1140/epjc/s10052-011-1554-0](https://doi.org/10.1140/epjc/s10052-011-1554-0). arXiv: [1007.1727](https://arxiv.org/abs/1007.1727) [physics.data-an], Erratum: *Eur. Phys. J. C*, vol. 73, p. 2501, 2013. DOI: [10.1140/epjc/s10052-013-2501-z](https://doi.org/10.1140/epjc/s10052-013-2501-z).
- [234] F. James and M. Roos, “Minuit: A System for Function Minimization and Analysis of the Parameter Errors and Correlations,” *Computer Physics Communications*, vol. 10, p. 343, 1975.

- [235] M. Baak, G. Besjes, D. Côté, A. Koutsman, J. Lorenz, and D. Short, “HistFitter software framework for statistical data analysis,” *Eur. Phys. J. C*, vol. 75, p. 153, 2015. DOI: [10.1140/epjc/s10052-015-3327-7](https://doi.org/10.1140/epjc/s10052-015-3327-7). arXiv: [1410.1280](https://arxiv.org/abs/1410.1280) [hep-ex].
- [236] L. Lista, *Statistical Methods for Data Analysis in Particle Physics*. Springer, 2016, vol. 909. DOI: [10.1007/978-3-319-20176-4](https://doi.org/10.1007/978-3-319-20176-4).
- [237] A. Wald, “Tests of Statistical Hypotheses Concerning Several Parameters When the Number of Observations is Large,” *American Mathematical Society*, vol. 54, p. 426, 1943.
- [238] R. D. Cousins, J. T. Linnemann, and J. Tucker, “Evaluation of three methods for calculating statistical significance when incorporating a systematic uncertainty into a test of the background-only hypothesis for a Poisson process,” *Nucl. Instrum. Meth. A*, vol. 595, no. 2, p. 480, 2008. DOI: [10.1016/j.nima.2008.07.086](https://doi.org/10.1016/j.nima.2008.07.086). arXiv: [physics/0702156](https://arxiv.org/abs/physics/0702156) [physics.data-an].
- [239] CMS Collaboration, “Search for disappearing tracks in proton–proton collisions at $\sqrt{s} = 8$ TeV,” *JHEP*, vol. 01, p. 096, 2015. DOI: [10.1007/JHEP01\(2015\)096](https://doi.org/10.1007/JHEP01(2015)096). arXiv: [1411.6006](https://arxiv.org/abs/1411.6006) [hep-ex].
- [240] ATLAS Collaboration, *SUSY July 2024 Summary Plot Update*, ATL-PHYS-PUB-2024-014, 2024. [Online]. Available: <https://cds.cern.ch/record/2904978>.
- [241] High Luminosity LHC Project, *The HL-LHC project*, 2022. [Online]. Available: <https://hilumilhc.web.cern.ch/content/hl-lhc-project>.
- [242] ATLAS Collaboration, *The HL-LHC project*, 2017. [Online]. Available: <https://cds.cern.ch/record/2285580>.